Transmission electron microscopy studies and simulations of heteroepitaxial diamond nucleation on Ir/YSZ/Si

Thesis

for the obtainment of the PhD degree
in Natural Sciences (Dr. rer. nat.)

submitted by

Rosaria Brescia

Chair for Experimental Physics IV
Institute for Physics
Faculty of Mathematics and Natural Sciences
University of Augsburg

First reviewer: Prof. Dr. Bernd Stritzker
Second reviewer: Prof. Dr. Ferdinand Haider

Oral exam date: December 11th, 2013

Contents

Introduction

The last decades have seen the emergence of diamond not only as a gemstone or an abrasive, but also as a promising material for many fields, ranging from electronics and optics to radiation detection, biosensing and electrochemistry. The wide range of potential applications depends on the peculiar properties of this material, such as extreme hardness, wide bandgap, high thermal conductivity, low thermal expansion, chemical inertness, transparency in a broad range of the electromagnetic spectrum and high carrier mobility. All these properties derive from its particular chemical and structural characteristics. On the other hand, the feasibility of the technological employment of diamond is based on the emergence of synthesis methods that, starting from the middle of the last century, have developed up to the industrial scale.

Depending on the envisioned use, the material quality can be tailored by choosing the suitable production technique and the specific process conditions. Most of the existing synthesis methods can be divided into high pressure, high temperature (HPHT) and chemical vapour deposition (CVD) techniques, which are already employed for commercial production of diamond crystals (Figure 1) [Adamas, Advanced Diamond Technologies, AOTC, Crystallume, Element Six, Komet-Rhobest, New Age Diamonds, Sumitomo]. In particular, for optical and electronic applications high purity and structural quality are required, which are allowed only by the plasma-assisted CVD technique. In particular, the competitiveness on the market would require single-crystal quality diamond films deposited on large non-diamond substrates. Several substrate systems have been explored so far, and the structural quality of the resulting diamond films has been thoroughly investigated. In parallel to this, the search for a suitable nucleation procedure led to the introduction of the bias-enhanced nucleation (BEN) treatment, which is the only method allowing the early generation of a high density of epitaxially oriented diamond grains.

Among the various systems for the fabrication of single-crystal diamond layers, thin epitaxial iridium films on top of several substrates constitute one of the most promising candidates. In particular, in view of a large scale production, the use of silicon as a single-crystal

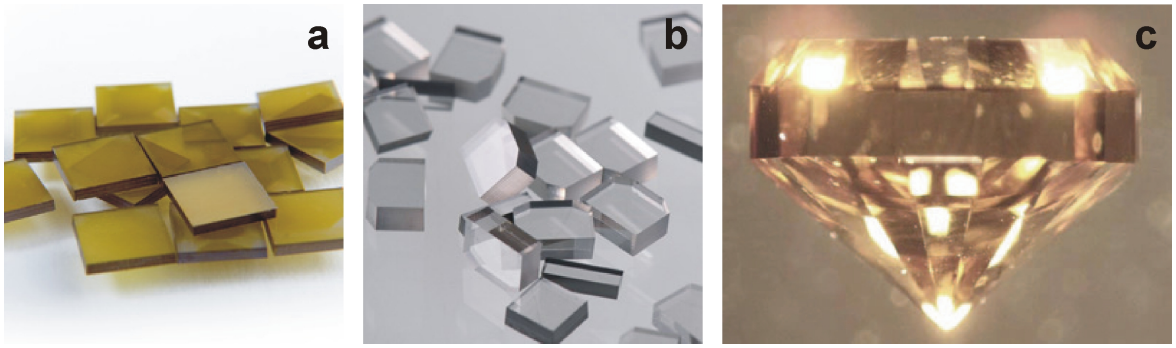

Figure 1 – Single-crystal diamonds fabricated via (a) high pressure, high temperature (HPHT) synthesis and (b-c) chemical vapour deposition (CVD) methods [Element Six, Yan(04)]. These crystals, exhibiting high transparency and (b-c) purity, are smaller than 1 cm^3.

bulk substrate would be the most convenient option, due to the availabilty of high quality material at low cost. Besides this, silicon also shows a good match in terms of thermal expansion coefficient with diamond, which is of fundamental importance when the process temperatures necessary for single-crystal diamond CVD growth are taken into account. Following these ideas, a multilayer system based on a thin Ir layer on a bulk Si substrate, with an intermediate yttria-stabilised zirconia (YSZ) buffer layer, has been proposed for large area diamond deposition. This complex structure offers a range of favourable characteristics in view of single-crystal diamond depositon, but at the same time requires an accurate control of all the intermediate fabrication steps. The orientation and microstructural quality of all the layers composing this system need to be investigated. Moreover, special attention should be devoted to the BEN treatment on Ir.

The studies described in the present PhD work are focussed on the analysis of the Ir/YSZ/Si multilayer system for BEN and deposition of single-crystal diamond, mainly by means of transmission electron microscopy (TEM). This technique is indeed one of the most promising in material science for the study of the morphology, crystal structure, composition and chemical binding, with high spatial resolution, of a wide range of materials. While X-ray diffraction (XRD) analyses provide precious averaged information on the crystalline and epitaxial quality of thin films, from which quantitative parameters (*e.g.*, tilt and twist) can be extracted to describe the orientational spread in a thin film, TEM is able to monitor the structure evolution accompanying macroscopic changes in texture or mosaic spread at a sub-nanometer level. For instance, former XRD studies on a wide range of samples have demonstrated a decrease in structural defect density within cubic YSZ films on Si(001) following high temperature thermal treatment. TEM analyses are therefore required to investigate this effect by direct imaging of the structural defects and their evolution with each thermal treatment step. Moreover, the arrangement of the different texture components within tetragonal YSZ films on Si(001) shows fundamental differences with respect to former literature reports, as deduced by XRD analyses. Therefore, TEM investigations are presented here, aiming at identification of the different components and at monitoring their evolution under different conditions.

TEM also offers the unique opportunity to directly image extremely small features, which are hardly detected by techniques with lower spatial resolution. This makes it, for instance, a valuable tool for the study of BEN of diamond on Ir substrates. As mentioned above, Ir is essentially the only technologically relevant substrate that facilitates nucleation of heteroepitaxial diamond grains with a sufficiently high density and degree of alignment, so that the film can transform into a single-crystal layer. This is due to peculiar nucleation mechanisms that are, for instance, profoundly different from the ones taking place on the more commonly employed Si substrates. Several studies have been focussed up to now on this topic, in order to get a better control on the nucleation stage and also to deduce general information concerning the promising diamond/Ir system. The aim of the present study was to employ TEM, and in particular high resolution TEM (HRTEM), to deduce some general aspects of BEN of diamond on Ir and monitor the first stages of diamond growth following BEN. In addition to this, further experiments and simulations were performed to clarify the nature of the BEN product on Ir, to suggest possible mechanims explaining the ordered arrangement of individual epitaxial grains within localized areas and, on the other hand, to motivate the different morphologies observed for the nucleation patterns, formed under apparently similar BEN process conditions. This part of the work will complete the picture available up to now and allow to formulate a comprehensive model of BEN on Ir.

Chapter 1

Fundamentals

1.1 Diamond and other carbon-based materials

Carbon (C) is a unique element in the periodic table, as it is able to exist in three different hybridisations (sp^1, sp^2, sp^3). This is the reason for the existence of several allotropes of pure carbon. Diamond, graphite, graphene, carbon nanotubes and the so-called diamond-like carbons (DLCs) are among the best known carbon-based materials (see Figure 1.1). Due to the different bonding nature, in some cases leading to ordered structures, these materials exhibit extremely different properties.

Diamond is a crystalline form of pure carbon in which each atom is tetrahedrally bonded to its four nearest neighbours in an sp^3 configuration. The nearest-neighbour distance between the covalently bonded carbon atoms is 1.54 Å at room temperature [Field(79)]. The crystal structure can be viewed as two interpenetrating face-centered cubic (fcc) structures, displaced along the body diagonal by 1/4 of its length. The unrivalled set of properties of diamond derives from its strong directional covalent bonds and from its atomic density, which is the highest among the known materials.

Graphite is the only other three-dimensional crystalline form of pure carbon, where all the atoms are in sp^2 configuration, each one forming strong in-plane bonds with its three nearest neighbours. The remaining electron forms an additional in plane π-bonding which reduces the bond length. Much weaker van der Waals forces are responsible for the bonding between different sheets. The ideal crystal structure of graphite consists therefore of parallel layers in which the atoms are arranged in a hexagonal structure, with a nearest-neighbour distance shorter than in diamond (1.42 Å), while the distance between neighbouring layers is 3.35 Å. Due to this planar structure, graphite is highly anisotropic, *e.g.* showing metallic behaviour in the basal plane and poor electrical conductivity perpendicular to it.

Two-dimensional crystalline carbon materials, like graphite monolayers (graphene) and fullerenes, have been discovered within the last three decades. Among them, graphene is undoubtedly one of the most intruiguing materials as, due to its bidimensional structure, it

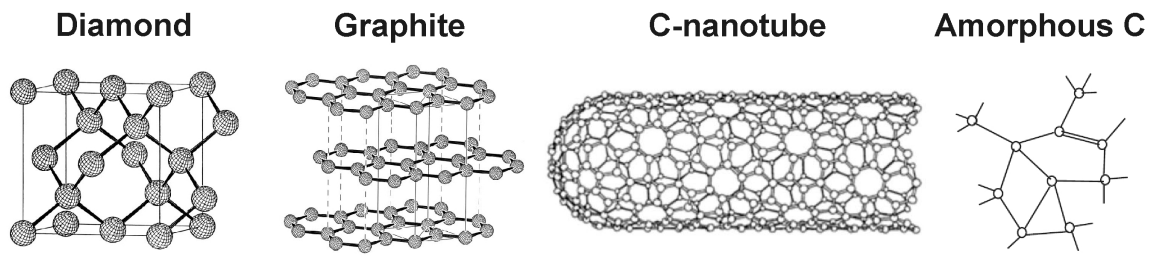

Figure 1.1 – Schematic drawings of some of the best-known carbon-based materials.

shows peculiar electronic and optical properties, coupled to interesting mechanical characteristics [Geim(07), Novoselov(05), Bonaccorso(10)]. Only few years after it has been reported for the first time, graphene represents at the same time a unique field for fundamental physics investigations and a promising material, *e.g.* for electronic devices and transparent electrodes, due to its optical transparency and high carrier mobility. Carbon nanotubes (CNTs), known for a longer time, deserve the attention of an increasing portion of the scientific community [Grobert(07)]. Ideal CNTs may be described as narrow strips of graphene rolled up to form cylinders, forming a one-dimensional structure with a nanometre-size diametre and a length up to the centimetres range. Structures comprising only one cylinder are termed single-walled nanotubes (SWNTs), whereas multiwalled nanotubes (MWNTs) contain two or more concentric graphene cylinders. Ideal SWNTs show different possible configurations, depending on how the graphene sheet is rolled up. Depending on several factors, *e.g.* configuration, aspect ratio, doping level and degree of order, CNTs can have extremely variable mechanical and electronic properties and are therefore promising for many applications.

Further carbon-based materials having a major role in today's science and technology are the DLCs, a class of amorphous carbons with a substantial sp^3 content (higher than $\sim$20%) [Robertson(02), Casiraghi(07)]. DLCs can show extremely variable properties depending on several factors, like the sp^3 content, the clustering and the orientation of the sp^2 phase and the hydrogen or nitrogen content. DLCs can have properties close to those of diamond, as high density and hardness, optical transparency and a wide bandgap, but these are achieved in disordered thin films. The major advantage of DLC layers compared to diamond films is the much lower cost, mainly due to the higher deposition rate at lower temperature, while they are limited in thickness by their compressive stress. DLCs are already employed as coatings, *e.g.* for magnetic storage disks, wear-resistant and antireflective coatings for tribological tools, razor blades, and they are also promising for the realization of biomedical and microelectromechanical systems.

1.2 Properties and applications of diamond

The increasing interest in the use of diamond for a huge range of applications derives from its unique properties [Field(79), Dischler(98), Wort(08)]. The best known characteristic of diamond is its unreached hardness (see Table 1.1) which, together with its extremely low friction coefficient, makes it the ideal material for coating of cutting tools.

The high thermal conductivity at room temperature (about 5 times as high as that of copper), combined with its wide bandgap, the high breakdown electric field and the high carrier mobilities and saturation velocities, make diamond extremely promising for applications in high-temperature and high-power electronics, where large amounts of heat are generated over small areas, creating a huge heat flux. The use of diamond removes in some cases the need of an add-on cooling system, since heat dissipation takes place through the material itself. Diamond is an interesting alternative to its major competitors as it can be used to fabricate heat spreaders for high-power laser diodes, switches, high-frequency FETs and also for submounts for integrated circuits and as a substrate material for multi-chip modules.

A further application field of diamond is infrared (IR) optics. Together with its broadband optical transparency (at wavelegths longer than 225 nm, with weak absorption in the IR due to two phonon processes), the mechanical strength, the high heat conductivity and the low expansion coefficient of diamond are ideal for the fabrication of windows for high power IR lasers. The transparency of diamond in a wide range of X-ray wavelengths, and the possibility of fabricating stable thin diamond films, makes it also competitive with the mature technologies based on beryllium, polymer and boron nitride for the realization of windows for X-ray detectors, X-ray tubes and X-ray litography membranes.

Lattice constant	3.567 Å
Atomic density	$1.77 \cdot 10^{23}$ cm^{-3}
Specific gravity	3.515 g cm^{-3}
Young's modulus	1050 GPa
Hardness (Knoop)	100 GPa
Bandgap	5.47 eV
Breakdown electric field	10^7 V cm^{-1}
Electron saturation velocity	$2{\cdot}10^7$ cm s^{-1}
Hole saturation velocity	$0.8{\cdot}10^7$ cm s^{-1}
Hole mobility	3800 cm^2 V^{-1} s^{-1}
Electron mobility	4500 cm^2 V^{-1} s^{-1}
Thermal conductivity	$>$ 20 W cm^{-1} K^{-1}
Thermal expansion coefficient	$0.8{\cdot}10^{-6}$ K^{-1}

Table 1.1 – Salient properties of natural diamond (at room temperature) [Field(79), Dischler(98), Wort(08)].

The use of diamond for fabrication of electronics is limited so far by the lack of a donor with acceptably low activation energy. Anyway, the presence of boron as deep acceptor makes it possible to realize temperature and pressure sensors for high temperatures and harsh environments. Metal-diamond-metal structures can also be used as photoconductive detectors for ultraviolet (UV), high energy radiation and particles, due to the wide bandgap and radiation hardness of diamond. Diamond has been lately investigated also for the fabrication of biosensors, due to its chemical inertness, biocompatibility and wide potential window, useful for electrochemical applications.

1.3 Synthesis of diamond

The huge number of potential applications of diamond requires a material with variable, but reproducible, characteristics. The scarce occurence and the small size of diamond stones in nature, together with the broad variation of their quality and impurity content, made it necessary to find methods to synthesise this attractive material.

In order to understand the synthesis techniques of diamond, it is fundamental to keep in mind the phase diagram of carbon (Figure 1.2). Natural diamonds form in the earth's upper mantle, at depths exceeding ∼150 km, in high pressure and high temperature conditions. These are the conditions in which diamond is stable (pressures and temperatures higher than 40 kbar and 1300℃, respectively), while graphite is the stable crystalline form of pure carbon at room temperature and atmospheric pressure. There are two major classes of techniques to synthesise diamond, both introduced in the early 1950s, working either in the stability region of diamond (high pressure, high temperature, HPHT) or at low pressures (chemical vapour deposition, CVD) [Prelas(98), Dischler(98)].

In HPHT techniques solid non-diamond carbon is transformed into diamond at high pressures and temperatures (p≥60 kbar, T∼1400℃), mimicking the natural formation process. However, it is not enough to bring graphite or other carbon-based materials into the diamond stability region to have the conversion, since a high energy barrier has to be overcome to break the carbon-carbon bonds. Metallic catalysts like nickel, iron and cobalt are therefore mixed with the carbon precursor in the HPHT reactors in order to achieve diamond formation from a molten phase. The stones synthesised via this technique have maximum sizes of ∼1 cm^3 [Abbaschian(05)] and a non-controllable content of impurities. Therefore alternative methods are necessary for applications needing higher purity and larger dimensions.

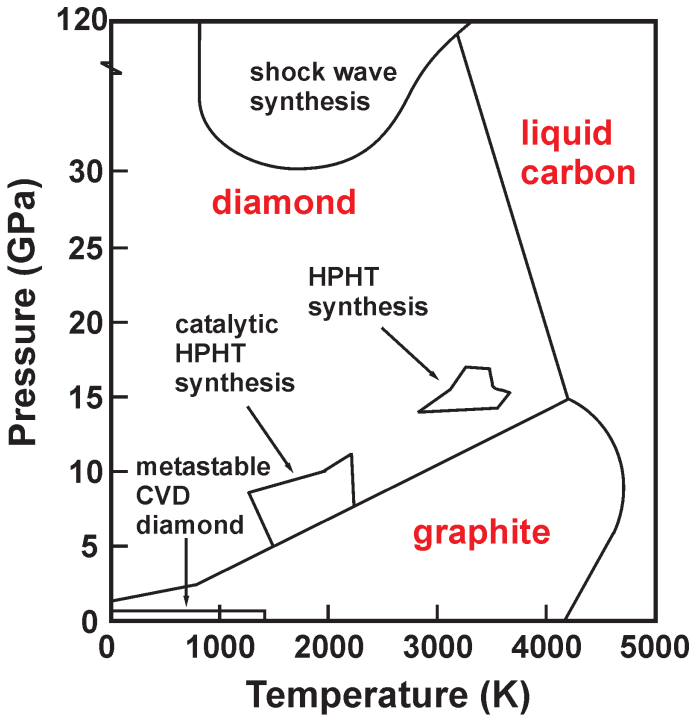

Figure 1.2 – Phase diagram of elemental carbon (based on [Bundy(89)]).

A technologically relevant alternative to the HPHT synthesis of diamond is offered by the CVD methods, which allow to deposit diamond films at sub-atmospheric pressures (1–1000 mbar) and at relatively low temperatures (500–1200°C) starting from the gas phase. The feed gas mixture in a diamond CVD process must contain both a carbon-containing species and a component (usually hydrogen) which stabilises the sp^3 diamond surface and etches non-diamond carbon phases. As a consequence, the diamond deposition process takes place in delicate conditions of an equilibrium between etching of the non-diamond species via atomic hydrogen and growth by means of hydrocarbon species. Other gases may be added to the feed gas in order to dope intentionally the material or to obtain different morphologies and, in the case of nitrogen, to increase the growth rate. The activation of the gas components is usually achieved thermally or via an intense electric field, generating a plasma. The substrate surface has to be kept at high temperature, but lower than that of the gas phase: while the latter has to be higher than 1500°C, for the generation of both the diamond growth species and the atomic hydrogen, the substrate temperature needs to be lower, so as to hinder diamond graphitisation.

The industrial application of diamond has been made possible by the good homogeneity, the relatively high growth rate and the up-scaling potential of the hot filament CVD (HFCVD) and microwave plasma CVD (MWPCVD) techniques. In the first technique the gas activation is obtained thermally, by means of a heated refractory metal wire located close to the substrate. The substrate temperature is typically 850°C and the employed gas mixture varies from 0.1 to 2 vol% CH_4 in H_2. The typical growth rate achievable is in the order of 1 μm/h. HFCVD is nowadays largely used for the deposition of diamond protective films on cutting tools and wear parts, having complex shapes or large areas. Moreover the relatively low activation temperatures required make it more convenient for the deposition on temperature-sensitive substrates.

The activation in MWPCVD techniques is obtained via the transfer of microwave energy to the gas phase: firstly the microwave electric field causes electron heating, followed by the transfer of the electron energy to the neutral gas, ending up in the dissociation of the molecules, the formation of active species and the production of secondary electrons,

which is necessary to ignite and sustain the discharge. Most MWPCVD reactors for diamond deposition use 2.45 GHz microwaves, due to the availability of components complying with international regulations. Independent of the particular reactor geometry, MWPCVD is intrinsically the most flexible technique in terms of the variety of gas precursors usable for diamond growth. It is essential for successful diamond deposition that the stoichiometric ratios between C, H and O are included in a certain region of the C-H-O triangular diagram by Bachmann [Bachmann(91)], independent of the particular precursors used. A wide range of growth rates and material characteristics can be obtained using MWPCVD depending on parameters like CH_4 concentration, temperature, gas pressure and flow, substrate material and microwave power. Anyway, undoubtedly MWPCVD is the technique allowing the deposition of the highest purity and structural quality diamond films. The main disadvantage of MWPCVD as compared to HFCVD is the sensitivity to any small object, tip or edge inside the reactor, which makes it inconvenient for the deposition of films on complex-shaped substrates. A major step towards the mass production of this material is for sure represented by the developing MWPCVD techniques working at 915 MHz, which are intrinsically better suited for deposition at higher rates on larger areas.

1.4 Heteroepitaxial growth of diamond

Both HFCVD and MWPCVD can be used for the deposition of large area polycrystalline films, formed by several μm-sized grains, which can be randomly oriented or exhibit a preferential orientation. In the last decade many studies and applications concerned also nano- and ultranano-crystalline films, *i.e.* films formed by randomly oriented grains with sizes in the 100 nm and 10 nm range, respectively. The presence of grain boundaries in these kinds of materials would be detrimental for electronics or optics, where high structural quality and purity are of primary importance. For these applications, the use of monocrystalline diamond is preferable. MWPCVD techniques are the most adequate for the deposition of electronic or optical grade single-crystal films on HPHT diamond stones (homoepitaxial films) or on foreign substrates (heteroepitaxial films).

Homoepitaxial CVD layers have recently shown extremely high electronic quality [Isberg(02)]. Nevertheless, the small dimensions of the substrates are still a major drawback for the mass production of this material and up to now, despite the large number of studies addressing this issue, wafer-size homoepitaxial single crystals have not yet been produced successfully. Heteroepitaxial growth of diamond remains therefore the only viable solution for the production of large area single-crystal diamond films for electronics. Heteroepitaxy is the deposition of a crystalline material on a likewise crystalline substrate consisting of a different material, with a well-defined orientation between the planes forming the interface and two crystallographic directions in the interface plane of the overlayer and the substrate. The choice of an efficient nucleation method and a suitable substrate is fundamental for the quality of the resulting diamond films. In the last decades many studies have been performed in this field [Nebel(03), Prelas(98), Schreck(09)-2].

1.4.1 Nucleation methods

Nucleation is a critical step in the growth of a material on top of a foreign substrate. Due to its relatively high surface energy ($\approx$ 6 J/m^2 [Field(79)]), diamond tends to grow in a three-dimensional (Volmer-Weber) mode on all the technologically relevant substrates (see Section 1.6.1 and [vonKänel(95)]). A closed film is formed therefore only when individual grains coalesce. As a consequence, a nucleation method promoting the creation of a higher surface density of nuclei is the optimum, as it allows the formation of a closed film at a lower thickness.

One of the most commonly used methods for diamond nucleation is an abrasive pretreatment of the substrate, consisting in polishing with an abrasive paste or ultrasonication in a suspension of abrasive powder, before introduction into the deposition chamber. Various powders, in the 0.1-60 μm range size, have been used, like cubic boron nitride (c-BN), Al_2O_3 and SiC, but the use of diamond powder is more effective in increasing the diamond nucleation density. This result substantiates the idea that an important contribution to nucleation stems from residual diamond seeds. By this simple method the nucleation density can be increased from $\leq 10^6$ cm^{-2}, without pretreatment, to 10^{11} cm^{-2}. The disadvantage of the abrasive pretreatments consists in the possible contamination or damage of the substrate surface, which is certainly detrimental for optical and electronic applications.

Seeding or coating of the substrates with different carbonaceous materials have been also demonstrated to improve diamond nucleation up to an estimated value of 10^{10} cm^{-2} [Barnes(93)]. For this purpose carbon fibers and clusters, hydrocarbon oils and amorphous carbon layers have been used. The procedure consists either in placing the carbon compounds on the substrate surface before introduction into the CVD reactor or in performing an initial deposition step under conditions favouring the formation of non-diamond carbon. This method is preferable to scratching when the damage of the surface is undesirable, but it is anyway not suitable for heteroepitaxy, as it usually produces an amorphous or polycrystalline layer on the substrate surface.

Implantation of low energy ($\leq$25 keV) ions of different substances (Si, Ar, H and CH_4) into Si substrates has also been proved to be successful to facilitate diamond nucleation densities above 10^9 cm^{-2} [Yang(95), Zhang(00)]. Without producing an appreciable surface mechanical damage, the implantation methods lead to the formation of an amorphous C layer with a distribution of randomly oriented nm-sized diamond particles, if the appropriate parameters are used. One of the most important factors believed to influence the generation of diamond particles in these processes is the implantation-induced surface stress.

The formation of epitaxial diamond films with the mentioned nucleation treatments or even without any treatment has been reported only for peculiar systems. On the one hand, epitaxial diamond films with excellent orientation have been prepared without the need of any pretreatment on c-BN single crystals [Koizumi(90)]. This material is indeed extremely interesting as a substrate due to the low lattice mismatch with diamond (1.3%), the high similarity of the zinc-blende and the diamond structures, and the high interfacial adhesion energy. However, the small size of available c-BN single crystals poses the same problem as the size of diamond substrates for homoepitaxial growth. Diamond epitaxial films have been deposited also on (111) surfaces of Pt, after seeding with diamond powder and annealing at high temperature [Tachibana(97), Tachibana(97)-2]. The major problem consists in the formation, besides epitaxial diamond, of a second variant rotated by 60°, which is difficult to suppress.

Oriented diamond grains can be formed, under well-controlled conditions, by the bias-enhanced nucleation (BEN) method, introduced in 1991 by Yugo et al. [Yugo(91)]. This procedure consists in the application of a voltage between the plasma and the untreated substrate, so that the latter is bombarded by the ions in the plasma, resulting in a shallow implantation. Several combinations of voltages and CH_4 concentrations were employed, but the most established techniques use negative DC biasing and slightly increased CH_4 content in the feed gas ($\approx$ 5%). The BEN procedure, initially introduced for MWPCVD reactors, can be successfully applied also to HFCVD reactors and DC plasma CVD setups. Without a particularly careful control, BEN is able to generate high densities of diamond grains (up to 10^{11} cm^{-2}). On the other hand, if a good epitaxial alignment of the grains is desired, the BEN process has to be carefully monitored. Schreck et al. [Schreck(97), Schreck(01)-1] demonstrated that a well-defined BEN process time window exists for silicon (Si) substrates, outside of which the epitaxial orientation of the generated nuclei is lost. The BEN current has

to be monitored so as to be able to stop the process right before the surface gets completely covered by diamond. At this time the BEN voltage can be turned off and conditions for textured growth ensure that a good quality epitaxial film is formed.

1.4.2 Possible substrates for large-area single-crystal diamond deposition

There are several important aspects to be considered in the search for appropriate substrates for large-area single-crystal diamond growth. First of all, the material has to be stable in the harsh CVD diamond growth environment, which involves high temperature ($\geq$700°C for single-crystal growth) and continuous ion bombardment. Moreover, the crystal structure of the substrate has to be similar to the diamond structure and the lattice constant should be close to that of diamond. Last but not least, thinking about the technological aspect, large-area substrates have to be available in high quality at a reasonable cost.

A wide range of materials has been examined for epitaxial growth of diamond. As mentioned in the former section, the most promising substrate would be c-BN, but single crystals are available only in small sizes. Among the other examined substrates, Si is certainly promising, since large area Si wafers are available at relatively low cost. One limiting aspect of this system is the relatively high lattice mismatch with diamond (a_{dia} = 3.567 Å, a_{Si} = 5.431 Å). Epitaxial diamond layers with low roughness (120 nm) and relatively low tilt values (3.98°) have been obtained on Si(001) at a thickness of about 140 μm [Jiang(00)]. Cubic silicon carbide (3C-SiC) has also been investigated as substrate for (001) diamond deposition, having also quite a large mismatch to the lattice constant of diamond (a_{3C-SiC} = 4.359 Å). Epitaxial films with smooth surface and low mosaicity (0.62° tilt) have been obtained on this material at a thickness of about 300 μm [Kawarada(97)].

Several non-carbide-forming materials have also been tried as substrates for diamond growth. Among them, iridium (Ir) was definitely the most promising one, showing an unrivalled high density of epitaxial nuclei ($\geq 10^8$ cm^{-2}), following the BEN treatment, since the first experiments [Ohtsuka(96)]. Being Ir a precious and expensive metal, bulk Ir substrates do not represent a convenient solution for diamond deposition. It is known that high purity and crystalline quality Ir films can be deposited on top of single-crystal oxides. This is the reason why several studies in this field report of few hundred nanometres thick Ir films on top of oxide crystals, *e.g.* MgO [Ohtsuka(96), Tsubota(00), Fujisaki(03)], $SrTiO_3$[Schreck(99), Kono(05)], α-Al_2O_3 [Bednarski(03), Samoto(08)]. The first single-crystal diamond films on Ir showed mosaicity values much lower than the best ones so far reported on Si and 3C-SiC, with the further advantage of a much lower thickness [Schreck(01)-2]. This result can be explained considering the different mechanisms leading to texture improvement in the different systems [Schreck(02)]. Due to the exceptional high density and epitaxial orientation of the diamond nuclei formed via BEN on Ir, these films can be transformed into single-crystal layers, thanks to mechanisms leading to the disappearance of grain boundaries. This leads to a dramatic improvement in mosaic spread with the film thickness. The highly oriented films on Si and 3C-SiC are instead limited by the comparatively low density and poor epitaxial orientation of the diamond grains generated by the BEN process. As a consequence, the grain boundaries persist even at high film thickness so that these films are supposed to never loose their polycrystalline character. These are the reasons making Ir the most promising material for single-crystal diamond deposition.

1.4.3 The Ir/yttria-stabilised zirconia/Si system for single-crystal diamond growth

Among the cited systems for Ir deposition, Al_2O_3 was the first possibility proposed to scale-up the process of single-crystal diamond deposition [Dai(03)]. Nevertheless, one aspect

to be kept in mind for large area diamond deposition is the huge thermal stress building up when cooling down the system after the deposition process (T $\geq$700°C for epitaxial diamond deposition). Studies of the systems diamond/MgO, diamond/$SrTiO_3$ and diamond/Al_2O_3 show that the thermal stress developed in these systems is much higher than the one building up in a diamond/Si system[1] [Gsell(04)]. Therefore, the best solution seems to be a Si-based system, which would moreover be promising for scaling-up due to the availability of large area single-crystal Si wafers. It has to be kept in mind, however, that a chemical bonding between Ir and Si is undesirable, as many Ir silicides could be formed, with non-cubic crystal structures and melting points lower than 1000°C. Buffer layers are therefore necessary for high quality Ir film deposition on Si. Apart from the Ir/CaF_2/Si [Wu(03)] system, which is not technologically relevant due to the poor thermal stability of CaF_2, the most promising structure for applications at present is Ir/yttria-stabilised zirconia (YSZ)/Si [Gsell(04)], where YSZ efficiently acts as a barrier against the interaction of Ir and Si. This multilayer structure meets the most relevant requirements for the deposition of large area single-crystal diamond films: in addition to the extremely low mosaicity and single-crystal quality ensured by the presence of Ir, this structure is thermally stable under diamond deposition conditions, it shows a good matching of the thermal expansion coefficients, a good adhesion and, last but not least, it offers the possibility of scaling up.

1.5 Yttria-stabilised zirconia (YSZ)

Zirconia-based ceramics constitute a group of materials of high interest in materials science, since by alloying and heat treatments a wide range of crystalline structures and related mechanical properties can be obtained [Kisi(98)].

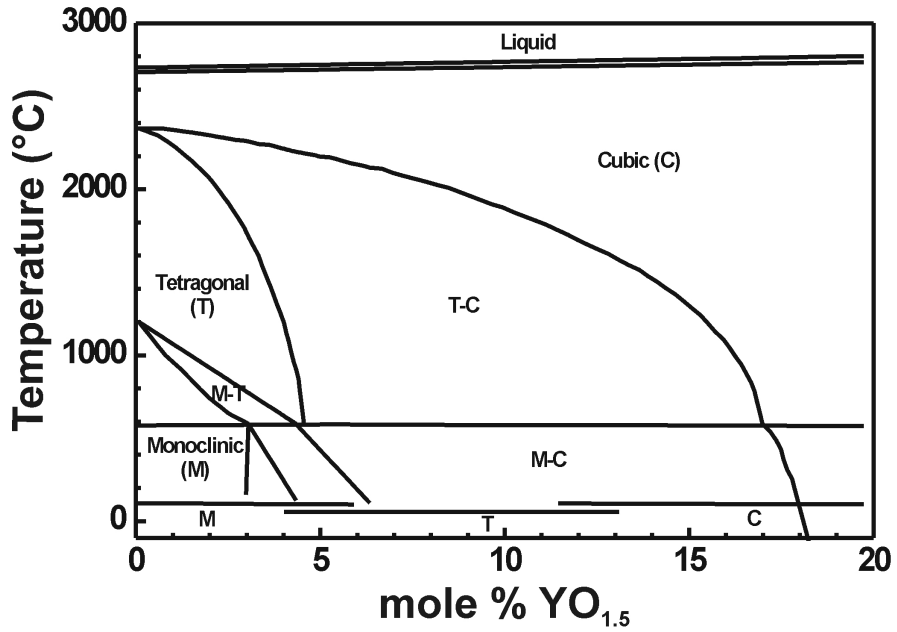

Figure 1.3 – Binary phase diagram of the zirconia-yttria system in the zirconia-rich region (based on [Kisi(98)]). Fields of metastable phases, occuring on rapid cooling, are also indicated at the bottom of the graph.

Pure stoichiometric zirconia (ZrO_2) has three polymorphic modifications at standard pressure (see x=0 axis in Figure 1.3). From 2377°C to the melting point at 2710°C ZrO_2 has the

[1] the thermal stress building up in thin intermediate layers can be neglected.

cubic fluorite structure (C) shown in Figure 1.4(a) (space group $Fm\bar{3}m$). At lower temperatures, between 1205°C and 2377°C, the stable phase of ZrO_2 has a tetragonal structure (T) (space group $P4_2/nmc$). This structure can be viewed as a slight distortion of the cubic fluorite structure due to a shift alternatively up or down along the [001] direction of the columns of oxygen atoms (as indicated by the arrows in Figure 1.4(b)). At lower temperature the structure changes to monoclinic (M), while at higher pressure orthorhombic structures have been observed.

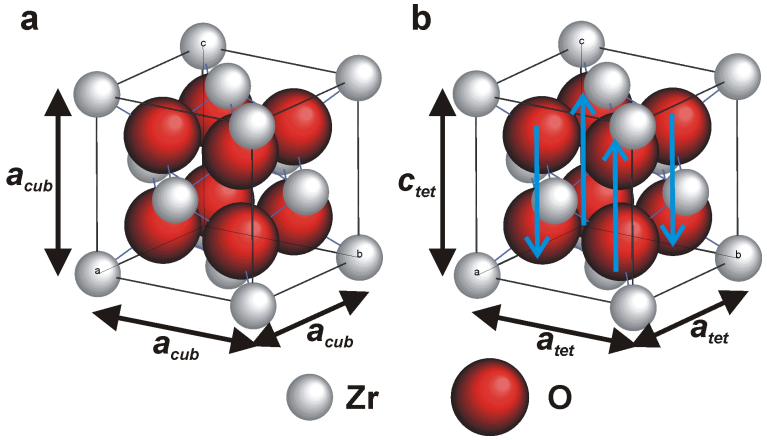

Figure 1.4 – (a) Cubic fluorite and (b) tetragonal structures of pure ZrO_2.

In order to stabilise at room temperature the high-temperature cubic and tetragonal phases, alloying of ZrO_2 with oxides containing cations having a lower valence than Zr is commonly performed. Among the most interesting of these alloys is yttria-stabilised zirconia (YSZ), where ZrO_2 is doped with yttria (Y_2O_3). The stabilisation of the high-temperature ZrO_2 phases is attributed to the oxygen vacancies formed to mantain charge neutrality. At the same time the yttrium atoms are incorporated by substituting for Zr atoms at the fluorite cation sites.

YSZ shows different crystal structures at room temperature, depending on the stoichiometric composition, as shown in Figure 1.3. For a molar fraction x of $YO_{1.5}$ in ZrO_2 between 0.12 and 0.30 the crystal structure is cubic, with the lattice constant a (in Å) at room temperature given by the equation [Kisi(98)]:

$$a = 5.1169 + 0.1526\ x \tag{1.1}$$

For lower yttria concentration ($0.04 \leq x \leq 0.13$) the structure is instead tetragonal, with the two different lattice parameters a and c given (in Å) by:

$$\begin{aligned} a &= 5.0801 + 0.3582\ x \\ c &= 5.1944 - 0.3045\ x \end{aligned} \tag{1.2}$$

It has to be underlined now that here and in the following discussions the face-centered cell is used instead of the primitive unit cell for easy comparison to the cubic phase. An useful visualization of the upper equations is given in Figure 1.5.

YSZ is an extremely interesting material for various applications, ranging from ceramic engineering to microelectronics. YSZ has also been proved to be an excellent buffer layer for the growth of high quality metal and oxide films and for high temperature superconducting thin films [Li(89)]. The oxygen ion conductivity makes YSZ a potential candidate for the fabrication of solid oxide fuel cells as well.

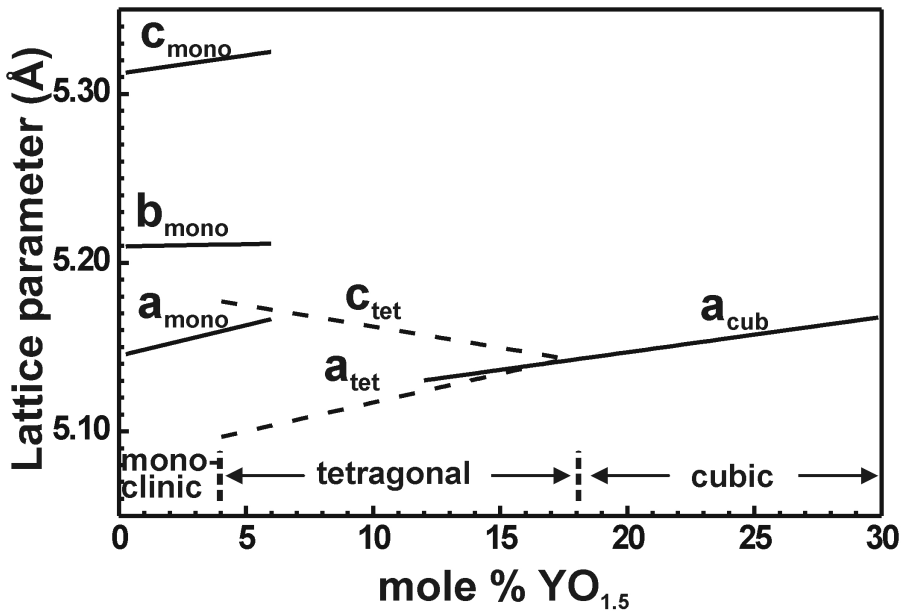

Figure 1.5 – Lattice parameters for the cubic, tetragonal and monoclinic phases of YSZ as a function of the molar concentration of $YO_{1.5}$ [Kisi(98)].

1.6 The mechanisms of bias-enhanced nucleation (BEN) of diamond

Since the introduction of the BEN treatment, many studies were addressed at a deeper understanding of the peculiar mechanisms taking place, which allow the unique epitaxial alignment of the nuclei for the diamond growth on a wide range of substrates. Before giving a brief survey of the proposed mechanisms of BEN on the most investigated substrate systems (Si, and much less 3C-SiC), a short treatment of the general theory of nucleation will be given.

1.6.1 Kinetics and energetics of nucleation

For the description of the nucleation and growth mechanisms, kinetics and energetics must be considered [Bechstedt(03)]. The nucleation process that can be described with the simplest model is the one occuring in a homogenous medium. In this context, the energy needed to form a nucleus is the algebraic sum of two terms: the work required for the formation of the surface and the one needed for or gained by the generation of the bulk.

Homogeneous nucleation occurs in conditions of supersaturation, *i.e.* when the partial pressure, P_0, of the nucleating gas species exceeds the equilibrium vapour pressure, P_∞, over the solid phase. The total free energy change for the formation of a spherical nucleus with radius r is given by:

$$\Delta G_{hom} = \Delta G_0 = \sigma \cdot 4\pi r^2 - \Delta G_v \cdot \frac{4}{3}\pi r^3 \tag{1.3}$$

where σ is the surface free energy per unit area and ΔG_v is the free energy per unit volume acquired by the system when the vapour is isothermally compressed:

$$\Delta G_v = \frac{kT}{V_m} ln \frac{P_0}{P_\infty} \tag{1.4}$$

where V_m is the molecular volume. Maximisation of equation 1.3 gives:

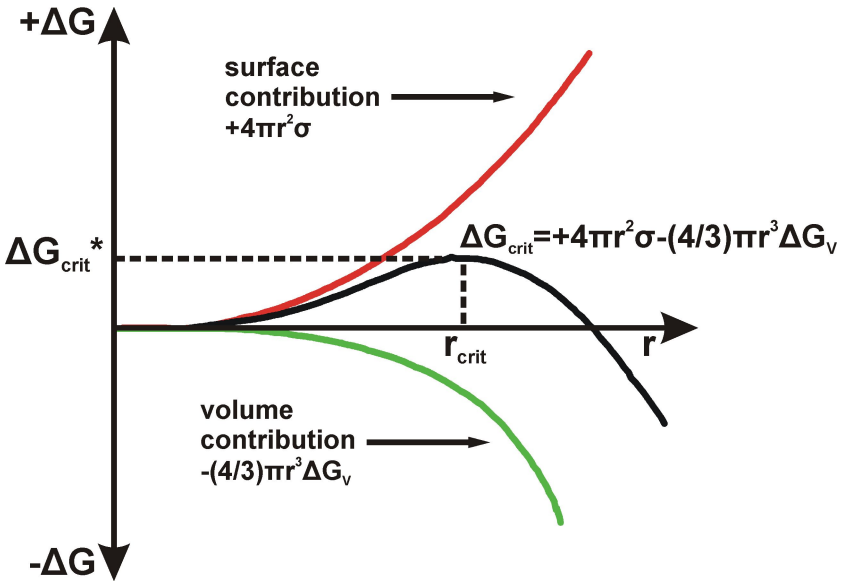

Figure 1.6 – Free energy change ΔG of nuclei as a function of their radii [Bechstedt(03)]. The surface and bulk contributions are shown.

$$\Delta G_v = -\frac{2\sigma}{r_{max}} \tag{1.5}$$

From equations 1.4 and 1.5 the Gibbs-Thomson relationship can be obtained:

$$RTln\frac{P_0}{P_\infty} = \frac{2\sigma V}{r_{crit}} \tag{1.6}$$

where V is the molar molume and $r_{crit} = r_{max}$ the radius of the critical nuclei. In the case of nucleation the Gibbs-Thomson relationship means that a large supersaturation is necessary in order to achieve a reduction of the radius of the critical nucleus.

A graphical representation of equation 1.3 is given in Figure 1.6. The salient information to be extracted from this plot is that, in an ensemble of particles formed with sizes statistically distributed around r_{crit}, further growth of clusters initially generated with $r < r_{crit}$ is energetically unfavoured, therefore these are prone to decay. On the contrary, particles formed with size larger than the critical nucleus ($r > r_{crit}$) have a higher probablity to grow further than to decay. This means that, once a droplet with the critical radius is formed, it tends to grow further, *i.e.* it behaves as a nucleus for growth of the new phase/material.

Nucleation occuring on a surface is called heterogeneous. The presence of a substrate can enhance nucleation, which is strongly dependent on the morphology of the substrate surface, on the contact angle between nucleus and substrate and on the surface energies of both the substrate and the overlayer. Generally in a vapour deposition process nucleation proceeds via atomic processes such as adsorption, desorption, diffusion and formation of clusters (see Figure 1.7). All these mechanisms depend on process parameters, besides the chemical nature of the atoms and the morphology of the substrate surface. If growth takes place under conditions not too far from equilibrium, the growth mode is determined by thermodynamics, *i.e.* the surface energy has to be minimized [vonKänel(95)]. Taking into account surface free energies of the substrate and the film, σ_s and σ_f respectively, and the interfacial free energy, σ_i, three different growth regimes can be distinguished: three-dimensional island growth (Volmer-Weber) if $\sigma_s < \sigma_f + \sigma_i$, layer-by-layer growth (Frank-van der Merwe) if $\sigma_s > \sigma_f + \sigma_i$ and an intermediate case (Stranski-Krastanov), where 3D islands grow on top of one or few epitaxial layers.

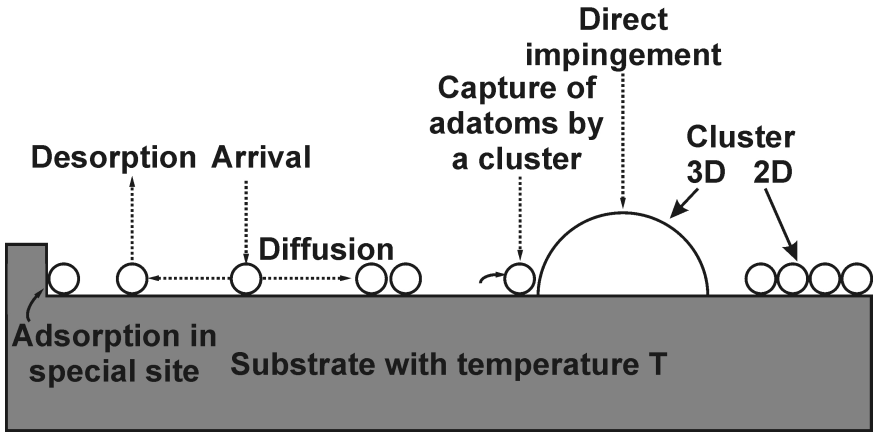

Figure 1.7 – Elementary processes taking place during a vapour deposition process [Nebel(03)].

1.6.2 Models proposed for BEN of diamond on Si and 3C-SiC substrates

As previously mentioned, due to its high surface energy, diamond tends to follow the Volmer-Weber growth mode on most of the substrates. Moreover, being diamond metastable at low pressures, CVD growth conditions are far from thermodynamic equilibrium. There are two main concepts proposed for the interpretation of the experimental observations of BEN of diamond on Si and 3C-SiC: surface effects, such as surface diffusion, and suplantation.

Concerning the models based on surface diffusion, from the comparison between theoretical and experimental data of time evolution of the density of nuclei and the first-nearest-neighbour-distance distribution, the initial stages of growth were described as a sequence of simple kinetic processes: adsorption of atoms from the gas phase, diffusion over the surface and formation of clusters [Jiang(94)]. Due to a strong contribution of diffusion caused by the continuous ion bombardment during BEN, stable clusters can then grow to larger islands, acting as sinks for diffusing adatoms in the neighbourhood. On the other hand, the formation and the shape of the diamond islands are controlled by the process thermodynamics.

The subplantation-based model is analogous to what was proposed for the formation of DLC: the energy of the accelerated ions generates a two phase carbon film in which few-nanometer-sized diamond (sp^3) nuclei are embedded in an amorphous (sp^2/sp^3) matrix [Gerber(95)]. The relatively high CH_4 fraction, the substrate temperature and the ion energies have to be tailored to enhance the sp^3 cluster formation and increase their size.

The surface diffusion mechanism, compatible with the classical nucleation theory (Section 1.6.1), allows to model the BEN process and the growth of diamond on Si and 3C-SiC in a reasonable way. BEN on Ir substrates, instead, shows significantly different features, which require a different approach for the formulation of a model. The subplantation model can explain part of the BEN process on Ir, but additional mechanisms are required to explain all experimental results. This subject will be treated in detail in Chapter 5.

Chapter 2

Analysis techniques

2.1 Transmission electron microscopy (TEM)

Transmission electron microscopy (TEM) is one of the most powerful techniques for the microstructural investigation of organic and inorganic materials, as well as of biological systems. Its major strength is the possibility to visualise with unmatched detail the structure of a specimen and to obtain at the same time crystallographic, morphological and chemical information at high spatial resolution [Fultz(01), Williams(09)].

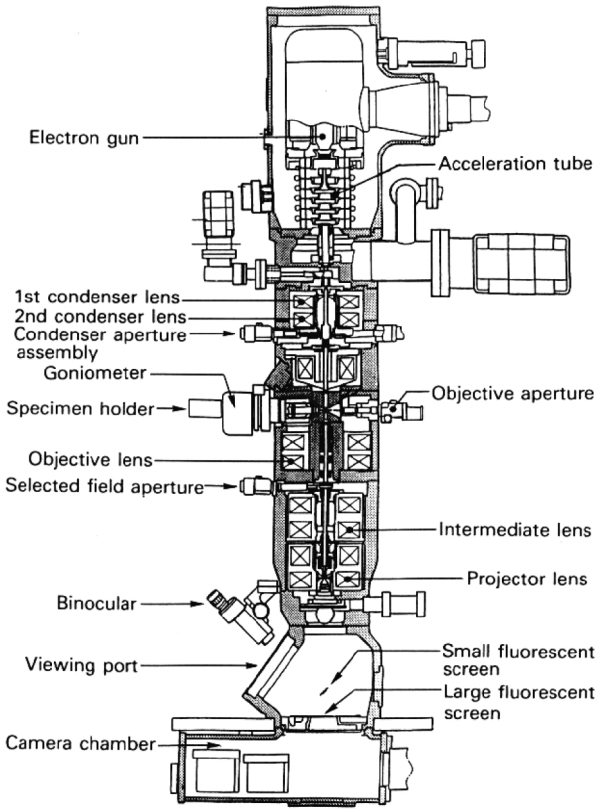

Figure 2.1 – Schematic structure of a transmission electron microscope (TEM) [Fultz(01)].

The schematic structure of a TEM is shown in Figure 2.1. The electrons emitted by a cathode are accelerated by a voltage typically between 80 kV and 1 MV. In this range of energies relativistic effects need to be taken into account, and the electron wavelength, $\lambda = h/p$, can be calculated according to the formula:

$$\lambda = \frac{h}{\left[2m_e eU\left(1+\frac{eU}{2m_e c^2}\right)\right]^{1/2}} \tag{2.1}$$

where U is the accelerating voltage and h, c, m_e and e are Planck's constant, the speed of light in vacuum, the electron rest mass and the electron charge, respectively. The resulting wavelength is in the order of 10^{-2} Å, two orders of magnitude below the interatomic spacings in solids. The accelerated electrons form a beam incident on the sample via a system of condenser lenses (CLs). The transmitted electrons form an image, by means of the objective lens (OL), which can be viewed on a fluorescent screen or recorded on a two-dimensional detector (image plates/CCD or CMOS-type camera) placed at the bottom of the instrument (see Figure 2.1).

The electron gun is one of the elements of a TEM that strongly affect its spatial and energy resolution. The simplest TEMs cathodes are sharply bent tungsten (W) wires emitting electrons due to the thermionic effect. In a thermionic gun the filament is heated up so that electrons with thermal energy higher than the work function of the material are emitted. Thermionic guns with the best performances are LaB_6 crystals, which offer the advantage of a lower work function than W. In a cold field emission gun (FEG) instead the cathode is a sharp tip, usually made of W, emitting those electrons which tunnel through the surface energy barrier of the material due to an intense applied electric field. A cold FEG is a point source of illumination, characterised by a lower energy spread and a higher brilliance with respect to the thermionic gun. This kind of cathode requires ultra-high vacuum (UHV) conditions, because it could easily be damaged by ions of gas atoms accelerated towards the tip due to the intense electric field. The vacuum and electric field requirements of the cold FEGs make nowadays preferrable a solution in which the sharp tip is slightly heated, the so-called thermal FEGs or Schottky effect cathodes. A thermal FEG provides a smaller source of illumination and higher brightness than a thermionic gun and is more stable than a cold FEG.

In modern TEMs, the electron optics consists of a system of magnetic lenses, which focus the electrons based on the Lorentz force. In the most common case, two CLs are used to form the electron beam incident on the sample, the first one producing a point source of illumination and the second one regulating the beam focussing at the specimen height. The OL and the intermediate lens have a fundamental role in the formation of images and diffraction patterns (as shown in the following sections). Magnetic lenses suffer, like glass lenses, of aberrations due to the change of the focus of the off-axis rays (spherical aberration), to the different focus of electrons having different energy (chromatic aberration) and to the truncation of the reciprocal lattice components due to the insertion of an aperture in the back focal plane of the OL (diffraction). Moreover, astigmatism is due to the not perfect cylindrical symmetry of a lens and causes a variation in the focussing strength with the azimuthal angle. This is anyway the only aberration which can be corrected manually by the TEM operator for the second CL and the OL by means of *stigmators*. In the following it will be clear how the lens aberrations, and in particular the spherical aberration of the OL, dramatically affect the ultimate resolution of a TEM.

In the next sections the attention will be focussed on the techniques used to obtain the results presented in this work and a brief introduction to each of them will be given.

2.1.1 Selected area electron diffraction (SAED)

One of the peculiarities of TEM is the possibility to obtain crystallographic information from a desired area of a specimen using the selected area diffraction (SAED) mode. A region of interest is selected by introducing an aperture in the image plane of the OL while viewing the specimen (Figure 2.2). TEMs are provided with a set of SAED apertures, with a

diametre usually in the range of 0.5-20 μm. When changing from image to diffraction mode, the current through the intermediate lens is decreased so that the ED pattern of the selected area is formed on the viewing device (Figure 2.2(b)).

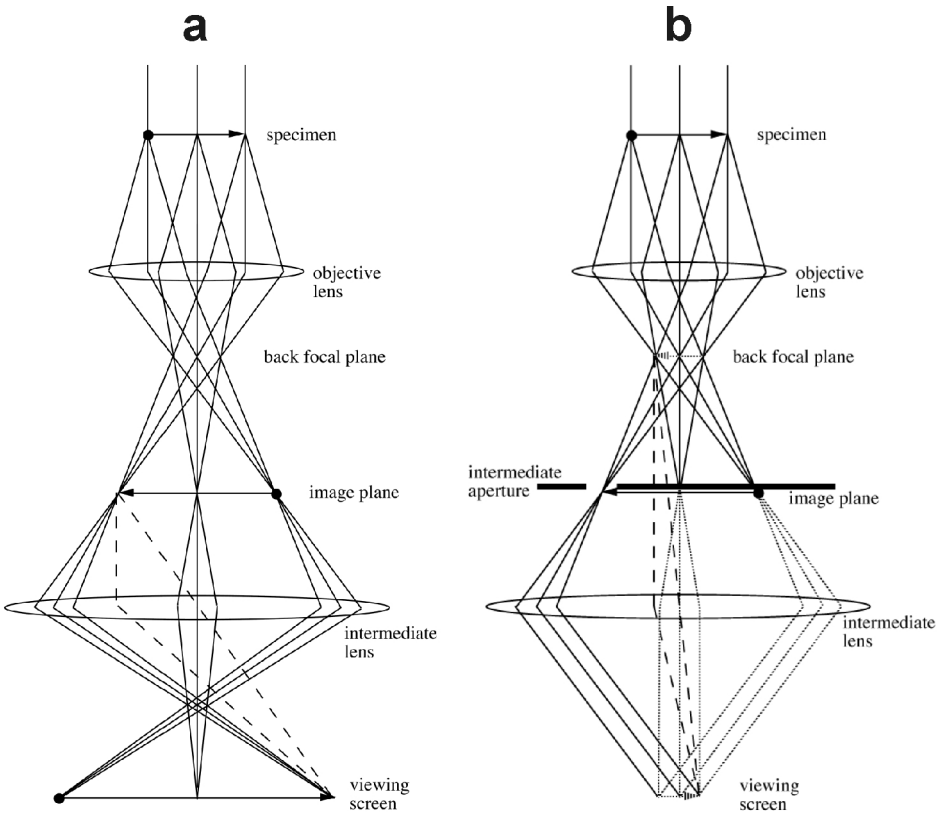

Figure 2.2 – Ray paths in a TEM in the (a) "apertureless" image and (b) selected area electron diffraction (SAED) modes [Fultz(01)].

The most intuitive way to understand the structure of a single crystal diffraction pattern in TEM is based on the *Ewald sphere* construction (see Figure 2.3(a)). This is derived from the Laue condition for diffraction:

$$\vec{k} - \vec{k_0} = \Delta\vec{k} = \vec{g} \tag{2.2}$$

where $\vec{k_0}$ is the electron beam wavevector, $\vec{k}$ a generic wavevector, with the same length as $\vec{k_0}$, and $\vec{g}$ a vector of the reciprocal lattice. The tails of the vectors $\vec{k_0}$ and $\vec{k}$ can be imagined to coincide with the centre of a sphere (the Ewald sphere) having their length as radius. A diffraction peak is therefore observed for those $\vec{k}$ touching a point of the reciprocal lattice, so that the difference vector, $\Delta\vec{k}$, is a vector of the reciprocal lattice.

In a TEM the Ewald sphere is rather flat, due to the short wavelength of the electrons. A single crystal specimen can be tilted so that two linearly independent vectors of its reciprocal lattice are perpendicular to the incident electron beam, which is parallel to $\vec{k_0}$. In this condition a SAED pattern is an almost planar section of the reciprocal lattice, containing its origin (*i.e.*, the transmitted beam) and few other reciprocal lattice points. Diffractions from this plane comprise the *zeroth-order Laue zone* (ZOLZ). In some cases, *e.g.* for materials with large lattice parameters, the ZOLZ appears surrounded by rings, the *higher order Laue zones* (HOLZ), which represent portions of the upper planes of the reciprocal lattice (see Figure 2.3(b)).

The first step in the interpretation of a SAED pattern is the identification of the trans-

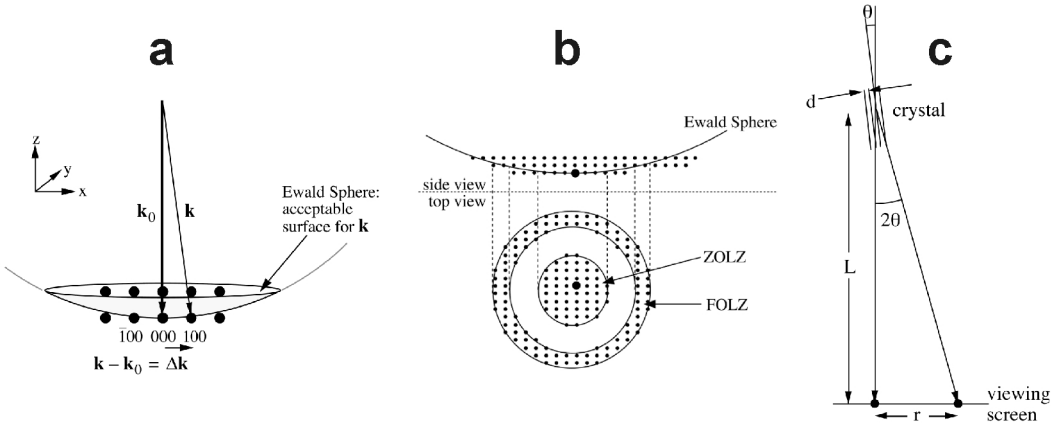

Figure 2.3 – (a) Ewald sphere construction and (b) its intersection with the reciprocal lattice of a simple cubic crystal, in particular showing the zeroth- and the first-order Laue zones. (c) Geometry of electron diffraction in a TEM [Fultz(01)].

mitted beam, the brightest spot in the centre of the pattern[1]. For each spot in the SAED pattern, the spacing, d, of the corresponding lattice planes can be determined. In the present work materials with cubic or tetragonal structures will be analysed. For a cubic crystal with lattice constant a, the interplanar spacing, d_{hkl}, of planes labelled by Miller indices (hkl) is:

$$d_{hkl} = \frac{a}{\sqrt{h^2 + k^2 + l^2}} \tag{2.3}$$

For a tetragonal crystal with lattice parameters a and c, the distance between the planes can be obtained from the following equation:

$$d_{hkl} = (\frac{h^2 + k^2}{a^2} + \frac{l^2}{c^2})^{-1/2} \tag{2.4}$$

According to Bragg's law, the diffraction peaks occur at angles, θ, such that:

$$2d\ sin\theta = \lambda \tag{2.5}$$

where λ is the electron wavelength[2]. The geometry of electron diffraction in a TEM is shown in Figure 2.3(c), which shows that:

$$tan2\theta = \frac{r}{L} \tag{2.6}$$

where L is a length which is the magnification of the diffraction pattern (the *camera length*). Typically in a TEM $\theta \approx 1^\circ$ for most materials. In the small angle approximation the following relationship (the *camera equation*), derived from equations 2.5 and 2.6, can be used to identify a diffraction feature in a SAED pattern based on its distance, r, from the transmitted spot:

$$d = \frac{\lambda L}{r} \tag{2.7}$$

The camera length, L, can be read on the console of a modern TEM during the acquisition of a SAED pattern. Nevertheless, for higher precision, a careful calibration might be performed using a known crystalline material before determining the lattice spacings of the analysed material. Besides the identification of individual diffraction features, in case of a single-crystal

[1] due to its high intensity, the undiffracted beam is often covered on purpose by the operator via a beam-stopper

[2] here only the first order of diffraction is considered.

SAED pattern the angles between two independent (not co-linear) spots in the ZOLZ allow to identify the particular plane of the reciprocal lattice of the material corresponding to the observed pattern, identified by specifying the normal to it, termed the *zone axis* (ZA). By convention, the ZA points towards the electron gun. Information about the structure of the reciprocal lattice parallel to the ZA can be obtained from the HOLZ.

As shown in the following chapters, SAED is a useful tool for the material analysis. First of all, it allows to map different regions of a TEM specimen and to identify them as amorphous, polycrystalline, highly oriented or single crystalline. In single crystals, the diffraction spot spacings, the angles between them and their relative intensities allow to identify the crystal structure and symmetry. The accuracy in the determination of lattice spacings and relative orientation relationship between different components is worse than in X-ray diffraction (XRD). However, the advantage of SAED is the possibility to acquire information from selected regions, down to the ≈100 nm-scale. Diffraction from areas smaller than this (*nanodiffraction*) is also possible using convergent beam electron diffraction (not described here).

2.1.2 Bright-field (BF) and dark-field (DF) imaging

While viewing the SAED pattern, an aperture (the *objective aperture*) can be inserted in the back focal plane in order to select only the transmitted spot. Switching back to the image mode, an image will appear on the screen generated only from the undiffracted electrons, and the areas of the specimen which are strongly diffracting will appear dark. In this case we talk about a *bright-field* (BF) image (see Figure 2.4(a)). If, on the contrary, one of the diffracted spots is selected, in the image mode only the areas of the sample diffracting the electrons so as to give rise to that spot will appear bright. For example, in this image mode (*dark-field (DF)* mode, see Figure 2.4(b)) the amorphous areas of the sample will always be dark. Both BF and DF images are characterised by a strong *diffraction contrast*, *i.e.* the variation in intensity of electron diffraction across the specimen, while "apertureless" images are comparatively featureless. The contrast in an "apertureless" image is mainly due to different masses of the elements or the variable thickness across the sample. A combination of DF images acquired with different spots can be used to identify different materials in the specimen or phases with different crystal structure or orientation.

Enhancement of the diffraction contrast can be useful to get insights into structural defects of a specimen. Two complementary methods are used for this aim, the *two beam bright field* and *weak beam dark field* (WBDF) modes. These are both based on the fact that the lattice planes are strongly bent in proximity of dislocations or structural defects. Therefore, BF or DF images with enhanced contrast can be obtained by tilting the sample with respect to the exact zone-axis orientation towards particular orientations. A two-beam BF condition is obtained when the SAED pattern has only one strong diffraction besides the transmitted beam, *i.e.* when the BF and the DF image obtained by selecting the intense diffraction spot are roughly complementary. The WBDF mode is the corresponding DF mode, in which the sample has to be tilted so as to give rise to an intense high-order diffraction spot. This mode allows to generate extremely sharp images of dislocation lines.

2.1.3 High resolution TEM (HRTEM)

High resolution TEM (HRTEM) images are phase contrast images resulting from the interference between forward-scattered and diffracted electron waves from the specimen. The highest possible spatial resolution can be obtained only by including as high as possible spatial frequency components (highest possible Δk). However, since higher frequency components are more affected by the spherical aberration effects due to the OL, a good quality

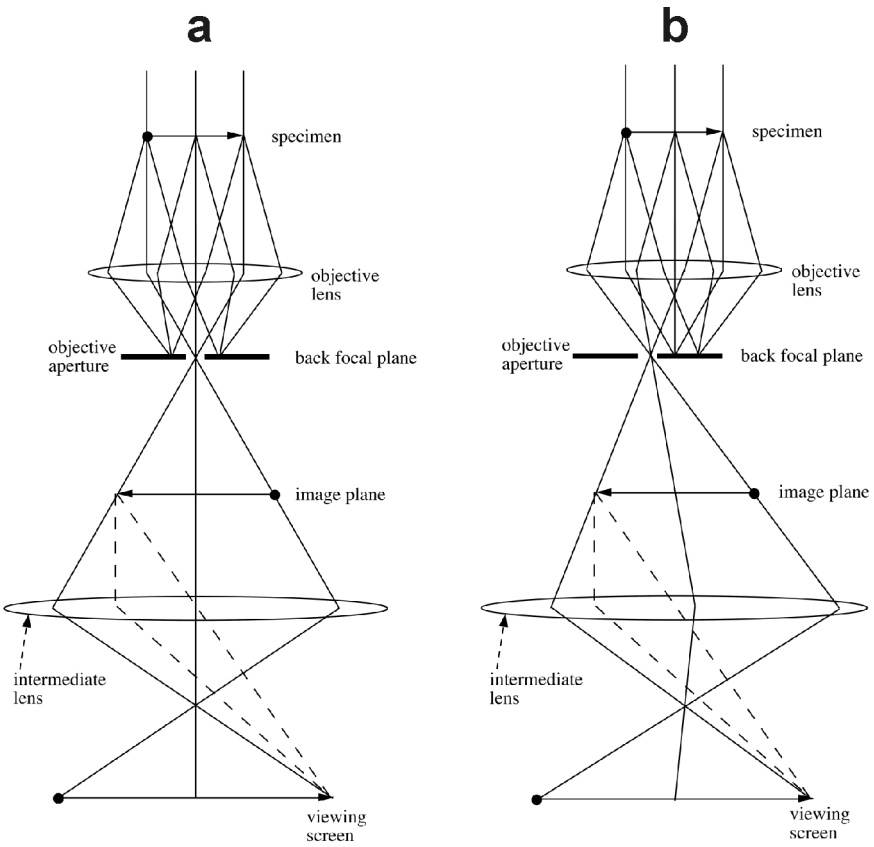

Figure 2.4 – Ray paths in a TEM in the (a) bright-field (BF) and (b) dark-field (DF) modes [Fultz(01)].

HRTEM image can be obtained only by introducing an objective aperture to select, besides the transmitted beam, at least some of the inner diffraction spots. The condition for HRTEM thus differs substantially from the one described above for the BF mode, where only the undiffracted beam forms the image.

A full comprehension of HRTEM image formation needs a wave optics approach, giving a good approximation of the correct electron wave mechanics treatment. In this analysis the phase alterations of the electron waves due to the specimen and the OL have to be taken into account. The contrast in a HRTEM image originates mainly from the phase shifts of the electron wavefront as it passes through the sample. The simplest approximation is that the specimen acts as a weak phase object, *i.e.* the amplitude of a transmitted wave function is linearly related to the projected potential of the specimen. The OL can be viewed as a device altering the phase of the electron wavefront, hence a finite coefficient of spherical aberration of the OL affects the quality of the final phase-contrast image. It is possible to partly compensate for the errors due to spherical aberration by adjusting the focus of the OL so as to optimize the range of angles for which entering rays suffer acceptable distortions. According to a standard criterion, the sharpest HRTEM image is obtained at the *Scherzer defocus*, and the corresponding resolution is given by the formula:

$$r_{Sch} = 0.66\ {C_S}^{\frac{1}{4}} \lambda^{\frac{3}{4}} \tag{2.8}$$

where C_s is the coefficient of spherical aberration of the OL and λ the electron wavelength. This is the minimum real space distance for which phase coherence is preserved at the Scherzer defocus. The Scherzer resolution is also often defined as the inverse of the spatial frequency corresponding to the first zero of the *contrast transfer function* of the OL at the Scherzer defocus. A full treatment and derivation of the formula can be found in any TEM text book.

The resolution in equation 2.8 is the definition of the *point resolution* of a TEM.

With typical instrumental parameters the point resolution of a TEM is in the order of 1 Å, that is two orders of magnitudes worse than the electron wavelength. In the meantime, with aberration corrected instruments and/or with careful image reconstruction procedures it is possible to reach sub-Å resolution [Hawkes(09), Erni10].

2.1.4 Electron energy loss spectroscopy (EELS) and energy dispersive X-ray spectroscopy (EDS)

Electron energy loss spectroscopy (EELS) is the analysis of the energy distribution of electrons that have passed through a TEM specimen. EELS yields valuable information on the sample due to the variety of mechanisms of inelastic interaction undergone by the electrons: crystal vibrations, inter-band transitions, plasmon excitations and core excitations. The EEL spectrum is generated via one or a combination of magnetic prisms, which disperse the electrons based on their energy (via the Lorentz force). The energy resolution is mainly limited by the electron source and, without monochromators, it is typically in the order of 1 eV. In the present work, EELS has been used only to estimate the thickness of TEM sections. For this aim, EEL spectra are acquired in the low loss region (<50 eV), where the height of the plasmon peak gives indication on the number of scattering events that have occured during the transit through the sample. Under single-scattering assumption, the thickness t is obtained as

$$t = \lambda_p \cdot \frac{I_p}{I_0} \tag{2.9}$$

where λ_p is the plasmon mean free path, I_0 is the intensity of the zero-loss peak (the peak centered at 0 eV) and I_p is the intensity of the first plasmon peak. In this work, the spectra have been acquired in diffraction mode from a region of the Si substrate, immediately beside the region of interest in the film, and a mean free path of 141 nm was assumed in Si (electron energy 200 keV, entrance aperture semi-angle 5.5 mrad).

Energy dispersive X-ray spectroscopy (EDS) is the analysis of the spectral distribution of X-rays emitted through de-excitation of atoms in a specimen after electron beam irradiation. The EDS maps shown in the present work were acquired in scanning TEM (STEM) mode in regions selected from high angle annular dark field (HAADF) images. This imaging mode was selected as it gives a contrast mainly related to the mean atomic number of the material, through a $\approx Z^2$ relationship. EDS was used to give a relative quantification of Y and Zr through the thickness of YSZ layers, based on the Cliff-Lorimer quantification method, valid for thin foils [Williams(09)].

2.1.5 Instrumentation and specimen preparation procedures

The studies shown in this work have been performed using three TEMs. A Philips CM30 instrument was employed, equipped with a LaB_6 thermionic cathode and an acceleration voltage of 300 kV (λ = 0.0197 Å). In this microscope tilting of the sample is possible up to ±45°and the point resolution is 2.5 Å. Most of the results presented in the Section 4.2 were obtained with this instrument, using photographic films. An ultra-high-resolution microscope (JEOL JEM-2100F), equipped with a thermal FEG and operated at an acceleration voltage of 200 kV (λ = 0.0251 Å), has been employed for most of the remaining analyses. In this instrument the FEG source and the improved design of the objective lens allow to reach a point resolution of 1.9 Å. The short distance between the objective lens pole pieces, necessary for the improvement of resolution, limits the tilt of the sample to ±25°. A Gatan Imaging Filter (GIF) unit is attached in series to the column in order to enable filtering of

the transmitted electrons and to finally acquire energy filtered micrographs, as well as EEL spectra, on a 2048×2048 pixels CCD camera. Image and SAED pattern acquisition was also performed employing image plates, flexible metal plates covered by an active layer, which can be read by an *ad hoc* scanner and afterwards erased and reused [Ditabis]. The third employed instrument was an ultra-high resolution instrument (JEOL JEM-2200FS) equipped with a CEOS image aberration corrector, an in-column (Omega) energy filter and a Bruker Quantax 400 EDS system with a 60 mm^2 silicon drift detector (SDD). The latter microscope was used only for the acquisition of EELS spectra and EDS spectra and maps. The first two instruments are hosted by the Institute of Physics of the University of Augsburg while the last one by the Department of Nanochemistry of the Italian Institute of Technology (Genova, Italy).

In all these instruments double-tilt sample holders were used for all the presented analyses, as these allow to tilt the single crystal specimens around two independent axes. This is necessary when the orientation along a precise crystallographic direction is desired for the planned investigations. The sample placement on these TEM holders allows for circular specimens with a 3 mm diametre.

A TEM specimen needs to be thin enough so that an appreciable number of electrons can go through it and provide the desired information. The preparation technique employed for the thin film samples analysed here was a standard technique for both *plan-view* (where the in-plane morphology and distribution of defects could be investigated) and *cross-section* (where the section and the interface between the different layers needed to be investigated) samples. In the first case 3-mm-diametre discs are cut out of the samples using an ultrasonic disc cutter and subsequently ground from the substrate side, using SiC grinding paper, down to a thickness of about 100 μm. After a final polishing step the samples are dimpled using a mixture of distilled water and diamond polishing paste, always from the substrate side, till the thickness in the centre of the dimple is about 25 μm. Also in this case a final polishing step is applied, before introduction into an ion milling setup, where low energy (3.5-4.5 keV) Ar ions are directed at a grazing angle (3-4°) onto the TEM specimen surface. This final procedure is stopped when a small hole is obtained in the centre of the sample: this indicates that there is an area around the hole (few tens of μm wide) where the thickness of the sample is optimum for TEM and, in the best case, for HRTEM analyses. The preparation of cross-section samples is different from the described one only for the first stages. In this case the sample is first of all cut in pieces about 1×2 mm^2 using a diamond wire saw. Afterwards pairs of pieces are glued together, with the film sides facing each other, using an epoxy. The two pieces system is then inserted and glued into a brass potlet, with a diametre of 3 mm. After this step the procedure is the same as the formerly described one, with grinding, dimpling and final ion milling. The main difference in this case is that grinding and ion milling are performed acting on both faces of the TEM sample, as they are equivalent.

2.2 Scanning electron microscopy (SEM)

Scanning electron microscopy (SEM) and the techniques related to it allow to examine morphology and chemical composition of specimens consisting of a huge variety of materials on a nanometre scale. With respect to TEM, which allows to obtain information with unmatched spatial detail from an extremely small area of a specimen (few μm^2), cm^2-sized specimens can be analysed by SEM, without the need of extremely high vacuum, high acceleration voltages and long, delicate and invasive preparation procedures.

The structure of a SEM is schematically shown in Figure 2.5(a) [Reimer(85)]. The electrons are emitted by an electron gun, which can be thermionic or a cold/thermal FEG. The emitted electrons are accelerated by a voltage of 1-50 kV. In this range relativistic effects can be neglected and equation 2.1 becomes:

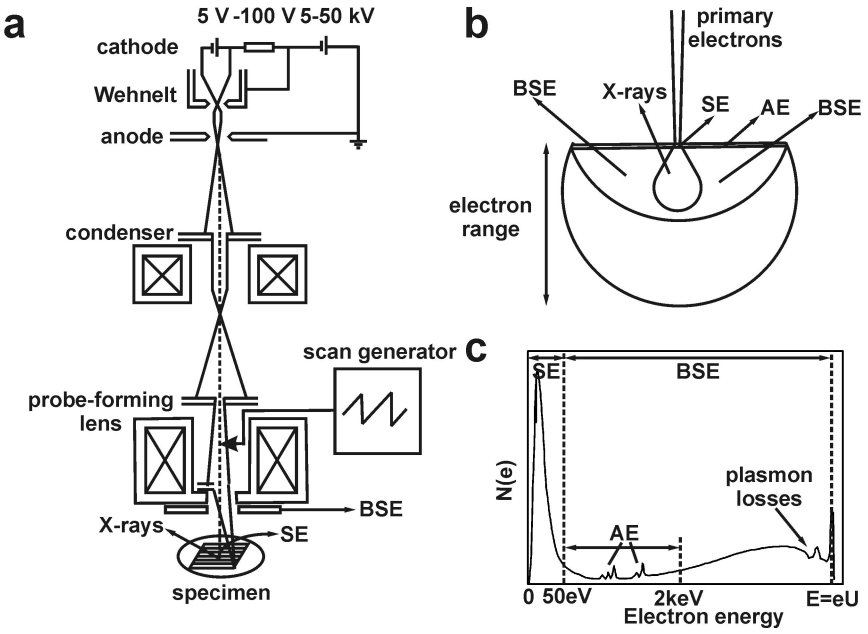

Figure 2.5 – (a) Schematic structure of a scanning electron microscope (SEM). (b) Origin and information depth of various particles emitted by a specimen under irradiation with primary electrons (PE) with range R. (c) Partition of the energy spectrum of the emitted electrons in a SEM [Reimer(85)].

$$\lambda = \frac{h}{\sqrt{2m_e eU}} \tag{2.10}$$

The electron wavelength calculated according to equation 2.10 is is in the order of 10^{-1} Å. The electron beam is focussed via a system of magnetic lenses, so that an electron probe with a diametre of 1-10 nm is formed on the specimen surface. This electron beam is scanned over the specimen by means of a deflection coil system in front of the beam-forming lens. The size of the beam at the specimen, limited by the size of the electron source and the aberrations of the magnetic lenses, determines the maximum spatial resolution of the SEM.

In a SEM the variety of electron-specimen interactions is used to form different images and give complementary qualitative and quantitative information. The primary electrons (PE) incident onto a sample stimulate the emission of electrons with various energies and X-rays, originating from different depths in the sample, up to a maximum range R which depends on the PE energy and the material density (see Figures 2.5(b) and 2.6). The emitted electrons are divided into secondary electrons (SE), Auger electrons (AE) and backscattered electrons (BSE) (see Figure 2.5(c)). The energy distribution of the SE is peaked at 2-5 eV, since these electrons are generated by an inelastic process involving a high energy loss. The AE are instead produced following the ionisation of an inner shell, with an analogous process to the one generating the X-rays. When an electron from an upper shell fills the hole, energy can be released in form of an X-ray photon or transferred to another electron of the atom, emitted from the material with a characteristic kinetic energy related to the binding energy of the ejected electron. Due to their relatively low energy, the SE and AE are generated in a surface layer of the specimen with a thickness of few nanometres. SE images are widely used in SEM, since they give information with high surface sensitivity about the topography and the difference between materials in terms of SE yield. BSE electrons are high energy electrons which have been backscattered by the atoms of the target without significant energy loss. The backscattering process is sensitive to the atomic number of the sample atoms and can thus provide a strong material contrast.

The SEM employed in the present study was a LEO DSM 982 Gemini instrument equipped

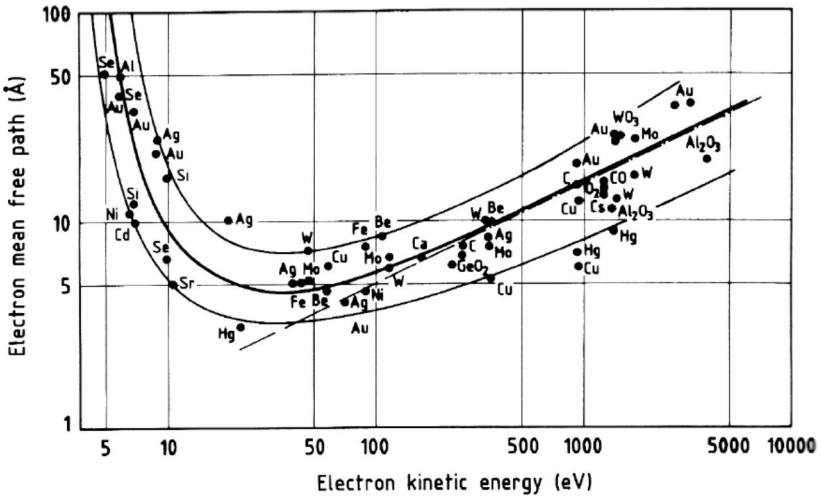

Figure 2.6 – Electron mean free path in matter as a function of the electron kinetic energy [Desjonquères(93)].

with a thermal FEG, with a maximum acceleration voltage of 30 kV. A peculiarity of this instrument is the presence of a detector of SE located inside the probe-forming lens (in-lens (*IL*) detector) besides a conventional SE detector (here called *SE*) located on the side of the sample, as in Figure 2.5(a). Due to the detection geometry, the *IL* detector allows a higher spatial resolution and a higher sensitivity to the material contrast, while the *SE* detector is more sensitive to the topographic contrast. In the present work SEM investigations were aimed at obtaining high resolution morphological images, showing material and topographic contrast. Therefore images were acquired using a combination of the *IL* and *SE* detectors, using an acceleration voltage in the range of 4-10 kV, with corresponding working distances (*i.e.* distance of the sample surface from the lower part of the probe-forming lens) of 3-6 mm.

2.3 Atomic force microscopy (AFM)

Atomic force microscopy (AFM) is a technique based on the measurement of the force between a sharp tip and a specimen, giving information about the surface topography of the latter on atomic scale [Binnig(86)]. The scheme of a modern AFM is shown in Figure 2.7. A micromachined cantilever spring with a small (few nm radius) sharp tip at one end is scanned over the surface of the specimen. The surface imaging is realized by detecting the tip-sample force in different locations while the probe is scanning the sample surface with the help of a piezoelectric actuator. The deflection of the cantilever is detected by monitoring the position of a laser beam reflected from the cantilever backside onto a segmented photodiode. A feedback control applied during imaging ensures that the tip-sample force is preserved at a constant level. The height image, in which brighter contrast is assigned to higher features on the surface, represents the vertical translations of the piezo-scanner needed to compensate the force variation when the probe is scanned over the sample surface.

In the AFM analyses presented in this work, the non-contact mode was used, in order to avoid the tip damage due to contact with the investigated diamond specimens. In this mode the tip hovers 50-150 Å above the sample surface and is still subjected to attractive Van der Waals forces to the surface, hence being able to follow its profile. Since the forces are substantially weaker than in contact mode, the cantilever is given a small oscillation. The oscillation frequency is close to the resonance frequency of the cantilever, so that the amplitude of the oscillations is maximised. In analogy to the contact mode, in the non-contact mode the oscillation amplitude is kept constant via the feedback control and the

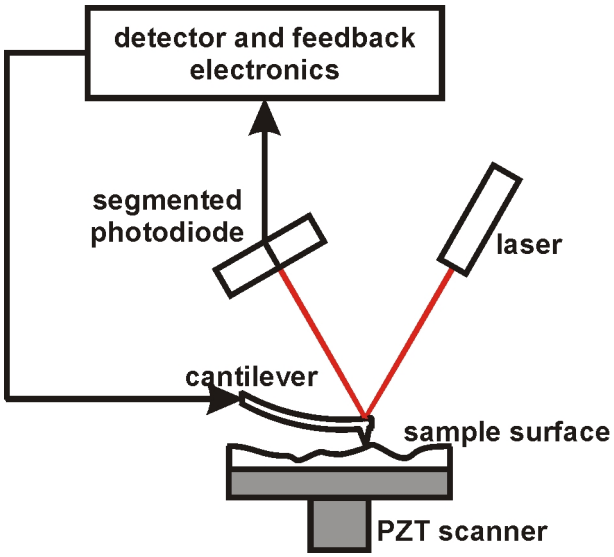

Figure 2.7 – Schematic structure of a modern atomic force microscope (AFM).

height information is obtained by the vertical translations of the piezo-scanner supporting the specimen.

The AFM analyses described in the present work have been performed using an Autoprobe CP-Research instrument of the company ThermoMicroscopes. The cantilevers are made of Si covered on the backside with a reflective gold layer. The photodiode in this instrument is composed of 4 sectors, allowing a more sensitive control over the position of the reflected laser beam, hence able to follow precisely the normal and lateral deflections of the cantilever.

2.4 Reflection high-energy electron diffraction (RHEED)

Reflection high-energy electron diffraction (RHEED) is a widely used tool in surface science thanks to its high surface sensitivity [Braun(99)]. This technique uses diffraction of electrons by surface atoms and provides information about their arrangement. Its highest potential is due to its compatibility with both (ultra) high vacuum and low pressure conditions, which makes it able to investigate the surface morphology during the deposition of crystalline films, *e.g.* by molecular beam epitaxy or pulsed laser deposition.

In RHEED electrons emitted by a cathode (usually a W filament) are accelerated to an energy typically between 10 keV and 50 keV. The specimen is arranged so that the parallel electron beam hits the surface at a grazing angle (typically smaller than 5°, see Figure 2.8). The high energy of the electrons would result in a penetration depth larger than ≈3 nm (Figure 2.6), but the grazing angle allows only a thin surface layer to be probed.

Due to the short electron wavelength (in the order of 10^{-1}Å, according to equation 2.10), in RHEED the Ewald sphere is rather large. The electron beam is partially reflected and partially diffracted by the surface, forming a pattern that is converted to visible light by a phosphor screen and detected by a CCD camera placed outside the high vacuum chamber. The projection of the transmitted beam on the phosphor screen represents the origin of the reciprocal lattice (Figure 2.8(a), later labelled as (000)). This spot is visible only for some sample geometries, as it is usually hidden by the sample itself (see Chapter 5).

In RHEED investigations the structure of the crystal beneath the surface does not give a significant contribution, due to the very small sampling depth of the electrons. Therefore, in most cases the involved volume can be approximated by a two-dimensional layer and, correspondingly, the reciprocal lattice degenerates into a series of one-dimensional rods

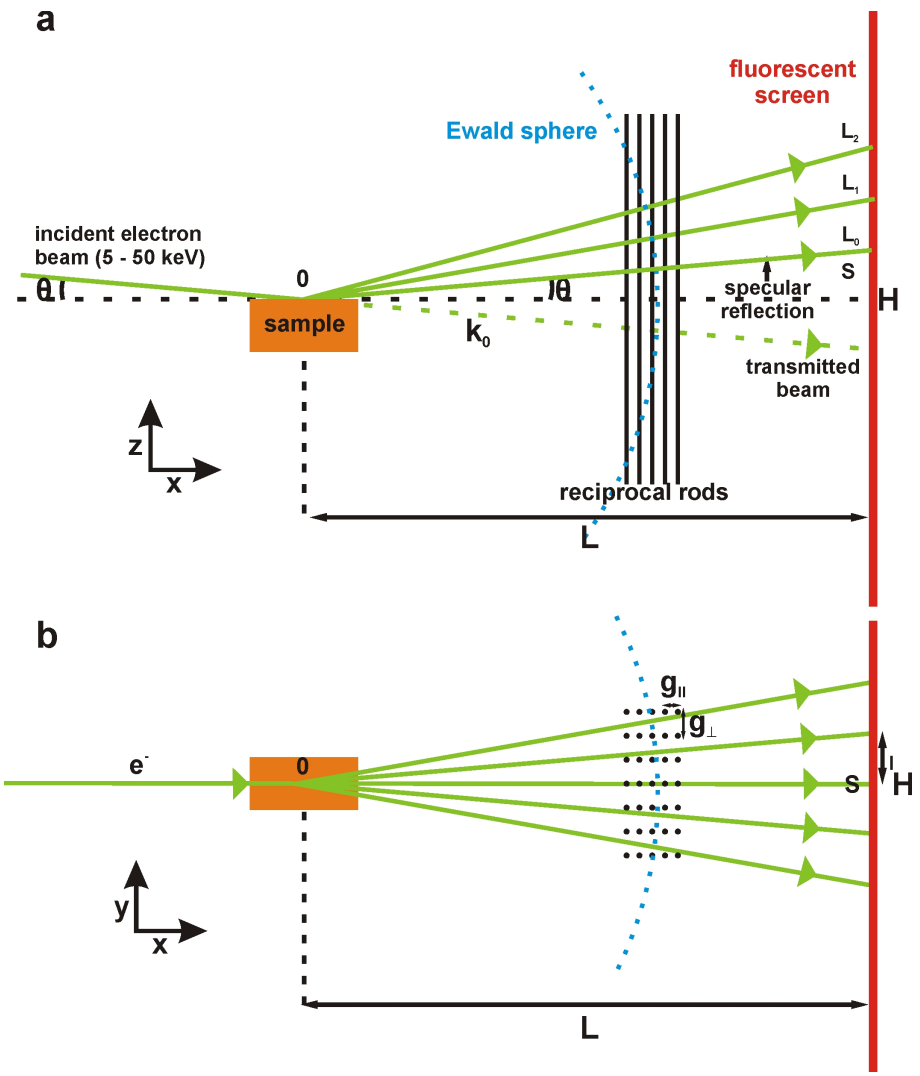

Figure 2.8 – Schematics of a reflection high-energy electron diffraction (RHEED) setup: (a) side and (b) top views [Braun(99)].

perpendicular to the surface (see Figure 2.8). Features appear in a RHEED pattern when the Laue condition (equation 2.2) is satisfied. The reflections occur on so-called *Laue circles* of radius L_n centered at H, the projection of the component parallel to the surface of the incident vector, $\mathbf{k}_0$, onto the screen. Due to the geometry of the experiment, they will show asymmetric spacing in the direction parallel ($g_{\parallel}$) and perpendicular ($g_{\perp}$) to the reciprocal lattice rod direction:

$$ng_{\parallel} = k_0 \left(cos\theta - \frac{1}{\sqrt{(L_n/L)^2 + 1}} \right)$$
$$ng_{\perp} = \frac{nl}{L} k_0 \tag{2.11}$$

where θ is the incidence angle, L the distance between the incidence point and the screen, and l the position of the diffraction feature on the screen with respect to the central reciprocal lattice rod, measured perpendicular to it (see Figure 2.8 and ref. [Braun(99)]). Indexing of the reciprocal lattice rods is similar to that of bulk reflections in SAED in a TEM.

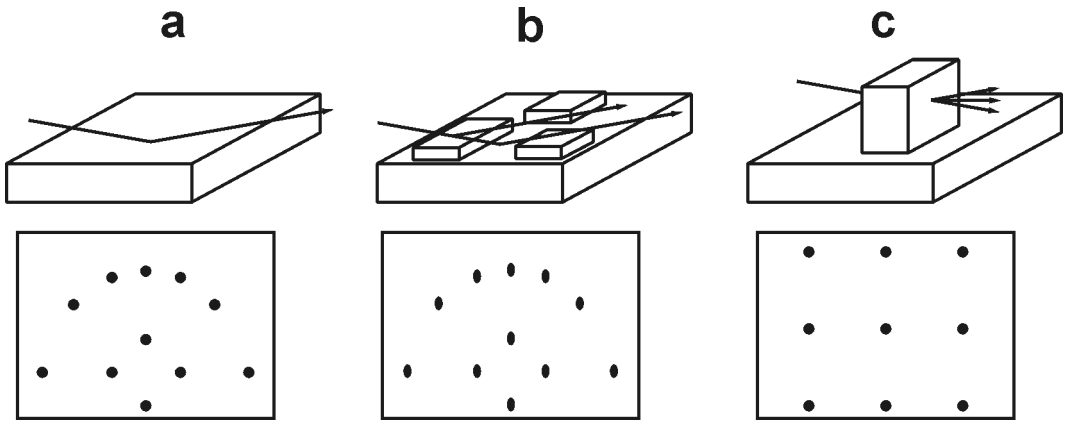

Figure 2.9 – RHEED patterns corresponding to different surface arrangements of a single crystal material: (a) flat surface, (b) surface made of extended terraces and (c) rough surface consisting of isolated epitaxial grains.

RHEED patterns easily allow to distinguish different surface arrangements. A single-crystal-quality sample with a flat surface, or a surface formed by extended terraces, or a rough surface with isolated grains, generate significantly different RHEED patterns (see Figure 2.9). In all these cases, the equations 2.11 allow to extract the lattice parameters and the crystal structure of the material. In particular, in case of a rough surface presenting 3D structures (Figure 2.9(c)), the degeneration of the reciprocal lattice into a set of rods is no longer valid, and a spot pattern appears in RHEED, in perfect analogy to the SAED pattern of a single crystal material. However, the RHEED pattern is always asymmetric, due to the small angle between the electron beam and the screen perpendicular (the incidence angle, θ).

The surface structure selectivity and the growth environment compatibility of RHEED make it an ideal tool to analyse the early stages of formation of a film. The time evolution of a RHEED pattern during the deposition of the first layers allows to "visualise" the three basic growth modes (Volmer-Weber, Frank-van der Merwe or Stranski-Krastanov, see Section 1.6.1).

The RHEED setup employed in the present work was a STAIB INSTRUMENTS electron gun installed in a high vacuum setup (base pressure of 10^{-8} mbar). The analyses were performed using an acceleration voltage of 30 kV between room temperature and 600°C

(specified in each case). The samples were mounted suspended in the chamber. Thus, the shadow edge is always in the upper part of the images.

2.5 X-ray photoelectron diffraction (XPD)

Photoelectron diffraction (PED) is a technique based on the scattering of photoelectrons, emitted from a specimen upon irradiation with UV photons or X-rays, by ordered structures at the sample surface [Hüfner(96), Desjonquères(93)]. This technique is intrinsically related to photoelectron spectroscopy (PES).

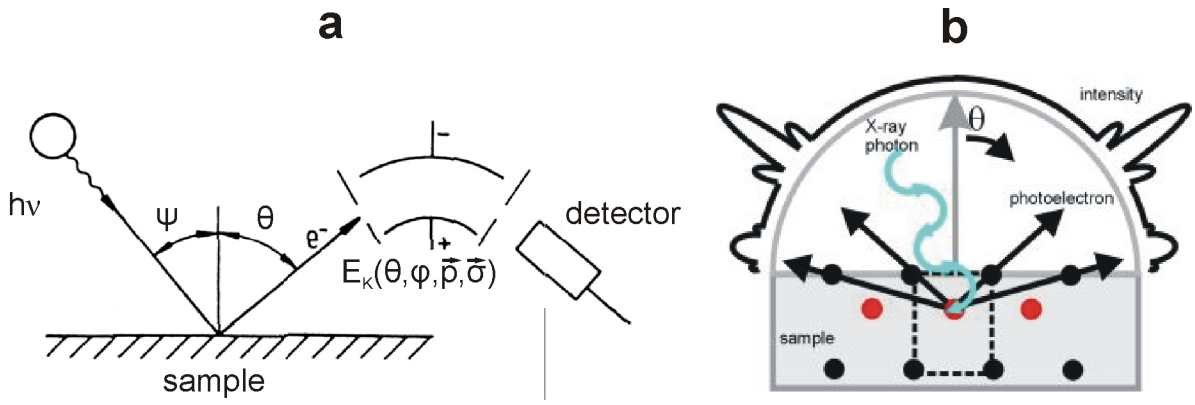

Figure 2.10 – (a) Schematic diagram of the setup of a photoelectron spectroscopy (PES) experiment [Hüfner(96)]. (b) Intuitive representation of the forward-scattering effect in X-ray photoelectron diffraction (XPD), which gives rise to the observed patterns.

In PES a beam of monochromatic photons irradiates the surface of a specimen and some of them transfer energy to electrons of the sample atoms. These are then emitted with a kinetic energy given by the following equation:

$$E_K = h\nu - |E_B| - \phi \tag{2.12}$$

where h is Planck's constant, ν the photon frequency, ϕ the material work function and E_K and E_B the kinetic energy and the binding energy of the emitted electron, respectively (see Figure 2.10(a)). Since the electron escape depth for electron energies between 10 and 2000 eV is of few Å, the emitted electrons in PES give information about few monolayers on the specimen surface (see Figure 2.6). PES carried out using X-rays (X-ray photoelectron spectroscopy, XPS) allows to analyse electrons generated via photoionization of core levels, which are characteristic of specific elements. The emitted electrons are collected by an electron energy analyser and from their energy spectrum the chemical composition and molecular binding of the surface layers of the specimen can be deduced.

On their way through the crystal to the sample surface the photoemitted electrons are scattered by the other atoms of the sample. In presence of ordered structures, the intensity of the emitted wave is modulated as a function of their orientation. In case the electron kinetic energy is fixed, hence the emitting atoms, X-ray photoelectron diffraction (XPD) monitors the intensity modulations when the electron current measured within a unit solid angle is detected at different polar (θ) and azimuthal (φ) angles (see Figure 2.10). A first understanding of XPD can be achieved viewing the electron beam in the detector as being the superimposition of the wave emerging directly from the emitting atom and waves which have been scattered by the neighbouring atoms of the crystal. In order to interpret XPD patterns one has to take into account that high energy photoelectrons emitted from a particular atom are scattered by neighbouring atoms predominantly into the forward directions. Therefore the emitted current

has a maximum along an axis that connects the emitter and a neighbouring atom, in the forward direction (see Figure 2.10(b)). A fundamental advantage of XPD over RHEED and low energy electron diffraction (LEED) is that it needs only a short-range ordered structure to generate a geometric pattern. Calculations of the photoelectron intensity indeed show that very few monolayers of an ordered structure can be enough to generate a geometric XPD pattern. XPD can therefore be used to analyse the structure and alignment of surface adsorbates or very thin layers deposited on the surface of a sample.

The XPD patterns shown in the present work (see Section 5) have been acquired by Dr. Thomas Brugger within the group led by Prof. Osterwalder at the University of Zürich (Switzerland). The XPS/XPD experiments were performed in a modified VG ESCALAB 220 photoemission spectrometer with a base pressure in the low 10^{-10} mbar region. The MgK_{α} source (1253.6 eV) of a twin anode was used for the photoemission experiments. The samples were fixed on a goniometric manipulator, which is capable of polar ($0° \leq \theta \leq 90°$) and azimuthal ($0° \leq \varphi \leq 360°$) motions. The XPD patterns were obtained by rotation of the sample and recording more than 4000 data points in the upper hemisphere above the surface. The data are stereographically projected on a plane and represented in grey scale, with maximum and minimum intensities as white and black, respectively.

Chapter 3

Synthesis techniques

3.1 Pulsed laser deposition (PLD)

The YSZ films studied in the present work were synthesised via pulsed laser deposition (PLD). This is a physical deposition technique that is nowadays widely used for the growth of complex oxide layers [Eason(06)]. In PLD a pulsed laser is focused onto a target of the material to be deposited. For sufficiently high laser energy density each pulse vaporises or ablates a small amount of the material creating a highly forward-directed plume, which provides the material flux for film growth. One of the most attractive characteristics of PLD is the possibility to achieve stoichiometric transfer of ablated material from multication targets to the deposited layers. A background gas is often introduced during PLD processes, having the double task of participating in the chemistry of film growth (especially in the case of oxygen during the deposition of oxides) and/or intentionally reducing the kinetic energies of the ablated species.

The PLD setup and process used for the deposition of the analysed YSZ films are accurately described in a former work [Gsell(07)-2]. A KrF excimer laser ($\lambda = 248$ nm, maximum energy 1200 mJ/pulse, pulse duration 20 ns) is employed and the deposition is carried out with a pulse energy of 850 mJ at a substrate temperature between 600℃ and 850℃. Commercial Si substrates, in 1×1 cm^2 pieces or 4 inch wafers, are used as substrates and a two-step process is typically applied. Firstly, a lowered oxygen partial pressure ($7\cdot10^{-7}$ mbar) is used in order to reduce the native SiO_2 layer on the substrate surface, allowing in this way the YSZ to orient epitaxially directly to the silicon lattice in the first stages of growth. Afterwards the oxygen partial pressure is increased to $5\cdot10^{-4}$ mbar till the end of the process. Due to the high oxygen diffusivity through the YSZ film during growth, finally a few nanometres thick amorphous SiO_2 layer regrows at the YSZ/Si interface, without affecting the epitaxial orientation of the YSZ film to the substrate. This effect, already observed in former studies [Bardal(94)], will be shown in detail in the cross-section TEM studies presented in Chapter 4.

3.2 Electron beam evaporation

The Ir films considered in the present work were deposited via electron beam evaporation, due to the high melting point of the metal (≈2446℃). The electron beam evaporation setup is a vacuum chamber ($p<10^{-6}$ mbar) where the sample can be heated up to a temperature of 900℃. In this technique the electrons are emitted by a cathode and then accelerated to an energy of about 8 keV. The electron beam, having a power of about 1-2 kW, is focused onto an Ir target, which evaporates locally. The deposition rate, measured by a quartz microbalance, can be varied in a broad range (0.002-0.05 nm/s) by changing the current

through the cathode. The substrates used for Ir deposition in the present work were YSZ/Si layers, in 1×1 cm^2 pieces or 4 inch wafers (see former section), and BEN samples, on top of which a thin Ir layer acted at the same time as a contrast and protective layer during cross section TEM preparation and investigation (see Section 5.1). More details about Ir deposition are described elsewhere [Gsell(07)-2].

3.3 Microwave plasma assisted chemical vapour deposition (MWPCVD)

The diamond samples analysed in the present work were prepared using two different MWPCVD reactors. For the production of most of the specimens for the study of BEN a modified MWPCVD commercial setup realised by the company ASTeX (Applied Science and Technology) was employed. For a small portion of the samples, as specified in Chapter 5, a MW system from the company IPLAS was used for BEN and deposition.

3.3.1 The ASTeX reactor

The system used in the present work was the second generation of MWPCVD reactors commercialised by the company ASTeX, introduced around 1990 [Prelas(98)]. The scheme of the reactor, including the vacuum and the gas feed circuits integrated in the deposition system installed in the diamond deposition laboratory at the University of Augsburg, is drawn in Figure 3.1. The deposition chamber is a double-walled, water-cooled steel cylinder, which acts as a resonant cavity for the 2.45 GHz microwaves generated by a magnetron (maximum power 1.5 kW). The microwaves are transmitted along a rectangular waveguide and emitted centro-symmetrically by a MW coupler inside the chamber, via an antenna, through a flat silica window located on its top. In optimized conditions the maximum of the electrical field strength is approximately in the centre of the chamber. The specimen is located on a graphite stage that can be inductively heated to 900℃ without the ignition of the plasma. The temperature of the graphite block is measured by a thermocouple and regulated via a PID-controller. The stage can be moved so as to modify the geometry of the cavity, so that the ball-shaped plasma forms directly above it. The temperature of the sample is measured by an infrared pyrometer (sensitivity in the wavelength range 0.90–1.08 μm).

The original ASTeX reactor was modified by adding an annular steel electrode that is electrically isolated from the whole chamber. This ring is suspended about 2 cm above the specimen and can be biased positively with respect to the chamber, which is at the same potential as the specimen holder.

The diamond films deposited on Ir considered in the present study were subjected to two steps: BEN and subsequent deposition. The experimental details of the two processes, as they were performed to prepare the samples concerned in the present work, are described in the following sections.

The BEN step

First of all, the specimen is introduced into the chamber through the 4.5 inch wide door. In this system the substrate for diamond deposition can be as large as a 4 inch wafer, even if homogenous conditions can be obtained only in the centre of the reactor, within an area having a diametre of few cm. In the experiments considered in the present work BEN and CVD deposition were carried out on ≈1×1 cm^2 Ir/YSZ/Si substrates. Prior to deposition, a pressure of 10^{-6} mbar is obtained inside the chamber by means of a rotary and a turbomolecular pump. Afterwards the feed gases (H_2, CH_4, N_2) are introduced into the chamber, with

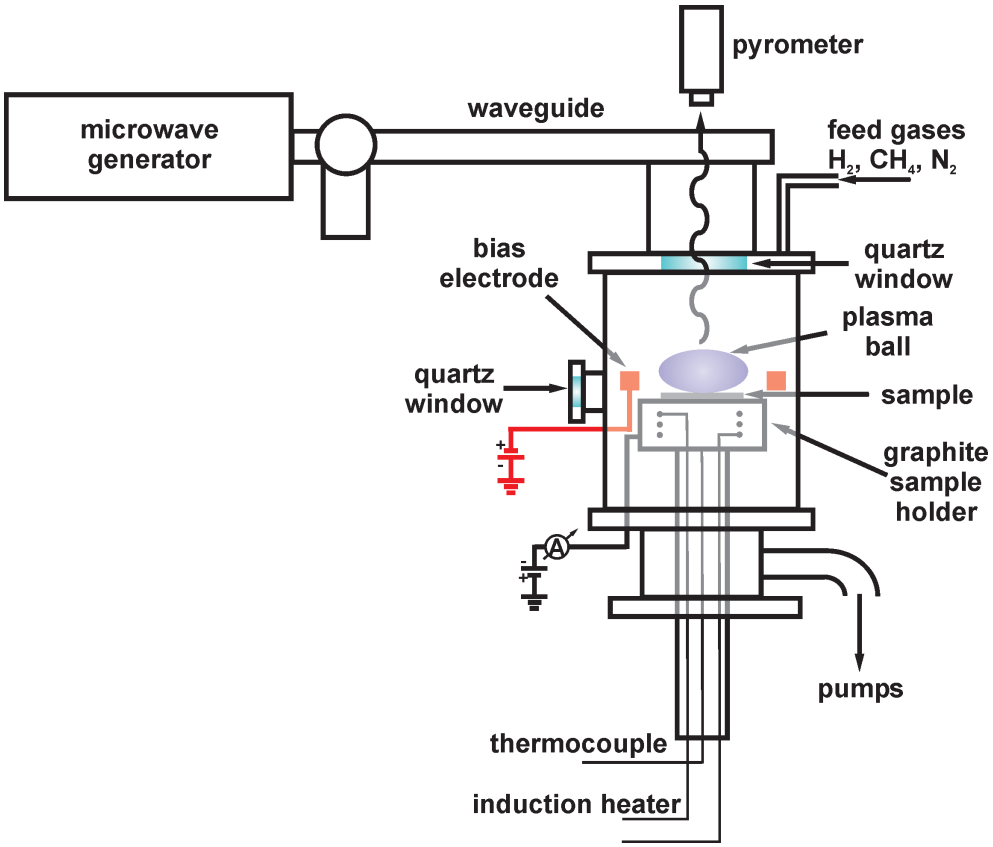

Figure 3.1 – Scheme of the ASTeX MWPCVD apparatus, including the vacuum and the gas feed systems, used for BEN and deposition of diamond films.

pressure and flow regulated down stream by a valve and upstream by mass flow controllers, respectively. The plasma is ignited typically in pure hydrogen in mild conditions, with a flow of ≈200 standard cubic centimeters (sccm) at a pressure of 15 mbar with a MW power of ≈500 W. After optimising the plasma conditions, *i.e.* the reflected MW power and the position of the sample relative to the plasma ball, pressure and MW power are increased typically to 30 mbar and 1100 W, respectively (see Table 3.1 for general process parameters). Once optimised the conditions, the carbon-containing gas (CH_4, typically 10-20 sccm) and, in some experiments, other gases (*e.g.* N_2 or Ar) are added. The H_2 flow is adjusted so that the total gas flow is 200 sccm.

As previously mentioned (see Section 1.4.1), the most established conditions for the BEN treatment consist in the application of a negative voltage to the substrate with respect to the ring, immersed in the plasma, so that the positive ions in the plasma shallowly bombard the substrate. To start the BEN process, the bias voltage is increased in few seconds to 250-300 V, so that the BEN process can start. During this stage, the bias current and the specimen temperature are monitored. The shape of the glow discharge formed during BEN and its evolution in time are observed through quartz windows on the sides of the chamber. It was already shown in literature, mainly concerning BEN on Si substrates, that an intense glow discharge is formed few millimetres above the substrate surface during the BEN process. The shape and brightness of this discharge are a fundamental hint to understand the stage of the nucleation process [Gsell(07)-2]. Typically the duration of the BEN step is between 30 minutes and 1 hour.

Table 3.1 – Typical process parameters for the BEN treatment and the growth step in the ASTeX and the IPLAS MWPCVD setups.

	Duration (min)	Pressure (mbar)	MW power (kW)	CH_4 (vol. %)	Temperature (°C)	Voltage (V)
BEN ASTeX	30-60	30-40	1100	5-10	700-850	250-310
BEN IPLAS	15-60	30-60	1600-2200	2	700-850	250-350
Growth ASTeX	0-600	30-45	1100	1	700-850	–
Growth IPLAS	0-100	25-50	2000	0.5	700-850	–

The deposition step

At the end of the BEN process, the bias voltage is abruptly switched off and the CH_4 concentration is decreased to a lower value (typically to 2 sccm, while the H_2 flow is increased to 198 sccm), so that the pure deposition step starts. In such conditions the glow discharge, typical of the BEN conditions, disappears and the plasma ball turns homogeneous. With optimised conditions, this kind of reactor is quite stable and can be operated many hours to obtain a thicker film.

3.3.2 The IPLAS reactor

Some of the diamond films used for test experimentaimed at understanding the nature of the BEN product (Section 5.2) were deposited using a modified MWPCVD system by IPLAS. In the IPLAS reactor the sample holder is placed in a quartz tube, 14.3 cm long, with an inner diametre of 14 cm. The maximum power generated is 6 kW, potentially allowing high deposition rates on large areas. The typical parameters used with this reactor are compared to the ones used for the ASTeX reactor in Table 3.1.

Chapter 4

TEM study of epitaxial YSZ layers on Si

One of the most promising substrates for the growth of large area single crystal diamond films is the Ir/YSZ/Si(001) epitaxial multilayer system (Section 1.4.3). In order to obtain the best quality single crystal diamond films the intermediate layers need to be optimised. Each of the layers needs to be as smooth and well oriented as possible in order to facilitate the improvement of the overgrowing layers. The present investigations are focussed on the first component of the multilayer system, *i.e.* YSZ films deposited by PLD on commercial Si substrates. Two targets with different stoichiometry ($YO_{1.5}/ZrO_2$ ratio) were used, leading to tetragonal and cubic crystalline structures, respectively (Section 1.5). Former comprehensive XRD analyses, monitoring in particular the evolution of mosaic spread (polar and azimuthal orientation spread), were performed on films of both structures with the aim of finding the optimum preparation conditions [Goldfuß(05), Fischer(06), Gsell(07)-2]. The results of such analyses evidenced strong variations of the film properties with thickness and thermal treatments. Post-deposition annealing treatments on one hand and thickness increase on the other were found to improve the mosaic spread and reduce the microstrain in cubic YSZ films. Moreover, XRD analyses evidenced the occurence of different texture components in tetragonal films, with the relative fraction varying with different preparation procedures.

The here presented TEM results complete the above described studies by analysing in detail the microstructural changes accompanying the observed texture variations. This study is carried out with the complementary use of the diffraction contrast TEM, SAED and HRTEM techniques. In the case of cubic YSZ films, threading dislocations are observed inside the films, and their distribution is found to vary among the different conditions. For tetragonal YSZ films, the structures corresponding to the different texture components are identified and their behaviour is examined for films deposited on (001)- and (111)-oriented Si substrates.

4.1 Reduction of mosaic spread and dislocation density in cubic YSZ layers on Si(001)

The use of YSZ films with cubic structure is the first choice when a layered system entirely made of cubic materials (Si, Ir and diamond) is concerned. For these experiments films were prepared on Si(001) by PLD with the setup described in Section 3.1, using a YSZ target with a $YO_{1.5}$ concentration of 21.4 mol%. This corresponds to a cubic structure with a lattice constant $a = 5.150$ Å (equation 1.1). In order to optimise the mosaic spread of these films two alternative ways were attempted: growing to high thickness and performing post-growth thermal annealing treatments. In the present study films with a thickness between 20 nm and 500 nm are analysed. The optimum annealing treatment for texture improvement, established

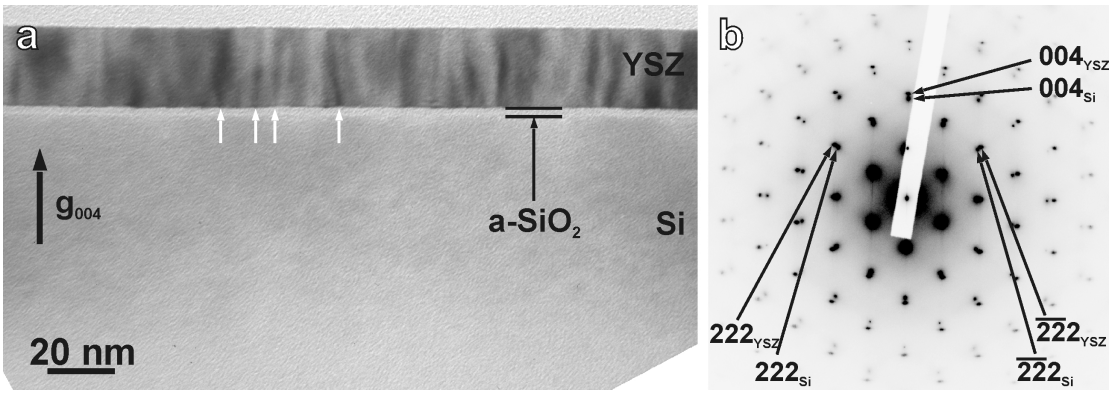

Figure 4.1 – (a) BF-XTEM image of an as-grown 24 nm-thick cubic YSZ film on Si(001), acquired with the maximum intensity in the (004) spot of YSZ. A thin SiO_2 film is present between Si and YSZ. The white arrows point to some dislocation segments in the YSZ film. (b) SAED pattern along the $[\bar{1}10]$ zone axis of Si and YSZ, showing the cube-on-cube orientation of the film on the substrate. The measured values for the in-plane and out-of-plane lattice constant are 5.176(±0.005) Å and 5.146(±0.005) Å, respectively.

in former studies, is performed in air at 1200℃ [Gsell(07)-2]. One of the most significant results of the XRD study of cubic YSZ films is the evolution of microstrain and texture with the annealing processes. The dramatic texture improvement with the thermal annealing was attributed to a variation in the dislocation density. The latter one was estimated from the tilt and microstrain values, and both methods indicate a decrease in dislocation density after thermal annealing. An analogous behaviour was reported with the increase of film thickness.

The microstructure of cubic YSZ films is here investigated by HRTEM and two–beam BF imaging (Section 2.1.2). The latter technique consists in acquiring BF images with the specimen tilted away from the exact zone axis orientation so as to excite one diffraction spot at a time. In this way the undiffracted beam and the strongest diffraction are the most intense ones (hence the name of the technique) and the undiffracted beam is selected for imaging. The result, in suitable conditions, is an increase of the diffraction contrast generated by the strain field due to dislocations [Fultz(01)]. The dislocations are visible as lines running through the sample, which will be addressed in the following as *dislocation segments*, as they are conceptually different from the *dislocation lines*, whose arrangement defines the nature of the dislocation. The dislocation itself does not generate any contrast, but it is visible because of the strong bending of the crystal planes generated in its surroundings. As a consequence, for instance, the dislocation segment can appear even tens of nanometres away from the dislocation core, in an image, depending on the diffraction condition. A dislocation is invisible with some diffraction spots $\mathbf{g}$ excited, while generating a strong contrast for some other spots, depending on its nature and on the direction of its Burgers vector. As a rule of thumb, dislocations are invisible when their Burgers vector $\mathbf{b}$ is parallel to the chosen diffraction vector $\mathbf{g}$ ($\mathbf{b} \cdot \mathbf{g} = 0$), while they become visible when $|\mathbf{b} \cdot \mathbf{g}| \geq 1/3$. The weak beam dark field (WBDF) imaging mode offers in general the optimum contrast conditions for dislocation analysis. However, in the present case, two–beam BF provides better results than WBDF imaging, due to the high density of defects.

An as-grown 24 nm-thick cubic YSZ film was analysed in cross-section TEM (XTEM). Clear features are visible only in two–beam BF mode with the (002n) spots excited, with the best conditions obtained with $\mathbf{g} = 004$ (Figure 4.1). Most of the visible dislocation segments in the film start at the bottom of the film and have a [001] line direction, ending at the film surface. These longitudinal defects are often found in films growing on top of misfitting substrates and they are identified as threading dislocations [Su(07), Wang(11), Hojo(11), Lu(07)]. These are formed by edge or mixed dislocations.

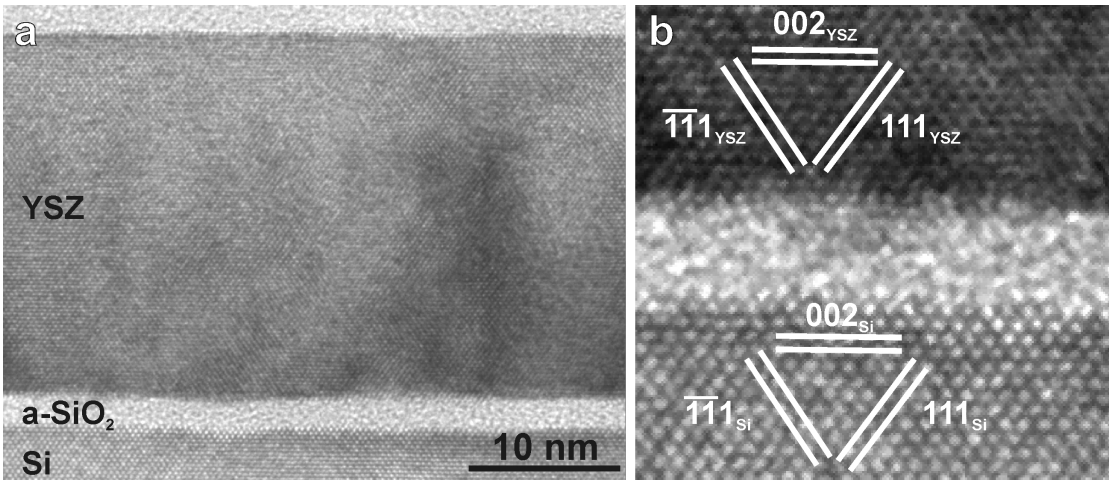

Figure 4.2 – (a) HRTEM image of the sample in Figure 4.1 ([$\bar{1}$10] zone axis) and (b) enlarged view of the interface region, showing the presence of a 2 nm-thick amorphous film between Si and YSZ.

HRTEM images of the same film show a disordered array of dislocations along the dislocation segments (Figure 4.2 and higher magnification, not shown here). No clearly defined grain boundaries can be distinguished, and in particular tilt boundaries, which are low angle grain boundaries in which an ordered array of dislocations is observed along the boundary line [Igarashi(06)]. An accurate Burgers vector analysis cannot be performed due to the high density of defects and consequent deformation of both this and the annealed film (see below). Further analyses, to be performed also considering different orientations (*e.g.* [001]) could allow to visualise the most often occuring dislocations with Burgers vector $\mathbf{b} = 1/2 <110>$ in the fluorite structure [Lei(01)]. HRTEM unambiguously shows the presence of a ≈2 nm-thick amorphous SiO_2 layer between the Si substrate and the YSZ layer, due to oxygen in-diffusion through the YSZ during the final stages of deposition. The single crystal quality of the YSZ film and its epitaxial relationship with the Si substrate are obtained during the early stages of PLD deposition, during which low oxygen partial pressure is used, so as to reduce the Si in the native SiO_2 and produce volatile SiO (see Section 3.1 and refs. [Bardal(94), Gsell(07)-2]). The absence of a direct YSZ/Si interface does not allow to identify misfit dislocations, that should be present, in the observed orientation, one every ≈4 nm due to the 5.4% misfit between Si and YSZ.

The microstructure drastically changes after thermal treatments, as observed for the same film after a short (1 h) annealing process in air at 1200°C (Figure 4.3). With the same diffraction vector excited, the density of longitudinal threading dislocations, directed from the interface with SiO_2 to the surface, appears lower than in the as-deposited film, while much shorter dislocation segments are visible in the middle of the film thickness. HRTEM analysis of the few observed longitudinal dislocation segments shows also in this case a disordered distribution of dislocations (Figure 4.4 and higher magnification). With the annealing process in air the amorphous SiO_2 film has grown thicker (74 nm, while after 16 h annealing it increases to ≈300 nm, see also following section). Also in this case, the lack of direct contact with the Si substrate is not detrimental for the epitaxial orientation of the YSZ film with respect to the Si substrate. Instead, an improvement in the mosaic spread of the film was found by XRD, and it can be attributed to the disappearance of the threading dislocations. The density of the threading dislocations, obtained from two–beam BF images, is in this case almost 3 times smaller than for the as-grown film (see Table 4.1). The decrease of the threading dislocation density with post-growth annealing treatments was already reported in literature for $SrTiO_3$ [Su(07)], $BaTiO_3$ [Sun(04)] and other misfitting epitaxial films [Morales(09)].

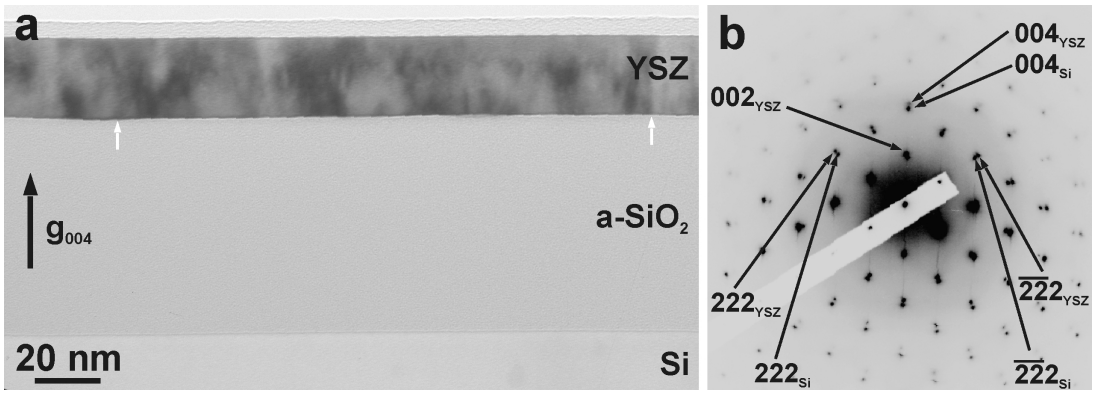

Figure 4.3 – (a) BF-XTEM image of a 24 nm-thick cubic YSZ film on Si(001) after 1 hour annealing in air at 1200℃, acquired in a two–beam condition with the maximum intensity in the (004) spot. In this case the intermediate layer between Si and YSZ is 74 nm thick. The white arrows point to some dislocation segments in the YSZ film. (b) SAED pattern along the $[\bar{1}10]$ zone axis of Si and YSZ, showing the epitaxial orientation of the film on the substrate. The measured values for the in-plane and out-of-plane lattice constant are 5.201($\pm$0.005) Å and 5.164($\pm$0.005) Å, respectively.

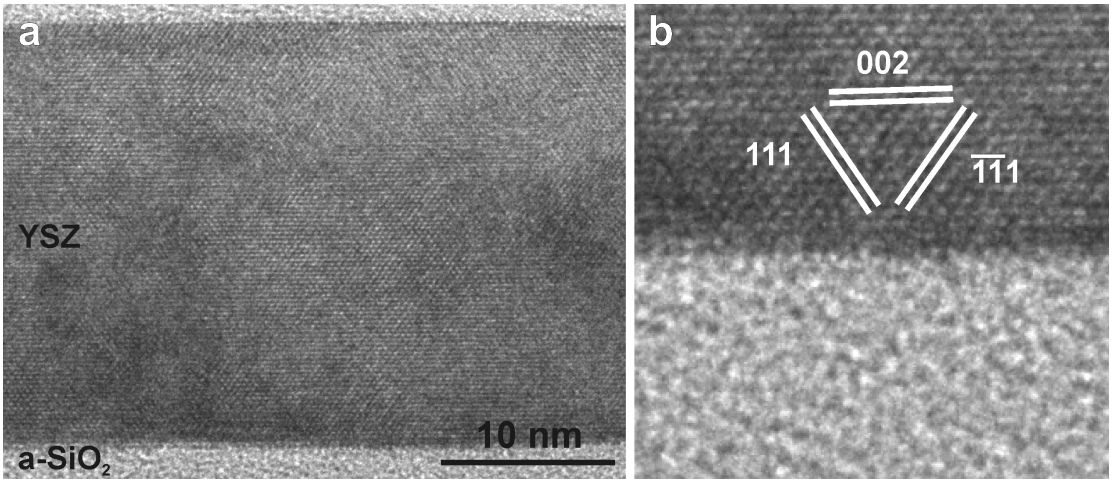

Figure 4.4 – (a) HRTEM image of the sample in Figure 4.3 ($[\bar{1}10]$ zone axis) and (b) enlarged view of the interface with the amorphous SiO_2 layer.

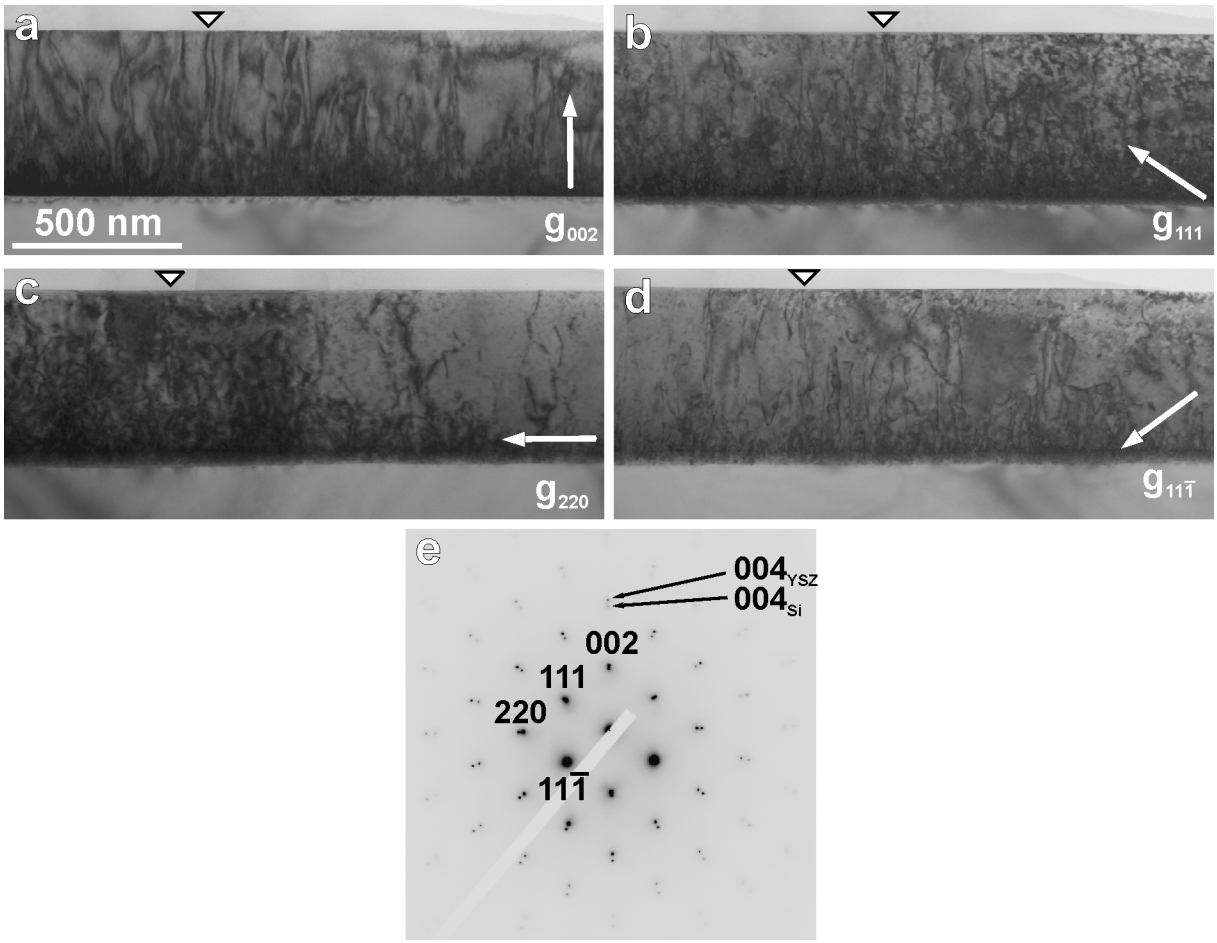

Figure 4.5 – Two–beam BF-TEM images of an as-grown 485-nm-thick cubic YSZ film on Si(001), showing changes in contrast with the diffraction vector **g**. The images are acquired close to the [$\bar{1}$10] orientation with excitation of different beams: (a) 002, (b) 111, (c) 220 and (d) 11$\bar{1}$ (common scale in all insets). The top arrows show a reference point common to all images. (e) SAED pattern corresponding to the exact [$\bar{1}$10] zone axis orientation. The values of the in-plane and out-of-plane lattice constant are 5.157(±0.005) Å and 5.148(±0.005) Å, respectively.

Table 4.1 – Values of dislocation density obtained from two–beam BF TEM images and from XRD data, deduced from tilt measurements [Gsell(07)-2]. As the XRD dislocation density data are missing for the 24 nm thick film, data are reported for a film of comparable thickness (30 nm), as-grown and after a 15 min annealing step. The values of the TEM section thickness, evaluated by EELS, are also reported.

	Film thickness (nm)	**Section thickness** (nm)	**Dislocation density** (cm^2)	
			BF–TEM	**XRD**
YSZ025	24	120	8×10^{10}	–
YSZ025 annealed 1 h	24	90	3×10^{10}	–
YSZ042	485	330	3×10^{9}	3.8×10^{9}
YSZ ref.	30	–	–	8.9×10^{10}
YSZ ref. annealed 15 min	30	–	–	2.8×10^{10}

For a quantitative evaluation of the dislocation density, images from at least two non-colinear vectors **g** would be needed. This would be the most reliable method for the determination of the density of dislocations with all Burgers vectors in a film. In the case of the 24 nm-thick film no clear features were visible with $\mathbf{g} \neq 002n$. Instead, two–beam BF images acquired on an ≈500 nm thick as-grown cubic YSZ film by exciting four non-colinear diffraction vectors show different features (see Figure 4.5). Clearly, different dislocation lines are visible with excitation of different diffraction vectors, and most of them are visible in at least two of the employed conditions. This is not surprising as the visibility criterion, $|\mathbf{b}\cdot\mathbf{g}| \geq 1/3$, can be satisfied for a certain dislocation for more diffraction vectors. The best orientations for counting dislocations are in this case $\mathbf{g} = 002$ and $\mathbf{g} = 11\bar{1}$, as the corresponding images are free of the wiggling contrast, due to inhomogeneous thickness, that would make the analysis more complicated.

The two–beam BF images of the 24 nm–thick film allow to estimate the dislocation density by counting the dislocation segments running from the bottom to the top of the film before and after annealing (Figures 4.1 and 4.3). For the 485 nm-thick sample both images in Figures 4.5(a) and (d) were used for the dislocation density estimation. For all these cross section samples a thickness (along the electron beam direction) in the order of ≈100 nm was evaluated by EELS (see equation 2.9 and Table 4.1). The results of these estimations are reported in Table 4.1, together with the dislocation density values deduced by XRD tilt measurements [Gsell(07)-2]. Despite the necessarily local character of the TEM analyses, the estimated density values are in extremely good agreement with the XRD-based estimations, which give instead an averaged information. These results confirm diffraction contrast TEM as a reliable method for the evaluation of the dislocation density in thin films [Kittel(05)].

The last point to be addressed concerning cubic YSZ films is the information deduced from SAED patterns. The analysed cubic YSZ films on Si(001) show a cube-on-cube relationship ($(001)_{YSZ}[110]_{YSZ}//(001)_{Si}[110]_{Si}$) (Figures 4.1(b), 4.3(b), 4.5(e)). Moreover, diffraction patterns of the examined specimens, having a 1‰ precision thanks to the internal calibration allowed by the spots of the unstrained Si substrate, allow to investigate the evolution of strain in the films. Fast Fourier transforms (FFTs) of HRTEM images are not considered in this analysis, due to the tiny probed area and their lower accuracy, as for the annealed film no internal reference is present (images cannot include both the YSZ film and the Si substrate, due to the thick amorphous SiO_2 layer between them). Strain can be present in films, with an isotropic (hydrostatic) component due to change in the stoichiometry, and a biaxial component due to different coefficients of thermal expansion of the two materials, and/or to the presence of growth strain. Moreover, in the present case the lattice constant of the substrate is 5.4% larger than the one of the growing film, therefore an additional misfit strain

component would be expected.

In the as-grown 24 nm-thick film, the out-of-plane plane lattice constant is 5‰ larger than the relaxed one (a = 5.150 Å), while the in-plane lattice constant is compatible with the unstrained one. This means that for this sample:

$$\epsilon_{11} = \epsilon_{22} = 0$$

and

$$\epsilon_{33} = 0.005$$

Assuming the relationships between the stress and the strain tensors in case of linear elastic behaviour, the symmetry of the elasticity tensor in a cubic material, and the elasticity coefficients of cubic YSZ (see appendix A), this means that the stress tensor in the as-grown film is:

$$\underline{\sigma}_{ag} = \begin{pmatrix} \sigma_{11} \\ \sigma_{22} \\ \sigma_{33} \\ \sigma_{12} \\ \sigma_{13} \\ \sigma_{23} \end{pmatrix} = \begin{pmatrix} 0.28 \\ 0.28 \\ 2.24 \\ 0 \\ 0 \\ 0 \end{pmatrix} (GPa) = \begin{pmatrix} 2.24 \\ 2.24 \\ 2.24 \\ 0 \\ 0 \\ 0 \end{pmatrix} (GPa) + \begin{pmatrix} 2.81 \\ 2.81 \\ 0 \\ 0 \\ 0 \\ 0 \end{pmatrix} (GPa) + \begin{pmatrix} -4.77 \\ -4.77 \\ 0 \\ 0 \\ 0 \\ 0 \end{pmatrix} (GPa)$$

where the first term in the last sum is ascribable to an isotropic (hydrostatic) stress component, inducing an overall dilation of the lattice (4‰), changing the lattice constant to a=5.171Å. This would correspond to a 35% $YO_{1.5}$ molar fraction, instead of the 21.4% evaluated for the YSZ target (see Section 1.5). The second term is the contribution of the thermal biaxial component, developing during cooling down from deposition temperature (750°C) due to the different thermal expansion coefficients of film and substrate (see appendix B), while the third term an instrinsic compressive stress contribution.

The annealed film shows instead a dilation in the whole lattice, with an in-plane expansion of 1% and 3‰ expansion out-of-plane. This means:

$$\underline{\sigma}_{ann} = \begin{pmatrix} \sigma_{11} \\ \sigma_{22} \\ \sigma_{33} \\ \sigma_{12} \\ \sigma_{13} \\ \sigma_{23} \end{pmatrix} = \begin{pmatrix} 3.69 \\ 3.69 \\ 2.12 \\ 0 \\ 0 \\ 0 \end{pmatrix} (GPa) = \begin{pmatrix} 2.12 \\ 2.12 \\ 2.12 \\ 0 \\ 0 \\ 0 \end{pmatrix} (GPa) + \begin{pmatrix} 1.57 \\ 1.57 \\ 0 \\ 0 \\ 0 \\ 0 \end{pmatrix} (GPa)$$

In the last sum, the isotropic component corresponds again to a 4‰ lattice expansion. This result would need to be further verified by XRD analyses, in most cases showing a good agreement of the lattice constant with the value expected based on the target composition [Gsell(07)-2]. The biaxial term component could be due to the different thermal expansion coefficients between YSZ and Si.

The thicker layer (485 nm) in Figure 4.5 shows that the in-plane and out-of-plane lattice constants are identical, within the measurement error, indicating the lack of strain in a layer grown to such high thickness, even without annealing treatments. However, for these thick films, showing negligible strain after the deposition, the formation of cracks along <110> directions is observed upon annealing (see Figure 4.6). These cracks were observed also at much lower thickness (*e.g.* 30 nm), forming after annealing treatments in order to accomodate the thermal strain. The formation of cracks in cubic YSZ films was already reported in literature for a 330 nm thick film, but in that case the lines were observed along

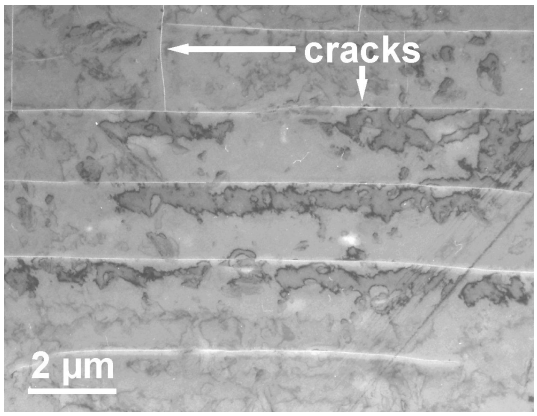

Figure 4.6 – Plan view BF image of a ≈480 nm-thick cubic YSZ film after thermal annealing in air at 1200°C for 16 h ([001] zone axis). The edges of the image are parallel to <110> directions of YSZ. The sharp and straight bright lines are thermal cracks formed in the layer, while the dark contrast bands are generated by diffraction contrast due to bending.

<100> directions [Lei(01)]. A viable solution for the realisation of cubic YSZ films with good texture and no cracks is the deposition of few nm thick films, followed by annealing and further growth. The texture and the strain field for films deposited following this procedure are acceptable in view of the whole multilayer deposition [Gsell(07)-2].

4.2 Microstructure of tetragonal YSZ buffer layers on Si substrates

For the epitaxial growth of a sequence of cubic materials, a cubic YSZ buffer layer would be the most natural choice. However, in the former section cracks have been shown to form upon thermal annealing, which is anyway a necessary step for the texture improvement. The only viable solution to obtain good values for texture and microstrain in a thin cubic YSZ film is a double deposition step, with an intermediate annealing treatment, as found in a former study [Gsell(07)-2]. A possible alternative solution can be the use of tetragonal YSZ films. The crystal symmetry of this structure implies the presence of different texture components in a thin film, which typically arrange in different domains, leading to the relief of structural strain [Lei(01)]. The tetragonal YSZ films analysed here were deposited by PLD using a target with a nominal 5.1 mol% $YO_{1.5}$ content on Si substrates using the setup described in Section 3.1. Assuming a 1:1 stoichiometry transfer during PLD, the prepared YSZ films were expected to have a tetragonal structure with the following lattice parameters (equations 1.2):

$$\begin{aligned} a &= 5.10 \text{ Å} \\ c &= 5.18 \text{ Å} \end{aligned} \tag{4.1}$$

with a c/a ratio of 1.016, indicating a small tetragonal deformation. Former quantitative XRD studies demonstrated that the prevailing component of the target has an effective stoichiometry of 4.7 mol% $YO_{1.5}$ [Gsell(06)], which however does not induce an appreciable variation of the lattice parameters within the experimental uncertainties concerned in the present study.

In the experiments described in this section the annealing step has always been carried out in air at 1200°C for 16 hours, which always results in the formation of a ≈300 nm thick amorphous SiO_2 layer between Si and YSZ. Most of the films analysed in the present section were deposited on Si(001) substrates, as this is the best orientation for single-crystal diamond growth. However, in order to estimate the arrangement of the different texture components following thermal annealing, some films were realised on Si(111) substrates.

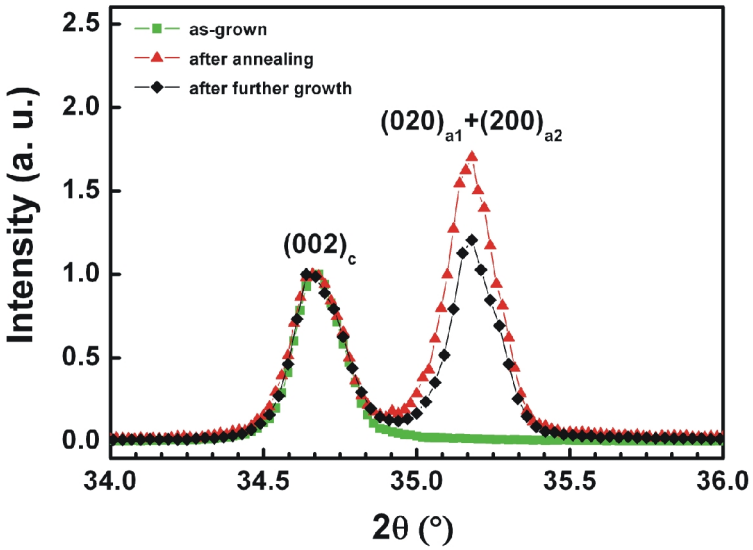

Figure 4.7 – XRD ϑ-2ϑ–scan ($\chi = 0°$) of sample YSZ229 as-deposited (100 nm thick), after annealing and after growth of additional 50 nm, in the region of the (200) and (002) peaks of tetragonal YSZ. The spectra are normalised to the intensity of the (002) peak.

4.2.1 Tetragonal YSZ films on Si(001)

For tetragonal YSZ films deposited on Si(001) substrates, an interesting effect accompanying annealing processes is observed in XRD ϑ-2ϑ–scans. In general, for these samples, ϑ-2ϑ–scans (performed in parallel beam geometry, with the reciprocal vector **g** perpendicular to the surface [Gsell(07)-2]) show a double peak, which is composed of the (200) and (002) peaks of tetragonal YSZ (Figure 4.7). The peak at lower ϑ (higher lattice plane spacing, d) is generated by a component (c) with the c axis perpendicular to the surface, and the peak at higher ϑ (lower d) is due to the two components (a_1 and a_2) with the a-axis perpendicular to the surface and the c-axis oriented parallel to the Si surface (see Figure 4.8). The ratio between the area under the two peaks, I(002)/I(200), gives an indication of the relative fraction of the texture components, and it should be 0.62 in case of statistical distribution of the three components, due to the relative occurence of the two types of components (1:2) and the slightly different structure factors of the (002) and (200) reflexes [Teufer(62)].

The effect of the annealing treatment is shown in Figure 4.7 for a 100 nm-thick film (sample YSZ229). In the ϑ-2ϑ–scan of the as-grown film only the (002) peak is present at $2\vartheta = 34.7°$($d = 2.58$ Å), while after annealing the (200)/(020) peak is also observed at $2\vartheta = 35.2°$($d = 2.55$ Å). The peak positions are compatible with the expected values for the lattice parameters within an error lower than 0.5%. This result indicates that for this sample the as-grown film is composed of only one texture component, with the c-axis oriented perpendicular to the Si(001) surface, while after the annealing treatment the material rearranges among the three components. Pole figures for the {211} peaks allowed to determine that the a_1 and a_2 components in the annealed sample occupy roughly equal volume portions [Gsell(07)-2]. For all the tetragonal films deposited with the same setup, a similar trend with annealing has been observed, with a fraction of c-oriented material higher than for statistical distribution for the as-deposited film and a relative decrease of it after the annealing treatment.

In order to verify the change in microstructure induced by the thermal treatment, plan-view TEM analyses were carried out on tetragonal YSZ films with variable thickness, as-grown and subject to annealing treatments. Low magnification plan-view TEM images of an as-grown film with a thickness of about 40 nm (YSZ15) do not show any particular

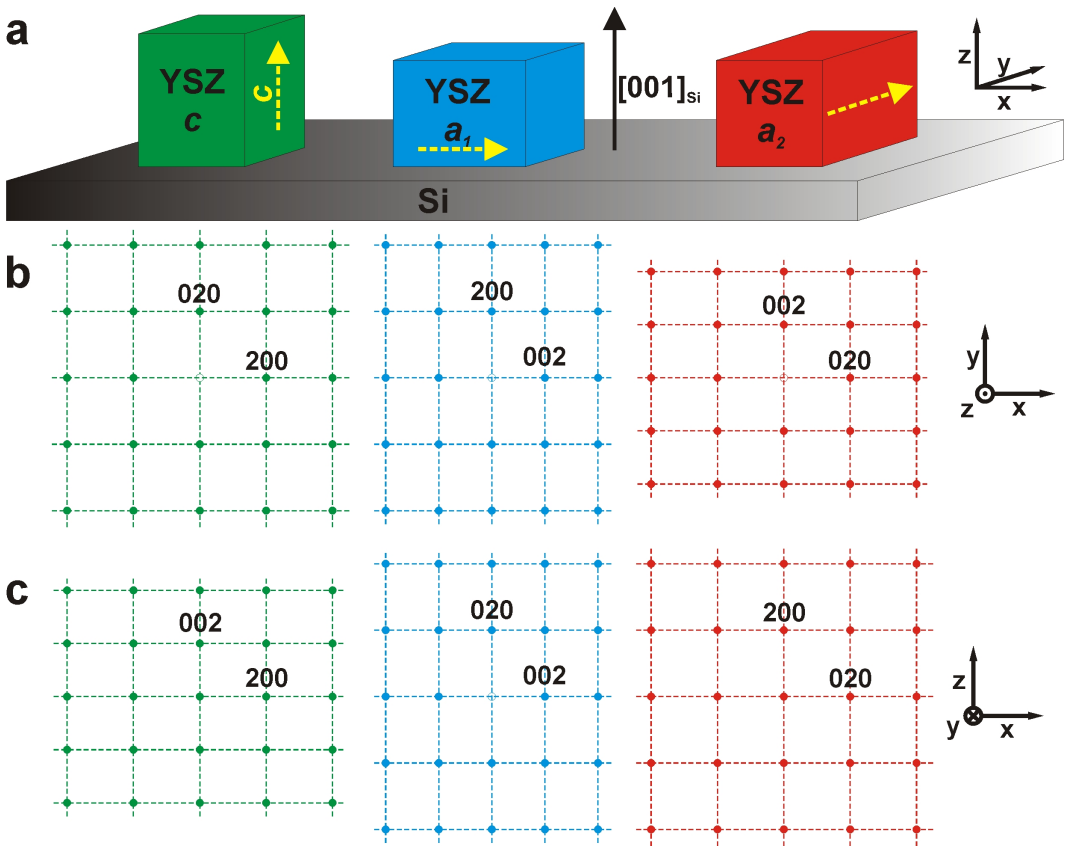

Figure 4.8 – (a) Schematic representation of the three possible texture components, c, a_1 and a_2, occuring in an epitaxial tetragonal YSZ film grown on Si(001) (for better visualisation, the case of c/a=1.25 is shown). (b-c) Corresponding schematical SAED patterns viewed (b) from top (plan view, [001] direction of Si) and (c) from front (cross section, [0$\bar{1}$0] direction of Si) for each component.

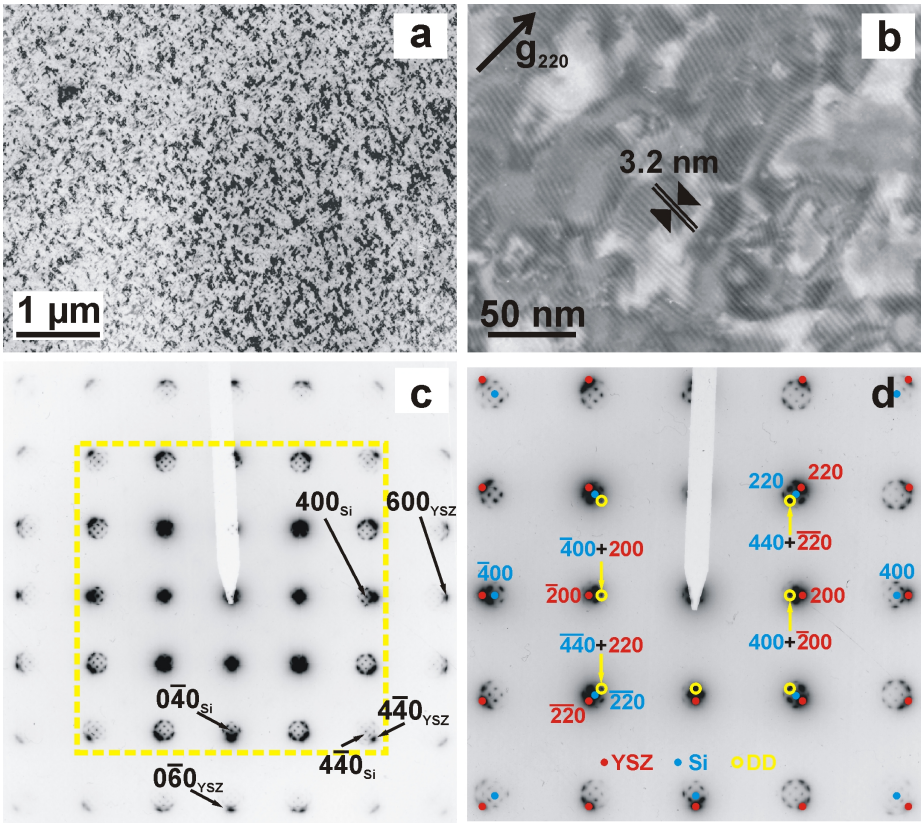

Figure 4.9 – (a-b): Plan-view BF-TEM images at different magnification and (c) corresponding SAED pattern along [001] of an as-grown 40 nm thick tetragonal YSZ film on Si(001) (YSZ15). In (d), magnification of the area in the yellow dashed box, the origin of some of the double diffraction (DD) spots is indicated.

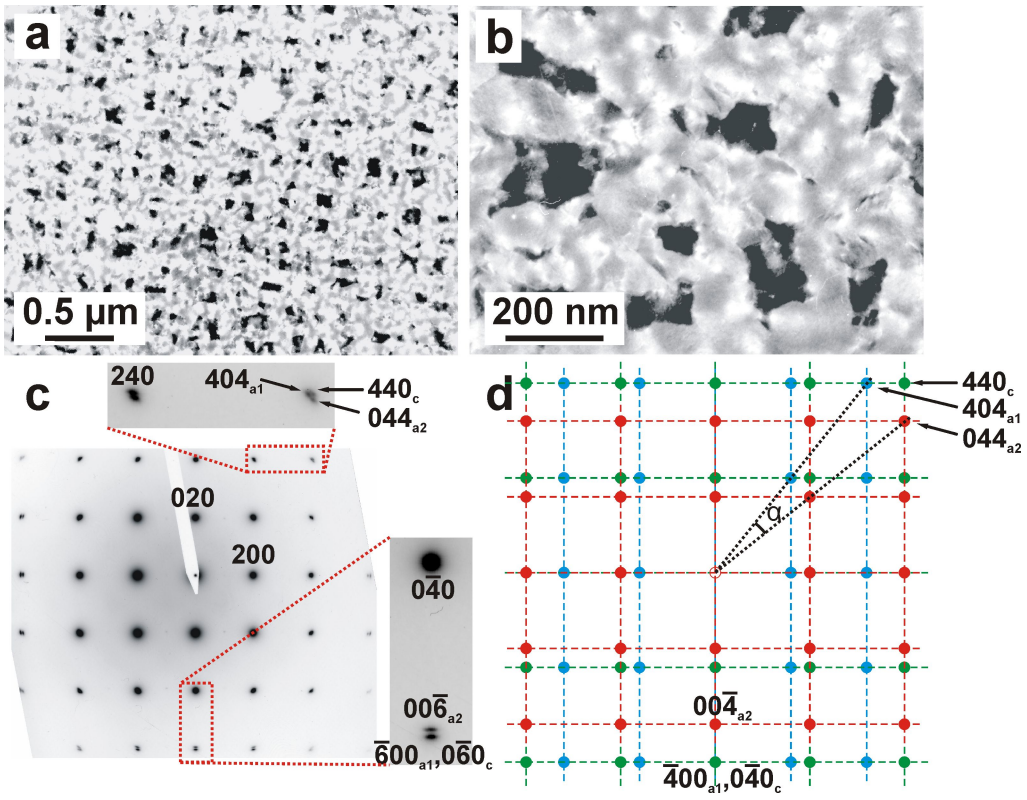

Figure 4.10 – (a-b) BF plan-view images of the same film in Figure 4.9 after the annealing treatment, showing the typical "chocolate-bar pattern" (image edges parallel to <100> directions of YSZ), and (c) corresponding SAED pattern ([001] zone axis). In the insets, magnification of some areas of the pattern are shown, in order to evidence the splitting of the higher order diffraction spots. (d) Schematic representation of the [001] SAED pattern expected from the combination of the three texture components without any twinning relationship (for the sake of clarity, $c/a = 1.25$ and the same colour code of Figure 4.8 have been chosen).

features (Figure 4.9(a)). The contrast in the image is diffraction contrast due to surface bending. SAED analyses of the same sample confirm an epitaxial orientation of the YSZ film with respect to the Si substrate, with a 1.5° twist around the common [001] direction, perpendicular to the surface (Figure 4.9(c)). In this case, a rough evaluation of the twist value from SAED patterns is given by the total azimuthal spread of the diffraction spots, intrinsically larger than the twist based on XRD φ-scans (typically 1° for up to 100 nm-thick YSZ films). Multiple diffraction spots formed due to combined elastic scattering in the Si substrate and in the YSZ film are observed (Figure 4.9(c-d)). The plan-view sample is indeed thick enough (≥40 nm along the electron beam direction) to include also the Si substrate. Only one texture component can be extracted for YSZ from the diffraction pattern, with the c-axis perpendicular to the Si(001) surface. The measured YSZ lattice constant a is 5.11 Å, compatible with the expected length of the a axis. Higher magnification BF images show fringes all over the image, with a characteristic spacing $D = 3.2 \pm 0.5$ nm (Figure 4.9(b)). The observed double diffraction pattern confirms that these are misfit *Moiré* fringes formed by parallel Si and YSZ lattice planes due to the lattice misfit in the two materials [Fultz(01), Williams(09)]. According to the formula:

$$D = \frac{d_1 \cdot d_2}{d_1 - d_2} \tag{4.2}$$

giving the period of the Moiré fringes, the spacing D fits quite well to the case $d_1 = d_{220,Si}$ = 1.92 Å and $d_2 = d_{220,YSZ}$ = 1.81 Å.

Plan-view TEM of the same film after annealing shows approximately rectangle-shaped

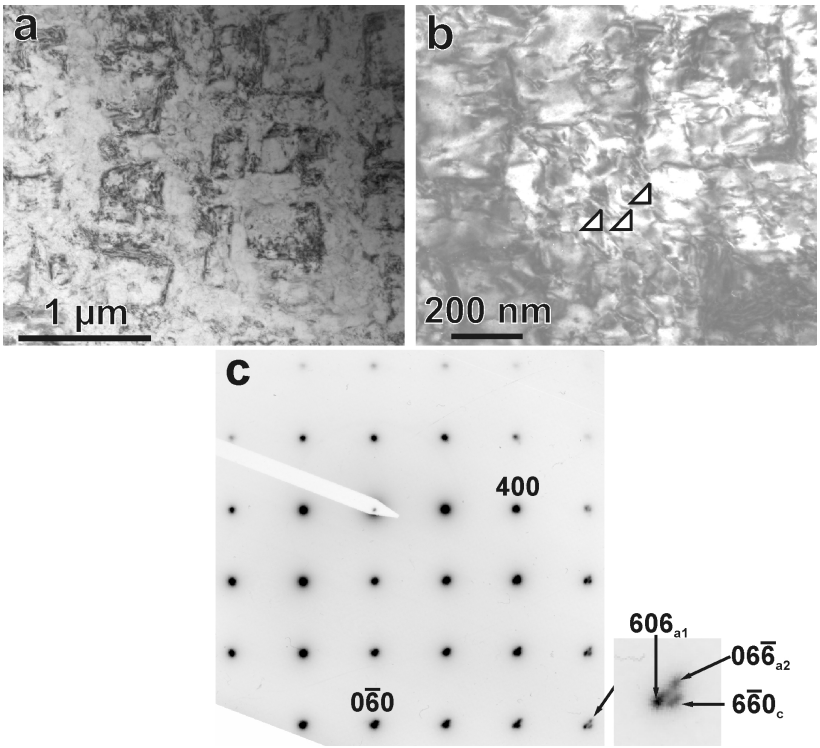

Figure 4.11 – (a-b) BF-TEM plan-view images of an annealed 100 nm-thick tetragonal YSZ film on Si(001) (YSZ229): (a) "chocolate bar" structure with rectangular features and (b) streaks aligned 45° relative to the rectangular domain edges (edges of images parallel to <100> directions of YSZ). (c) SAED pattern acquired along [100] using the smallest aperture (560 nm diametre).

features with the edges roughly aligned along <100> directions of Si, with an average edge size of 80 nm (Figure 4.10(a-b)). The SAED pattern acquired along [001] shows only spots due to YSZ, since in this case the thickness of the plan-view sample includes a portion of the ≈300 nm-thick amorphous SiO_2 film formed upon annealing, but not the single-crystal Si substrate (Figure 4.10(c)). The clear splitting of the higher order diffraction spots suggests that more texture components are present. In particular, the splitting of the (006) spots allows to evaluate a c/a ratio of 1.014, compatible with the expected value for relaxed tetragonal material. The {440} spots show a splitting into three components, where the angle between the ones not aligned with the geometric diagonal is 0.83°. In case the three texture components are oriented independently of each other (no twinning on {110} planes), the expected SAED pattern is schematically represented in Figure 4.10(d), where the angle between the {440} spots of the a_1 and a_2 components is:

$$\alpha = \text{arctg}(a^*/c^*) - \text{arctg}(c^*/a^*) = \text{arctg}(c/a) - \text{arctg}(a/c) \tag{4.3}$$

This angle is 0.90° for the expected ratio $c/a = 1.016$ and 0.80° for the $c/a = 1.014$ measured in this case. In case of twinning on {110} planes, the {100} spots would form a ≈0.9° angle and the angle between the {440} spots of the a-components would be 2α (≈1.8°). The observed pattern is then in full agreement with an independent orientation of the three texture components. However, it was not possible to select regions corresponding to individual texture components, even using the smallest aperture for SAED, having a diametre of 560 nm.

A 100 nm-thick tetragonal YSZ film on Si(001) (sample YSZ229) does not show any clear feature in plan-view TEM after deposition, in analogy to what was observed for the 40 nm-thick film. Only c-axis orientation is revealed by SAED patterns, in complete agreement with XRD characterisation of the same sample (see Figure 4.7). After annealing, a rather

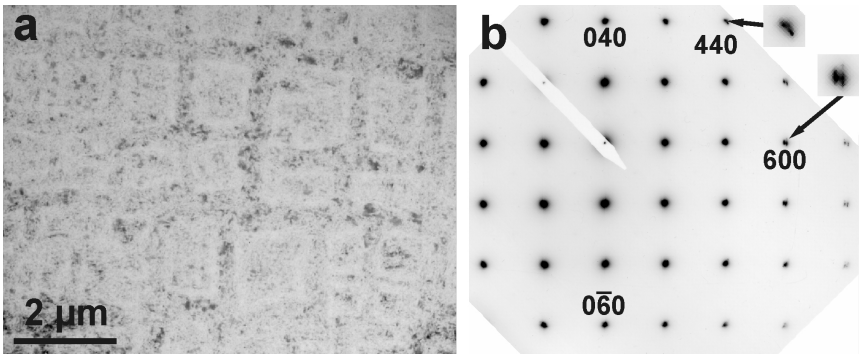

Figure 4.12 – (a) BF-TEM plan-view image of a 100 nm-thick tetragonal YSZ film on Si(001) (YSZ229) subject to thermal annealing and further 50 nm growth (contrast inverted for better visualisation). (b) Corresponding SAED pattern, acquired with the smallest aperture. The contribution of several texture components is clearly visible in the top right insets, showing higher magnification of some significant portions of the pattern.

sharp "chocolate-bar" structure appears, with rectangular features having side lengths of about 400 nm (Figure 4.11). Higher magnification images show some streaks aligned along <110> directions. The size of the rectangular features did not allow again to isolate SAED patterns from the rectangular features, or from the regions between them. It is however interesting to see that the SAED pattern confirms the independent alignment of the three texture components (Figure 4.11(c)). The extracted lattice parameters are $a = 5.12$ Å and $c = 5.18$ Å ($c/a = 1.012$). Moreover, the {660} spots show a clear splitting into three components, with an angular distance of 1°, which confirms that no twinning is present on the {110} planes. The same sample was subject to a further 50 nm growth step after the annealing process, without any significant variation neither in the size nor in the surface coverage with the rectangular domains (Figure 4.12).

A thicker (nominal 200 nm) tetragonal YSZ film was deposited on top of a 4 inch Si(001) wafer (YSZ062), with a radial thickness inhomogeneity due to the intrinsic characteristics of the PLD setup. At this thickness (≥150 nm) a "chocolate bar" pattern is found directly after growth. Edge sizes and area coverage of the rectangular domains increase with increasing thickness (Figure 4.13(a-b)). Instead, after annealing the area coverage and the edge size decrease (Figure 4.13(c)). No thermal cracks are found in this film neither before nor after annealing, confirming the expected lower strain developing in tetragonal films with respect to cubic films, even at such high thickness. On the other hand, this is also confirmed by the observation that the c/a ratio is roughly constant in all the analysed films, independent of thickness and post-deposition treatment. Plan-view TEM (Figure 4.14(a-b)) of the annealed 240 nm-thick piece shows sharp rectangular domains, with the edge size of ≈900 nm. In this case SAED patterns could be acquired from individual features. The pattern obtained selecting one rectangular feature is shown in Figure 4.14(c), where identical d-spacings are measured along the two <100> directions and no spot splitting is observed. This result allows to identify the rectangular features as c-oriented domains (Figure 4.14(e)). SAED patterns recorded selecting only the area between the c-domains instead shows a splitting of all the high-order peaks, indicating a contribution from different texture components (Figure 4.14(d)) The observed pattern is compatible with a combination of the two a-oriented components without any twinning relationship (see Figure 4.14(f)). The SAED pattern in Figure 4.14(d) is generated from an area showing streaks along <110> directions, which could be the domain walls of the a-oriented components [Lei(01)].

BF-XTEM images of the same annealed thick tetragonal YSZ film do not show clear features (Figure 4.15(a)). Sharp lines along <101> are visible in DF images when {202} spots, common to Si and YSZ, are selected (Figure 4.15(e)). Regions delimitated by <101>-

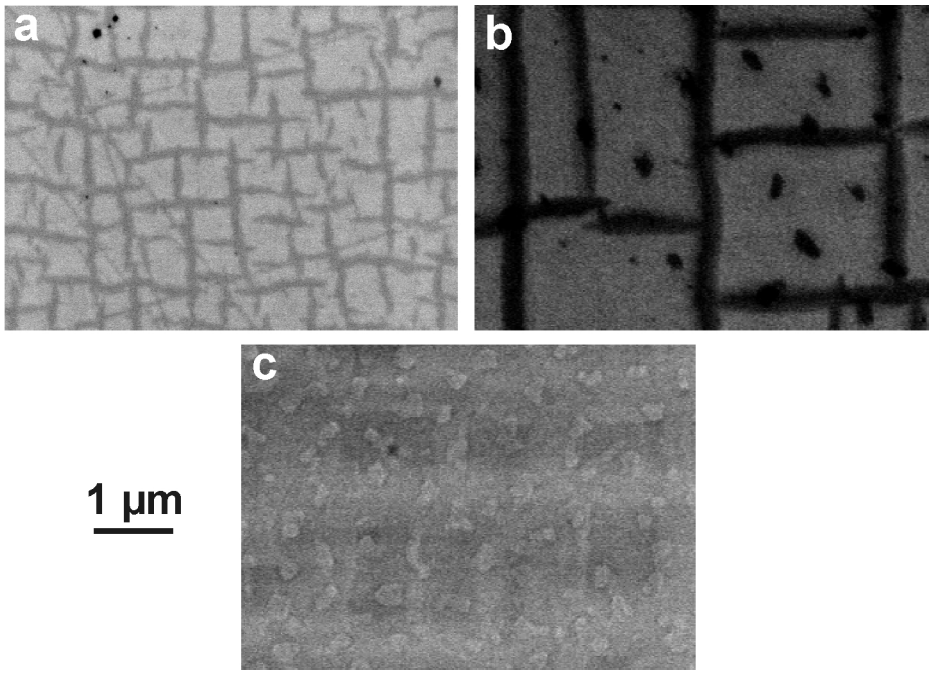

Figure 4.13 – IL-SEM images of different pieces of the sample YSZ062 with different thickness: (a) 150 nm as-grown, (b) 240 nm-thick as-grown and (c) annealed. The scale is common for the three images and their edges are parallel to <100> directions of Si. The spots on the surface of the samples are due to the so-called 'droplet formation' sometimes accompanying PLD deposition, *i.e.* the transfer of small particles of the YSZ target onto the film.

oriented streaks are observed in DF, divided into two size ranges, narrower ones (≈100 nm) and wider ones (≈550 nm). A SAED pattern obtained along <100> of Si using the smallest aperture shows the combination of a *c*-oriented and an *a*-oriented domain (Figure 4.15(b)). The relative orientation of the two components is however ambiguous: the $\{\bar{6}00\}$ spots of the two variants form a 0.7° angle, and 1.1° are formed by the {404} spots. These values do not fit exactly neither to an independent orientation of the two variants nor to the case of twinning on the {101} planes (Figure 4.15(c-d)). However, the reason for this ambiguity might be a slight polar misorientation (tilt) of the two variants, which have always been found as independently oriented in the averaging plan-view investigations. Weaker spots are also present in the SAED pattern, corresponding to {102} positions. In particular, a rather intense $(10\bar{2})$ spot appears between the $(00\bar{2})$ and the $(20\bar{2})$ spots of Si and YSZ. This fluorite-forbidden reflection is expected to appear for a tetragonal component with the *c*-axis perpendicular to the film surface, therefore related in this case to the *c* component. DF imaging by selecting this spot shows that the wider domains get bright while all the rest stays dark. This confirms that the wider 45°-oriented domains are the ones with the *c*-axis perpendicular to the Si surface. This is in complete agreement with the plan-view results, according to which the *c*-domains are much larger than the *a*-domains (Figure 4.14). The corresponding spots generated by the a_1 texture component should be found along the [001] direction of Si, but they are not visible probably due to the imperfect zone axis orientation. Therefore no DF-imaging was possible for this other component. The cross section slice can be imagined as the one enclosed between the dashed yellow lines in Figure 4.14(a). However, the size of the *c*-oriented domains observed in XTEM is smaller than the average one evaluated from PV images, but the extremely variable size of the various domains explains this result.

A comprehensive plan-view TEM study of the microstructure of thick (370 nm) tetragonal YSZ films grown by PLD on Si(001) was reported by Lei et al. [Lei(01)]. Large rectangle-shaped features were identified as *c*-oriented domains and the streaks forming 45° with their walls were deduced to be walls of the *a*-oriented domains. The presence of domain walls

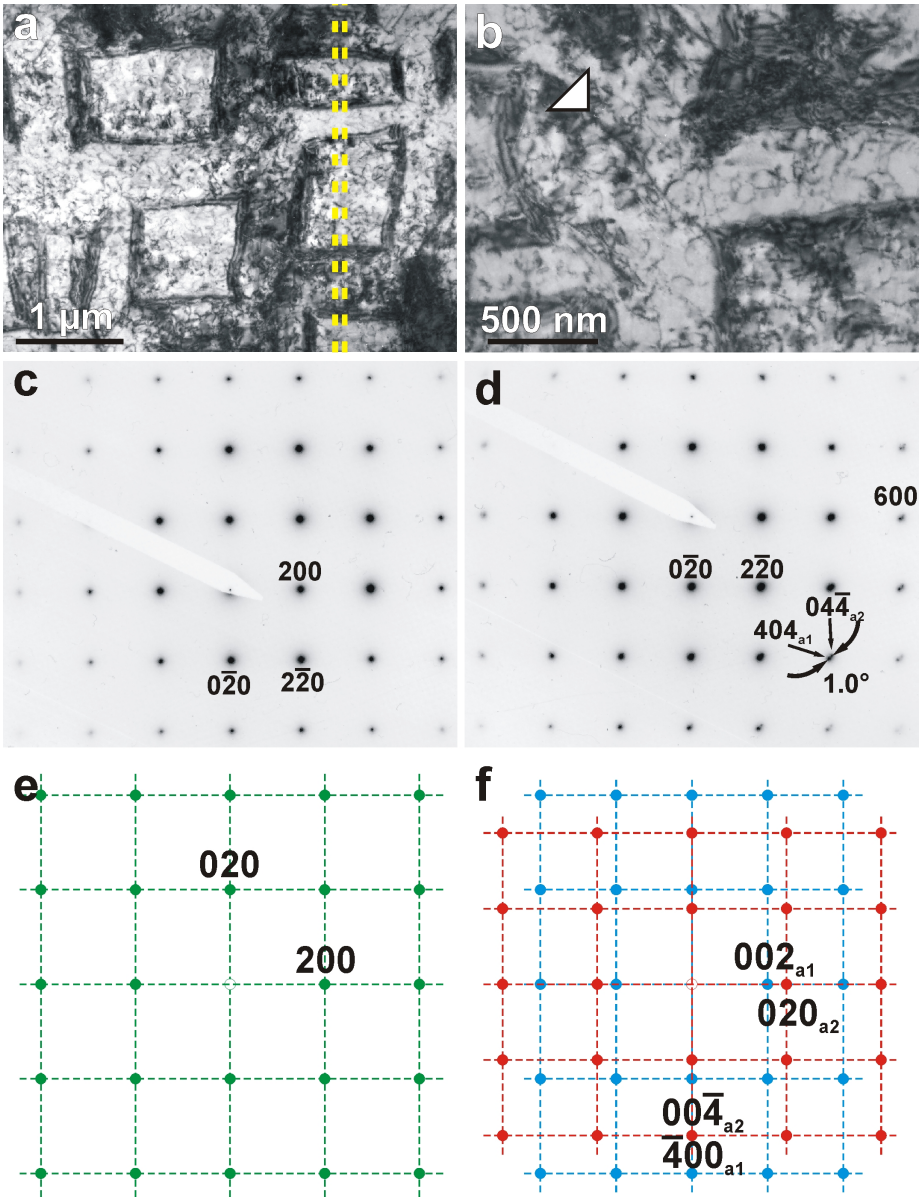

Figure 4.14 – (a-b) Plan-view BF-TEM images of an annealed 240 nm-thick piece of a tetragonal YSZ film grown on a 4 inch Si(001) wafer (sample YSZ062). (c-d) SAED patterns along [001] of YSZ acquired using the smallest SAED aperture from (c) a single rectangular domain and (d) the area between rectangular domains. (e-f) Schematic [001] SAED patterns corresponding to (e) *c*-oriented material and (f) combination of a_1 and a_2 components without any twinning relationship (same colour code as in Figure 4.8, $c/a = 1.25$).

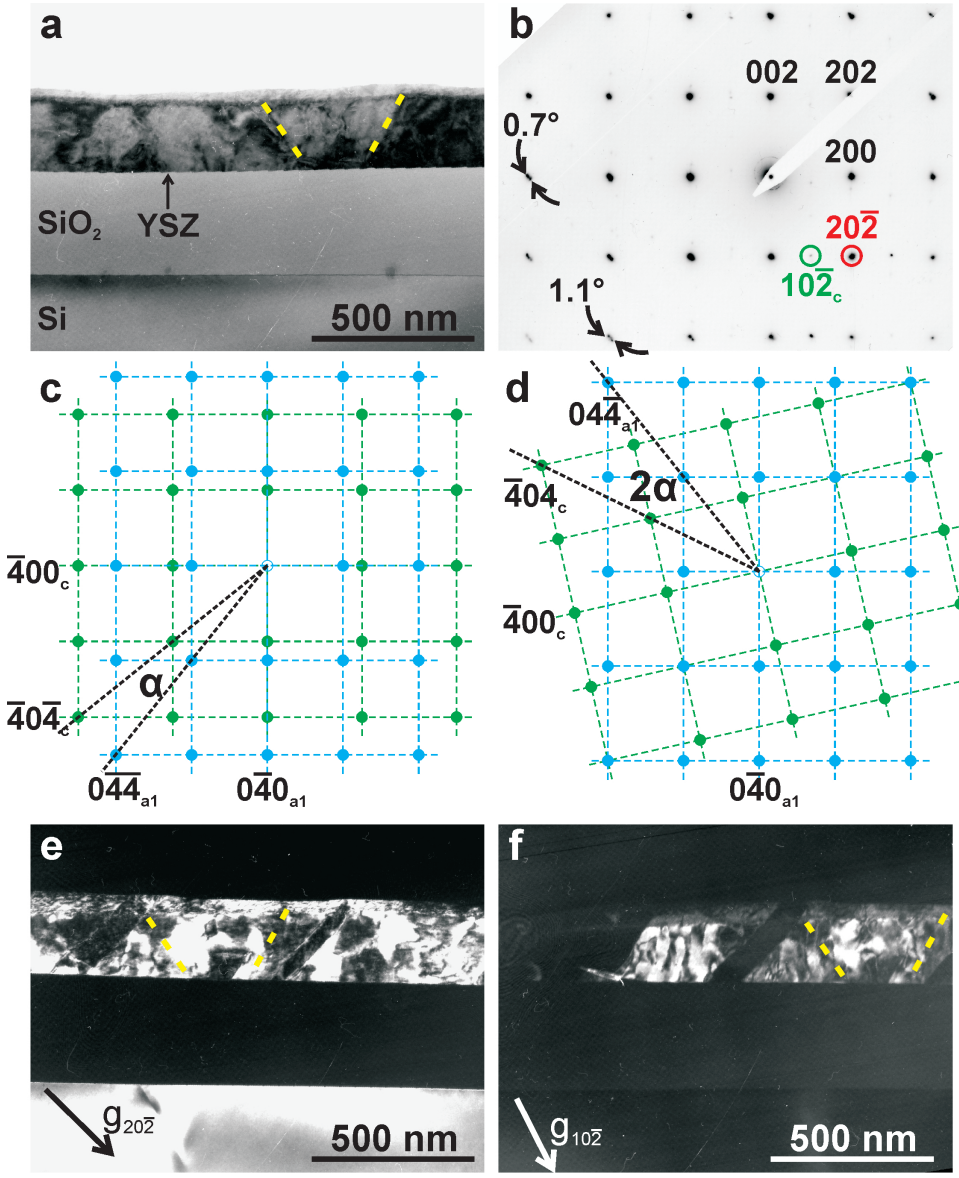

Figure 4.15 – (a) BF-XTEM image of an annealed 240 nm-thick piece of a tetragonal YSZ film grown on a 4 inch Si(001) wafer (sample YSZ062). (b) SAED pattern along $[0\bar{1}0]$ zone axis obtained using the smallest aperture. (c-d) Schematic representation of cross section SAED patterns in case of (c) independent orientation of a *c*-oriented and an *a*-oriented domain and (d) twinning on a {101} plane of the two variants (same colour code as in Figure 4.8). (e-f) DF images of the same area acquired selecting the (e) $(20\bar{2})$ and the (f) $(10\bar{2})$ spot (dashed yellow lines indicate reference features in the images).

Table 4.2 – List of the YSZ films analysed by TEM in the present section, with indication of the fraction of the *c*-oriented material derived from XRD ϑ-2ϑ–scans (ref. [Gsell(07)-2]) and from plan view TEM images. All these samples were deposited by PLD using a tetragonal YSZ target (5.1 mol.% $YO_{1.5}$) on Si(001) substrates as described in Section 3.1. Some of the samples (ann.) were annealed in air for 16 h at 1200℃ after deposition.

	Thickness (nm)	**c-material portion** %	
		XRD	TEM
YSZ015	30-40	71	100
YSZ015 ann.	30-40	50	12
YSZ229	100	100	100
YSZ229 ann.	100	36	28
YSZ229 ann. + 50 nm	150	46	32
YSZ062	150	??	65
YSZ062	240	??	75
YSZ062 ann.	250	??	44

forming 45° with the Si substrate surface was deduced by tilting experiments, but never directly visualised. No direct identification of single types of domains could be done due to the geometry of plan-view specimens and to the lack of distinctive fluorite-forbidden spots. Moreover, SAED studies of those films allowed to deduce a structure consisting of alternating differently oriented tetragonal domains sharing the {101} planes of YSZ, in twinning relationship with each other. In the present films, the {101} planes of the three texture components do not exhibit any twinning relationship, as clearly proved by all SAED investigations of plan-view samples. This result is in agreement with previous XRD pole-figure analyses of annealed tetragonal YSZ films on Si(001), showing the parallel orientation between the crystallographic axes of the three texture components [Gsell(07)-2]. The only ambiguous result has been obtained from the cross-section SAED of two domains, but more statistical results would be needed for a conclusive statement. The present XTEM investigations unambiguously allow the direct visualisation of the different texture components. The film structure appears similar to the polydomain tetragonal zirconia organised in "colonies", reported by Baither et al. [Baither(97)]. However, a major difference consists in the reported twinning of the three variants on common {101} planes, that has not been observed here. Moreover, in the specimens investigated in the cited reference, all three tetragonal variants are organised in thin plate-like domains, ≈100 nm wide and ≈1 μm long. In the present case the kinetics and the specific symmetry imposed by epitaxial growth causes a discrimination between the *c*-domains, which are favoured by the growth conditions, and the *a*-components, that are organised in smaller domains, forming a substructure identical to the one reported by Baither et al. [Baither(97)].

From the plan-view TEM analyses of tetragonal YSZ films the relative volume fraction of the *c* and the a_i components can be extracted (see Table 4.2). This evaluation is performed by estimating the coverage of the investigated area with rectangular domains, formed by the *c*-oriented material. This procedure however is affected by unavoidable errors. First of all, in some cases (especially for thicker films) the domain walls are not well defined in the plan-view images. Moreover, these calculations are performed based on two–dimensional images, which do not take into account the topographic steps upwards observed in AFM corresponding to the *c*-domains. However, the latter contribution can be neglected, as the step is always much smaller than the film thickness (≤3%), as determined by AFM. In addition to this, it is always important to keep in mind that TEM images provide local information. However, rather than single values, the trend is interesting. This says that a high portion (>50%) of *c*-oriented

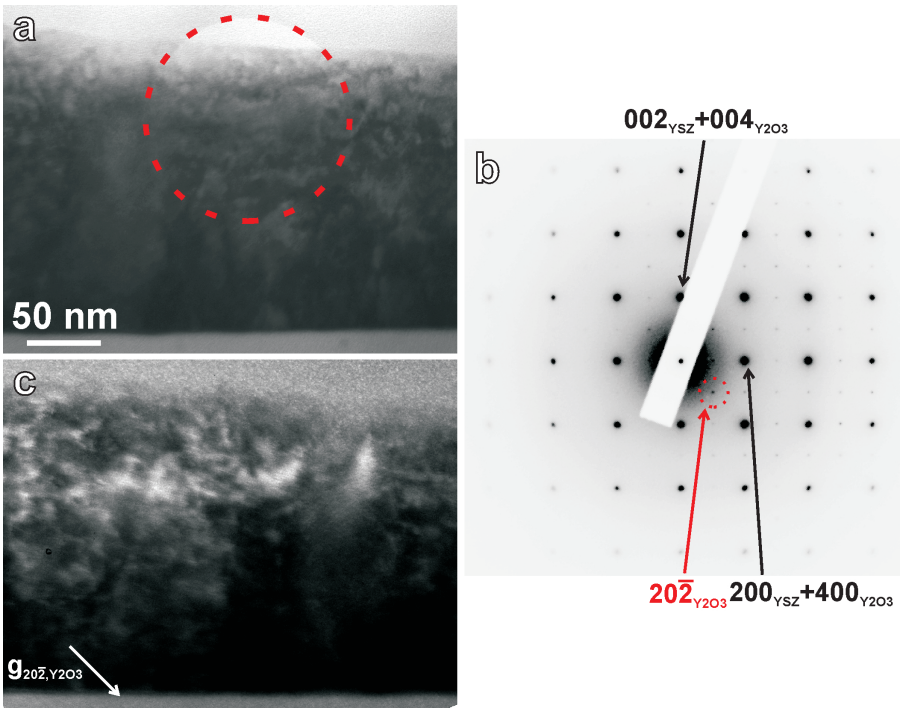

Figure 4.16 – (a) BF-XTEM image of the same sample in Figure 4.15 and (b) corresponding SAED pattern acquired selecting the area included in the dotted circle (analyses performed using the JEM 2100F instrument, $[0\bar{1}0]$ zone axis). Weak spots at intermediate positions between the tetragonal YSZ spots can be attributed to a cubic Y_2O_3 phase with doubled lattice constant [Scott(75)]. (c) Corresponding DF image acquired by selecting the spot ascribable to $\{20\bar{2}\}$ planes of a cubic Y_2O_3 phase.

material is present in as-deposited films. This amount decreases after thermal annealing in air, and shows negligible change after further deposition. Based on these results, it is difficult to extract a trend with increasing film thickness. However, the observed trends confirm the results of XRD analyses, which are surely more reliable for an exact quantification, especially due to their non-local character [Gsell(07)-2].

XTEM-SAED patterns obtained selecting small areas close to the surface of an annealed 200 nm thick tetragonal film reveal the presence of weak spots at all intermediate positions among the tetragonal YSZ spots (Figure 4.16). In former XRD studies the segregation of yttria due to annealing processes was hypothesized as a possible explanation of the observed decrease in the lattice constant of cubic YSZ [Gsell(07)-2]. RHEED analyses showed super-structure features appearing after annealing of both cubic and tetragonal YSZ films [Gsell(07)-2]. In the case of tetragonal films, the periodicity of the super-superstructure streaks was 1/2 of the one of the fluorite streaks. A cubic Y_2O_3 phase with type C rare earth oxide structure, with double lattice constant as the tetragonal one, would indeed explain the spots observed in SAED [Scott(75)]. Dark field micrographs obtained selecting such spots confirm that the signal is generated by a region close to the film surface (Figure 4.16(c)). An alternative explanation would be the presence of YSZ precipitates of a different phase in the analysed area [Schoenlein(80)]. The lack of these superlattice peaks in XRD ϑ-2ϑ–scans could be attributed to the small volume percentage of the segregated phase. EDS maps acquired over the same area of the film, and over several other areas of the sample, point to a surface depletion in Y, which would agree with formerly reported secondary ion mass spectrometry (SIMS) analyses of similar samples [Gsell(07)-2] (Figure 4.17). An average Y/Zr atomic ratio of 7.2% closer to the interface to the SiO_2 layer turns into 5.3% towards the film surface. This lower Y content could correspond to a monoclinic YSZ phase (Figure 1.5), giving indeed rise to spots forbidden for tetragonal YSZ. However, as it is clear from the Figure 4.16(d),

the Y-related peak for these low concentrations is extremely low, and the peak fitting needed for the quantification can lead to errors larger than the statistical error bars shown here.

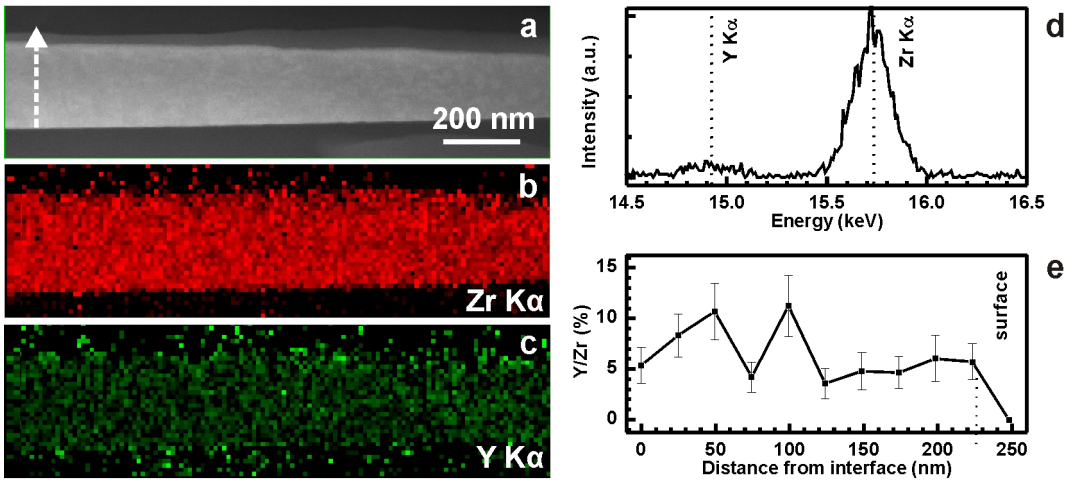

Figure 4.17 – a) STEM-HAADF image of the same region in Figure 4.16 and (b,c) corresponding EDS elemental maps of Zr and Y. (d) Region of the EDS spectrum including the Y and Zr Kα peaks, used for the relative quantification. (e) Line profile, along the film thickness (arrow line in (a)), of the Y/Zr ratio.

4.2.2 Tetragonal YSZ films on Si(111)

Several literature reports indicate the <111> directions as the most favourable for the observation of the three variants in tetragonal materials. These show the appearance of fluorite-forbidden {121} spots, each of them generated by a single texture component [Heuer(88)]. In the above presented plan-view analyses of tetragonal YSZ deposited on Si(001) (Section 4.2.1) no fluorite-forbidden spots were observed in SAED patterns. The direct visualisation of individual texture components was therefore not possible. Only XTEM analyses of a thick YSZ film allowed the identification of *c*-oriented domains. A further attempt to analyse the distribution of the three texture components detected in both XRD and in SAED patterns was therefore done analysing thin tetragonal YSZ films on top of Si(111) substrates.

Plan-view TEM analyses of an as-deposited 40 nm thick tetragonal YSZ film on Si(111) do not show defined features (Figure 4.18(a)). At high magnification, Moiré fringes are visible (Figure 4.18(b)), with a spacing of ≈3.2 nm as observed in an analogous film on Si(001) (Figure 4.9). These can be interpreted as misfit fringes generated by the {220} planes of Si and YSZ (see Figure 4.9 and discussion), which is confirmed by the typical multiple diffraction spots observed in SAED patterns (Figure 4.18(c-d)).

After annealing the same film shows a disordered array of features delimited by steps forming ≈90° among each other (Figure 4.19(a-b)). The regions delimited by such steps could be single-texture domains with rectangular shape, in analogy to what observed in case of (001) orientation, despite the totally different symmetry of this orientation. SAED patterns show the presence of all the three fluorite-forbidden {112} spots (Figure 4.19(c)). However, DF images acquired selecting the three non-colinear {112} spots (*e.g.*, Figure 4.19(d)) show bright regions only corresponding to the domains walls. This is different to what observed in the case of tetragonal zirconia foils, where plate-like domains were observed along <111> direction, with the edges of the domains of the three tetragonal variants pointing perpendicular to the foil [Baither(97)]. In the present case it seems that the fluorite-forbidden spots are not generated by the three tetragonal texture components but from segregated phases with a lower symmetry crystal structure, localised in small peripheral regions. However, further

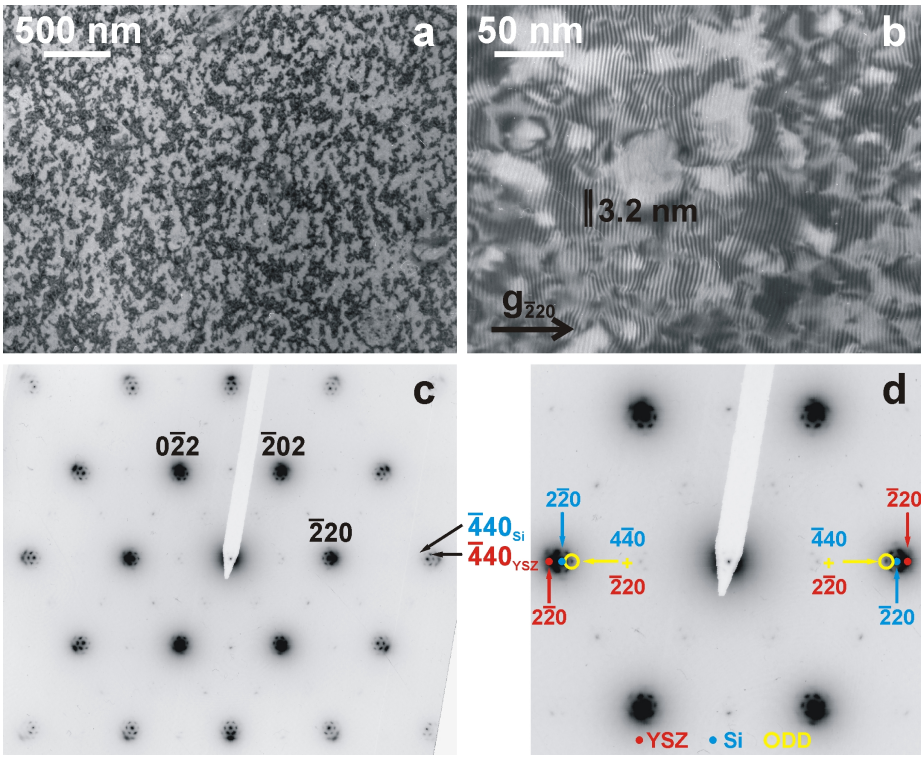

Figure 4.18 – (a) Low and (b) high magnification plan view BF-TEM image of a 40 nm-thick tetragonal YSZ film on Si(111) (sample YSZ16). A Moiré pattern is visible in (b), with a spacing of 3.2 nm. (c) SAED pattern of the sample along [111] zone axis of Si. In (d) the origin of some of the double diffraction (DD) spots is indicated.

investigations on thicker films deposited onto Si(111) substrates, expected to result in larger domain sizes, could help toclarify this point.

4.2.3 Discussion

The presented TEM study of tetragonal YSZ films on Si(001) substrates provide a precious support to the previously obtained XRD results. The presence of the three texture components and the variable volume fraction occupied by the three texture components is confirmed by the present study, and the features corresponding to the two types of components (*c*-oriented and *a*-oriented) are addressed. This results confirm some of the ones previously reported in literature, however enriching them with a systematic study of the effect of annealing treatments and thickness increase. This is particularly interesting in view of the following deposition of additional epitaxial layers. In this perspective, the here observed epitaxial relationship of all three variants with respect to the Si substrate and the absence of twinning, which represents a significant difference compared to what was reported previously, makes these tetragonal YSZ layers interesting also as buffer layers for following epitaxy. However, as demonstrated by accurate texture studies, the Ir epitaxial films that are deposited on top of YSZ as buffer layers of the final single crystal diamond deposition are characterised by a ≈1 order of magnitude improvement in texture. This implies that the quality of the intermediate YSZ barely affects the Ir, hence the diamond film quality, if the texture values are in the order of 1°. For this reason, the higher uniformity of the cubic YSZ films, having identical lattice parameters in all three directions, makes them preferrable over the tetragonal YSZ layers for following Ir deposition.

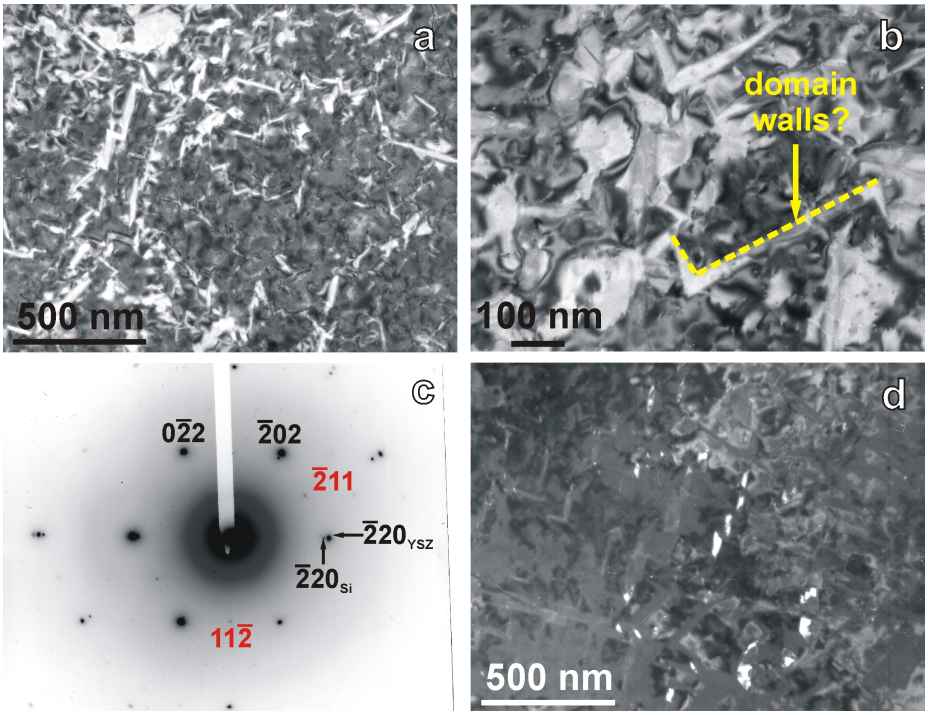

Figure 4.19 – (a) Low and (b) high magnification plan view BF-TEM images of the same sample in Figure 4.18 after annealing. (c) Corresponding SAED pattern along [111] zone axis. (d) DF-TEM image of the area in (a) acquired selecting the (11$\bar{2}$) spot.

Chapter 5

Study of BEN of diamond on iridium buffer layers

As briefly mentioned in Section 1.6.2, BEN on Ir shows completely different features with respect to the more often studied analogous process on Si and 3C–SiC substrates [Schreck(01)-1, Schreck(09)-2]. First of all, for successful nucleation of diamond on Ir, harsher conditions (*i.e.*, higher BEN voltage) are needed with respect to the case of Si (250–300 V for Ir instead of the typical 150–200 V for Si). After a typical BEN process on Si, the substrate is completely covered by few-hundred-nanometers-sized diamond grains, with a variable degree of epitaxial orientation depending on the process parameters. On the other hand, only two groups reported of 5–20 nm diamond grains immediately after the termination of the BEN process on Ir [Bednarski(03), Fujisaki(03), Golding(04)], while all other groups were not able to visualise diamond grains at this stage. Another experiment demonstrated that bulk diamond is unstable under typical conditions for BEN on Ir (60 minutes at ≈250-300 V), showing that extended diamond grains (≈100 nm) completely vanish [Hörmann(01)]. This is clearly in contrast with the classical nucleation theory (Section 1.6.1), according to which grains of that size should only grow further. From the experimental point of view, this implies a significant difference in the possibility of controlling diamond nucleation by monitoring the bias current. While during BEN on Si a steep increase of bias current is observed, ascribed to the coverage of the substrate surface with a diamond layer [Schreck(95)], no appreciable variation of the BEN current is registered during nucleation on Ir. This is probably due to the absence of extended diamond grains after successful BEN.

One aspect often observed after BEN on Ir is the formation of an array of 2–3 nm deep grooves along low indices crystallographic directions in the substrate surface, which was also reported by several groups [Tsubota(00), Hörmann(01), Sawabe(00), Golding(04)]. In a cross-section HRTEM study [Sawabe(00)] the hills formed during BEN on Ir were identified as nucleation sites for diamond, hence considered essential for successful BEN. However, later studies demonstrated nucleation occuring on both roughened and flat Ir substrates [Schreck(06), Gsell(07)-1].

Another peculiar aspect of BEN on Ir, described by several authors working with MW-PCVD systems, is the appearance of μm–sized regions directly after BEN, visualised in SEM as bright areas when the *IL* secondary electron detector, sensitive to the work function contrast, is used (see Section 5.1.1) [Tsubota(00), Schreck(03), Golding(04)]. Epitaxial diamond grains emerge from these areas after a short deposition step, while non-epitaxial grains with a much lower density evolve in the outer areas [Saito(98), Fujisaki(03), Schreck(03)]. The term *domains* was used to designate such bright areas containing the nuclei for epitaxial diamond growth. An interesting feature of the domains is that their surface lies ≈1 nm lower than the surrounding area, as demonstrated by recent AFM studies [Gsell(07)-1].

The direct evidence of the presence of diamond after a successful BEN process on Ir

has been looked for using several techniques. A very thin carbonaceous layer, 0.5–2 nm thick, is formed on the Ir substrate during the BEN process, as deduced by XPS [Kono(04), Kono(05), Aoyama(07), Gsell(08)], elastic recoil detection (ERD) measurements [Bauer(02)] and XTEM [Schreck(06)] for different setups. Spectral features characteristic of diamond bonding between carbon atoms were found by laterally resolved X-ray absorption spectroscopy [Bernhard(06)] and small spot Auger spectroscopy (AES) [Gsell(07)-2, Schreck(09)-1] within the domains. However, the low amount of material and its defective nature make it difficult to detect crystalline diamond features in it, even with surface-sensitive techniques. For instance, RHEED investigations carried out by different groups [Ohtsuka(96), Gsell(08)] were not able to find signatures of crystalline diamond after BEN. Only two publications report of RHEED spot patterns due to diamond formed during the BEN process [Fujisaki(03), Tsubota(00)], but probably these results were due to uncontrolled short growth stages after switching off the bias voltage (>20 s, from the comparison with the results in Section 5.1.1). So far, attempts to directly visualise diamond crystal structures in HRTEM after BEN on epitaxial Ir/$SrTiO_3$(001) failed [Schreck(06)]. Only XPD analyses performed by one Japanese group on samples of A. Sawabe and by the group of J. Osterwalder (University of Zürich) on BEN samples from the diamond film group at the University of Augsburg were able to detect C 1s patterns in agreement with thin epitaxial diamond films [Kono(04), Kono(05), Aoyama(07), Gsell(07)-2, Schreck(09)-1].

In the present chapter some conclusive studies aimed at a deeper understanding of the processes taking place during BEN of diamond on Ir are presented. First of all, in Section 5.1 analyses of samples subject to the BEN process on the (001) and (111) surfaces of single-crystal Ir layers are shown, with particular attention to the Ir/YSZ/Si substrate system, together with studies on samples subject to very short growth steps after BEN. The results of these investigations allow to extract essential data about the internal structure and composition, the dimensions and the areal density of the nuclei formed during BEN. In Section 5.2, ion implantation experiments into epitaxial diamond films are presented, reporting attempts to create, under controlled conditions, damage levels similar to the one generated by BEN. In the following Section 5.3, calculations based on a three-dimensional finite element model are performed in order to evaluate the possible effects of the elastic misfit strain at the interface diamond-iridium on the formation and arrangement of diamond structures during the BEN process. Finally, Monte Carlo simulations are described (Section 5.4), which were able to reproduce the formation of different types of two-dimensional patterns during BEN, due to different conditions of equilibrium between lateral spread and etching of diamond nuclei. With the results of these and former studies of BEN on Ir, a comprehensive model of the processes taking place during the BEN treatment is suggested (Section 5.5).

5.1 BEN and early stages of diamond growth on Ir studied by HRTEM and electron diffraction

BEN studies on epitaxial Ir films using different plasma CVD techniques have been reported for the substrate systems Ir/MgO(001) [Ohtsuka(96), Tsubota(00), Fujisaki(03)], Ir/$SrTiO_3$(001) [Hörmann(01), Bednarski(03)] and Ir(001)/$Al_2O_3(11\bar{2}0)$ [Bednarski(03)]. The epitaxial multilayer Ir/YSZ/Si(001) has emerged lately as the most promising substrate for the deposition of large area single crystal diamond films (see Section 1.4.3). As a consequence, most of the HRTEM studies of BEN and short deposition steps in the present section are focussed on samples realised via MWPCVD processes on this system. In order to get a deeper insight into the mechanisms of BEN, some significant specimens based on different systems are also examined by HRTEM. A paragraph is also devoted to the analysis of BEN on the Ir/YSZ/Si(111) multilayer, a system which clarifies some general aspects of BEN on Ir and opens at the same time an additional technologically interesting path.

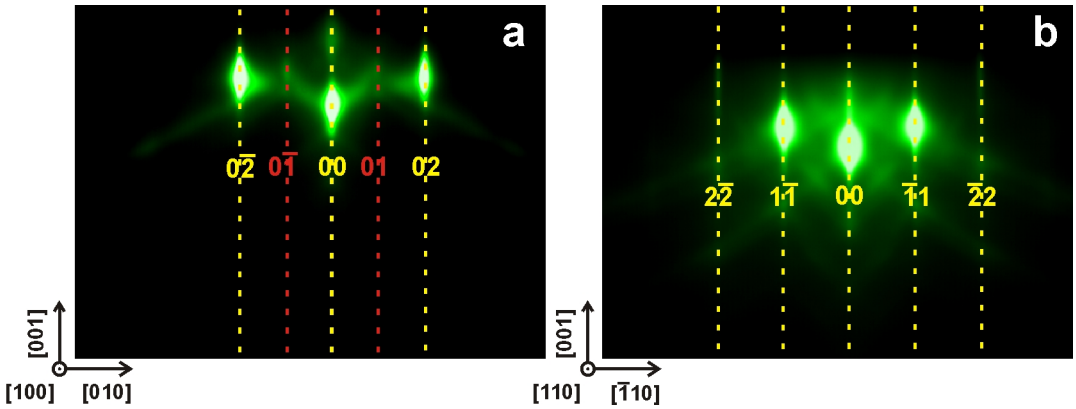

Figure 5.1 – RHEED patterns, acquired at 300°C, of an as-deposited epitaxial Ir/YSZ/Si(001) film along (a) [100] and (b) [110] azimuth. The red dashed lines in (a) indicate the diffraction-forbidden 01 reciprocal rods.

5.1.1 The Ir/YSZ/Si(001) system

For all the samples analysed in the present section, if not otherwise specified, epitaxial Ir films (≈150 nm thick) deposited onto ≈40 nm thick YSZ films on 0.5 mm-thick 4-inch Si(001) wafers were used as buffer layers. Detailed process conditions for the preparation of these layers are described in Sections 3.1 and 3.2. Diamond BEN and growth were performed in the ASTeX MWPCVD reactor on 10×10×0.5 mm^3 pieces cut from 4 inch wafers of these substrates, with process parameters specified in Section 3.3 and in appendix D.

Before preparation for XTEM investigations, the samples were annealed two hours in vacuum (≈10^{-6} mbar) at about 500°C inside the e-beam evaporation chamber (Section 3.2). This mild annealing was aimed at the removal of a possible carbon layer adsorbed on the sample surface after extraction from the CVD reactor. The samples were subsequently slowly cooled down to 300°C and then covered with a 5–15 nm thick Ir film using a deposition rate of 0.02 nm/s. Temperature and deposition rate were chosen to give the Ir layer a chance for oriented growth. The deposition of such a thin layer of a heavy metal has the aim of protecting the BEN layer and facilitating the discrimination between the thin carbon layer formed during BEN and the epoxy used in XTEM preparation [Schreck(06)].

Study of BEN

The single crystal quality and the epitaxial orientation of the Ir films were firstly assessed via X-ray diffraction (XRD) analyses. Typical values for the mosaic spread are in the range 0.15–0.2°. RHEED patterns acquired on such Ir(001) layers, typically similar to those shown in Figure 5.1, consist of parallel streaks, indicating the single crystal nature and smoothness of the surface (Section 2.4). The spacing, $g_\perp$, between the reciprocal lattice rods corresponds to the distance between the {020} lattice planes in Ir, $d_{020,Ir} = 1.92$ Å. As the z coordinate is degenerate in RHEED for such extremely flat surfaces, the rods are indexed only with the first two Miller indices, hk.

As observed on the Ir/$SrTiO_3$(001) system using the same deposition setup [Schreck(03)], successful diamond nucleation on the multilayer system Ir/YSZ/Si(001) results in the formation of domains, identified with the *IL* detector of a SEM (Section 2.2) (Figure 5.2(a-b)). As previously mentioned, this detector is sensitive to the work function contrast, while the conventional lateral *SE* detector is more sensitive to the topographic contrast. The domains are clearly visible in *IL*-SEM images while generating almost no contrast in micrographs acquired using the *SE* detector (see Figure 5.2(b-c)).

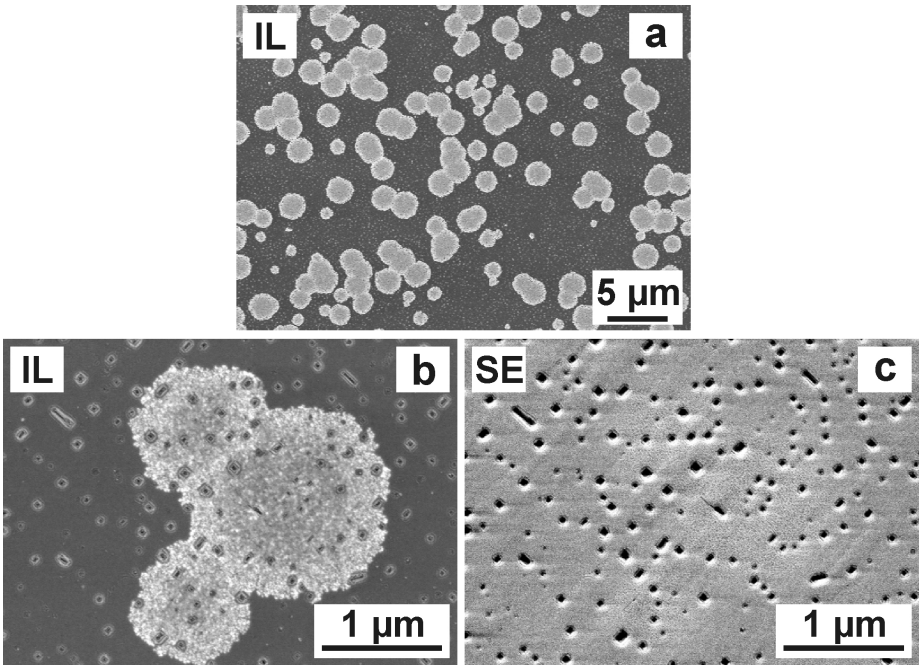

Figure 5.2 – (a) Domains on Ir/YSZ/Si(001) in an *IL*-SEM micrograph, demonstrating successful nucleation after BEN; (b) and (c): comparison between images at higher magnification of the identical area of the sample in (a) acquired using the *IL* and *SE* detectors of the SEM, respectively. The edges of the images are parallel to <100> directions of the epitaxial Ir film. The rectangular holes in the substrate were present on the Ir film prior to the BEN treatment.

Under some conditions the BEN process, carried out using the same setup and similar parameters, generates a homogeneous coverage with domains over a large area, without distinguishable individual domains (*e.g.*, sample D15 in Figure 5.3(a)). As in the case of circular domains, the presence of diamond nuclei is proved by the closed epitaxial film developing all over the sample after a short deposition step (Figure 5.3(b)). This kind of samples are ideal for TEM investigations due to the high probability that diamond nuclei are present in the tiny piece to be analysed. On the other hand, in some cases the BEN treatment can completely fail, not generating diamond nuclei at all even when identical parameters are used. This behaviour is due to the small uncontrollable differences in the ion bombardment conditions that determine whether diamond nucleation takes place or not [Gsell(07)-1] and strongly affect the domain shape (Section 5.4).

The samples showing successful nucleation after the BEN treatment were characterised by RHEED and HRTEM so as to detect crystalline diamond in the reciprocal and in the real

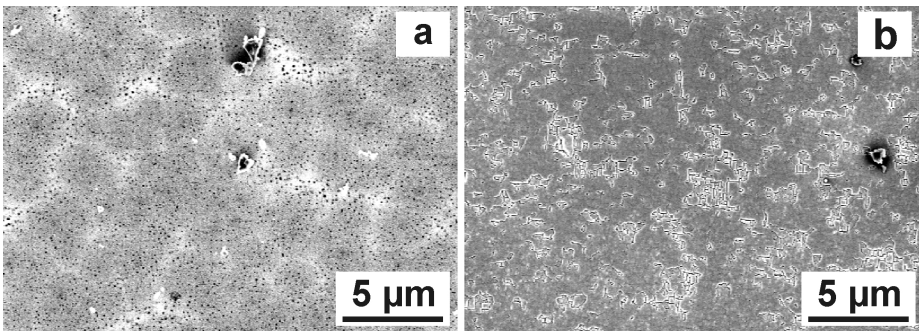

Figure 5.3 – *IL*-SEM images of the sample D15, showing 100% coverage (a) with domains after BEN on Ir/YSZ/Si(001) and (b) with epitaxial diamond after a successive 15 min deposition step. The edges of the images are parallel to <110> directions of the epitaxial Ir substrate.

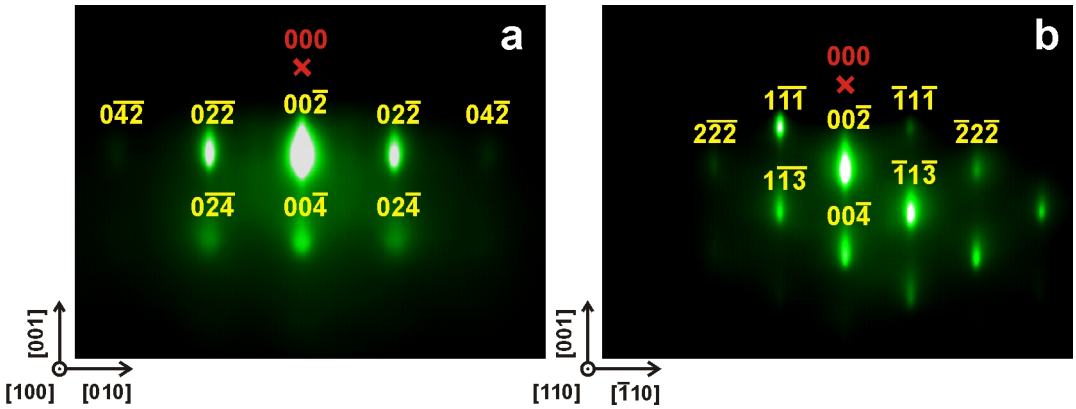

Figure 5.4 – RHEED patterns, collected at 430°C, of the BEN sample D15 along (a) [100] and (b) [110] azimuth of Ir. All the spots can be indexed as 3D Ir spots. The position of the origin of the reciprocal lattice, (000), is indicated by the red cross in these and in the following RHEED patterns.

space, respectively. Typical RHEED patterns along the two main in-plane crystallographic axes after a successful BEN treatment on Ir/YSZ/Si(001) are shown in Figure 5.4. These patterns can be attributed to a rough Ir surface, for which the streaks of the as-grown flat film (*i.e.*, Figure 5.1) evolved into spots (Section 2.4). In this case, the diffraction spots can be indexed with the full set of Miller indices, in analogy with SAED patterns. However, in contrast with SAED, RHEED patterns are slightly compressed in the direction connecting the (00n) spots due to the small tilt angle of the incident beam with respect to the phosphor screen normal. The three-dimensional Ir pattern is due to the holes present in the Ir film prior to the BEN treatment (the samples in Figures 5.2, 5.3 and 5.5 were prepared using this Ir film, while the RHEED pattern in Figure 5.1 was recorded on a flatter one). No features are present in the RHEED pattern which can be attributed to diamond, confirming the results of the former studies of BEN specimens prepared on Ir/$SrTiO_3$(001) substrates inside the same ASTeX setup [Gsell(08)].

The sample D21, showing a 100% domain coverage (Figure 5.5(a)), was analysed by XTEM (Figure 5.5(b)), showing a bright slit between the Ir substrate and the Ir covering layer used for contrast enhancement. This layer can be identified as the carbon film formed during the BEN process, in analogy to what observed in a previous TEM study of a BEN sample on Ir/$SrTiO_3$(001) [Schreck(06)]. Discontinuities in the bright slit are due to transmission effects, as the steps in the Ir substrate superimpose on the C-layer. HRTEM images of this sample mostly show an amorphous structure within the bright slit (Figure 5.5(c)). In some areas crystalline structures are visible. The measured lattice spacings are the 2.22 Å and 1.92 Å corresponding to the {111} and {002} planes of Ir, respectively, and the fast Fourier transform (FFT) of the whole area is identical to the one of only the Ir substrate (Figure 5.5(d)). The reason why Ir crystalline structures are found in the bright BEN layer is that the transmission geometry leads to superimposition effects. As in the already cited study [Schreck(06)], no diamond nuclei are visualised by HRTEM inside the BEN layer. Small and highly defective diamond grains in the BEN layer can yield a convincing explanation for the absence of any diamond-related structures in HRTEM as well as in the RHEED analyses. The covering Ir layer shows an almost perfectly epitaxial orientation with the underlying Ir, only slightly misoriented (≈4° tilt around [110] of Ir for the area in Figure 5.5(c)). Being the carbon layer TEM-amorphous, the epitaxial orientation of the covering layer with respect to the Ir substrate was allowed by its discontinuity at the holes in the substrate, which may have acted therefore as contact points between the two layers. In this way the Ir covering layer had the chance to reproduce almost perfectly the orientation of the substrate.

The thickness of the BEN layer, averaged over various HRTEM images from different

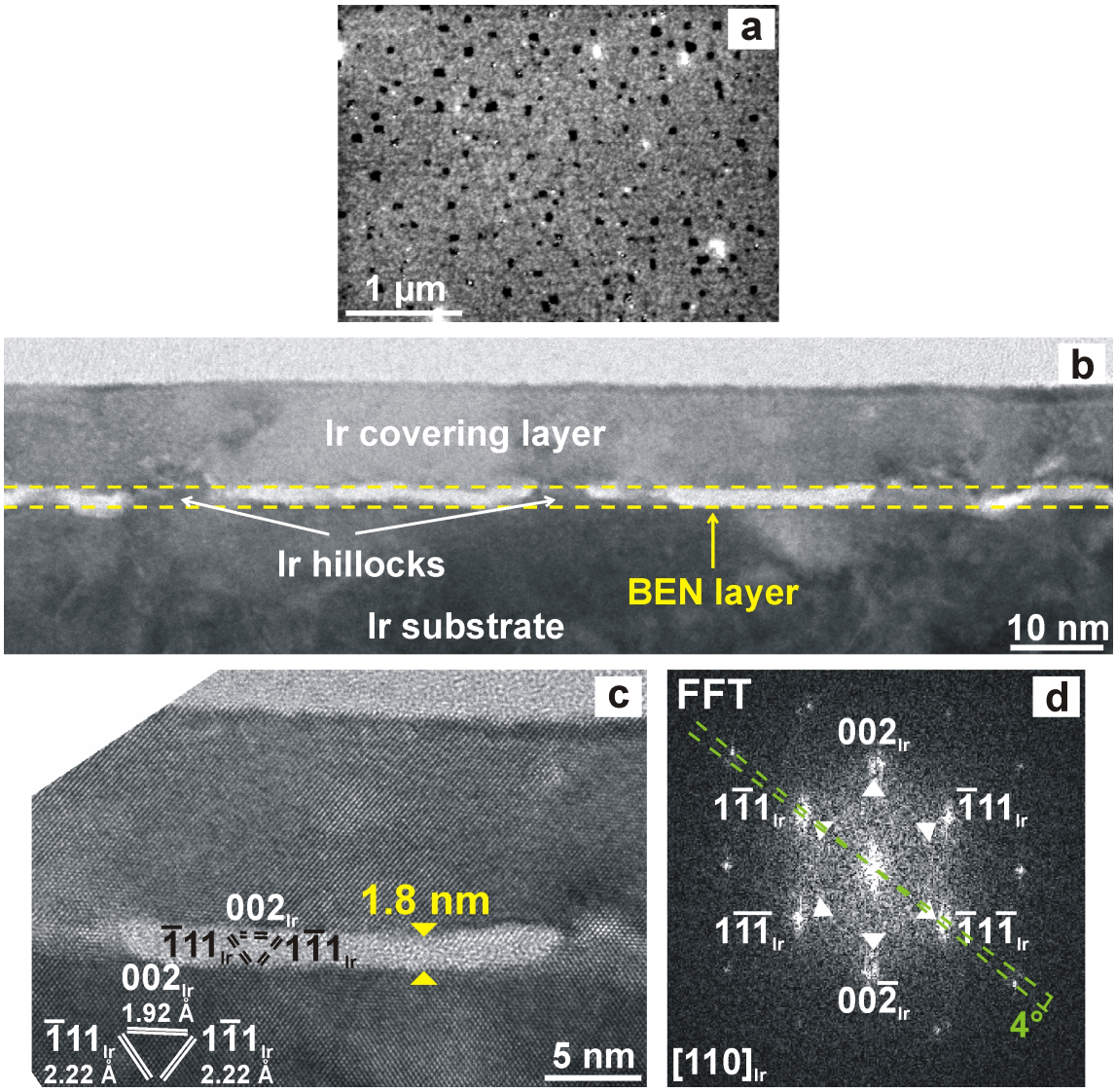

Figure 5.5 – (a) *IL*-SE micrograph of the sample D21, exhibiting 100% domain coverage on Ir/YSZ/Si(001) (edges parallel to <110> directions of Ir). (b) Low magnification XTEM images show a bright layer between the Ir substrate and the Ir covering layer. (c) HRTEM image acquired along the [110] zone axis of the Ir substrate, showing only crystalline patterns attributable to Ir, also inside the BEN layer. (d) The FFT of an area in (c) shows the [110] pattern of Ir, with a slight tilt (≈4° rotation around the [110] direction of Ir, perpendicular to the plane) between the Ir substrate and the epitaxial covering Ir layer.

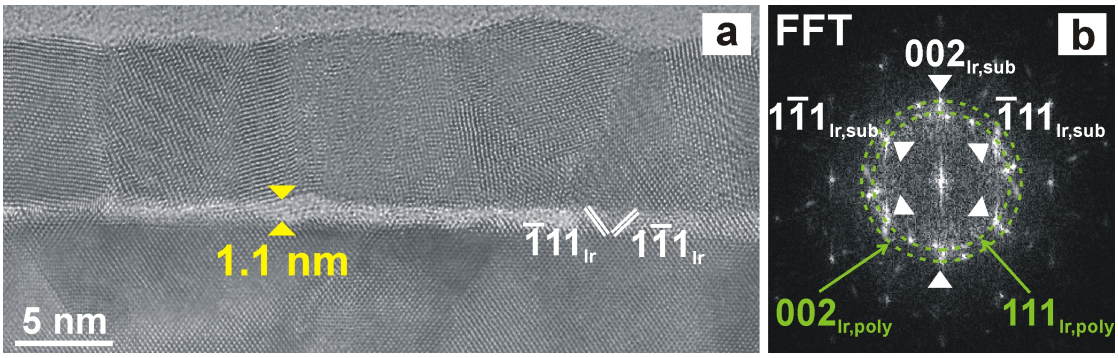

Figure 5.6 – (a) HRTEM image along the [110] zone axis of the Ir substrate of a sample showing successful nucleation after BEN on Ir/$SrTiO_3$(001) [Schreck(06)]. No crystalline features attributable to diamond are observed within the bright BEN layer. (b) The FFT of (a) shows the single crystal pattern of the Ir substrate and rings due to the polycrystalline covering Ir film.

areas, is 1.8 nm (Figure 5.5(b-c)). A HRTEM image of a sample showing successful BEN on Ir/$SrTiO_3$(001), studied in a former work [Schreck(06)], is reported in Figure 5.6(a) for a comparison. In this case an average thickness of 1.1 nm can be determined for the bright slit from HRTEM images. A more accurate value of 0.75±0.23 nm was derived for this specimen by scanning TEM (STEM) analyses carried out using the high angle annular dark field (HAADF) signal. The FFT of Figure 5.6(a) shows that in this case the continuous coverage of the Ir substrate with TEM-amorphous carbon did not allow an epitaxial orientation of the covering Ir layer, which grew instead polycrystalline due to the flatter Ir substrate topography (compare Figure 5.6(b) with Figure 5.5(d)).

In a former study, an identical carbon coverage of ≈1 nm was evaluated by XPS for two BEN samples on Ir/$SrTiO_3$(001), one with and one without domains [Gsell(08)]. This would suggest a similar thickness of the BEN layer independent of the success or failure of the nucleation treatment. From the two samples, the one showing the typical regular roughened structure but no domains was analysed by XTEM (Figure 5.7). As for the mentioned specimen with successful BEN on Ir/$SrTiO_3$(001) (Figure 5.6 and ref. [Schreck(06)]), some areas of this sample are flat (Figure 5.7(b)) and others are grooved (Figure 5.7(c)). For both area types, the carbon layer forms a continuous slit between the Ir substrate and the Ir covering layer. The HRTEM images of the two types of areas (Figure 5.7(d) and (e)) show an amorphous structure of the BEN layer. The only crystalline structures visualised within the bright layer correspond to Ir. The average thickness evaluated in the rough area (2.4 nm) is higher than the one evaluated in the flat region (1.7 nm). Both values are higher than the ≈1 nm evaluated by XPS, but not far from the 0.5-2 nm thickness previously reported [Bauer(02), Kono(04), Kono(05), Schreck(06), Aoyama(07), Gsell(08)]. The Ir covering layer is in this case polycrystalline with random orientation, confirming the amorphous nature of the BEN layer and its continuity over the Ir substrate.

A sample prepared via BEN in a pure DC discharge setup with a CH_4/H_2 gas mixture was also analysed by HRTEM. The peculiarity of this sample is the extreme flatness of its surface after BEN, allowing to identify a clear ≈1 nm step downwards as the AFM tip moves from the outside to the inside of a domain (Figure 5.8(a–b)) [Gsell(07)-1, Gsell(07)-2]. XTEM analyses of this flat sample (Figure 5.8(c)) also show a continuous bright slit between the Ir substrate and the covering layer, with a thickness in the 1–2 nm range. Moreover, XTEM images evidence a clear step between different areas. HRTEM analyses of the two areas do not indicate any variation in the nature of the carbon-based material inside the bright slit, which appears TEM-amorphous all over the sample. It can be observed, anyway, that the height difference between the top of the carbon layer in the two areas, which is also reproduced by the step between the top of the covering Ir layer on the two areas, is about 2.4

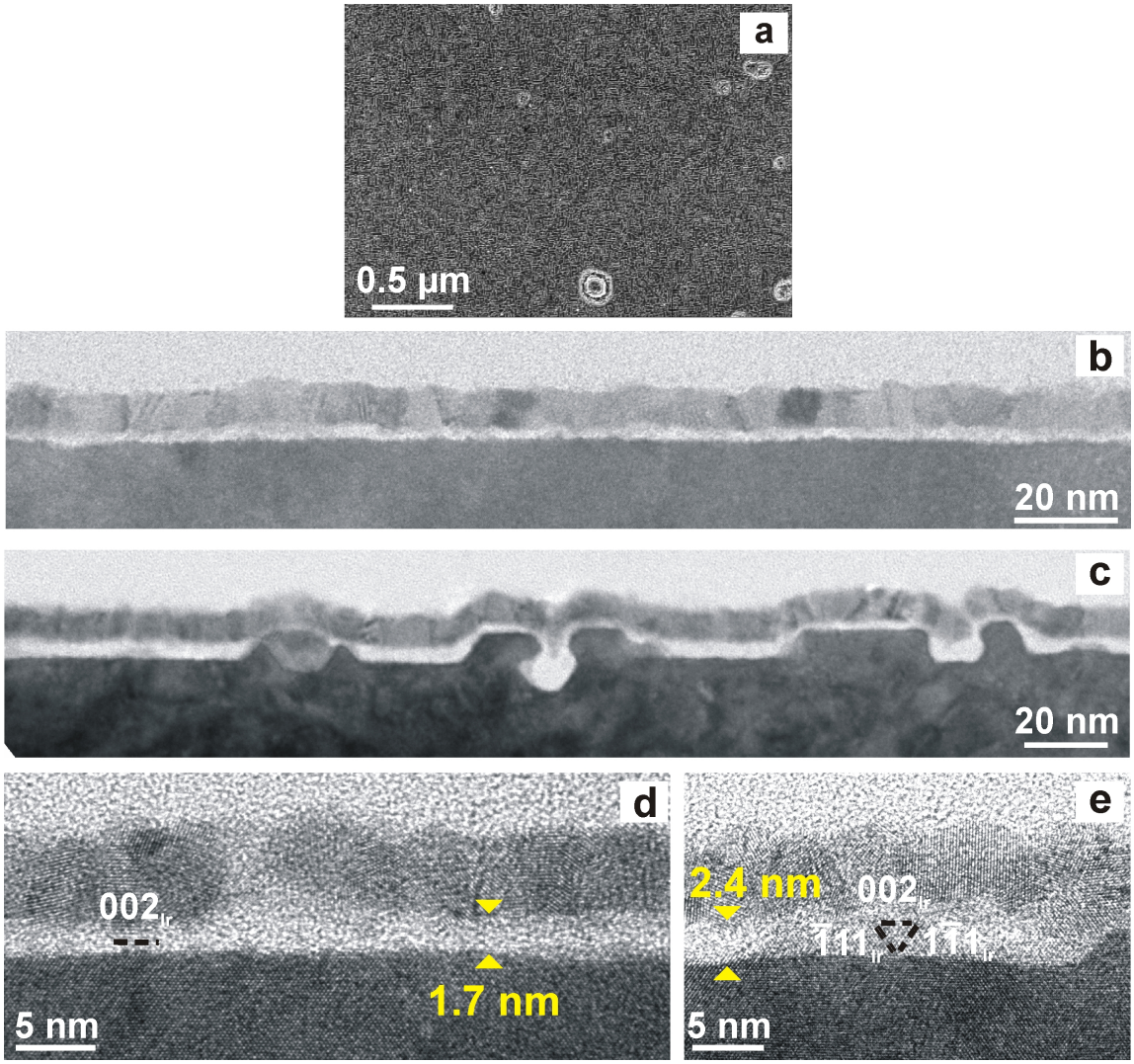

Figure 5.7 – (a) *IL*-SE micrograph of a BEN sample showing a clear roughening but no domains after BEN on Ir/$SrTiO_3$(001) (edges of the image parallel to <110> of Ir); low magnification XTEM acquired in (b) flat areas and (c) grooved areas, with (d) and (e) corresponding HRTEM images, respectively ([110] zone axis of the Ir substrate).

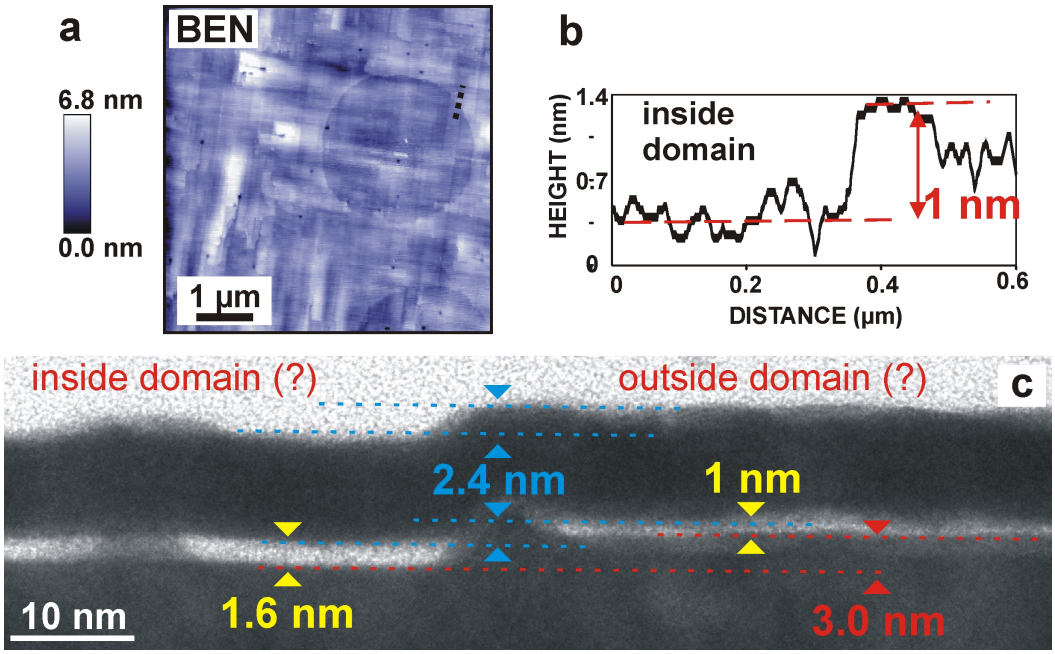

Figure 5.8 – (a) AFM image of a specimen showing flat domains after DC-BEN on Ir/YSZ/Si(001) and (b) line profile across the edge of a domain, showing the average 1 nm step downwards inside the domain with respect to the surrounding region [Gsell(07)-1, Gsell(07)-2]. HRTEM images in cross section (c) of this sample show a step between areas with different thickness, which might correspond to the edge of a domain.

nm. This topographic feature could be ascribed to the transition domain-surrounding area, though it is higher than the maximum step (1.7 nm) measured by AFM. If this assumption is correct, the lower region (on the left side in Figure 5.8(c)) should correspond to a domain, while the higher one (on the right side) should be the region outside the domain. Under the same assumption, the BEN layer should be thicker (1.6 nm) inside the domain and thinner outside (1 nm). This interpretation of the image would however disagree with the results of recent AES experiments [Gsell(07)-2, Schreck(09)-1], which measured ≈2.0 nm and ≈1.7 nm outside and inside the domains, respectively. Even if absolute values estimated by AES can be subject to rather big errors, the relative difference should be correct. A first hint on a possible explanation for these contradicting observations can be deduced from the 3 nm high step in the Ir substrate layer (see Figure 5.8(c)). Basically two different scenarios may be considered: (i) the step is an intrinsic feature of the domain formation process, which is accompanied by the etching of 2-3 nm of the Ir substrate during BEN, or (ii) the step in the present TEM sample was already present before the BEN procedure. The analysis of some samples which have been grown for several seconds after the BEN treatment, presented in the following section, will allow to understand which of these two possible explanations is more plausible.

An independent evaluation of the carbon coverage after BEN on Ir/YSZ/Si(001) was obtained by XPS (not shown here, analysis carried out by T. Brugger). The amount of carbon evaluated for the sample D15 (Figure 5.3(a)) was 19 atoms per surface Ir(001) atom. As the diamond (001) surface contains 1.16 atoms per each atom of the 1×1 Ir(001) surface, this corresponds to 16.4 monolayers (MLs), if a homogeneous coverage is assumed. One ML is here 0.89 Å, a quarter of a diamond lattice cell. The coverage evaluated by XPS corresponds therefore to 1.5 nm. This value is quite close to the 1.8 nm thickness of the BEN sample D21 (Figure 5.5), characterised by a comparably high coverage with domains. As mentioned above, a ≈1.0 nm coverage was estimated by XPS for the BEN samples on Ir/$SrTiO_3$(001) [Gsell(08), Gsell(07)-2].

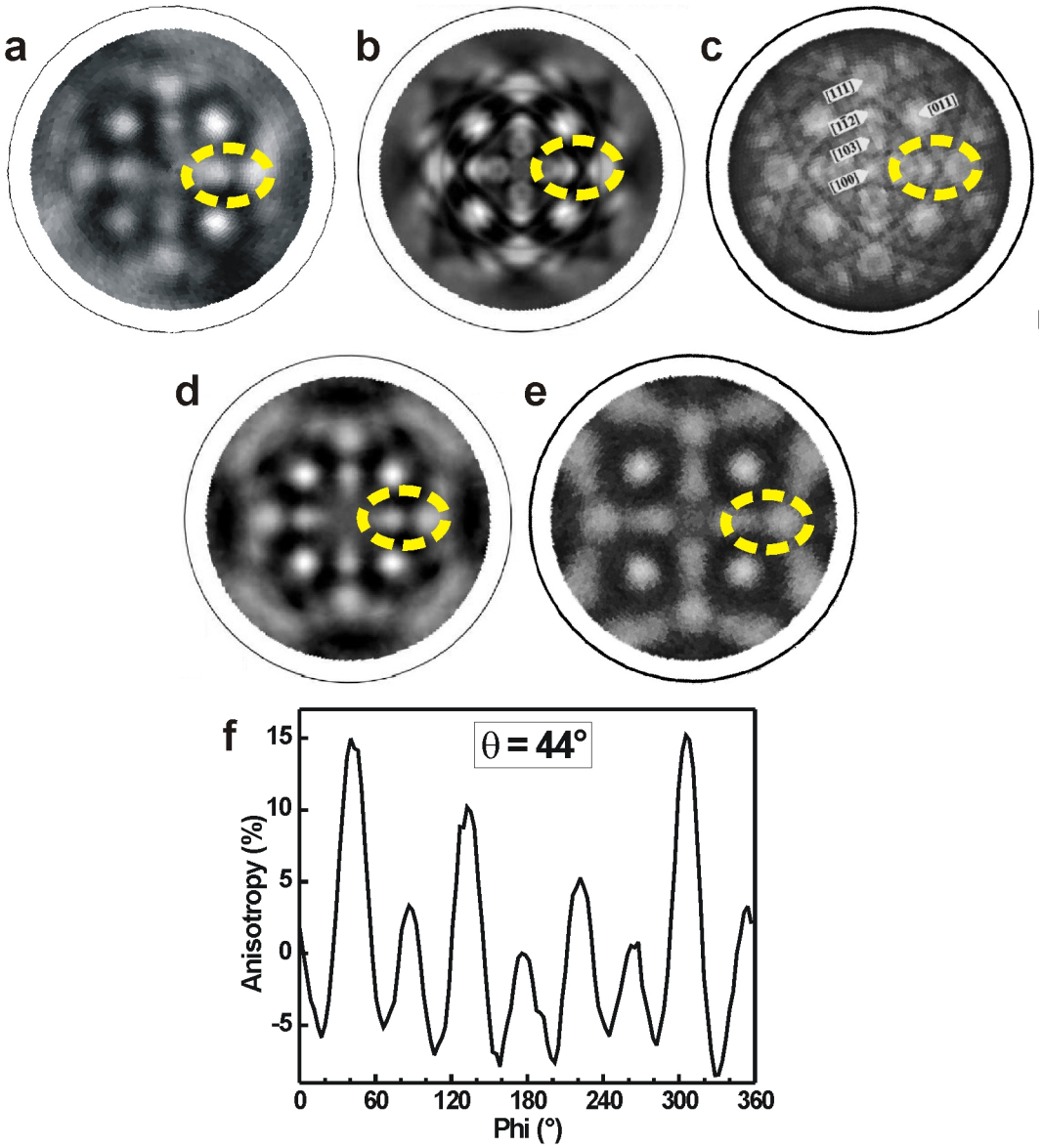

Figure 5.9 – (a) XPD patterns of the C 1s core level for the sample D15, showing a 100% domain coverage after BEN on Ir/YSZ/Si(001). The pattern is compared to reference C 1s patterns recorded on (b) a 13 μm thick single crystal diamond film on Ir/$SrTiO_3$(001) [Gsell(08)], (c) the (001) surface of a natural diamond [Küttel(94)], (d) a sample showing domains after BEN on Ir/$SrTiO_3$(001) [Gsell(08)] and (e) a highly oriented diamond film produced using BEN and 1 h deposition on Si(001) [Schaller(95)]. The yellow circles highlight significant features in the patterns. (f) Azimuthal scan over a range 0–360° extracted from the pattern in (a) for the polar angle $\theta = 44°$, where the maximum average anisotropy was measured for the sample D15.

The photoelectron diffractogram of the C 1s signal for the sample D15 shows a clear four-fold symmetry (Figure 5.9(a)), in agreement with the one observed on diamond (001) reference surfaces. Various similarities can indeed be observed between the pattern in Figure 5.9(a) and reference patterns for a 13 μm thick single crystal diamond film on Ir/$SrTiO_3$(001) [Gsell(08)] and the one recorded on the (001) surface of a natural single crystal [Küttel(94)], not only in the four-fold structure but also in some details of the fine structures (as the area evidenced by the yellow ovals in Figure 5.9(a-c)). However, the overall fine structure is more fuzzy and partly lost for the BEN sample. As the image in Figure 5.9(a) has not been processed, there are asymmetries in the pattern, not related to diamond structures but to a tilt of the sample and effects from the small size and asymmetric shape (*i.e.* this sample was half of the original 1×1 cm^2 piece). The XPD C 1s pattern of a sample showing successful nucleation after BEN on Ir/$SrTiO_3$(001) [Gsell(08)] (Figure 5.9(d)) shows akin structures, but slightly more defined features. The pattern in Figure 5.9(e) is the one reported in literature for a highly oriented diamond film deposited on top of a Si(001) substrate following BEN and 1 h growth [Schaller(95)]. It is interesting to observe that after only BEN on Ir(001) the order in the carbon layer, assessed not only by the four-fold symmetry but also by the fine structure, is comparable to the one obtained after 1 h textured growth on a Si(001) substrate.

A quantitave information which can be extracted from XPD analyses is the so-called *anisotropy*. In each azimuthal scan, for a fixed polar angle θ, the photoelectron signal has a modulating intensity, I, varying around a certain average, I_a. The anisotropy is defined as $(I - I_a)/I_a$. In Figure 5.9(f) the anisotropy is plotted against the azimuthal angle, φ, for the polar angle $\theta = 44°$. The maximum anisotropy was found for the sample D15 corresponding to this polar angle. More precisely, in this case a maximum anisotropy value for the whole XPD pattern cannot be defined, because of the asymmetry due to the measurement artefacts. The average anisotropy of the four maxima, corresponding to the four <101> directions due to the shortest nearest-neighbour distance of carbon atoms in the crystal lattice, is 19±4%. In former studies of BEN on Ir(001) in different setups, the anisotropy values of the C 1s signal were used to deduce the volume fraction of crystalline diamond islands embedded in an amorphous carbon matrix, based on the comparison with diamond reference samples [Kono(04), Kono(05), Aoyama(07)]. In this case, assuming a 100% coverage of the surface of D15 with domains, the maximum value is coincident with the measured value (19±4%). This value is in perfect agreement with the ≈18% obtained in the former work on BEN on Ir/$SrTiO_3$(001) [Gsell(08)], where the comparison with the 67% anistropy for the diamond reference in Figure 5.9(b) led to the conclusion that at least one fourth of the carbon atoms within the BEN layer reside in a crystalline environment, which is therefore valid also for the BEN sample on Ir/YSZ/Si(001).

Early stages of growth after BEN

As confirmed in the former section, RHEED and HRTEM investigations of samples after BEN on Ir(001) buffer layers on any substrate system are not able to detect the presence of crystalline diamond nuclei. Moreover, no individual grains were ever identified within the domains by SEM, AFM and TEM, apart from few reports about 5-20 nm grains [Bednarski(03), Golding(04), Fujisaki(03)]. As already discussed, we see some basic ambiguities concerning the process control or the real nature of imaged structures in the latter publications. A thorough study is therefore reported here with the aim of monitoring the earliest appearance of crystalline diamond in RHEED and HRTEM after BEN by applying very short growth steps. The results of this investigation allow to extrapolate to the internal structure of the carbon layer and especially the diamond nuclei during ion bombardment.

The samples described in the present section underwent very short growth steps (5–120 s) performed immediately after the BEN treatment on Ir/YSZ/Si(001) by simply switching

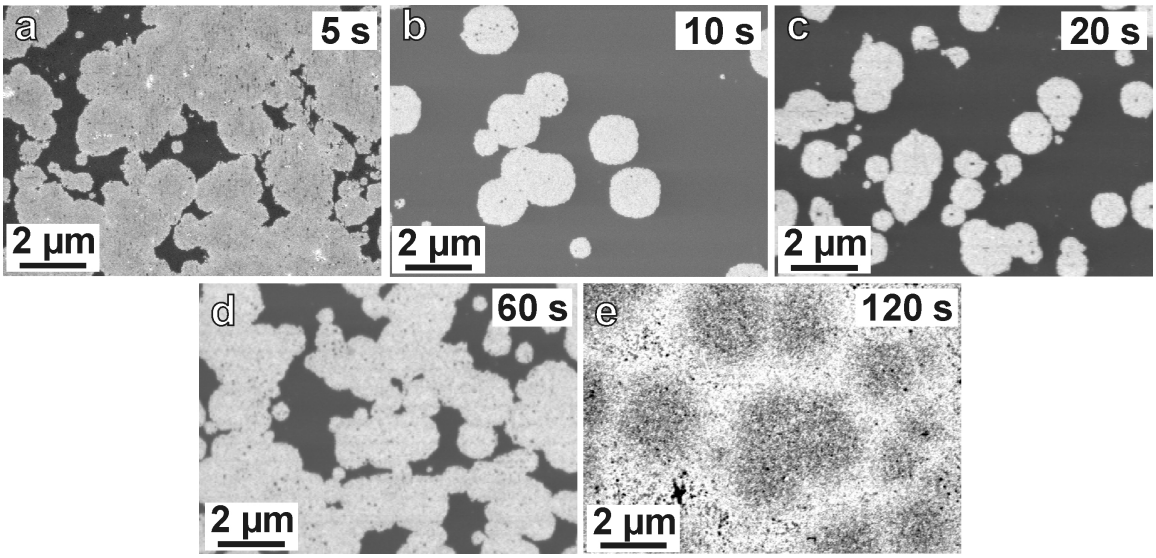

Figure 5.10 – Low magnification *IL*-SEM images of samples prepared by BEN and subsequent 5–120 s growth steps on Ir/YSZ/Si(001) (edges of the images parallel to <110> directions of Ir).

off the bias voltage. The gas composition (10% CH_4 in H_2) and the externally set support temperature (so as to have 750-780°C for the specimen under BEN conditions) were not changed, as the duration of the growth steps was below the response time of the whole system to gas composition and temperature changes (see appendix D). In order to be able to compare the results, the same conditions were used for the 2 minutes grown sample, even if the response time of the system to gas exchanges is approximately 1 minute. Anyway, switching off the bias voltage, without changing the heater temperature, leads to a decrease of the sample temperature from 750–780°C to ≈700°C, a more appropriate temperature for (001)-textured growth, in less than 1 minute.

The samples were first analysed by SEM in order to check the presence of diamond grains. As shown in Figure 5.10, the shortly grown samples are characterised by bright circular areas. Although the term 'domain' is not appropriate in this case, as it refers to the structures generated during a pure BEN treatment, it will be used in the following for the sake of brevity to designate the areas containing the epitaxial diamond grains. The coverage of the substrate with the domains varies from almost 100% (2 min grown sample) to less than 50% (10 s and 20 s grown samples), depending on uncontrollable differences in the local conditions during BEN. Higher magnification SEM images (Figure 5.11) allow to identify individual grains within the domains and to estimate their surface density. Apart from the sample subject to 2 min growth, these samples do not show the regular roughening observed after BEN in the same setup on Ir/$SrTiO_3$(001) [Hörmann(01)] (*e.g.*, see Figure 5.7(a)) and on Ir(001) buffer layers on other substrates [Tsubota(00), Sawabe(00), Golding(04)]. The only three-dimensional structures found in some specimens are holes in the Ir substrate (*e.g.*, see the 10 s grown sample in Figure 5.11), which were most probably present in the Ir layers prior to the BEN treatment.

The topography of the samples was characterised using AFM (Figure 5.12). The spatial resolution achievable with this method (limited by the finite size of the probe) allows to give an independent quantitative evaluation of the surface density and the average height of the diamond grains, to be compared with the results of SEM and TEM analyses. First of all, it is interesting to compare the average height of the grains after a short growth step to the 1 nm-depression measured inside the domains directly after BEN (Figure 5.8(a-b)) [Gsell(07)-1]. After only 5 s growth AFM analyses show that the diamond grains stick out by 1.5 nm in average from the surroundings. In the 2 min grown sample it was not possible to measure

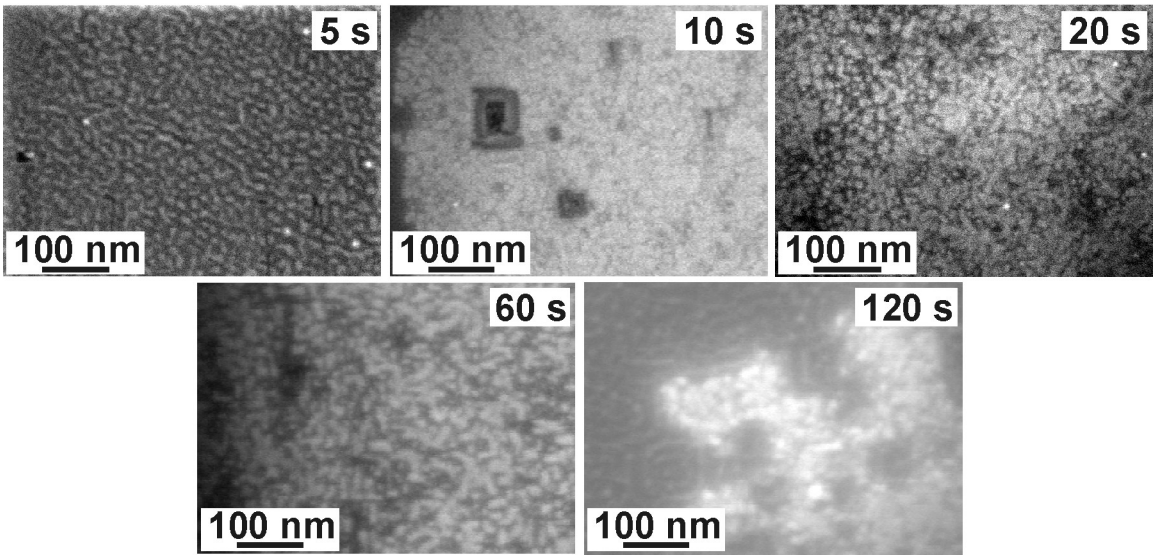

Figure 5.11 – High magnification *IL*-SEM images acquired within the domains of the same samples in Figure 5.10 (edges of the images parallel to <110> directions of Ir).

such a step, due to the complete coverage with grains in the central area of the sample.

RHEED analyses of the shortly grown samples along the [100] direction of Ir (Figure 5.13) show, already starting from 5 s growth, the presence of weak and broad spots ascribable to diamond features, superimposed to the much sharper features (spots or streaks) due to Ir, always visible due to the incomplete coverage of the substrate with diamond. The angular broadening of the diamond spots indicates a few degree mosaicity (tilt and twist) of the tiny isolated diamond grains with respect to the epitaxial orientation in these early stages of growth. After 1 min growth the diamond spots are clearly distinguishable from the sharp Ir spots. RHEED patterns of the same samples were also acquired along the [110] direction of Ir (Figure 5.14), where it is possible to distinguish diamond-related spots only after 1 min deposition. This suggests that the patterns reported by Fujisaki et al. [Fujisaki(03)] might have been recorded on samples subject to an uncontrolled deposition step longer than 20 s following BEN.

For the lowest growth time explored (5 s), three samples (D95, D96 and D99) were analysed, in order to compensate for the high relative uncertainty (1 s) on the duration of this extremely short deposition process. Indeed, the three samples show different scenarios. On one hand, the sample D99 (Figure 5.15) exhibits isolated grains, mostly small ones, with average lateral size of ≈10 nm (Figure 5.15(a)). Few larger grains, with lateral size up to ≈50 nm (Figure 5.15(b)), are also found. The height in the two types of structures is comparable (≈2.4 nm). Epitaxial crystalline diamond is detected by HRTEM in both smaller and larger grains (Figure 5.15(c)).

The sample D96 (Figure 5.16) also shows a mixture of small isolated grains, with an average lateral size of ≈10 nm (a), and few larger (≈40 nm) grains (not shown here). Besides, in some areas a continuous extended layer is found on the Ir substrate (Figure 5.16(b)). HRTEM shows that these areas consist of single crystal diamond growing epitaxially on the Ir substrate (Figure 5.16(c)). In these areas the covering Ir layer has a single crystal nature as well. In some other areas a continuous ≈1 nm-thick a-C film is found (Figure 5.16(d)). An indirect proof of the amorphous nature of this layer in these areas is the polycrystalline structure of the covering Ir film, visible in FFTs of the HRTEM images (Figure 5.16(e)).

A careful analysis of the epitaxial diamond film found in the sample D96 (Figure 5.17(a)) shows that this layer is structurally relaxed, as misfit dislocations are present at the interface

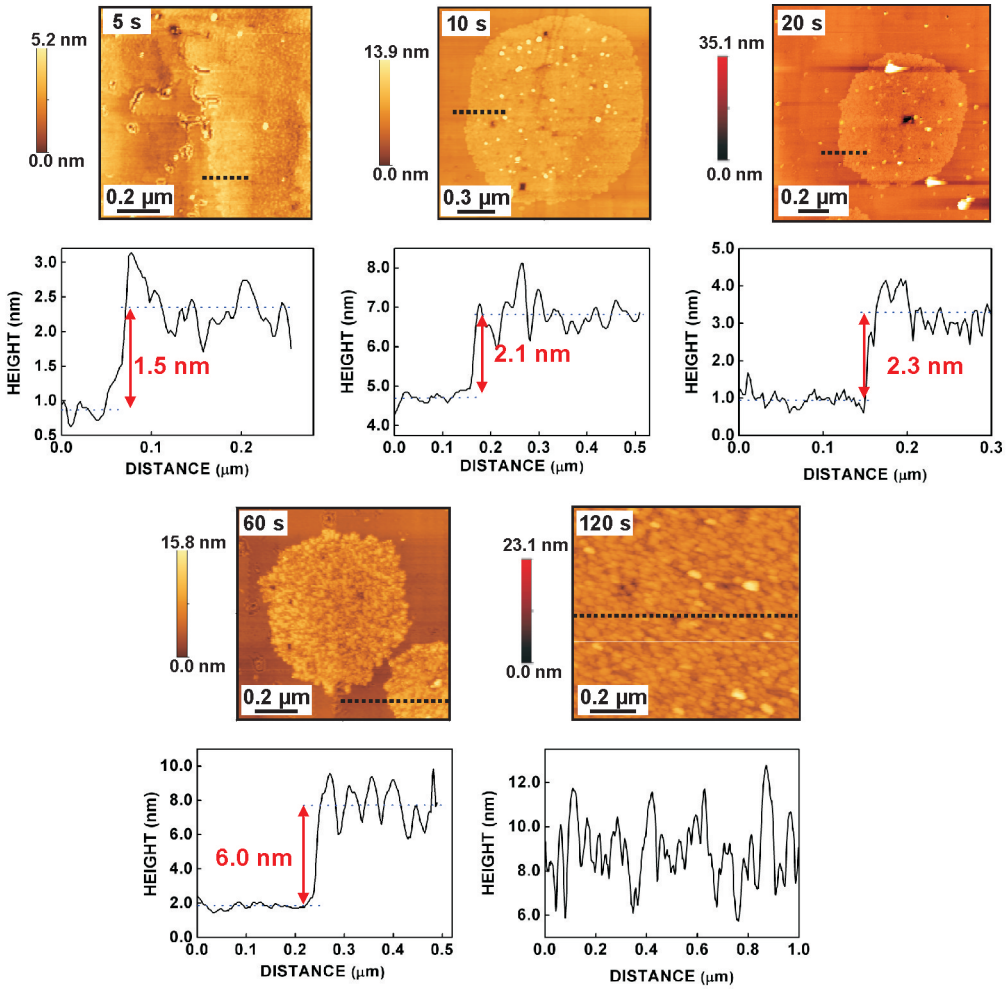

Figure 5.12 – AFM images and corresponding line scans of samples subject to 5–120 s growth steps. The dashed line in each AF micrograph corresponds to the linescan reported below.

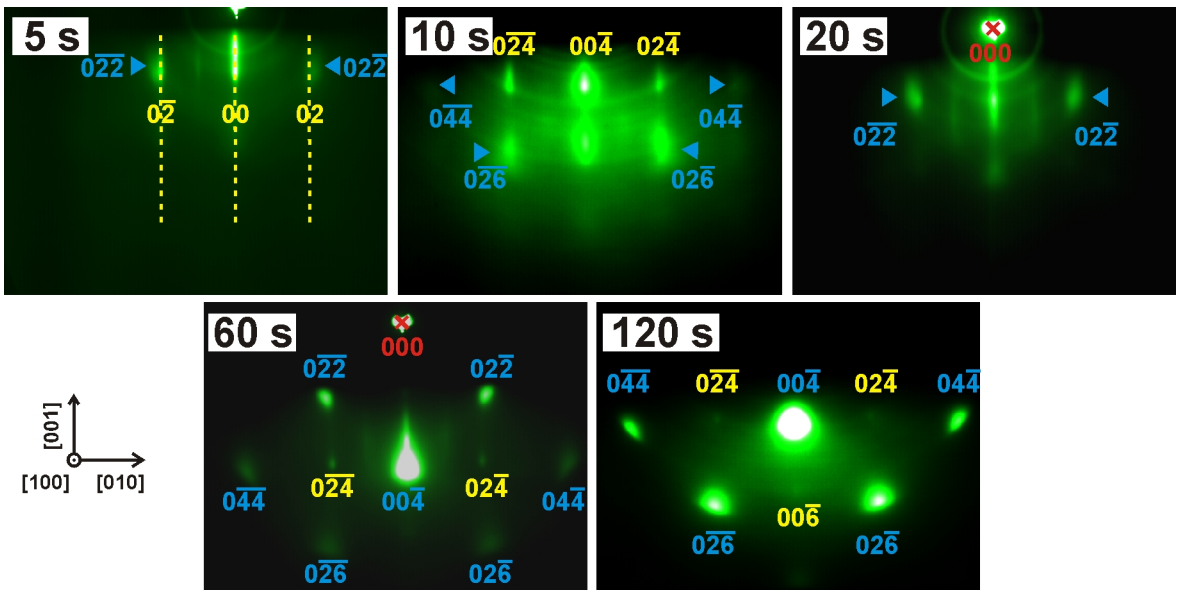

Figure 5.13 – RHEED patterns of samples subject to 5–120 s growth steps acquired with electrons incident along the [100] direction of Ir. The spots stemming from diamond are indexed in blue or pointed to by blue arrowheads, while the yellow symbols indicate Ir-related features.

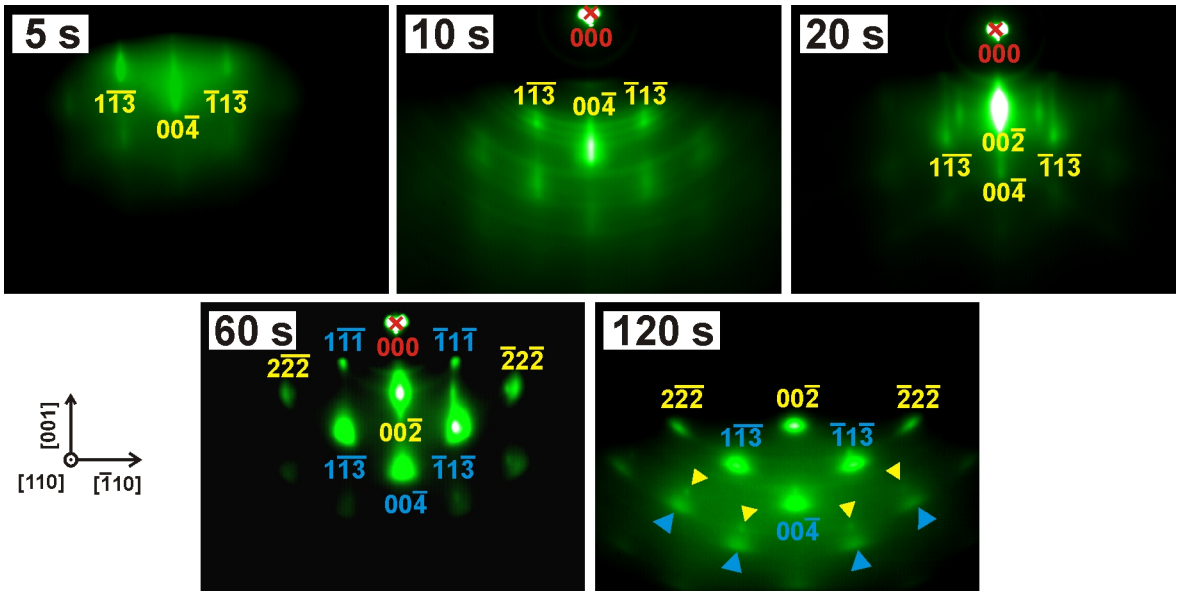

Figure 5.14 – RHEED patterns of samples subject to a 5–120 s growth step acquired with electrons incident along the [110] direction of Ir. The spots stemming from diamond are indexed in blue or pointed to by blue arrowheads, while the yellow symbols indicate Ir-related features.

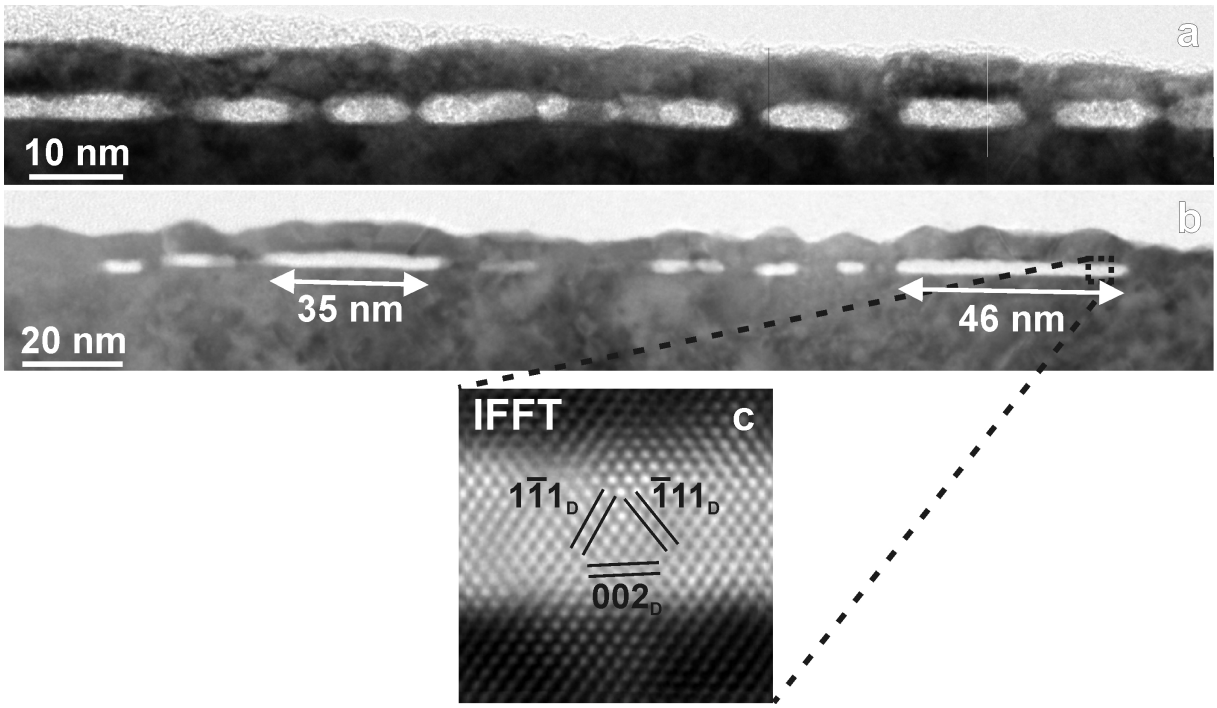

Figure 5.15 – XTEM images of the sample D99, subject to 5±1 s growth after BEN. The sample shows a mixture of (a) isolated ≈10 nm wide grains with (b) few larger grains. Epitaxially oriented diamond is found both in small and (c) large grains (Fourier-filtering has been used here to emphasize crystalline features).

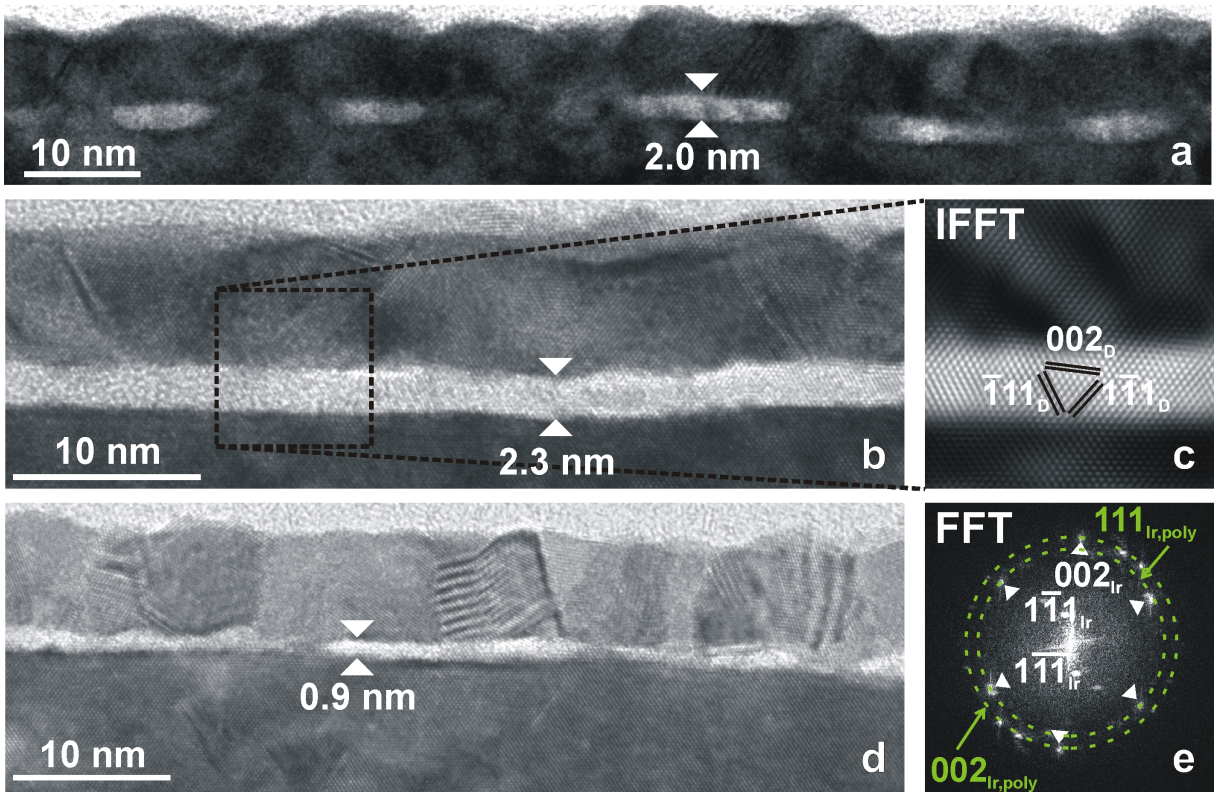

Figure 5.16 – XTEM images of the sample D96, subject to 5±1 s growth after BEN. Besides (a) isolated ≈10 nm wide grains, the sample shows (b) extended continuous layers, composed of (c) epitaxially oriented diamond. In some areas (d) a residual amorphous carbon layer is found. The random orientation of the polycrystalline covering Ir layer is visible in the FFT of HRTEM images in (e), where the spots due to the single crystal substrate are those indicated by the arrows, while the remaining spots are due to the covering Ir layer. No spots are generated by the bright layer, indicating its amorphous nature.

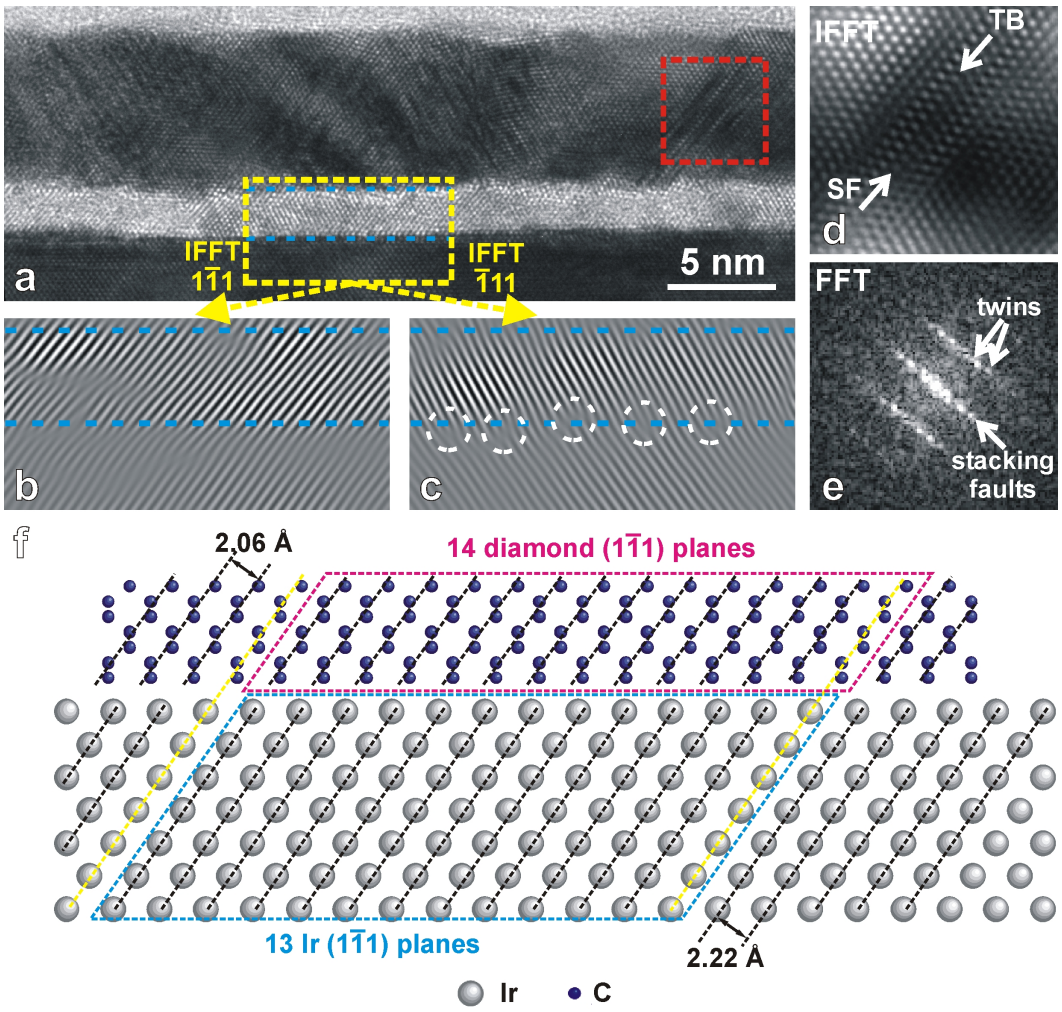

Figure 5.17 – (a) Detail in a HRTEM image of an area of the sample D96 including an epitaxial diamond layer on Ir ([110] zone axis). (b) and (c) are inverse FFTs of the area inside the yellow box in (a) selecting the $\bar{1}11$ and $1\bar{1}1$ sets of spots, respectively, which allow to identify the misfit dislocations at the Ir–diamond interface (the inserted extra planes are enclosed within the white circles). (d) is the Fourier-filtered image of the area enclosed in the red box in the Ir covering layer in (a) and (e) is the corresponding FFT, which shows twin boundaries (TB) and stacking faults (SF) along the [1$\bar{1}$1] direction of Ir. (f) Schematic drawing of the epitaxial interface, also viewed along the [110], between fully relaxed Ir and diamond, showing the occurence of 1 extra $1\bar{1}1$ plane in diamond every ≈13 $1\bar{1}1$ planes in Ir due to the ≈7% lattice misfit.

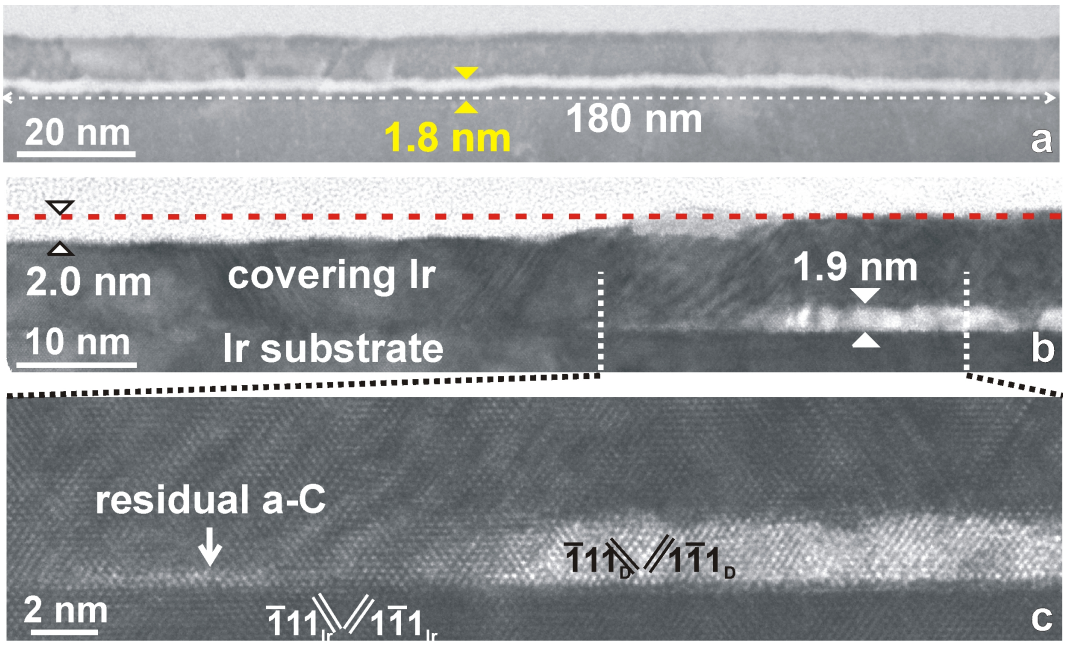

Figure 5.18 – XTEM images of the sample D95, subject to 5±1 s growth after BEN. (a) A continuous layer, wider than 180 nm, consisting of single crystal diamond growing epitaxially on the Ir substrate. (b) Transition between the nucleated area, containing (c) epitaxial crystalline diamond grains, and the outer area, where a residue of the amorphous carbon layer is found.

between the thin diamond layer and the substrate (Figure 5.17(b-c)). The misfit dislocation density is in good agreement with the expected value in case of full relaxation: five extra diamond {111} planes are observed along a 9.5 nm wide interface region, indicating a 1.9 nm average distance between neighbouring misfit dislocations. In case of full relaxation, a pair of {111} diamond extra planes (one $(\bar{1}11)$ and one $(1\bar{1}1)$) would be expected every 13 {111} planes of Ir, *i.e.* every 3.5 nm (see Figure 5.17(f)).

Moreover, in case of biaxial strain due to pseudomorphic growth ($\epsilon_{\parallel} \approx 7.7\%$), the out-of-plane strain, $\epsilon_{\perp}$, should be given by:

$$\epsilon_{\perp} = -\frac{2c_{12}}{c_{11}}\epsilon_{\parallel}$$

with c_{11} and c_{12} coefficients of the elastic tensor of diamond (see appendix A for definition of these coefficients and their values). In case of pseudomorphic nature of the diamond film at this stage, the observed spacing between the (002) planes should be ≈1.75 Å, which cannot be distinguished with the available resolution from the $d_{002} \approx 1.78$ Å of relaxed diamond. The epitaxial diamond layer regions allow the covering Ir to grow epitaxially, but with many structural defects, as twin lamellae and stacking faults (see Figure 5.17(d-e)), allowing the relaxation of the misfit strain in this additional layer.

The sample D95 (Figure 5.18) is similar to D96, with a mixture of large isolated grains (not shown here) and extended regions (wider than 230 nm) with continuous epitaxial diamond layers. In this sample clear transitions between empty regions and areas containing epitaxial grains were visualised and identified as the edges of domains. Residues of the amorphous carbon layer were found outside the domains. These features make this sample ideal to verify the possible presence of a step in the Ir substrate. Such a topographic feature could be at least partly responsible for the 1 nm step measured in AFM after the BEN treatment on rough and flat samples (see Figure 5.8 and refs. [Gsell(07)-1, Schreck(09)-1]). First of all, in Figure 5.18(b) there is a clear ≈2 nm step in the top Ir layer, which corresponds to the height of the diamond grains. Moreover, in HRTEM (see left part of Figure 5.18(c)) a very

Table 5.1 – List of specimens subject to BEN and short deposition steps on Ir/YSZ/Si(001) analysed in the present section, with a list of the parameters extracted using the different techniques: diamond grain density (SEM, AFM and TEM, the latter calculated), inter-grain distance (TEM), lateral size (TEM) and height (AFM and TEM) of the grains.

	Growth step (s)	**Grain density** ($\cdot 10^{11}$cm^{-2})			**Distance** (nm)	**Lateral size** (nm)	**Height** (nm)	
		SEM	AFM	TEM			AFM	TEM
D95	5±1	–	–	4.6±3.7	14.8±5.9	9.1±5.9	–	1.7±0.2
D96	5±1	2.1±0.2	2.5±0.1	6.5±3.1	12.4±3.0	9.6±5.0	1.5±0.4	2.0±0.6
D99	5±1	–		4.7±1.5	14.6±2.3	9.6±1.9	–	2.4±0.2
D88	10±1	3.6±0.6	2.8±0.1	1.9±1.4	22.8±8.6	7.7±2.3	2.1±0.6	2.8±0.2
D83	20±1	2.9±0.6	3.5±0.5	4.0±2.2	15.8±4.4	10.5±3.0	2.3±1.5	3.7±0.3
D74	60±1	2.1±0.4	3.6±0.4	3.7±2.5	16.4±5.5	13.7±2.6	6.0±1.3	8.0±1.8
D54	120±1	1.7±0.3	–	2.7±1.0	19.2±3.7	???	–	13.8±3.5

thin (≈3 Å) residue of a-C layer is visible immediately outside the domain, indicating the interface between the Ir substrate and the Ir covering layer, which lies at the same level as the base of the diamond grain in the domain. This stands for the absence of any topographic feature in the Ir substrate which could contribute to the AFM–measured step after BEN. This result stands against the interpretation of the HRTEM image in Figure 5.8(c), together with the AES results concerning the thickness of the BEN layer inside and outside the domains [Schreck(09)-1]. Based on these new results on the specimen D95, the attribution of the two areas in Figure 5.8(b) and (c) to the inside and the outside of a domain must be definitely discarded. The 3 nm step observed in the Ir substrate therein can simply be attributed to terraces in the Ir substrate and the different thickness of the BEN layer in the two areas to a partial coverage of the BEN layer in the thinner-looking area due to superimposition effects, unavoidable in TEM.

Low magnification TEM images of the samples subject to longer growth steps, between 10 s and 2 min, show facetted grains between the Ir substrate and the covering layer deposited before TEM preparation (Figure 5.19). In the 10 s and 20 s grown samples the grains are isolated and the continuous amorphous carbon layer found after BEN, which would be visible between the grains, has already completely disappeared. After 1 min deposition the islands are starting to coalesce. In the 10–60 s grown samples the weak or absent substrate roughening allows to visualise the complete shape of the grains, while the ones of the 2 min grown specimen are partly hidden by 3–5 nm hillocks in the Ir substrate.

HRTEM analyses of these specimens (Figure 5.20) allow to identify the diamond lattice structure inside the perfectly epitaxial grains. For those grains, the lattice images and their FFTs show the following crystallographic relationships: $(001)_{diamond}//(001)_{Ir}$ and $[110]_{diamond}//[110]_{Ir}$. Some of the grains show few degrees tilt with respect to the Ir substrate, while for those having few degrees twist the lattice structure is not visible at all. HRTEM shows that between the diamond grains, where the continuous carbon layer has disappeared, the covering Ir layer grows epitaxially on the Ir substrate. A careful analysis of the heterointerface between the growing diamond and the Ir substrate by means of inverse FFTs of the HRTEM images (*e.g.* shown in Figure 5.21 for the sample subject to 1 min growth after BEN) shows the presence of misfit dislocations distributed with the expected density (see Figure 5.17(f)). The presence of misfit dislocations, due to the lattice mismatch between diamond and Ir, is a proof of the strong binding between the two materials and of the full relaxation of the diamond structure at this stage of growth.

The complete analysis of the whole series 5 s – 2 min growth, using SEM, AFM and TEM,

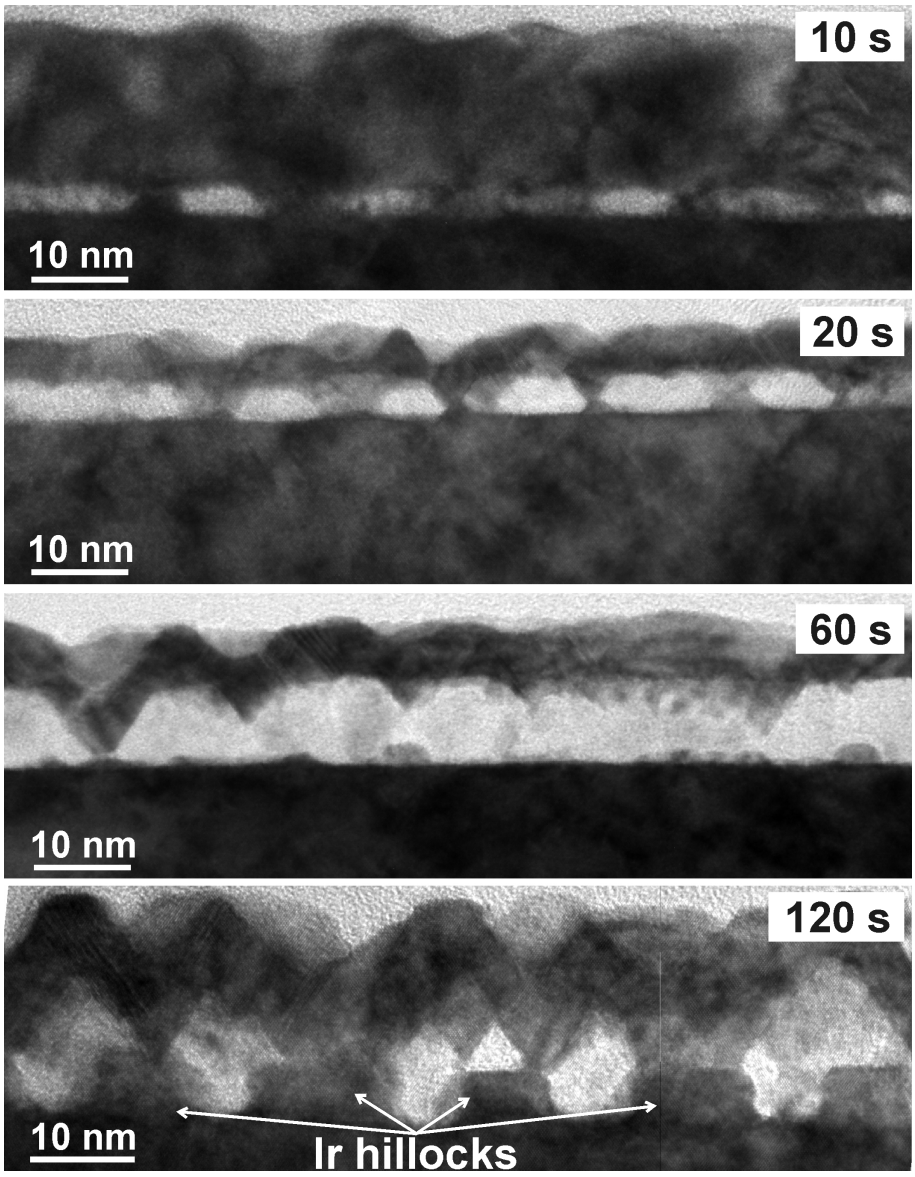

Figure 5.19 – XTEM images of samples subject to 10–120 s growth steps after BEN on Ir/YSZ/Si(001).

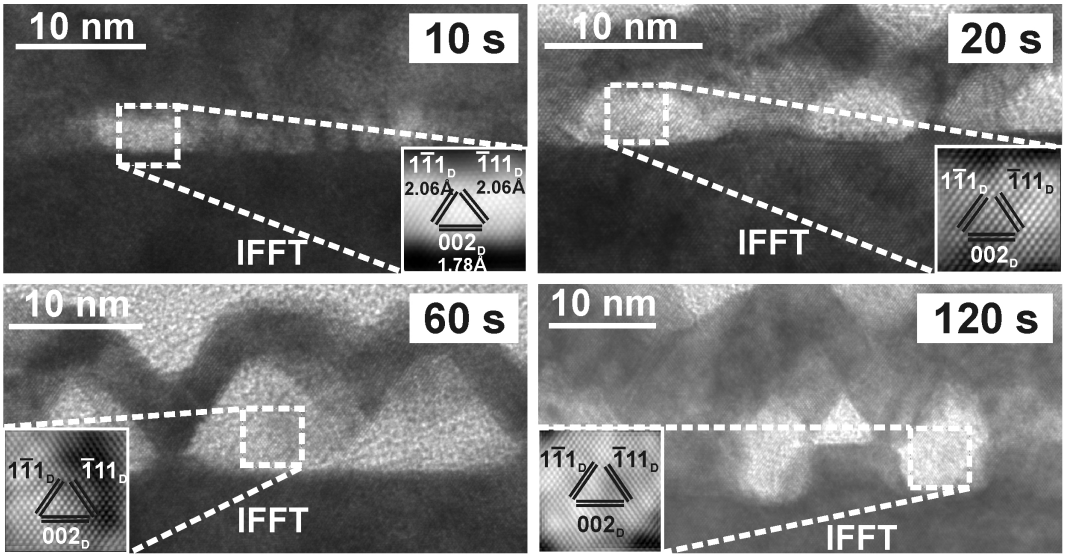

Figure 5.20 – HRTEM images of the samples in Figure 5.19 acquired along the [110] zone axis of Ir. The insets show inverse FFTs of regions of one epitaxial grain for each sample, where the diamond lattice structure is observed.

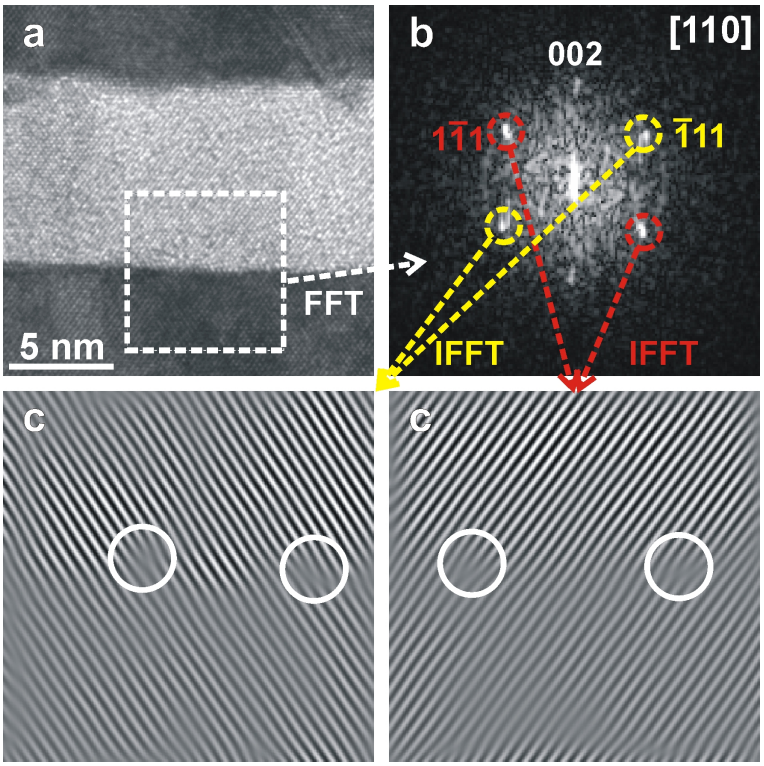

Figure 5.21 – (a) HRTEM image along [110] of an area of the sample subject to 1 min deposition after BEN and (b) FFT of the interface area in the square, showing the epitaxial orientation of diamond with respect to the Ir substrate. (c) and (d) are the inverse FFTs of the selected area calculated using two different sets of spots, so as to evidence the misfit dislocations at the interface between Ir and diamond.

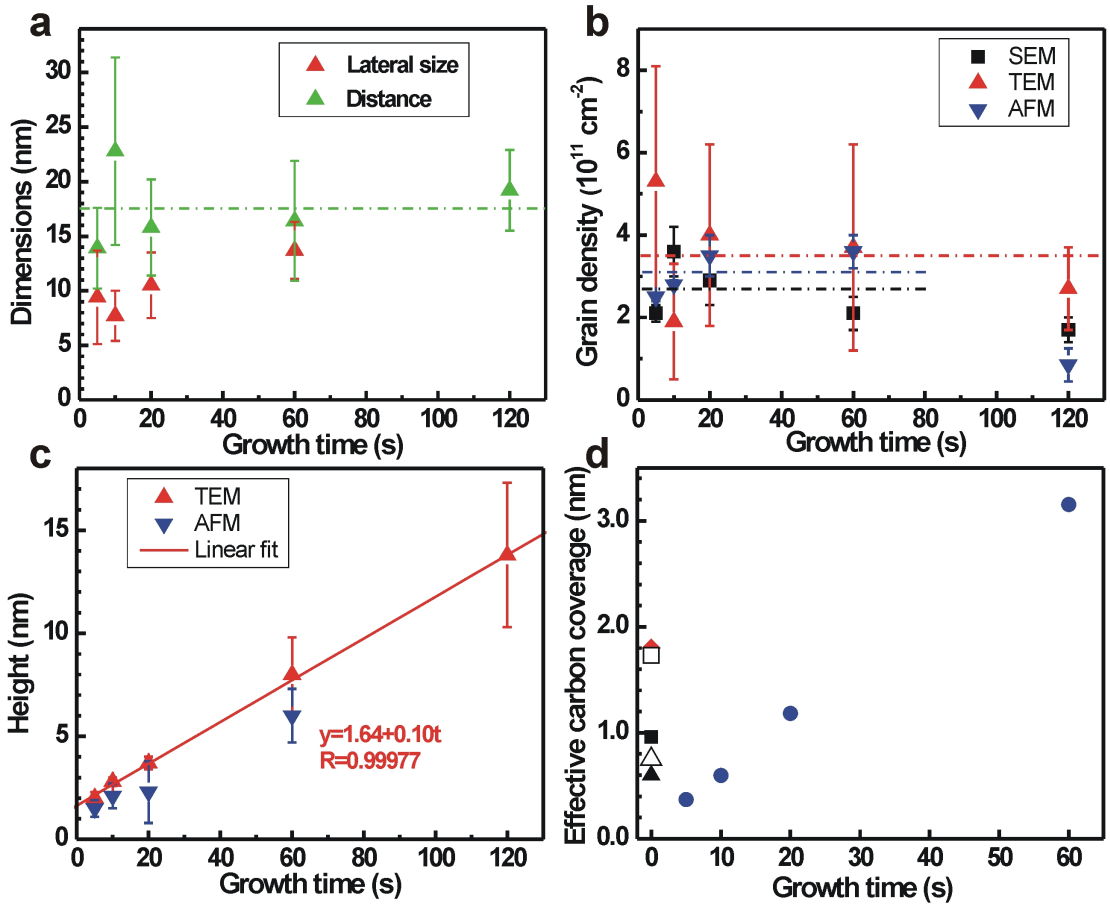

Figure 5.22 – Plots of the evolution with the deposition time of (a) dimensions (lateral size and distance between the grain centres), (b) areal density (TEM, SEM, AFM), (c) height (AFM, TEM) of the diamond grains and (d) effective carbon coverage, defined as the thickness of a carbon layer with the density of diamond assuming that all carbon atoms are bound in diamond islands (Table 5.1). The dotted lines in (a) and (b) indicate the average values, while in (c) the red line indicates the linear fit of the TEM height data. For the data point at 0 s growth time (*i.e.* immediately after BEN) in (d) the carbon coverage deduced in Section 5.1.1 (red) and from former ERD (full black triangle, [Bauer(02)]), HRTEM (hollow black triangle, [Schreck(06)]), XPS (full square, [Gsell(08)]) and AES (hollow square, [Schreck(09)-1]) studies was converted into an effective diamond layer thickness.

allows to monitor the evolution of the size of the islands, the distance between them and their areal density in the early stages of growth (see Table 5.1 and and Figure 5.22). All these observables were evaluated in different positions and an average was then calculated. These results allow also to compare the three microscopic techniques and evaluate their reliability for the analysis of such nanostructured systems. The average distance between the grain centres, directly evaluated via XTEM analyses, scatters around an average of 18 nm in the whole explored time range. This value is slightly lower than the 25 nm determined in a former study of a 2 min grown sample on Ir/$SrTiO_3$(001) [Schreck(06)]. The constancy of the inter-distance can be explained if the array of grains is formed during BEN and keeps unchanged after switching off the bias voltage. During deposition the centres of the grains, thus their inter-distances, are fixed, while they are free to grow laterally and perpendicular to the substrate surface. The lateral size of the grains shows indeed an increase between 20 s and 1 min deposition. For a longer growth time it is not possible to estimate a width for single islands, as the coalescence process has already started. The grain areal density, derived directly from SEM high magnification and AFM images and indirectly from the distance, d, determined from TEM images as $D = d^{-2}$, shows some statistical variation with the deposition time, yielding an average value of $3{\cdot}10^{11}$ cm^{-2}. The value determined by TEM is higher than the ones obtained by SEM and AFM, but it also has a higher uncertainty, as it is evaluated from a much smaller number of particles. However, the value determined for the grain density is in very good agreement with what reported in former studies for pure BEN [Golding(04)] and for 2 minutes growth after BEN on Ir(001) [Schreck(06)].

The grain height, evaluated by AFM and TEM, increases with the deposition time, as expected (Figure 5.22(c)). The AFM-determined values are systematically lower than the TEM-determined ones, due to the finite size of the AFM tip and to the not perfect flatness of the surface over the investigated range. Therefore the TEM value will be considered more reliable, in case the transmission artefacts can be excluded. The height variation is quite in good agreement with a linear increase with the deposition time (correlation factor, R, for the linear fit in Figure 5.22(c)>99.9%), with a vertical growth rate of 1 Å/s = 0.36 μm/h, compatible with the values typically determined for diamond growth with the used parameters. The intercept at t = 0 s is ≈1.6 nm, which should correspond to the height of the nucleation centres formed during BEN, before the beginning of the deposition process. The latter value can surely not be assumed as an exact one, but as an indication of the height of the grains formed during BEN. One can observe that this value is comparable to the 1–2 nm determined for the thickness of the BEN layer. Combining the information from SEM (areal density) and TEM (inter-distance and height), the amount of carbon bound in form of crystalline diamond as a function of the growth time was calculated. The result converted into an effective diamond film thickness is plotted in Figure 5.22(d). For the calculation a 100% coverage of the surface by domains is assumed. The data points at 0 s growth time correspond to the carbon coverage measured after BEN by TEM on several samples in the previous section and in former studies [Bauer(02), Schreck(06), Gsell(08), Schreck(09)-1], converted to an effective diamond layer thickness. Extrapolation of the amount of crystalline carbon towards zero indicates that there is a minimum in the overall coverage of carbon on the surface after a few seconds of growth. This is in perfect agreement with the XTEM presented results, showing that the continuous 1–2 nm BEN layer is largely etched off after ≈5 s deposition while the crystalline diamond phase growing out of the nuclei has not yet increased significantly.

In order to complete the present study of the early growth stages of diamond on Ir/YSZ/Si(001), XPD analyses were carried out in order to monitor the development of the fine structures and the maximum anisotropy value after short growth steps. The pattern of the C 1s core signal of a sample grown 1 min after BEN (Figure 5.23(a)) is less blurry than the one recorded right after BEN on the same substrate system (Figure 5.9(a)), due to the absence of the

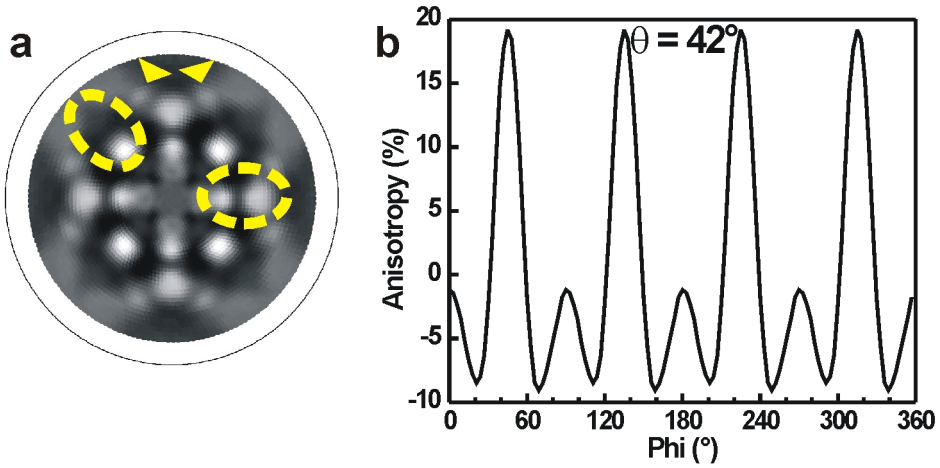

Figure 5.23 – (a) XPD pattern of the C 1s core level for a sample subject to 1 min growth after BEN on Ir/YSZ/Si(001). The yellow markers highlight some significant features, to be compared to the reference patterns in Figure 5.9. (b) Azimuthal scan over a range 0–360° extracted from the pattern in (a) for the polar angle $\theta = 42°$, where the maximum anisotropy value is observed.

amorphous carbon layer and the defective crystalline matrix surrounding the crystalline features, and due to the higher structural purity of the crystalline particles at this stage of growth. At the same time this pattern shows more fine structure, more similar to the one of the thick heteroepitaxial diamond film than to the one of an epitaxial film produced by BEN and 1 h deposition on Si(001) (panels (b) and (e) in Figure 5.9, respectively). The maximum anisotropy value (28%) in this case is found for the polar angle $\theta = 42°$. This value is much lower than the 67% determined for a reference thick heteroepitaxial diamond film on Ir/YSZ/Si(001) (Figure 5.9(b) [Gsell(08)]), indicating that after only 1 min growth diamond is still defective and, also, still shows some orientational spread.

5.1.2 The Ir/YSZ/Si(111) system

Most of the studies focussed so far on BEN of diamond on Ir were conducted on the Ir(001) surface, as CVD growth of diamond gives the minimum defect densities in {001} growth sectors. It is well known, indeed, that the developoment of contact twins is difficult to suppress on {111} facets [Wild(94), Helming(95), Tachibana(97)]. Nonetheless, epitaxial diamond films with (111) orientation would be interesting for many technological applications. As an example, the n-type doping of diamond by incorporation of phosphorus impurities was found to be more effective for (111)-oriented substrates [Koizumi(97)]. Moreover, (111)-oriented diamond films could provide interesting growth surfaces for (0001) oriented wurtzite-type wide band gap semiconductor layers (e.g AlN, GaN and ZnO) aimed at the fabrication of heterojunction devices [Miskys(03)]. For these reasons the investigation of epitaxial BEN and growth of diamond on the promising Ir/YSZ/Si system in (111) orientation might open appealing opportunities.

The following experiments were carried out on epitaxial Ir films deposited on YSZ/Si(111) wafers. The details of the preparation of these multilayer substrate systems are described by Fischer et al. [Fischer(08)]. It is important to note that both the YSZ and the Ir layer deposited on the Si(111) substrate consist of one single texture component, without any indication of twinning. BEN experimental parameters were similar to those used for the Ir/YSZ/Si(001) system (see Section 3.3 and appendix D).

SEM investigations of BEN samples on Ir/YSZ/Si(111) show the appearance of the circu-

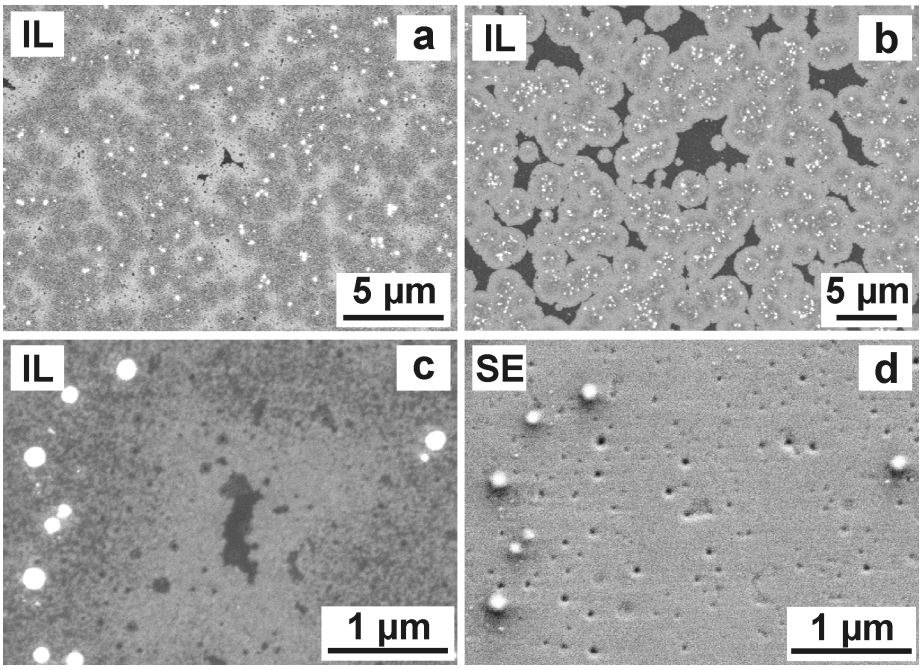

Figure 5.24 – *IL*-SEM micrographs of (a) a central area and (b) a peripheral region of the sample D141, showing almost 100% coverage with domains and a lower concentration of domains, respectively, after BEN on Ir/YSZ/Si(111). The comparison between images of exactly the same area of the sample acquired using the (c) *IL* and (d) *SE* detectors of the SEM confirms a "domain-like" behaviour (compare with Figure 5.2). The visible pits on the substrate were present before the BEN treatment.

lar bright areas, akin to those seen on Ir(001) (Figure 5.24(a-b)), which are visible only using the *IL* detector and not with the *SE* detector (Figure 5.24(c-d)). As for BEN on Ir(001) the growth of epitaxial diamond grains starts from these areas. This indicates that the formation of domains is a general phenomenon on Ir single crystal surfaces, independent of the orientation. As already observed for the respective (001) orientation, the examined samples do not show a pronounced roughening apart from some pits in the substrate (see Figure 5.24(d)), most probably present already before the BEN process.

The RHEED pattern of the BEN sample D141 on Ir/YSZ/Si(111), acquired along $[\bar{1}10]$ of Ir, shows intermediate characteristics between a streak and a spot pattern, confirming the weak roughening of the Ir surface. It can completely be indexed as an Ir pattern (Figure 5.25). XTEM analyses of the same sample show a bright continuous slit, with a thickness of ≈1.3 nm, between the Ir substrate and the Ir covering layer (Figure 5.26). In HRTEM images at various positions along the slit, no indications of crystalline diamond nuclei can be found. Only structures ascribable to Ir are observed in some regions (Figure 5.26(b)). The presence of a continuous amorphous layer within the bright slit is in accordance with the polycrystalline nature of the covering Ir layer (Figure 5.26(c)).

The carbon coverage on the Ir film determined by XPS on the sample D141 corresponds to 14 carbon atoms per Ir(111) surface atom. Assuming a homogeneous, closed carbon layer, a thickness of 12.1 MLs, corresponding to ≈1.2 nm, was determined (1 ML diamond (111) = 0.103 nm, see Figure 5.27(a)). This value fits well the width of the slit visualised in XTEM images. XPD measurements taken for the C 1s photoelectrons yield a distinct pattern with a high contrast, exhibiting a clear threefold symmetry (Figure 5.27(b)). For comparison, the diffractogram of the (111) surface of a natural single crystal taken from ref. [Küttel(94)] is included in Figure 5.27(c). The main intensity maxima and the dominant bands are nearly identical in patterns (b) and (c). This indicates that a high fraction of the carbon atoms at the surface of the BEN sample is arranged in a single crystal diamond structure with epitaxial

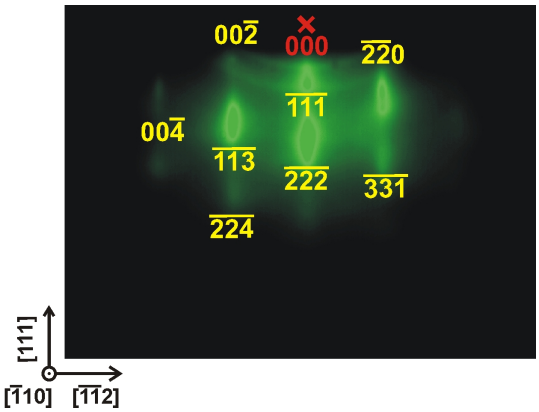

Figure 5.25 – RHEED pattern, recorded at 660°C, of the sample D141 along [$\bar{1}$10] azimuth of Ir. All the spots can be indexed as Ir spots.

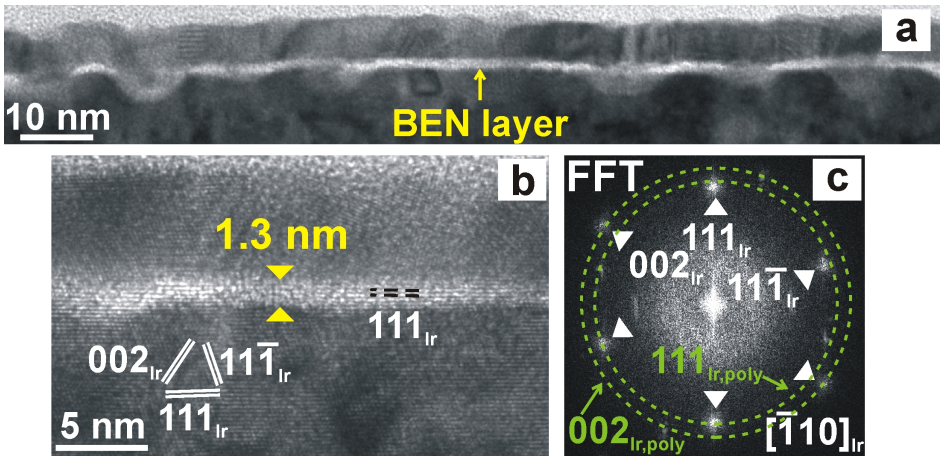

Figure 5.26 – XTEM images (a) show a bright layer observed in the sample in Figure 5.24 between the Ir substrate and the Ir covering layer. (b) HRTEM images acquired along the [$\bar{1}$10] zone axis of the Ir substrate show only crystalline patterns ascribable to Ir. (c) The FFT of the HRTEM image (b) shows the [$\bar{1}$10] pattern of the single crystal Ir substrate and some isolated spots due to the polycrystalline covering Ir film.

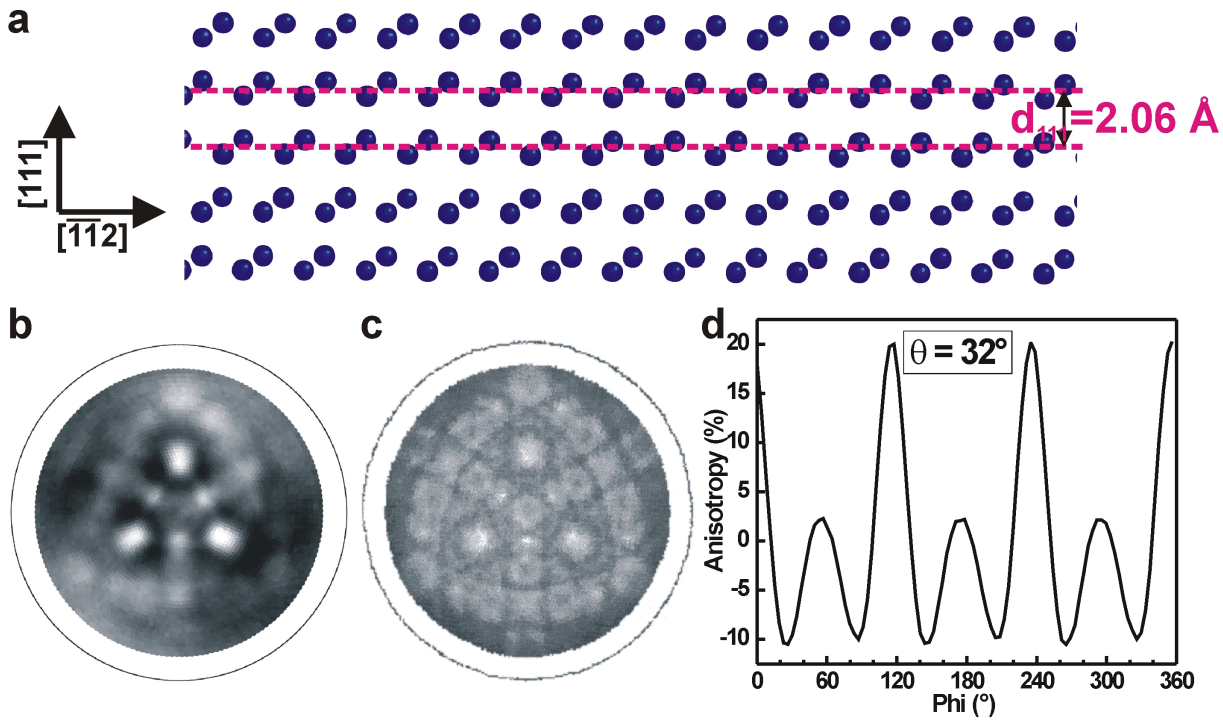

Figure 5.27 – (a) Sketch of a slab of the diamond structure viewed along the [$\bar{1}$10] axis, showing that, due to the two-atom-containing base, two monolayers of carbon atoms are found within d_{111}, the distance between two neighbouring {111} planes. (b) XPD pattern of the C 1s core levels for the sample D141, compared with (c) the analogous pattern reported in ref. [Küttel(94)] for the (111) surface of a natural diamond single crystal. The C 1s pattern in (b) contains raw data, without any symmetry averaging. (d) Azimuthal scan over a range 0–360° extracted from the XPD pattern of the C 1s signal in (b) for the polar angle $\theta = 32°$, where the maximum anisotropy was recorded.

(111) orientation. Due to the disorder generated by the ion bombardment, the pattern shows significantly less fine structure than the natural single crystal pattern. Even the strong ion bombardment during BEN did apparently not induce defects generating diamond in twin orientation relationship. As discussed for BEN on Ir(001), the ion bombardment induced defects may be responsible for the absence of some fine structure. All the present observations concerning the BEN layer lead to the conclusion that the mechanisms of diamond nucleation on Ir(111) are absolutely identical to those on Ir(001).

A maximum anisotropy of 20% is measured for the C 1s photoelectron signal collected for this sample at the polar angle $\theta = 32°$(Figure 5.27(d)). As the coverage with domains is ≈100% (Figure 5.24(a)), 20% is roughly the real maximum anisotropy. This value also fits to those obtained for BEN samples on Ir/$SrTiO_3$(001) [Gsell(08)] and Ir/YSZ/Si(001) (Section 5.1.1), indicating that this value is typical for the BEN process on Ir performed in the same ASTeX setup, independent of the particular substrate system and orientation. This value is also in quite good agreement with the 26% reported by Kono et al. [Kono(05)] and the 22% reported by Aoyama et al. [Aoyama(07)] as well. However, all these values are significantly lower than the 46% evaluated by Kono et al. [Kono(04)], most probably due to the uncertainties in the evaluated coverage of the surface with domains after BEN.

5.1.3 Discussion

The results presented in this section confirm the interest in the new Ir/YSZ/Si multilayer system for the realisation of large area epitaxial diamond films. Moreover, the analyses of

the pure BEN layers on both (001) and (111) surfaces demonstrate some general features of this process on Ir. First of all, the formation of domains, observed for both orientations, can be now seen as a general phenomenon on Ir single crystal surfaces, independent of the particular multilayer system and orientation. However, in contrast with other substrate systems [Hörmann(01), Golding(04)], the regular roughening consisting in ridges and furrows along the low indexed crystallographic directions is mostly absent on Ir/YSZ/Si. Following BEN, a continuous carbon layer is formed on the Ir substrate, as in the case of $Ir/SrTiO_3(001)$. The thickness determined by XTEM is in the range 1–2 nm, in agreement with the values derived from XPS measurements. This value is slightly higher than the ≈1 nm of the BEN layer on $Ir/SrTiO_3(001)$. It is interesting to observe that a homogeneous coverage with carbonaceous material is also the result of a failed BEN process on $Ir/SrTiO_3(001)$. However, in this case the XTEM-determined thickness (≈2 nm in average between flat and grooved areas) is higher than the XPS-determined 1 nm. A continuous coverage with carbon has also been found on a flat DC-BEN sample on the Ir/YSZ/Si(001) system, with a thickness of ≈1.3 nm. One can conclude that direct visualisation by XTEM of the result of the BEN treatment, successful or failed, shows a ≈1–2 nm carbon layer homogeneously covering the Ir substrate. XPS results confirm this thickness range. HRTEM does not show any crystalline diamond features within the carbon layer, which is TEM-amorphous all over the sample for both (001) and (111) orientations. RHEED patterns also do not show any features ascribable to diamond. XPD is the only technique unambiguously detecting a short-range crystalline order inside the BEN layer after successful BEN, with a maximum anisotropy value of ≈18% obtained for different systems.

Regarding the short growth series, the results obtained on the shortest growth step deserve a brief discussion. The three samples to 5±1 s deposition seem to reflect different stages of the first very few seconds of growth following the BEN process: D95 and D96 show roughly the same instant and D99 seems to represent an immediately successive stage. The presence of residues of the a–C layer in D95 and D96 indicates that the process of etching of the amorphous carbon phase under deposition conditions is still not completed. The sample D99, not showing any a–C residues, probably corresponds to a slightly later (not more than 2 seconds) stage. In samples D95 and D96 carbon is present everywhere, in form of crystalline diamond (inside the domains) and residues of amorphous carbon (outside the domains). This is not surprising, as a continuous carbon layer was found both after successful and failed BEN treatments (Figures 5.5-5.8). These results demonstrate that ≈5 s is the critical duration of the deposition step needed for the complete etching of the a–C layer formed during BEN.

The presence of the continuous epitaxial diamond layer, wider than ≈200 nm, which is found in D95 and D96, but not in D99, is more difficult to explain. The latter specimen shows epitaxial diamond areas extended for a maximum of ≈50 nm. Extended epitaxial diamond regions are not even found for deposition times longer than 10 s, up to 1 min, when coalescence between individual grains starts to take place. This seems to indicate that such an epitaxial diamond layer derives from some extended structure formed during the BEN treatment which is destroyed within the first 5±1 s of deposition. In contrast to the a-C film, which is etched away under deposition conditions, this layer is most probably subdivided into small epitaxial diamond grains. This idea is supported by the presence of the larger isolated grains found in D99, which are always absent after slightly longer deposition processes (10 s). A possible explanation for the formation of an extended epitaxial diamond layer during BEN, which would be unstable in deposition conditions, will be presented in a following section (see Section 5.3).

With the density and dimension data extracted from the short growth experiments, the maximum anisotropy value of ≈19% measured for the BEN samples can lead to an estimation of the size of the nuclei formed by BEN. With an average distance of 18 nm, and with one quarter of carbon arranged in a crystalline environment, the diamond crystallites formed

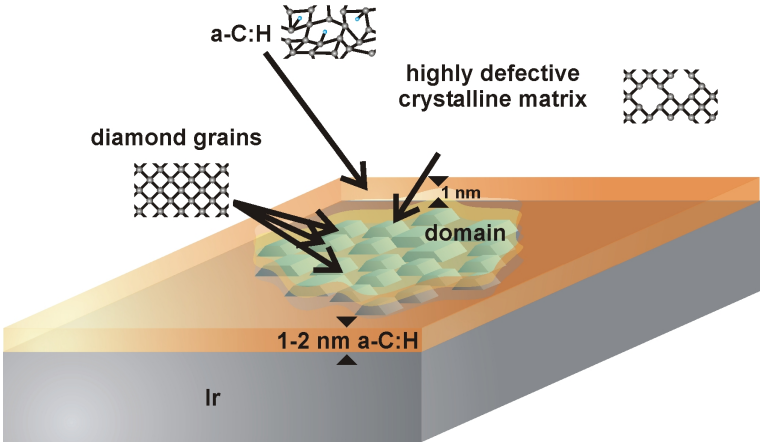

Figure 5.28 – Schematic model of the structure of the BEN layer, as deduced from combined analyses of samples subject to BEN and short growth on Ir(001) buffer layers.

during BEN should be ≈9 nm wide. This is approximately the lateral size of the grains observed after 5 s deposition. Moreover, the linear fit of the height of the grains extrapolates a value corresponding to BEN of 1.6 nm. Certainly structurally perfect crystalline diamond grains 1.6 nm high and 9 nm wide would generate visible features in RHEED patterns and crystalline structures in HRTEM, while they were never seen after a pure BEN process. Even more, it should be possible to detect in RHEED and HRTEM continuous epitaxial diamond layers as those seen after 5 s deposition for samples D95 and D96, if they were present after BEN. XPD is instead able to see crystalline diamond patterns at the BEN stage due to its higher sensitivity to local order. However, only a small fraction of the XPD signal can be attributed to perfect crystalline diamond grains. The XPD results can be explained by postulating inside the domains extremely small epitaxially oriented crystalline structures which form the nuclei in the sense that they will survive the change from BEN to growth. These are embedded in a highly defective crystalline structure with epitaxial orientation (see scheme in Figure 5.28). Outside the domains, a DLC-type hydrogenated amorphous carbon matrix is found [Gsell(07)-1].

5.2 Structural damage close to the surface of a thick diamond film created by keV carbon ion implantation

In a recent study, a BEN layer showing domains on Ir/$SrTiO_3$(001) was examined using a combination of electron diffraction techniques [Gsell(08)]. LEED did not show any pattern, neither due to the diamond nuclei nor to the Ir substrate. At the same time, in RHEED a clear pattern ascribable to the roughened Ir substrate, but no signatures of diamond, were detected. However, the XPD analyses of the C 1s core signal of the sample showed a clear four-fold pattern comparable to the one of highly oriented diamond (Figure 5.9(d)). The detected pattern could not be due to the forward-focussing of the C 1s signal by the atoms of the single crystal Ir substrate, which are organized in a *fcc* lattice, as no pattern was observed for the C 1s signal on an analogous BEN sample without domains. The overall result on the BEN sample showing domains demonstrates that the epitaxial diamond crystallites in the domains are large enough to produce an XPD pattern, but smaller than the coherence length of the electrons in RHEED and LEED. Moreover, the difference between the RHEED and LEED results is due to the corresponding electron mean free path (≈4 nm for the RHEED 30 keV electrons, ≤ 1 nm for the LEED 50-300 eV electrons, see Figure 2.6), which in case of the latter technique is too short to obtain a signal from the Ir substrate.

In order to explain the anisotropy in the C 1s XPD patterns after successful BEN (Figure 5.9(a,d)), 9 nm wide perfectly crystalline grains would be required, which have never been detected by RHEED and HRTEM in samples showing domains (Section 5.1). A significant contribution to the signal might instead come from a defective crystalline matrix, ordered enough to generate the four-fold C 1s pattern but too defective to be detected by HRTEM or RHEED. In addition, this ordered defective carbon phase is unstable under the deposition conditions, as after few ($\approx$ 10) seconds of deposition it is completely etched off. While the matrix covering the BEN sample outside the domains has the characteristics of a DLC phase, amorphous and with a high content in sp^3 bonding [Robertson(02), Casiraghi(07)], the material surrounding the nuclei within the domains would be a phase with crystalline diamond order, characterised by a highly defective nature, a higher density and a higher Young's modulus [Schreck(09)-1] (see model in Figure 5.28).

In the experiments to be presented in the current section, ion implantation was employed for the creation of damage, under controlled and tunable conditions, into thick diamond layers. Implantation doses, and consequently the damage level, were varied while monitoring the C 1s XPD signal and the RHEED pattern. The experiments aimed at the artificial creation of damage conditions in a diamond layer, which are identical or at least similar to those observed after a successful BEN treatment. The confirmation of this point would substantiate the hypotesis concerning the nature of the matrix - a defective diamond matrix - that, within the domains, surrounds the nanometer-sized grains that later act as proper nuclei for the following epitaxial growth of diamond. On the other hand, this would show that RHEED patterns disappear faster (*i.e.*, at a lower damage level) than XPD ones. Based on the critical damage found in these experiments, diamond deposition was carried out onto thin damaged diamond films in order to verify the damage level above which the orientation information is lost and epitaxial growth is not possible any more.

5.2.1 Ion-implantation-induced damage of thick films

Ion implantation is a non-equilibrium method to insert atoms into a material, which has the side effect of introducing high levels of radiation damage as well. For standard semiconductors, ion implantation followed by a suitable annealing step, aimed at the removal of the structural damage, is often performed in order to induce controlled doping. In the case of diamond, ion implantation offers the unique possibility to force any dopant atom, independent of size or solubility, into such a strongly bonded and extraordinarily dense crystal lattice. At the same time, however, the radiation damage is more difficult to remove while retaining the diamond phase, as annealing treatments can also induce graphitisation of the damaged regions. Due to these peculiarities, implantation of ions into diamond has been widely investigated [Prawer(95), Prins(03)]. Most of the studies on this topic were focussed on the variation of the electrical conductivity with the implanted dose. In particular, several studies underline the existence of a critical dose, D_c, above which implantation leads to a damaged phase that, after annealing, is converted into graphite.

In the present case, the damage generation was itself the principal purpose of the ion implantation. For these experiments, few μm thick heteroepitaxial diamond films on Ir/YSZ/Si(001) were employed as targets. Carbon ions (C^+) were chosen because they are not alien to the diamond matrix. Moreover, these ions are similar in mass to the hydrocarbon ions bombarding the surface during the BEN treatment ($CH_x{}^+$, with x$\in$[0,4] [Katai(00)]). It is well known, anyway, that the effect of ion implantation in terms of damage can be attributed to the volume density of introduced defects, irrespective of the ion species [Prawer(95)]. In the present experiments, ion implantation was performed at room temperature in order to avoid re-crystallisation of the damaged phase. Moreover, ion bombardment-induced heating of the sample was negligible with the low beam current densities used ($\approx$7 $\mu A/cm^2$).

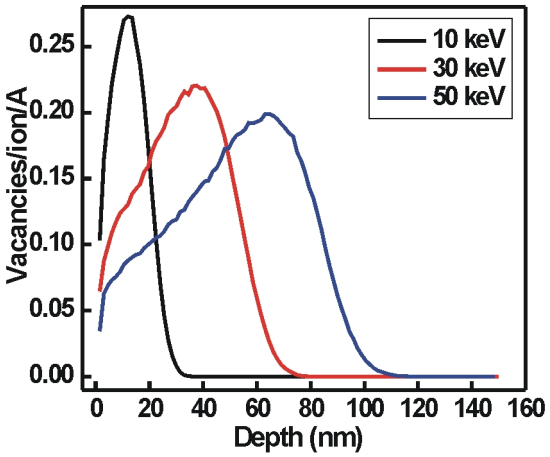

Figure 5.29 – Profile of damage due to C^+ ions of variable energy into diamond, as calculated by TRIM. The damage at the surface, assumed for the calculations of the dose D^*, is the value observed for zero depth.

First of all, the damage profile with depth induced by C^+ ions into diamond has been estimated using TRIM (the TRansport of Ions in Matter), a Monte Carlo code of the package SRIM (the Stopping and Range of Ions in Matter) that calculates the interactions of energetic ions with amorphous solid targets [SRIM, Ziegler(09)]. The values for the displacement energy and the lattice binding energy for the calculations were assumed as 45 eV and 2 eV, respectively [Prelas(98)]. The TRIM calculations, and the implantation experiments based on them, were focussed on the damage of a thin layer (≈50 nm) directly below the surface of thick heteroepitaxial diamond films. This choice was due to the fact that the resulting specimens needed to be characterised by surface sensitive techniques as RHEED and XPD. For this aim, TRIM calculations were carried out for ion energies of few tens of keV (Figure 5.29). In particular, C^+ ions with an energy of 30 keV generate damage into a ≈70 nm thick surface layer of an amorphous carbon film with the above parameters. A reference dose value can be obtained via the equation:

$$D^* = \frac{N_D}{N_V}$$

where N_D is the atomic density of diamond ($1.77 \cdot 10^{23}$ atoms/cm^3 [Field(79)]) and N_V is the number of vacancies per ion and per Å at the very surface of the specimen, which in the case of 30 keV C^+ ions is 0.065 vacancies/ion/Å. By definition, D^* is the dose at which the volume density of vacancies is equal to the atomic density of diamond. According to TRIM this corresponds to $2.7 \cdot 10^{16}$ ions/cm^2 at the surface implanted with 30 keV C^+ ions. In other words, after implantation with a dose of about D^*, all atoms at the surface of the film have been displaced once (on average). It is important to underline that TRIM does not consider any relaxation mechanism, even in case of such a high damage level.

Identical pieces with a size of 1×1 cm^2 were cut from a ≈5 μm thick large area epitaxial diamond film deposited via MWPCVD using the IPLAS setup (Section 3.3.2). The film was deposited onto an Ir/YSZ epitaxial multilayer on top of a 3 mm thick 4 inch Si(001) wafer. For all the pieces the silicon substrate was afterwards thinned by grinding and polishing down to a thickness of ≈0.5 mm in order to meet the geometric requirements of the XPD measurement setup. A final 30 min growth step was then carried out in order to etch off possible residues of contamination or damages of the surface due to the mechanical thinning procedure. SE micrographs show the surface morphology of the starting sample (Figure 5.30(a-b)) and of its surface after the final 30 min deposition growth step (see Figure 5.30(c-d)).

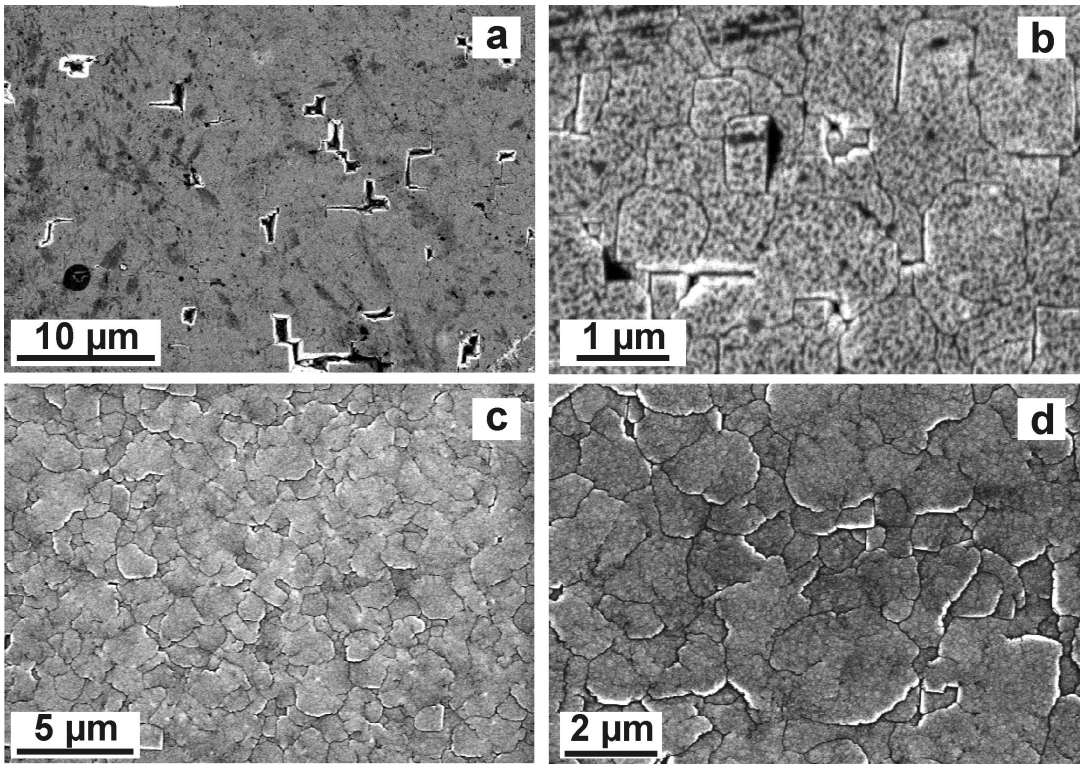

Figure 5.30 – SE micrographs of a ≈5 μm thick epitaxial diamond film on Ir/YSZ/Si(001) (a-b) at the end of the growth process and (c-d) after the final 30 min growth step following the mechanical thinning procedure. The edges of the images are parallel to <110> directions of Ir.

Implantation was performed using 30 keV C^+ ions with doses between $4{\cdot}10^{15}$ ions/cm^2 ($0.15{\cdot}D^*$) and $4{\cdot}10^{16}$ ions/cm^2 ($1.5{\cdot}D^*$). After implantation, the samples show a microstructure like in Figure 5.31 in SEM, without any appreciable difference between the different doses. From the comparison with Figure 5.30(c-d), one can observe that the microstructure is preserved. In addition to this, the more fuzzy contrast in the images can be attributed to a partial surface amorphisation due to implantation.

RHEED characterisation of implantation-damaged samples

The RHEED investigations of the ion damaged samples were performed at room temperature, in order to avoid thermal annealing of the defects created by ion bombardment. The

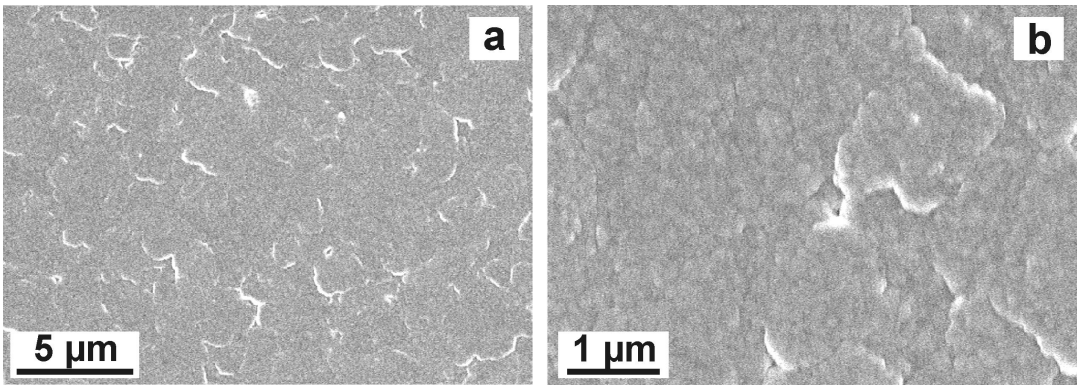

Figure 5.31 – SE micrographs of the sample in Figure 5.30(c-d) after ion implantation with $6{\cdot}10^{15}$ ions/cm^2 ($0.22{\cdot}D^*$). The edges of the images are parallel to <110> directions of Ir.

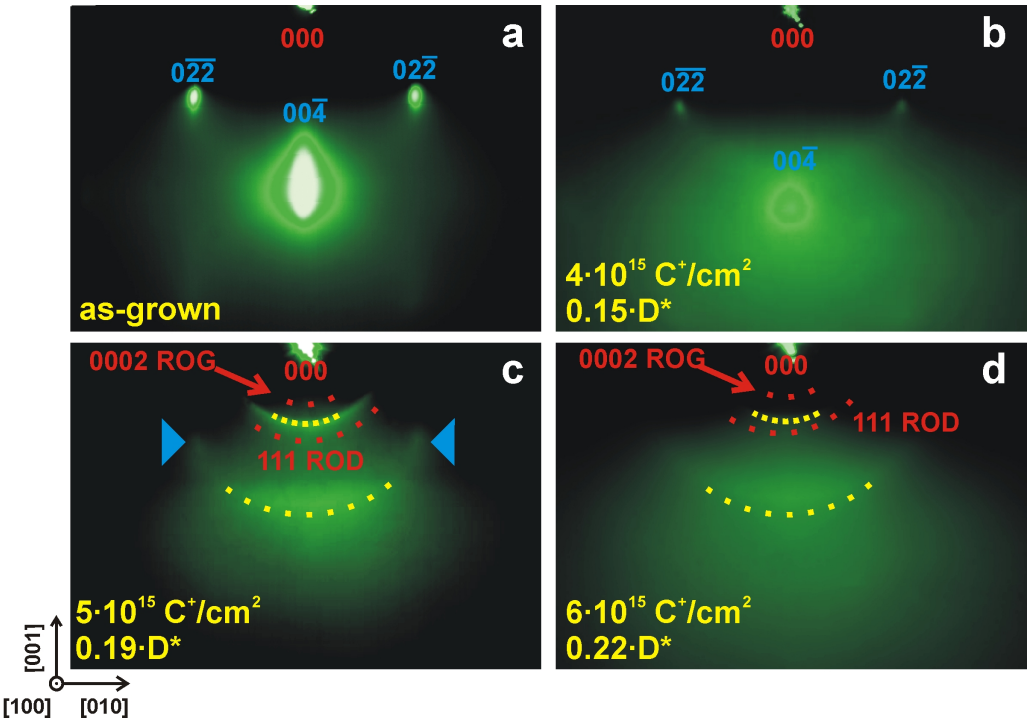

Figure 5.32 – RHEED patterns along [100] azimuth of the ≈5 μm thick sample (a) as-grown and (b-d) after implantation with increasing doses of C^+ ions, indicated in each pattern. The blue features in (a-c) indicate single crystal diamond-related spots. In (c) and (d) the positions where bright rings would appear in case of randomly oriented graphite (ROG) (the (0002) planes) or randomly oriented polycrystalline diamond (ROD) are indicated in red.

clearest patterns were obtained along the <100> directions (Figure 5.32). In the RHEED pattern of the sample before implantation, the diffraction spots of 3D scattering at a single crystal diamond surface are visible (Figure 5.32(a)). At the lowest dose ($4{\cdot}10^{15}$ ions/cm^2, $0.15{\cdot}D^*$) a diffuse background accompanies the 3D diamond spots (Figure 5.32(b)). The background can be attributed to a partial amorphisation of the surface layer of the crystal that leads to incoherent scattering of electrons, in agreement with the SEM results after implantation (Figure 5.31). At the next higher dose ($5{\cdot}10^{15}$ ions/cm^2, $0.19{\cdot}D^*$) the diffuse background increases, but still two weak spots corresponding to diamond are visible (Figure 5.32(c)). The RHEED patterns acquired from samples bombarded with higher doses ($\geq 6{\cdot}10^{15}$ ions/cm^2, $0.22{\cdot}D^*$) do not show any features, apart from an intense diffuse background (Figure 5.32(d)). The bright rings visible in these patterns, starting from the dose of $5{\cdot}10^{15}$ ions/cm^2, can be attributed to diffraction of the central beam due to some aperture in the optical path between the phosphor screen and the image detector. In particular, the smaller ring (indicated in yellow in the figure) would correspond to a spacing of 2.5 Å, not ascribable to lattice planes neither of diamond nor of graphite. In presence of randomly oriented polycrystalline diamond (ROD) or graphite (ROG), the most intense rings would be visible at the positions indicated in the figure, corresponding to the (0002) planes of graphite (3.40 Å) or to the {111} planes of diamond (2.06 Å), which generate the strongest diffraction features [Hassel(24), NBS(53)]. Moreover, in presence of ROD or ROG, additional arcs with larger radii would be present, corresponding to lower lattice spacings.

The dose at which the RHEED spots of diamond disappear, D_R, deduced from these analyses, is between $5{\cdot}10^{15}$ ions/cm^2 ($0.19{\cdot}D^*$) and $6{\cdot}10^{15}$ ions/cm^2 ($0.22{\cdot}D^*$). Corresponding to this dose range, the thickness of the sputtered target layer, T_D, is given by:

$$T_D = S_{tot} \cdot \frac{D}{N_D}$$

Table 5.2 – Summary of the results of ion implantation and electron diffraction experiments with 30 keV C^+ ions on ≈5 μm thick epitaxial diamond films on Ir/YSZ/Si(001).

Implantation dose (ions/cm^2)	**Damage** (vacancies/atom at 0 nm depth,%)	**RHEED pattern**	**XPD pattern**	**XPD C 1s maximum anisotropy** (%)
$4{\cdot}10^{15}$	15	YES	YES	5.9
$5{\cdot}10^{15}$	19	YES	YES	1.3
$6{\cdot}10^{15}$	22	NO	YES	1.0

where S_{tot} is the total amount of sputtered target atoms for 30 keV C^+ ions (estimated by TRIM), D the dose and N_D the density of diamond. Given that S_{tot} ≈0.2 atoms/ion, the sputtered thickness is approximately 7 Å. As the sputtered thickness is 1% of the thickness of the damaged layer (≈70 nm), the sputtering effects can be neglected in the following considerations. The transition dose range corresponds to a damage between 19% and 22% (obtained by dividing the dose by D^*) of the layer in proximity of the film surface. This can therefore be defined as the critical damage level, $D_{R,crit}$, corresponding to which RHEED-coherence is lost and no RHEED pattern of diamond is visible any longer.

XPD characterisation of implantation-damaged samples

XPD patterns of the C 1s signal were acquired on the same implanted samples characterised by RHEED. Of particular interest was the result corresponding to the critical damage level. The pattern acquired from the sample implanted with the minimum dose, $4{\cdot}10^{15}$ ions/cm^2, shows rather defined features (Figure 5.33(a)), comparable to the ones observed on a BEN sample with domains on Ir(001) (*e.g.* Figure 5.33(d)). In analogy to what has been observed on the BEN sample, the pattern is less sharp than the one of single crystal diamond, and the fine structure is partly lost (see Figure 5.9(b-c)). The maximum anisotropy for this sample is anyway rather low (5.9%) (Figure 5.33(e)), due to the high fraction of amorphous material generated in the surface layer by the energetic C^+ ions already at this dose.

The pattern observed on the sample implanted with a dose of $5{\cdot}10^{15}$ ions/cm^2 is more fuzzy, with a maximum anisotropy of 1.3% (Figure 5.33(b,e)). The similarities to the pattern observed after successful BEN are still clear. For the sample implanted with the dose $6{\cdot}10^{15}$ ions/cm^2 the XPD C 1s pattern is even weaker (the maximum anisotropy is 1%), but it still shows similarities to the BEN sample (Figure 5.33(d)). It has to be remarked, however, that the maximum anisotropy is in this case registered for a polar angle $\theta = 52°$, instead of the 45° of the BEN sample and of the reference single crystal diamond samples (Figure 5.33(d) and Figure 5.9(b-c)). This is due both to the weakness of the signal and to possible measurements artefacts (see caption of Figure 5.33). The results of the RHEED and XPD analyses are summarised in Table 5.2.

5.2.2 Diamond deposition onto ion-damaged thin films

With the experiments presented in the previous section we monitored the progressive increase of structural damage in a crystalline diamond matrix induced by bombardment with keV carbon ions using two complementary methods, RHEED and XPD. For both techniques the signals fell below the detection level (or almost below, as in the case of XPD) at similar damage levels of about 20% vacancies per atom, as deduced by TRIM calculations.

In a final experiment series we addressed the question on the absolute sensitivity of RHEED and XPD for the presence of structures which can work as nuclei for the subse-

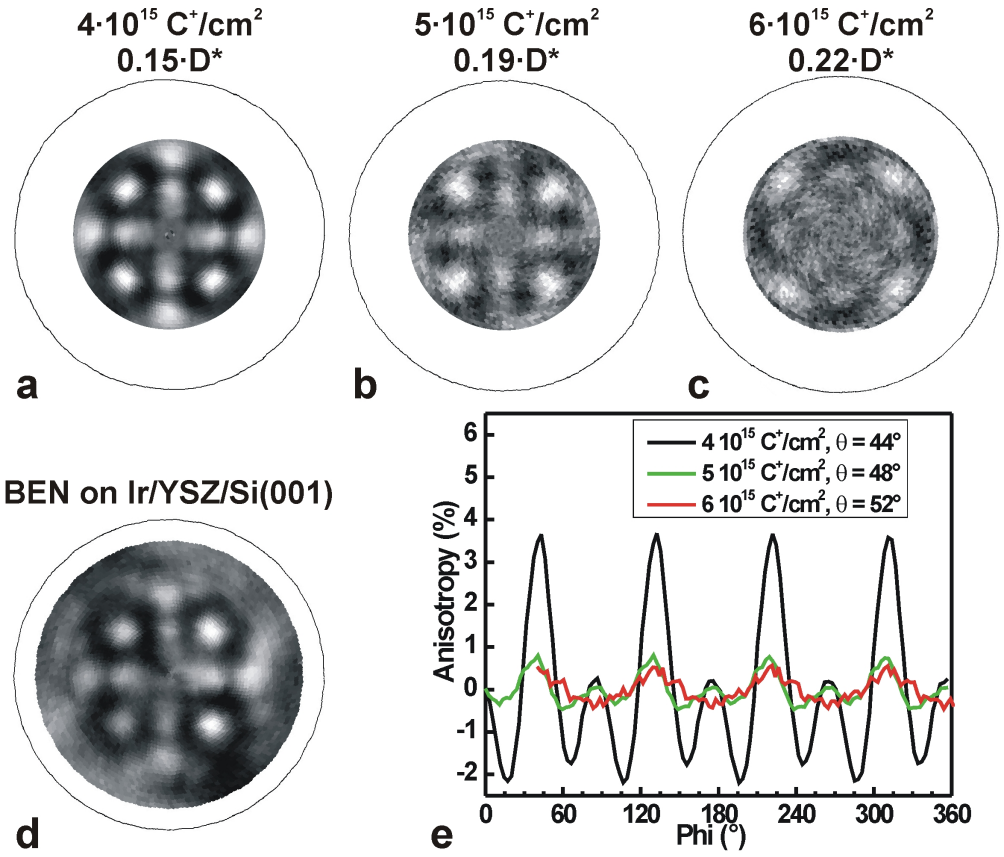

Figure 5.33 – (a-c) XPD patterns of the C 1s core level signal recorded for pieces of the ≈5 μm thick epitaxial diamond film on Ir/YSZ/Si(001) after implantation with 30 keV C^+ with different doses, indicated in the image. All the patterns result from four-fold and azimuthal angle averaging of the original data, carried out in order to remove measurement artefacts. The pattern is shown only up to 57° due to the asymmetries at higher angles caused by the not perfectly horizontal position of the sample surface in the measurement setup (the samples have been thinned from the substrate side). (d) XPD patterns of the C 1s core level signal detected on a BEN sample showing 100% domain coverage on Ir/YSZ/Si(001) (already reported in Figure 5.9(a), and here for ease of comparison). (e) Azimuthal scans extracted from the patterns in (a-c) at the polar angle corresponding to the maximum anisotropy for each of the implanted samples.

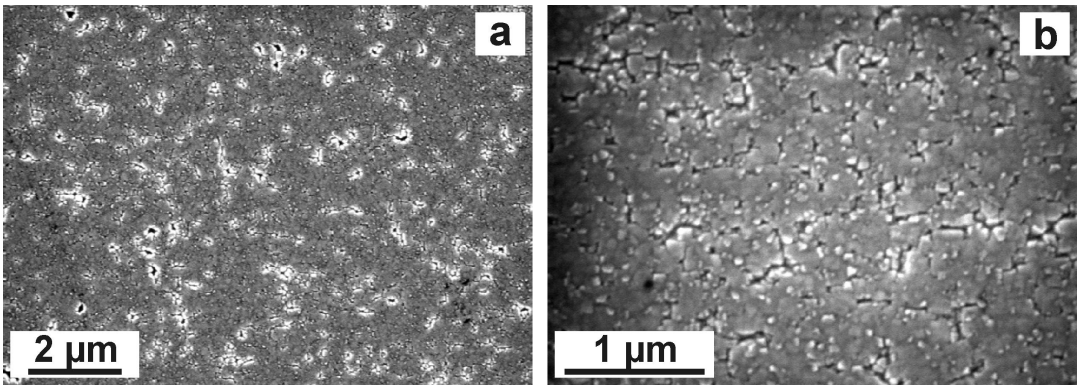

Figure 5.34 – SEM image of an as-grown ≈80 nm thick heteroepitaxial diamond film on Ir/YSZ/Si(001), at different magnifications (edges of images parallel to <110> directions of Ir).

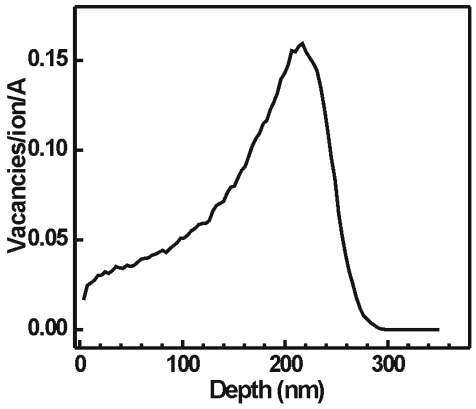

Figure 5.35 – Depth profile of damage due to 190 keV C^+ ions into diamond as calculated by TRIM.

quent growth of homoepitaxial diamond. This study is analogous to the one carried out by Gsell et al. [Gsell(05)], where the BEN layer itself was damaged by increasing doses of ions and following deposition steps were applied in order to study the stability of the epitaxial diamond nuclei embedded in the 1-2 nm layer. In the case of the present study, performing growth on the ion-damaged surface layer of a thick diamond film there would be the risk that the damaged layer is rapidly etched within the first minutes of the CVD process so that homoepitaxial growth finally occurs on the undamaged regions. In order to avoid this artefact, ≈80 nm thick heteroepitaxial films grown on Ir/YSZ/Si(001) were used for these experiments. The SEM images show almost all the area covered with ≈100 nm epitaxial diamond grains, most of them already merging together (Figure 5.34).

A kinetic energy high enough (190 keV) so that most ions are stopped in a depth > 100 nm, *i.e.* so that the maximum of the depth profile of implanted ions is greater than the diamond layer thickness, was chosen (Figure 5.35). For 190 keV C^+ ions a damage of 22% vacancies per surface atom, *i.e.* about the critical damage as deduced from the former experiments, would correspond to a dose, $D_R^{'}$, of $\approx 1.2 \cdot 10^{16}$ ions/cm^2. Therefore, for doses equal to $D_R^{'}$, and higher, the diamond order is expected to be completely destroyed.

The 1×1 cm^2 pieces of the ≈80 nm thick diamond films implanted with different doses ($\approx 0.5 \cdot D_R^{'}$, $1.2 \cdot D_R^{'}$ and $\approx 3 \cdot D_R^{'}$, see Figure 5.36) still show unvaried morphology with respect to the initially epitaxial diamond grains. A 30 min growth step, in conditions favouring epitaxial growth of diamond, carried out on the samples implanted with higher doses, leads to the formation of polycrystalline diamond films, still closed but with a high roughness

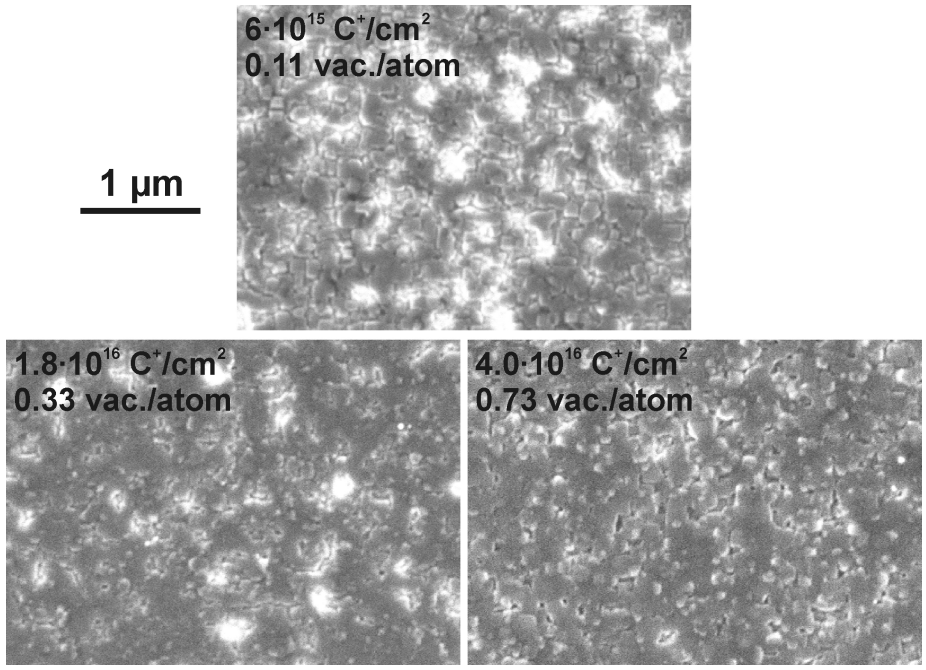

Figure 5.36 – SEM image of three pieces of the ≈80 nm thick diamond film on Ir/YSZ/Si(001) in Figure 5.35 implanted with 190 keV C^+ ions at different doses, indicated in each image (edges of images parallel to <110> directions of Ir).

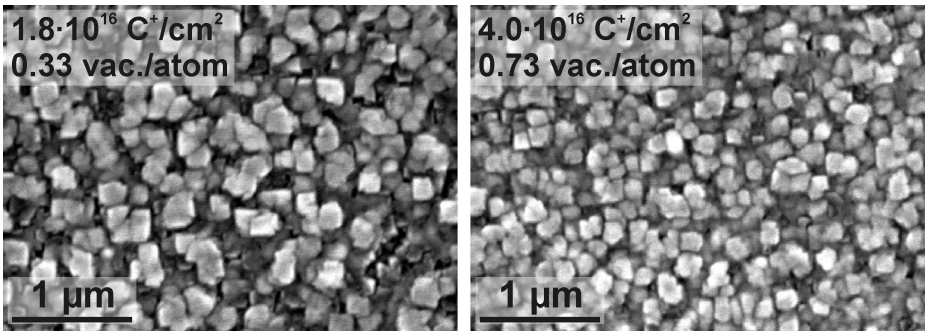

Figure 5.37 – SEM image of two pieces of the ≈80 nm thick diamond film on Ir/YSZ/Si(001) implanted with 190 keV C^+ ions at different doses, indicated in each image, after a growth step of 30 min (edges of images parallel to <110> directions of Ir).

(Figure 5.37). Only a fraction of the grains (≈60%) in the sample implanted with $1.2 \cdot D_R^{'}$ are epitaxially oriented, with an average size of 190 nm. The percentage of epitaxially oriented grains (≈10%) is much lower in the sample implanted with $\approx 3 \cdot D_R^{'}$, which shows also smaller grains (≈150 nm).

The results of the post-implantation deposition experiments are summarised in Table 5.3. It can be seen that, at $1.8 \cdot 10^{16}$ ions/cm^2, corresponding to a damage of 33% displaced atoms, epitaxially oriented diamond grains with a density of 10^9 cm^{-2} are still clearly visible, with a ratio of the epitaxial to the non-epitaxial ones higher than 50%. At this damage level, RHEED would not give any signal and for XPD, based on the ion damage experiments, an anisotropy value well below 1% would be expected, *i.e.* close to the detection threshold. This suggests that the growth experiments are by far the most sensitive measure to determine the presence of crystalline carbon structures which could serve as seeds or nuclei on which homoepitaxial growth could take place.

Table 5.3 – Summary of the results of ion implantation with 190 keV C^+ ions, and following diamond deposition experiments on ≈80 nm thick epitaxial diamond films on Ir/YSZ/Si(001). For the sample subject to the lowest implantation dose no growth experiment was performed.

Implantation dose (ions/cm^2)	**Damage** (vacancies/atom, %)	**Epitaxial crystallite density** (%)
$6{\cdot}10^{15}$ ($\approx 0.5{\cdot}D_R'$)	11	-
$1.8{\cdot}10^{16}$ ($\approx 1.2{\cdot}D_R'$)	33	60
$4{\cdot}10^{16}$ ($\approx 3{\cdot}D_R'$)	73	10

5.2.3 Discussion

Ion implantation-induced damage of thick diamond films has been widely investigated as a side effect in studies aimed at the creation of controlled doping [Prawer(95), Prins(03)]. Some studies were focussed on the damage effect itself, in particular monitoring the RHEED pattern [Vavilov(74)]. These authors report the disappearing of the diamond RHEED pattern corresponding to a damage of about 10% vacancies/atom. In the present study, instead, the RHEED pattern disappears corresponding to damage level of 22% vacancies/atom. At comparable damage levels, Vavilov et al. [Vavilov(74)] report of rings ascribable to turbostratic carbon in RHEED and of a pattern due to weakly ordered graphite structures at higher doses. In contrast to this, in the present work no features ascribable to ordered carbon phases are detected by RHEED at higher damage levels. However, the cited work [Vavilov(74)] was carried out on the (111) surface of a natural diamond, which has different properties compared to the here considered (001) surface [Prelas(98)].

The critical damage range resulting from the present experiments is also much higher than the one (≈3% vacancies/atom) which leads to an increase in electrical conductivity as reported by Prawer et al. [Prawer(95)] after implantation at room temperature with different ions. This discrepancy is not suprising, as the effects of doping on electronic properties can be evident already at impurity levels of $\approx 10^{-8}$, while for structure-sensitive methods concentrations in the 10^{-3} or 10^{-2} range are needed. In the present experiments, indeed, an increased background signal due to electrons incoherently scattered by the amorphous carbon accompanies the crystalline diamond features in the RHEED pattern. Even if at this stage the material is partly crystalline, the amount of sp^2 amorphous or graphitic carbon might already induce an appreciable increase in the electrical conductivity.

In the above described electron diffraction investigation of ion-implantation-damaged thick diamond films, a critical damage level, $D_{R,crit}$, was extracted (19-22% vacancies/atom at 0 nm depth), at which the RHEED pattern of diamond disappears. Corresponding to this, an XPD pattern is still present, but with a residual anisotropy value of only 1%. This result has to be compared to the analogous studies on the carbon layer generated by a successful BEN treatment, where the absence of a RHEED pattern corresponds to anisotropy values in XPD of 19%. Two alternative explanations can be considered to understand this discrepancy.

On one hand, it has to be kept in mind that both RHEED and XPD, applied to characterise the BEN layer, probe signals originating from the thin carbon layer as well as from the Ir substrate. While the selection of the C 1s photoelectron signal allows the discrimination of the carbon layer contribution in XPD, in RHEED the decomposition of the patterns due to film and substrate is less straightforward. Due to this difficulty, the early disappearance of the RHEED pattern in the BEN layer, as compared to the artificially damaged bulk diamond, could at least partially be attributed to the more critical visibility of diamond-related RHEED patterns from a 1 nm thickness carbon layer on a single crystal Ir substrate. However, the fact that crystalline diamond is not detectable not only in RHEED but also in

HRTEM, where the separation of Ir- and diamond-related signals is easier, yields a strong argument against this explanation.

The second possible explanation refers to the differences in the defect structure present in both experiments. Defects are generated in both cases by atomic displacements induced by scattering of the incident ions. In the BEN experiments, implantation of these ions also contributes significantly to the effect, while the 30 keV carbon ions used here to damage thick diamond films are stopped outside the range of interest. According to the composition of the gas phase in the CVD reactor, the ion bombardment during BEN also involves an appreciable amount of hydrogen. Finally, the ion implantation was performed at room temperature, while the typical substrate temperature during the BEN treatment is 750-800℃. According to Prins [Prins(92)], interstitial carbon atoms and vacancies start to diffuse at about 300 K and 800 K, respectively, therefore relaxation processes must be highly efficient within the BEN layer during BEN. Based on the present experiments, it can be presumed that there are profound differences between the defective crystalline structures formed by BEN and the statistically distributed defects generated in the keV carbon ion implantation process at room temperature.

Some further insights into these contradictory observations may be gained from HRTEM analysis of the diamond films damaged by ion bombardment. It would be interesting to determine the damage level at which crystalline diamond patterns disappear for this technique as well.

The growth experiments performed on ion-damaged thin epitaxial diamond films show instead that, after inducing a slightly higher damage (≈33% vacancies/atom) than the critical one (≈22% vacancies/atom), the deposited films turn polycrystalline, with only 60% of the grains epitaxially oriented. Higher damage levels induce progressive decrease of epitaxial orientation of the grains. This result shows a good quantitative agreement with the ones reported by Gsell et al., even if conducted on a different system and in different implantation conditions [Gsell(08)]. Additional combined implantation and growth experiments are needed to check the exact dose at which films turn from flat to rough and polycrystalline.

5.3 Finite element (FE) model of elastic strain-driven interactions between diamond islands on Ir(001) during BEN

As shown in Section 5.1, a peculiarity of diamond nucleation on Ir single crystal layers on different substrate systems, with both (001) and (111) orientations, is the formation of the domains, μm-sized areas containing nucleation centres with an average density of $\approx 3 \cdot 10^{11}$ cm^{-2}. Golding, Bednarski and their co-workers [Bednarski(03), Golding(04)] support the idea that such an arrangement of crystallites can be explained as a liquid-like array derived from a carbon condensate created during the BEN process. According to them, the observed array is formed during the nucleation, which begins synchronously with the cessation of the bias current due to thermal quench. However, the idea of a self-organisation process starting at the end of the bias-induced ion bombardment was demonstrated to be rather unlikely according to recent observations that domain pattern formation is a continuous process occuring during BEN [Gsell(07)-1].

At the border of the domains the density of the diamond nuclei abruptly changes by many orders of magnitude within a distance of less than 100 nm. The length scale of variations in the gas phase is approximately given by the mean free path of the particles in the gas phase, which is well above 1 μm in the employed conditions. This implies that the local gas conditions cannot be responsible for the domain formation. This suggests that domain formation is controlled by surface processes. Moreover, a strong interaction between neighbouring grains seems to be the only possibility to explain the formation of the described patterns, better

than independent nucleation events.

Systems composed of heteroepitaxial islands on a lattice mismatched substrate are often efficiently modelled via interaction mechanisms based on elastic strain fields [Christiansen(95)]. In a similar way, in the present section a finite element model is described, aimed at studying this interaction by calculating the elastic energy density of tiny diamond islands on an iridium substrate. The geometry of the system was chosen on the base of experimental results of former studies of BEN and the early stages of growth. The aim of the simulations is to obtain a scenario of elastic interactions between the diamond grains and to discuss their implications on a possible model describing the self-organization of epitaxial diamond grains on iridium during the BEN process and the first few seconds of deposition.

5.3.1 The finite element method

The finite element method (FEM) is a powerful means to predict the behaviour of complex physical systems, by providing a solution of the partial differential equations describing them [Dhatt(12)]. To solve a structural mechanics problem, a three-dimensional continuous system can be subdivided into several basic components with finite size and simple geometries (*finite elements*), interconnected at their nodes. The interaction between the elements is evaluated on the basis of laws describing continuous linear-elastic systems. The response of the original system is considered to be approximated by that of the discrete model constructed by connecting or assembling the collection of all elements.

The FEM has been widely used since the middle of the 20th century both to simulate physical systems, on the basis of models, and to numerically approximate mathematical problems. It is nowadays a precious tool to analyse more or less complex systems whose behaviour cannot be described using analytical functions. The field where the FEM finds nowadays most applications is mechanics of man-made systems (*e.g.* airplanes, vehicles, buildings, electronic elements) where changing environmental conditions may cause stress, deformation and wear. Three-dimensional (3D) FE simulations (FES) have been also applied in the last decades to numerically analyse the structure, the defects and the strained state of heterostructures and stress fields in various film/substrates systems [Michler(99), Christiansen(99)]. Various models have been employed to study the mechanics of few-nm-sized island growth process in strained epitaxial systems [Johnson(97)]. Moreover, the emerging attention towards nanostructured systems led to the extension of the FEM to nanometre-scale systems. The success of the method in the latter case was not obvious due to the continuum assumption inherent to FE modelling. Recent studies [Li(02), Mo(09)] compared the results of experiments and molecular dynamics simulations of nanometre-scale problems with those obtained by FES, concluding that the latter ones can be applied also in these cases, under proper assumptions. Several studies were also successful in modelling the elastic behaviour of CNTs by FES [Liu(05)].

In the present work the commercial software suite ABAQUS [Abaqus] was used for all the stages of the FES, including model generation, analysis and results evaluation and visualization. This software is commonly used for FE calculations of strain developed due to lattice misfit or temperature effects in thin films systems (*e.g.*, [Michler(99), Schreck(00)]).

5.3.2 Assumptions of the model

The basic assumption of the present calculations is that in the first stages of diamond growth on Ir during the BEN treatment is *pseudomorphic*. In this case the interface between diamond and iridium is *coherent*, *i.e.* diamond adopts in-plane the same lattice parameter of the substrate at the interface. This growth regime is possible when the thickness of the growing layer is lower than a critical value, beyond which the misfit strain is so high that

stress relaxation by insertion of misfit dislocations is energetically favourable [vonKänel(95)]. For the misfit between diamond and Ir, the corresponding critical thickness is about 0.5 nm. Thus, as the presented models concern diamond structures generated during BEN and the thickness of the BEN layer is in the range 1-2 nm, this assumption is not unrealistic. However, even for the case of partial relaxation the basic behaviour should not change. The following models are based on a (001)-oriented Ir substrate with its characteristic surface geometry, as most of the available experimental data on BEN refer to this surface.

As in former works (*e.g.* [Christiansen(95)]), the geometric lattice misfit between film and substrate, defined as

$$\frac{\Delta a}{a_D} = \frac{a_{Ir} - a_D}{a_D}$$

with a_D and a_{Ir} the lattice constants of diamond and Ir, respectively, is simulated in the present FE models as a thermoelastic effect. This means that the elastic misfit strain is induced by a corresponding biaxial thermal strain, according to the equation:

$$\epsilon_{th,xx} = \epsilon_{th,yy} = \int_{T_i}^{T_f} (\alpha_D - \alpha_{Ir}) dT \tag{5.1}$$

between initial and final temperatures, in the present case assumed as differing by 1°C. The considered processes take place at the BEN process temperature, approximated as equal to the deposition temperature (DT), which is ≈700°C. In this assumption, T_i = 974 K and T_f = 973 K. The fictitious thermal expansion coefficients are assumed as α_{Ir} = 0.0 K^{-1} and α_D=$\epsilon_{D,DT}$ for the Ir substrate and diamond, respectively. The elastic misfit strain in diamond at deposition temperature $\epsilon_{D,DT}$ is calculated from the lattice parameters at the same temperature, according to the formula:

$$\epsilon_{D,DT} = \frac{\Delta a_{DT}}{a_{D,DT}} \tag{5.2}$$

with a thermal expansion coefficient given by:

$$\alpha(T) = c_0 + c_1 T + c_2 T^2 \tag{5.3}$$

The lattice parameters at room temperature (RT) assumed for diamond and iridium are [Landolt(92)]:

$$a_{D,RT} = 3.567 \text{ Å at } 298 \text{ K}$$
$$a_{Ir,RT} = 3.839 \text{ Å at } 291 \text{ K}$$

With such assumptions, and using the values reported in appendix B for the c_i coefficients for diamond and iridium, to be used in equation 5.3, the results for the lattice constants at deposition temperature are the following:

$$a_{D,DT} = 3.574 \text{ Å}$$
$$a_{Ir,DT} = 3.859 \text{ Å}$$

so that the diamond-iridium geometric misfit at deposition temperature, coincident with the fictitious thermal coefficient α_D assumed for diamond for the present FE calculations, is:

$$f = \epsilon_{D,DT} = \frac{a_{Ir,DT} - a_{D,DT}}{a_{D,DT}} = 0.0797 \text{ K}^{-1} \tag{5.4}$$

For FE calculations diamond and iridium were assumed to have a linear elastic behaviour, even if this is a rough approximation in the case of a misfit strain as high as 8%. This means that the stress tensor $\underline{\sigma}$ is assumed to be related to the elastic strain tensor $\underline{\epsilon}$ via the elasticity

tensor $\underline{\underline{C}}$, according to the equations and via the elasticity coefficients c_{ii} reported in appendix A.

Both the substrate and the film/island have been assigned an intrinsic coordinate reference system, with the axes parallel to the <100> crystallographic directions in the two systems. A tied contact, which generates a permanent bond between two surfaces during the entire analysis, is assumed at the interface between diamond and the substrate. Boundary conditions have been imposed so as to prevent the bending of the substrate and to make the system periodical.

After meshing and running the simulations, values are computed for the following variables:

- the components of the stress tensor at integration points, $\underline{\sigma}$ ($\underline{S}$);
- the strain energy density at integration points, u (SENER);
- the total strain energy in each element, E (ELSE);
- the volume of each element, v (EVOL).

5.3.3 Verification of the FE model for a two-dimensional film

The first step of the calculations was to verify the reliability of the FE model by comparing its output in the case of a system made of a laterally infinite diamond film on top of a much thicker Ir substrate to the analytical solutions. For the simulations concrete assumptions for the specific dimensions have been made. As shown in Section 5.1, a thickness of 1-2 nm has been found in XTEM and XPS analyses for the BEN layer, comparable to what was detected by various other techniques in previous studies. All the studies substantiate the presence of a carbon matrix surrounding the crystalline structures. As such structures were not directly visualised by HRTEM within the BEN layer, no precise assumptions can be made on their extension within the matrix after the BEN process. As a first approximation, a thickness of 1 nm was assigned to the two-dimensional (2D) film in our calculations, as for the islands modelled in the following stages. The Ir substrate was assigned a higher thickness, sufficiently large to make it behave as an infinitely thick substrate.

For the FE calculations the film and the substrate were modelled as solid deformable tetragonal boxes, 20×20×1 nm^3 and 20×20×10 nm^3 in size, respectively. The geometry of the modelled substrate-film assembly is shown in Figure 5.38. The film and the substrate were decomposed into 2000 and 4000 eight-node rectangular elements, respectively. The output value of the in-plane components of the stress tensor of the diamond film calculated via the FES should be in agreement with the analytical formula [Nix(89)]:

$$\sigma_{11} = \sigma_{22} = (c_{11} + c_{12} - \frac{2c_{12}^2}{c_{11}}) \cdot \int_{DT}^{DT+1} (\alpha_D(T) - \alpha_{Ir}(T))dT \qquad (5.5)$$

With the coefficients reported above and in the assumed conditions (Section 5.3.2), $\sigma_{11} = \sigma_{22} = 9.341 \cdot 10^{-2}$ TPa. The analytical calculations predict an out-of-plane component $\sigma_{33} = 0$ and a stress-free substrate.

In Figure 5.39(a) the values of the in-plane component of the stress tensor at integration points, σ_{11}, in the modelled system are plotted in colour scale. The in-plane stress calculated with the FES is tensile and constant in the diamond film, with a value in perfect agreement with the analytical one (equation 5.5):

$$\sigma_{11,FES} = \sigma_{22,FES} = 9.341 \cdot 10^{-2} \text{ TPa}$$

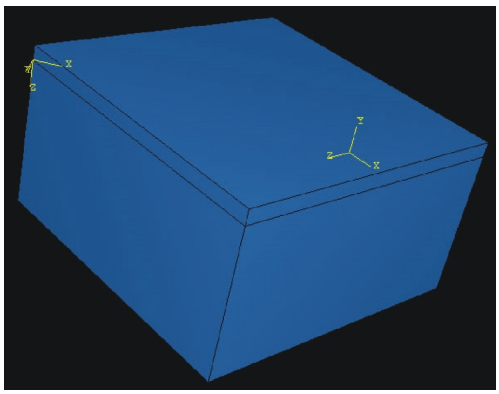

Figure 5.38 – Geometry of the model used for the FES of a pseudomorphic 2D diamond layer on an Ir substrate.

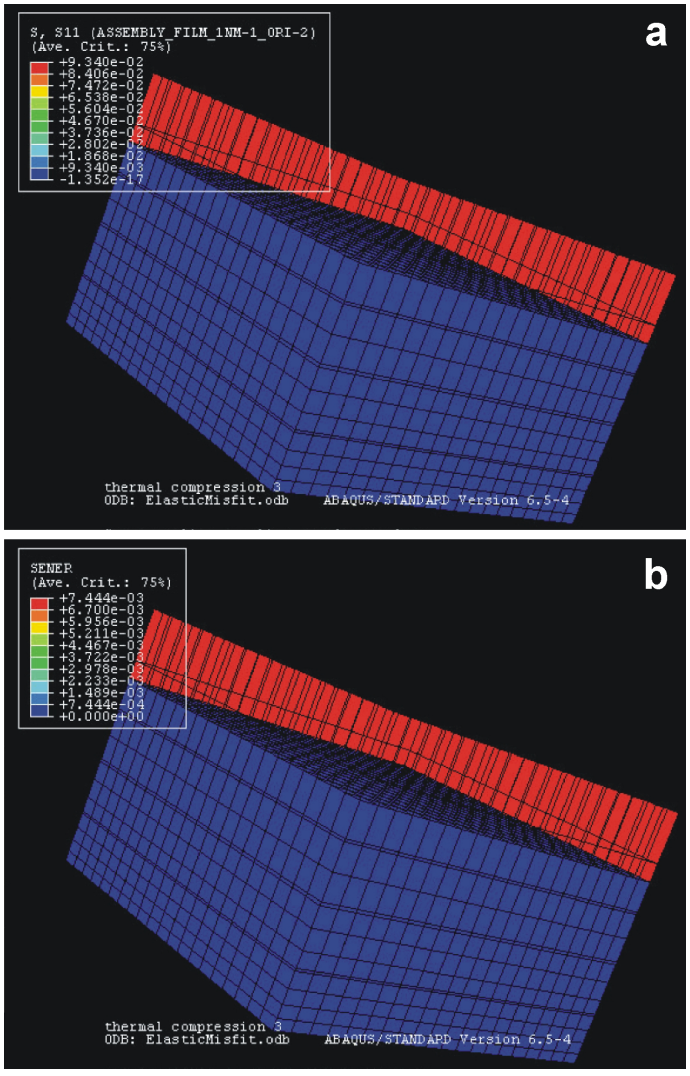

Figure 5.39 – Values of (a) the in-plane stress tensor componenent σ_{11} (S_{11}) and (b) the strain energy density u (SENER) at integration points in the modelled system (the deformation is magnified by a factor of 150 for better visualisation). A colour scale is used for the amplitude of the two parameters.

Moreover, the out-of-plane component σ_{33} and the stress in the substrate are many orders of magnitude lower.

The value of the elastic strain energy density in the film obtained with the respective analytical expression:

$$u = \sigma_{11}\epsilon_{11} = \sigma_{22}\epsilon_{22} = 9.341 \cdot 0.0797 \cdot 10^{-2} = 7.445 \cdot 10^{-3} \mu\text{J}/\mu\text{m}^3$$

is also in agreement with the $7.444{\cdot}10^{-3}$ μJ/μ m^3 calculated as ratio between the total strain energy and the total volume of the diamond film, obtained by the sum of E and of v of all elements, respectively, as given by the FES (Figure 5.39(b)).

As the results obtained for the 2D film perfectly reproduce the analytic results, this model has been assumed as starting point for the calculations concerning more complex 3D geometries of the diamond features.

5.3.4 FE model for regular arrays of islands with the shape of truncated pyramids

In the second set of calculations a regular array of diamond islands on an Ir substrate has been modelled. The islands are assumed as truncated pyramids with {001} base and top facets and {111} side facets. The horizontal edges of the islands are therefore aligned along <110> directions of Ir and diamond. This assumption is based on the most frequently observed shapes by SEM and TEM analyses of the early stages of diamond growth on Ir substrates (see Section 5.1 and ref. [Schreck(03)]). The height of the islands, h, is 1 nm, the same as for the 2D film.

Each island is assumed as a 3D solid deformable shape, 1 nm high, with varying edge size, l (2 nm, 6 nm, 10 nm, 20 nm) and consequently width-to-height ratio, l/h (Figure 5.40(a-b)). Only one quarter of the island was modelled, for symmetry reasons, with two faces perpendicular to the substrate and two forming an angle of 54.74° with the substrate surface (Figure 5.40(c)). The top face is parallel to the substrate surface. The horizontal edges of the island form an angle of 45° with the [100] and [010] directions. The substrate has the same characteristics as in the former model (Section 5.3.3), apart from a variable edge size of the square base, so as to obtain variable distance, d, between the single islands (0 nm, 8 nm, 20 nm, 30 nm).

The values of the in-plane stress tensor, σ_{11}, and the strain energy density, u, calculated at integration points in the modelled system, are shown in Figures 5.41 and 5.42, respectively. The maximum value of σ_{11} in the diamond grain ($1.306{\cdot}10^{-1}$ TPa in the lower corner) is higher than in the case of the 2D film, but the total strain energy density in the island is lower ($2.18{\cdot}10^{-3}\mu\text{J}/\mu\text{m}^3$). This is due to the fact that the strain is partially relaxed in the latter case due to the finite size of the diamond structure. The lowest value of u in the diamond grain is found at the top free corner of the island. The distribution of the strain energy density is analogous to the one of the in-plane stress, having a maximum at the lower corner and a minimum at the free corner. However, the maximum strain at the lower corner is probably an artefact ascribable to the imposed tied contact, which is clearly not completely realistic.

In Figure 5.43 the values of the energy density in the diamond island are plotted as a function of the edge size, l, for different values of the distance between neighbouring islands, d, compared with the 2D film case. The strain energy density in the islands is lower than in the 2D film case even when the substrate is completely covered with grains ($d = 0$ nm). In the modelled system an abrupt decrease in the strain energy density in the islands is registered when d increases from 0 nm to 8 nm, while it stays constant when d in the range 8–30 nm. Moreover, the strain energy density in the diamond island increases with the lateral size for any value of d. In particular, reduction of the lateral size from 20 nm to 2 nm for large

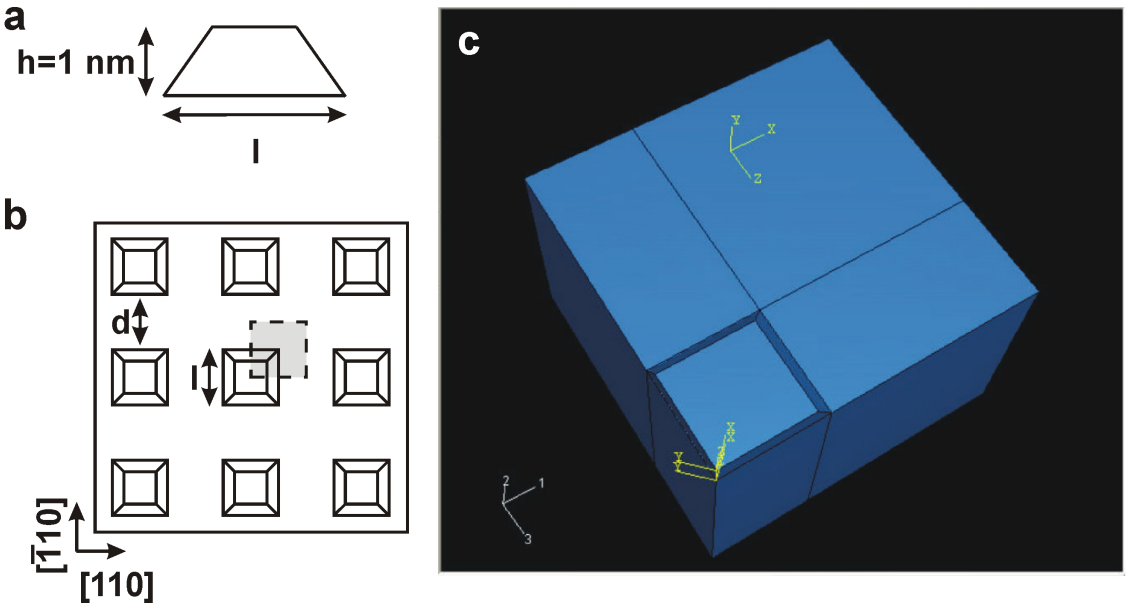

Figure 5.40 – Schematic drawings of (a) cross-section of one truncated pyramidal island and (b) top view of an array of islands, with highlighted in grey the portion considered for the calculation. (c) 3D geometry of the system modelled in the FES, with one quarter of an island on top of a ten times thicker substrate, in the case of edge size $l = 10$ nm and intra-grain distance $d = 20$ nm.

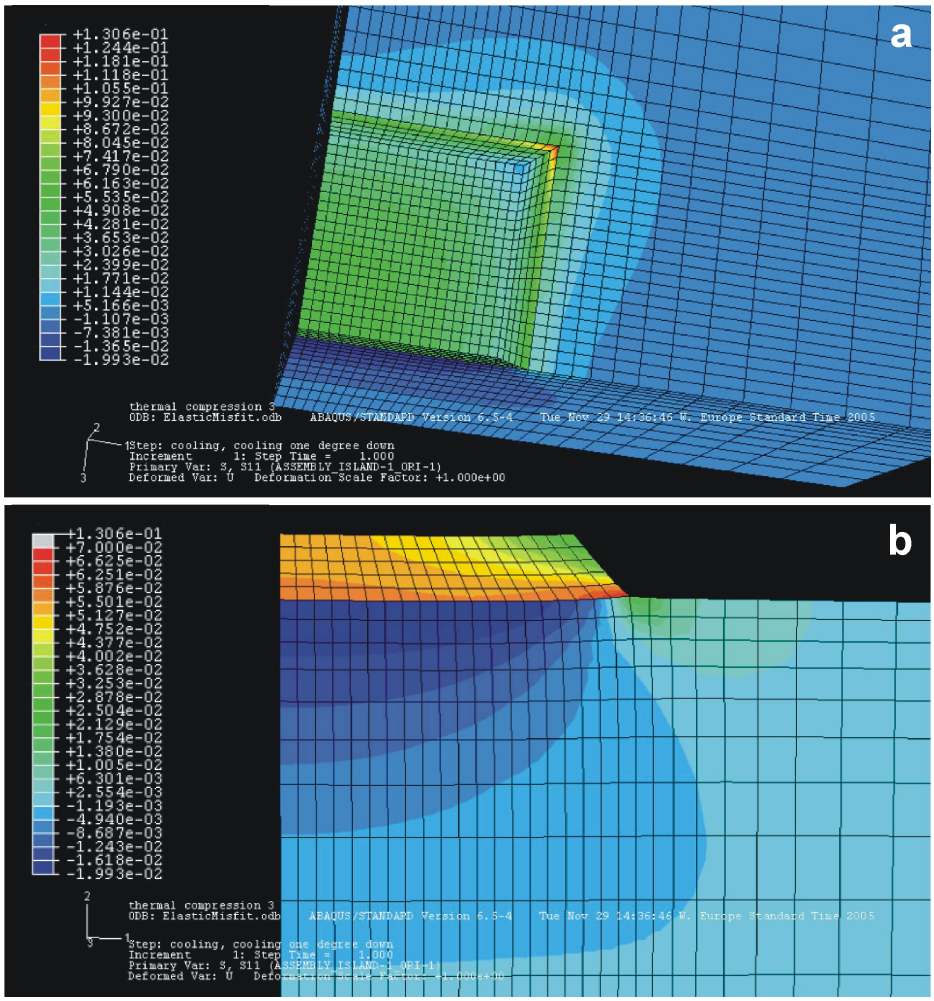

Figure 5.41 – Values of the in-plane stress component σ_{11} (S_{11}) calculated at integration points in the modelled array of single islands viewed (a) from the top and (b) from the side.

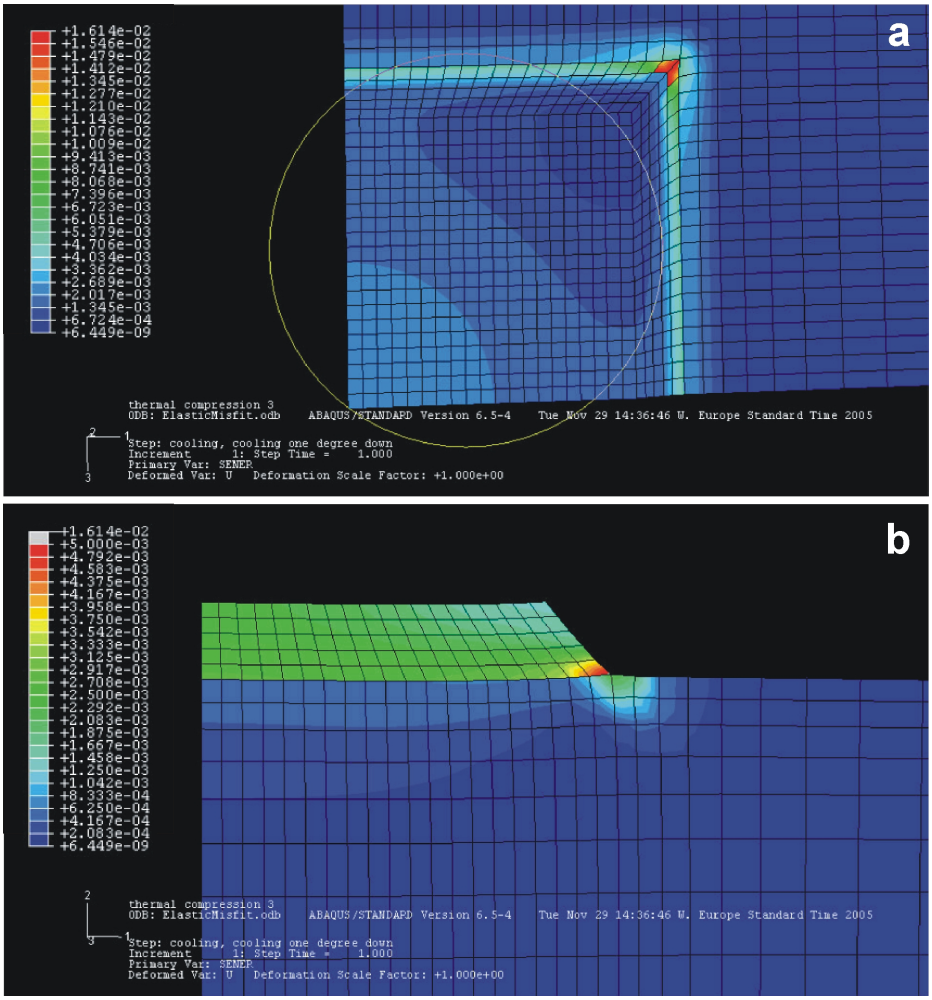

Figure 5.42 – Values of the strain energy density u (SENER) calculated at integration points in the modelled modelled array of single islands viewed (a) from the top and (b) from the side.

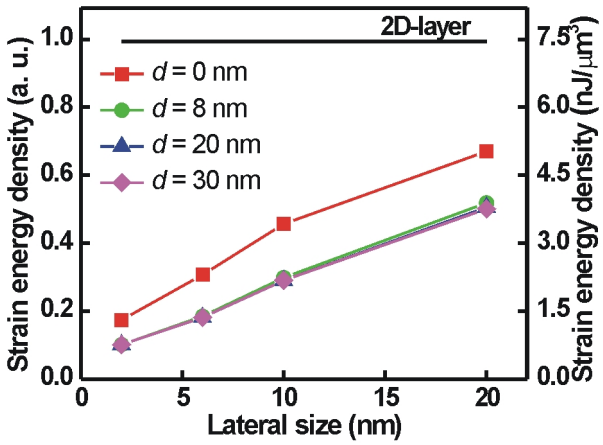

Figure 5.43 – Average strain energy density in a single island as a function of the lateral size of the island for different values of the distance between neighbouring islands, d. The axis on the right side shows the absolute values, while on the left side the values are normalised to the strain energy density in an infinite 2D layer.

distances between the islands (d = 20–30 nm) reduces the normalised strain energy density from 0.5 to 0.1.

The case $d = 0$ nm, corresponding to a substrate completely covered with diamond grains, is particularly interesting. It can be simply deduced from the 2D layer situation by removing wedge-shaped parts of the film. For the wide islands (l = 20 nm) this results in a strain energy reduction by 33% and for the narrow islands (l = 2 nm) by 83%. Finally, it can be observed that for the 2 nm wide islands the normalised energy density decreases from 0.17 to 0.1 when the grains which are initially in contact ($d = 0$ nm) move far away (d = 20–30 nm). It can be underlined that even in the case $d = 0$ nm there is no finite contact area between neighbouring islands. Thus, the observed variation with the distance clearly indicates an interaction between the islands mediated by the underlying iridium substrate.

5.3.5 FE model for regular arrays consisting of pairs of islands

In the second set of calculations a pair of diamond islands, each one with the same geometry as in the former set of simulations, has been modelled (Figure 5.44). The height of the islands was not varied (h = 1 nm) and a fixed edge length of 2 nm was assumed for the base. As there is no experimental report of the grains formed during BEN, this is a reasonable value which could agree with the missing HRTEM and RHEED observations of crystalline diamond structures. Anyway, the exact size of the grains is not fundamental, as the aim of the present simulations is to study the general behaviour. The distance, d, between the two islands of the pair has been varied between 0 nm and 15 nm. In order to simplify the boundary conditions to be applied, a regular arrangement of such systems has been considered. The distance between neighbouring pairs of islands has been kept constant at 20 nm: according to what was found in the simulations of the arrays of single islands, the interaction between diamond grains is negligible for inter-distances higher than 8 nm. For symmetry reasons in this case one half of the two-islands system was modelled.

The strain energy variation within the modelled system is shown in Figure 5.45. In (a) one can clearly see the strain energy concentration at the lower edges of the islands, again with a maximum at the corners. In (b) the extension of the strain fields into the iridium substrate is emphasised. The average strain energy density within one island of the pair, normalised to the value for the 2D film, is plotted in Figure 5.46 versus the distance within

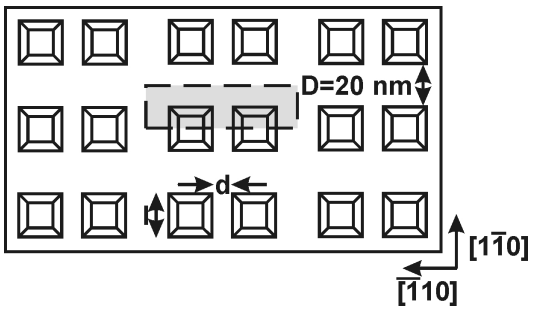

Figure 5.44 – Schematic drawing of the modelled array of pairs of islands, viewed from the top. The shaded area included in the dotted rectangle is the portion modelled for the calculations.

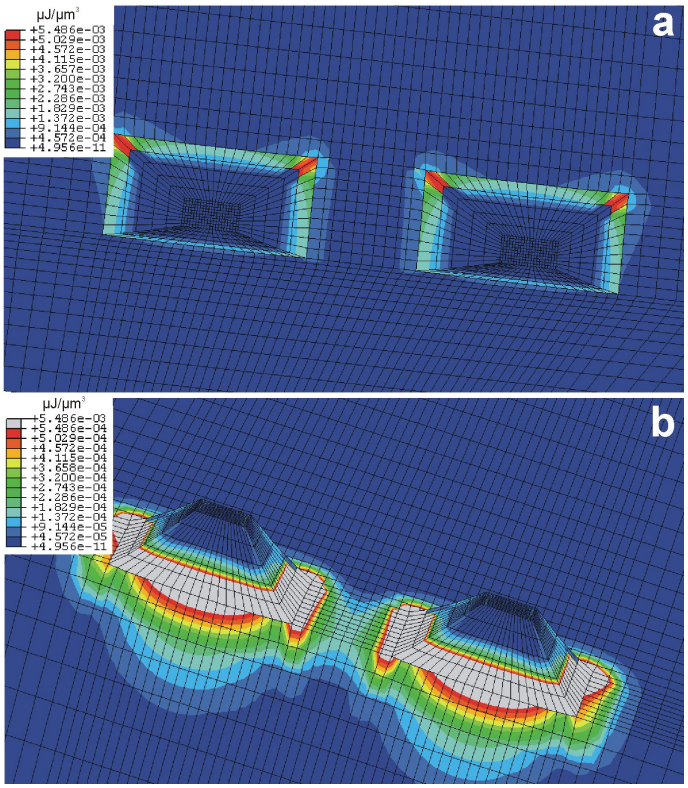

Figure 5.45 – ABAQUS calculation of the strain energy density distribution in the case of a periodic array of pairs of 2 nm wide islands in the case $d = 1$ nm. The intensity scaling has been chosen (a) in the top view to emphasise the strain energy density distribution within the islands and (b) in the side view to highlight the range of lower values in the substrate.

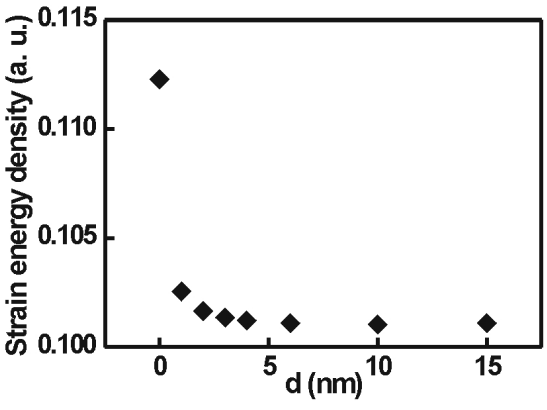

Figure 5.46 – Average strain energy density (normalised to its value in a 2D film) in one island of an array of pairs of 2 nm wide grains as a function of the distance, *d*, between the innermost edges.

the pair. A reduction of this quantity is observed with an increase of *d*. From $d = 0$ nm to $d = 1$ nm the change is significant, levelling off quickly for $d > 3$ nm. The total effect (15 nm compared to 0 nm) of 10% is about 4 times smaller than for the regular array in the first set of simulations, where 4 nearest neighbours are present.

In the case of the pair of islands the strain profile within the individual grain is expected to be no longer symmetric along the interconnecting axis. To check the magnitude of this asymmetry the strain energy density along this axis is plotted for a pair of islands in direct contact (Figure 5.47(a)) and with a distance of 6 nm (Figure 5.47(b)). In the first case the strain energy density at the innermost edge is 50% higher than at the outermost edge. This asymmetry is nearly completely absent when the islands are 6 nm away from each other. The asymmetry ratio between the strain energy density at the inner and the outer edge versus the distance between the innermost edges is plotted in Figure 5.47(c). The asymmetry disappears for $d > 3$ nm, in analogy to the behaviour of the average strain energy density (Figure 5.46).

5.3.6 Discussion

The first important result of these FES concerns the variation of the average strain energy density in the 1-nm-high islands as a function of their lateral size. Splitting of the 2D layer into isolated islands induces an appreciable relaxation of the diamond structures. However, due to the low thickness of the structures, surface energy contributions cannot be neglected. For the 2 nm wide islands in direct contact the reduction in strain energy density is $6.2{\cdot}10^{-3}$ $\mu J/\mu m^3$. At the same time the surface energy contribution (normalized to the volume of the islands) increases by $16{\cdot}10^{-3}$ $\mu J/\mu m^3$, assuming a surface energy density of 6 J/m^2 [Field(79)]. This would overcompensate the strain reduction term and should impede splitting of the islands. To resolve this contradiction one has to consider that the value in ref. [Field(79)] was deduced from cleavage experiments. The surface energy is a function of temperature and can be lowered drastically by reconstruction, hydrogen termination and also by defects [Zhang(94)]. Therefore, an important role of the surface energy *e.g.* in stabilizing the lateral growth cannot be excluded, but it is difficult to quantify its contribution.

Another interesting result of the FES is the variation of the strain energy density in the islands with their inter-distance. For the pair of islands and even more for the array of islands the energy density increases monotonically when the islands come close together. Thus, the elastic interaction should lower the probability of nucleation of new diamond islands in the immediate neighbourhood of already existing islands.

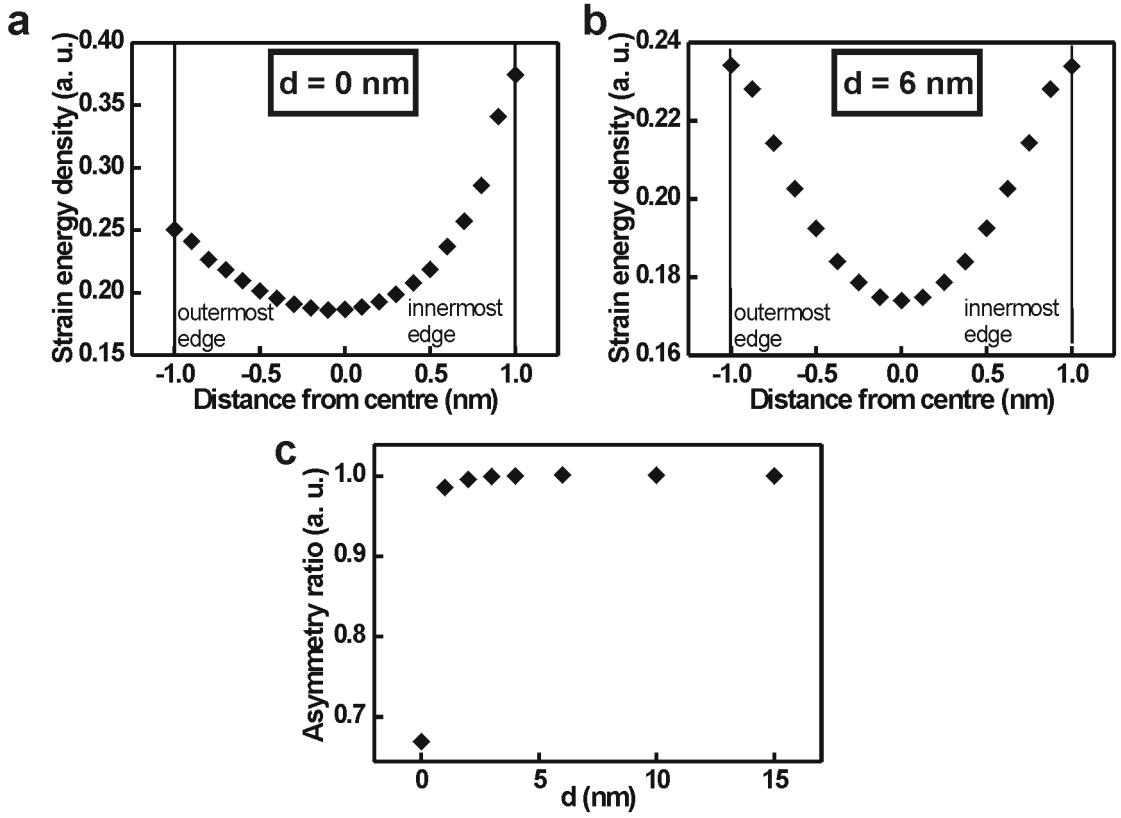

Figure 5.47 – Strain energy density profile within one island in the pair, for (a) $d = 0$ nm and (b) $d = 6$ nm. The profile was taken at the island/substrate interface along the interconnecting line between the centres of the pair. The plot in (c) shows the variation with d of the asymmetry in the strain energy density inside one island of the pair, calculated as the ratio between the value at the outermost edge and the value at the innermost edge.

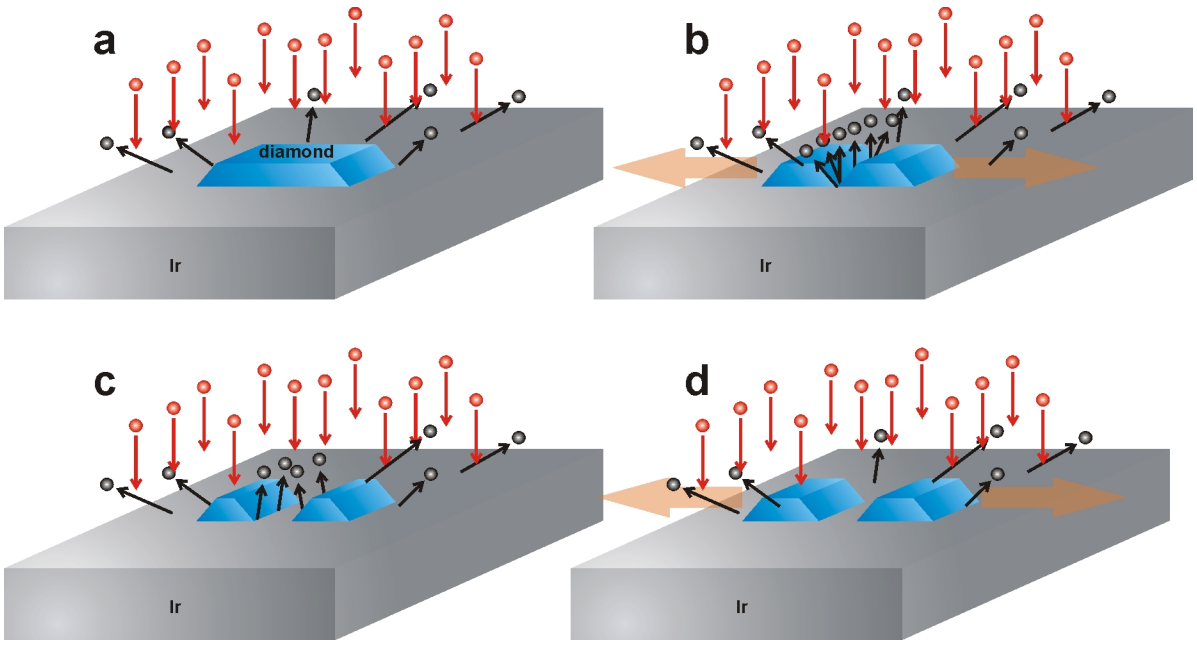

Figure 5.48 – Schematic model representing the elastic strain-driven mechanisms which could take place during the BEN process, according to the results of FE simulations: (a) an extended pseudomorphic diamond layer on Ir is unstable under the strong ion bombardment. (b) Eventually the 2D layer splits into smaller islands, with edges in contact with each other. The higher elastic strain between the islands causes a higher etching probability in this region than in the outer one, leading to (c) a size reduction of the diamond islands in the inner regions. While the higher strain still leads to preferential etching of the islands in the region where they face each other, (d) deposition can take place in the outer regions. According to the proposed model, this series of elastic-strain driven processes leads then to splitting of extended pseudomorphic diamond layers into individual islands and in a "walking away" of the latter ones from each other till they reach a distance corresponding to negligible elastic interaction between neighbouring islands via strain in the iridium substrate.

The results of the FE calculations open a possible scenario of the mechanisms taking place during BEN (Figure 5.48). As mentioned in the introduction of the chapter, under BEN conditions bulk diamond is etched. At the same time tiny crystalline diamond structures are formed, which are initially free to grow laterally, forming extended layers (Figure 5.48(a)). The permanent intense ion bombardment can easily provide defects which act as weak points where the splitting of extended pseudomorphic layers starts. After the splitting the grains are still in immediate neighbourhood (Figure 5.48(b)). But experimentally, at the earliest stage analysed, they are typically found at a distance of $\approx$ 18 nm. The simulations show that the elastic energy density decreases from zero distance up to 3 nm. Due to the strong bond between diamond and iridium it is unlikely that the grains move as complete entities. As reported in former studies [Gsell(07)-1] the carbon layer on iridium under harsh biasing conditions is in a dynamic equilibrium between deposition and etching. The local etching or growth of an existing island will depend on the energy density at that specific point. As shown in the simulation of pairs of islands, there is a pronounced asymmetry between the innermost and the outermost edges when the islands are very close to each other. Due to this asymmetry, etching may dominate at the innermost edge while at the same time growth may be favoured at the outer edge (Figure 5.48(c-d)). As a result, the islands globally "walk away" from each other. Figure 5.47(c) shows that this effect should level off at a distance of few nanometers, *i.e.* further effects could be responsible for the final 18 nm intra-grain distance that has been observed experimentally.

The simulations presented in this section concern very small islands and rather large strain values, *i.e.* conditions for which continuum theory with linear constants of elasticity is close to its limits. However, recent studies have shown that FE modelling can provide reasonable information about the behaviour of nanometer-sized systems [Li(02), Mo(09), Liu(05)]. On the other hand, a 1 nm thickness could be already enough for an epitaxial diamond film on Ir to start to partially release the stress via dislocation formation. However, the aim of the present study was to derive general trends, decay lengths for the strain fields around the islands and length scales for the interaction more than absolute values of the stress fields and of the strain energy densities, which would surely be affected by partial relaxation of the stress.

5.4 Monte Carlo modelling of the formation of two-dimensional patterns of nuclei

A further interesting aspect of BEN of diamond on Ir is the significant variation in morphology of the produced nucleation patterns, under similar experimental conditions. As most of the analyses of BEN and the available experimental data were recorded on Ir(001), the following work addresses this system. While the most common case is the formation of circular domains showing a roughly homogeneous contrast over the whole area (see Figures 5.2(a-b) and 5.49(a)), in some cases the shape of homogeneous domains is anisotropic, showing rather straight edges along low index crystallographic directions (see Figure 5.49(b)). The result of some of the BEN treatments are domains with an apparently fuzzy structure (see Figure 5.49(c)) while with a much lower frequency annular structures are encountered (termed *rings*, and in the extreme case *corrals* in the following). After the BEN treatment, a ring has a structure similar to the one in Figure 5.49(d), where a weak contrast variation can still be observed between the outer annulus and the inner area of each of the coalescing circular domains. The peculiarity of the rings is clearer after a short growth step, when the diamond structures evolving from the BEN-generated features better show the difference between the various areas. In Figure 5.50(a-d) four different areas in a sample grown 15 minutes after BEN are shown. Figure 5.50(a) shows a closed epitaxial diamond area which must have evolved from a homogeneous domain, like the ones in Figure 5.49(a) and (b). The structure

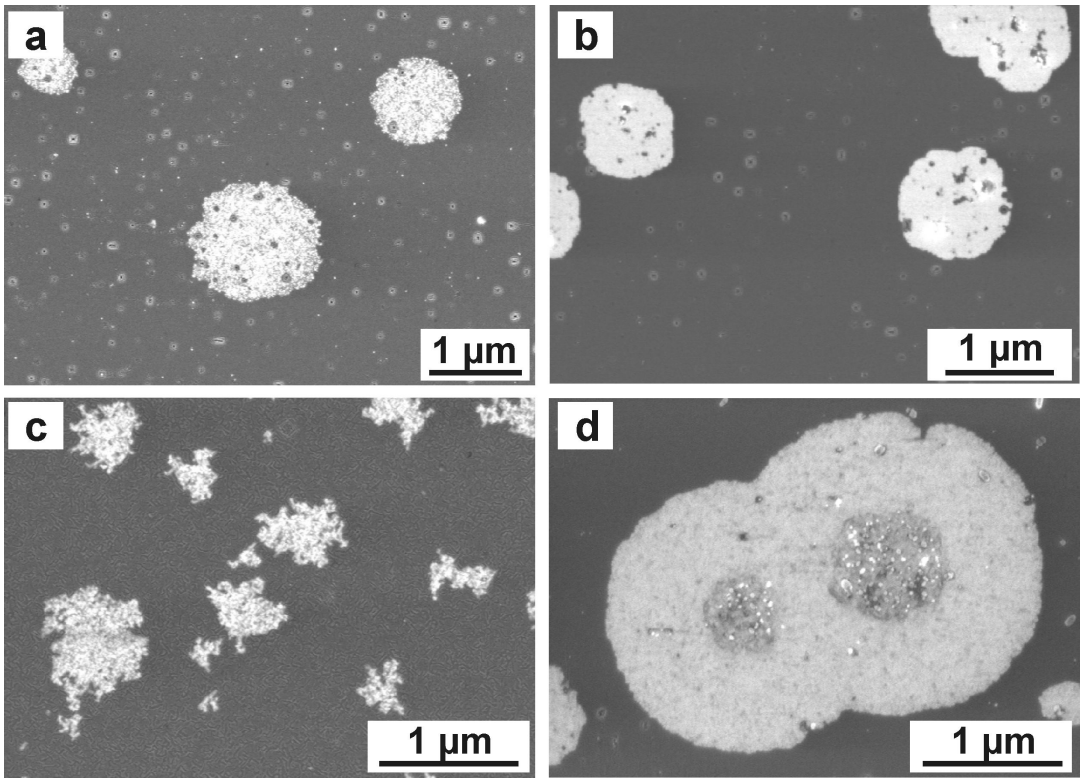

Figure 5.49 – *IL*-SEM images of different nucleation patterns observed after BEN of diamond on Ir(001): (a) circular, (b) rectangular, (c) fuzzy and (d) annular domains. The edges of all the images are aligned along <110> directions of Ir.

in Figure 5.50(b) differs from (a) only for the central area, showing individual epitaxial grains surrounded by a single cyrstal diamond area. The inner highly oriented polycrystalline area is larger in Figure 5.50(c), showing also a lower density of the diamond grains, and in Figure 5.50(d) the epitaxial diamond area is restricted to a thin outer ring (*corral*), while in the inner area diamond grains are growing with a low density. This is more clearly visible in Figure 5.50(e), where an area of image Figure 5.50(d) is shown at a higher magnification. It is essential to underline here that the process conditions for all these samples were similar (see appendix D).

The existence of different shapes of domains can be explained keeping in mind a former study [Gsell(07)-1]. In that work the experimental results distinctly showed that during the same BEN treatment the predominant process taking place can change among different regions of the specimen: while lateral expansion of the domains by means of generation of new nuclei (termed in the following treatment 'lateral spread') can dominate in one area, few millimetres apart etching and erosion of the formerly existing domains can prevail. These significant differences can be attributed to local uncontrollable variations in the experimental conditions (*e.g.* surface temperature, ion accelerating field). The upwards bending of the thin plasma sheath forming over the negatively biased substrate during BEN is a possible explanation for the considerable changes in the conditions at the sample surface in the millimetre range. Such a delicate equilibrium between deposition-lateral spread and etching-erosion can explain the different observed nucleation patterns. The homogeneous domains seem to be formed under conditions of dominating lateral spread, whereas the fuzzy domains indicate an important role of intensive etching. An etching process which is more effective in the central area than at the peripheral areas of domains can explain the different ring structures in Figure 5.50, the strength of which determines the different size of the central eroded area, where no growth of continuous epitaxial diamond is possible any longer.

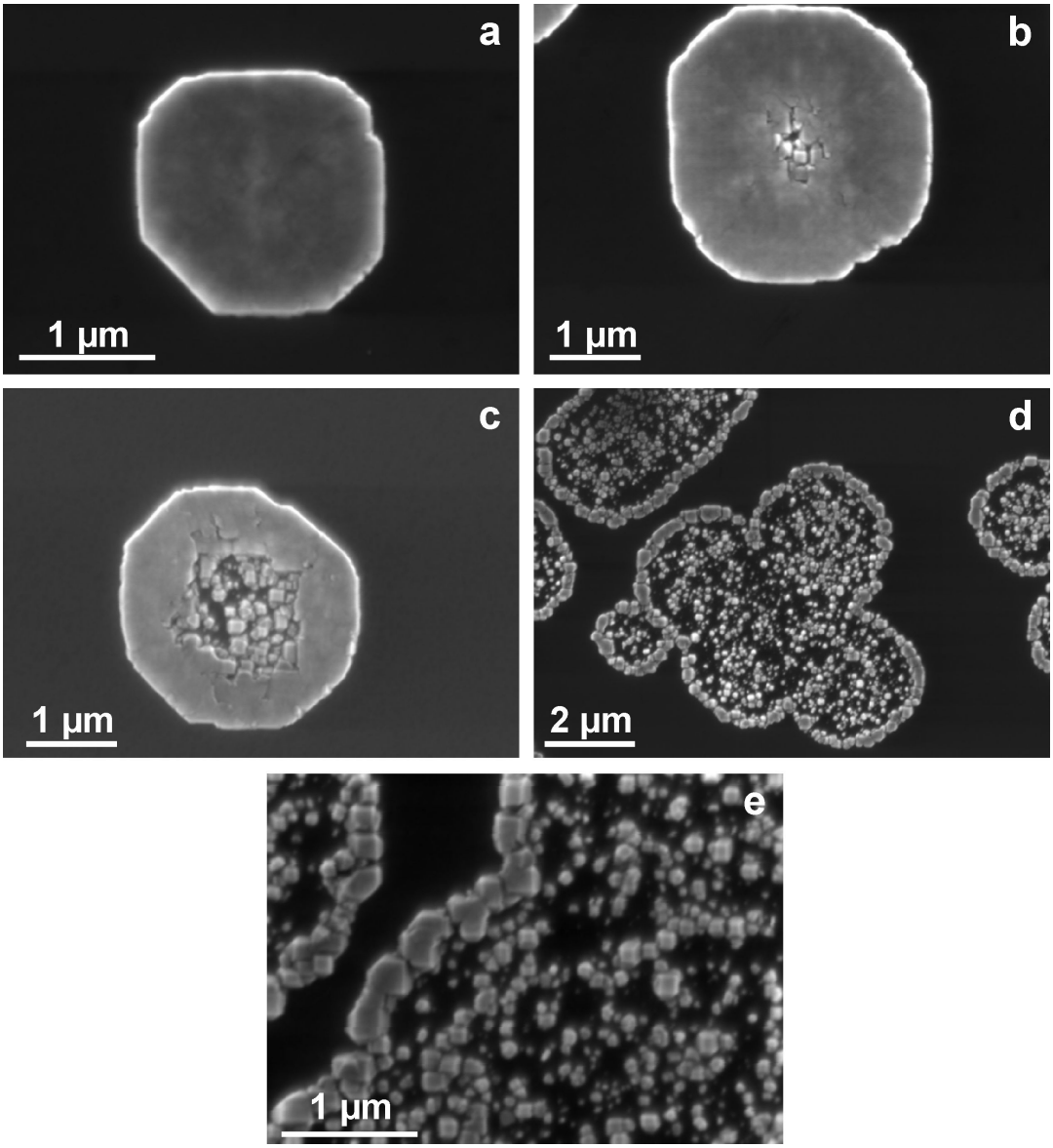

Figure 5.50 – SEM images of a sample showing *rings* and *corrals* after BEN of diamond on Ir(001) and 15 minutes growth. Images (a)-(d) were acquired from different areas of the same sample, while (e) is a high magnification image of an area in (d). The edges of all the images are aligned along <110> directions of Ir.

The aim of the Monte Carlo simulations discussed in the present section was to generate all the different observed patterns with a simple common nucleation model. The basic processes combined in the model are lateral spread, via generation of secondary nuclei, and etching of the existing nuclei. The two mechanisms take place simultaneously and the equilibrium between them, which can be externally changed by varying few basic parameters, determines the final morphology of the nucleation area. According to our idea of the nucleation process, shortly outlined at the end of the former section, the common model has to assume one real nucleation event (the "parent" nucleus), which acts as a seed for the formation of "daughter" nuclei in the neighbourhood, resulting in the formation of a nucleation pattern via lateral spread. A random etching process has to take place simultaneously, able to destroy the nuclei so as to generate a pattern like in Figure 5.49(c). A slightly modified etching process is assumed to explain the formation of the observed *rings* and *corrals*.

5.4.1 Monte Carlo simulations

Monte Carlo (MC) simulations are computer methods based on stochastic models, which can be used to numerically solve complex problems not having exact analytical solutions. The name 'Monte Carlo' was chosen by Metropolis due to the extensive use of random numbers in the calculation [Metropolis(49)]. In the MC method mathematical problems are treated by finding probabilistic analogues which are then solved by stochastic sampling experiments. These sampling experiments, involving the generation of random numbers followed by some arithmetic and logical applications, generate a trajectory in the phase space sampled from a chosen statistical ensemble. The randomness of the generation of numbers mimics the randomness of microscopic phenomena in a real experiment. The computer works as a virtual laboratory, in which a certain system is analysed. Such a computer simulation can be considered as a numerical experiment. Macroscopically observable quantities are influenced by statistical fluctuations, as in a real experiment. The reproducibility of an experiment has therefore a statistical character.

Being deterministic, computers are not able to generate real random numbers. Fortunately, MC simulations are realisable using deterministic *pseudorandom* numbers which are most often generated by a linear congruential generator (LCG) [Park(88)]. Given a number to start with–generally called a *random number seed*– the LCG generates unrelated pseudorandom numbers. The output of random number generators is tested with rigorous statistical tests to ensure that the numbers are random in relation to one another. For multiple trials, different random number seeds must be used.

5.4.2 Program for the simulation of nucleation pattern formation

At the start of the simulation program a two-dimensional matrix of square cells is created. The assumed square symmetry mimics the symmetry of the (001) surface of Ir, where the considered processes take place. In these calculations only the in-plane development of the nucleation patterns is concerned, while the third dimension, perpendicular to the substrate surface, is neglected. This assumption is justified by the negligible thickness of the BEN-deposited carbon layer, lying in the range of 1-2 nm independent of the parameters and of the duration of the treatment, with respect to the dimensions of the nucleation patterns (Section 5.1.1 and refs. [Bauer(02), Schreck(06), Gsell(08), Schreck(09)-1]). As an arbitrary choice, the edges of the matrix are set parallel to <110> directions, so as to be able to directly compare the obtained patterns to the SEM images in Figures 5.49 and 5.50. If each cell is assumed to contain a single diamond nucleus (which evolves into one of the diamond grains seen after a short growth step), the edge length of each cell can be set to 18 nm, the average distance between diamond grains experimentally found in short growth experiments (Section 5.1.1). With this assumption, if we choose a matrix made of 201×201 cells, its lateral

size (≈3.6 μm) is comparable to the average size of the observed domains. Each cell can be in one of two states: *nucleus (N = 1)* or *non-nucleus (N = 0)*. In the following both the "parent" and the "daughters" nuclei will be termed 'nuclei', as they all serve as nuclei for the following epitaxial diamond growth. At the start of the program, a nucleus is created in the central cell of the matrix (N(101,101)=1), while all the others are empty ($N = 0$). With this assumption the central cell acts as the "parent" nucleus. During the simulation run, the cells of the matrix are selected randomly and their state is changed from *0* to *1* or viceversa with different probabilities, as described in detail in the following sections. The flow chart of the simulation program is shown in Figure 5.51 and a scheme of the different involved steps is drawn in Figure 5.52.

Lateral spread

As clarified at the beginning of the present section, lateral spread is meant here as the lateral expansion of the domain by generation of new nuclei in the neighbourhood of already existing nuclei. For the sake of brevity, in the following lateral spread will be referred to simply as nucleation, since it consists in the generation of entities which act as nuclei for the following epitaxial diamond growth. In this program nucleation is a process resulting in the change of the state of a cell from *N = 0* to *N = 1*. The basic assumption, according to the hypothesized nucleation mechanism, is that nucleation takes place with a higher probability in proximity of an already existing nucleus, increasing with the number of surrounding nuclei. Another possibility is that, since the substrate surface is not isotropic, the nucleation process itself proceeds anisotropically along different crystallographic directions. These effects were taken into account to model a simple nucleation process.

At each loop the state of a randomly selected cell, (x, y), is checked. If the cell is empty (*N(x,y) = 0*), a finite nucleation probability, p_N, is calculated. The state of the 8 next-neighbouring cells (with coordinates $(x \pm v, y \pm w)$, with v and w integers in [0,1]) is checked. If all the neighbouring cells are empty, the nucleation probability p_N is zero. If some of them contain nuclei, p_N is determined as follows:

$$p_N(x,y) = \sum_{|v| \neq |w|} S \cdot N(x+v, y+w) + \sum_{|v|=|w|} S \cdot A \cdot N(x+v, y+w) \qquad (5.6)$$

where S and A are adjustable parameters (the *nucleation strength* and the *anisotropy*, respectively). The first term of equation 5.6 adds to p_N the value S for each non-diagonal neighbour in the state *N = 1*, while the second contributes with $S{\cdot}A$ for each diagonal neighbour on *N = 1*. This definition of p_N makes the nucleation more probable with increasing number of nucleated cells in the surroundings. An increase in the value of S implies an increase in the nucleation probability. The parameter A allows for the possibility of generating anisotropic patterns. The values of S and A are set so that, in case all the next neighbours are in the state *N = 1*, p_N is lower than or equal to 1.

After the calculation of p_N, a pseudo-random number $r \in [0,1[$ is generated. If $r \leq p_N$, nucleation takes place. A new loop then starts, and the program runs till the nucleated area reaches at least one edge of the matrix.

Random etching

In case the selected cell contains a nucleus (*N(x,y) = 1*), etching can take place. Etching is a process resulting in the change of the state of a cell from *N = 1* back to *N = 0*. A random etching process can have analogous characteristics as the above-described nucleation process, in terms of influence of the neighbouring area and possible anisotropy, and its strength depends on the calculated etching probability, p_E. As in the case of nucleation, the state of the

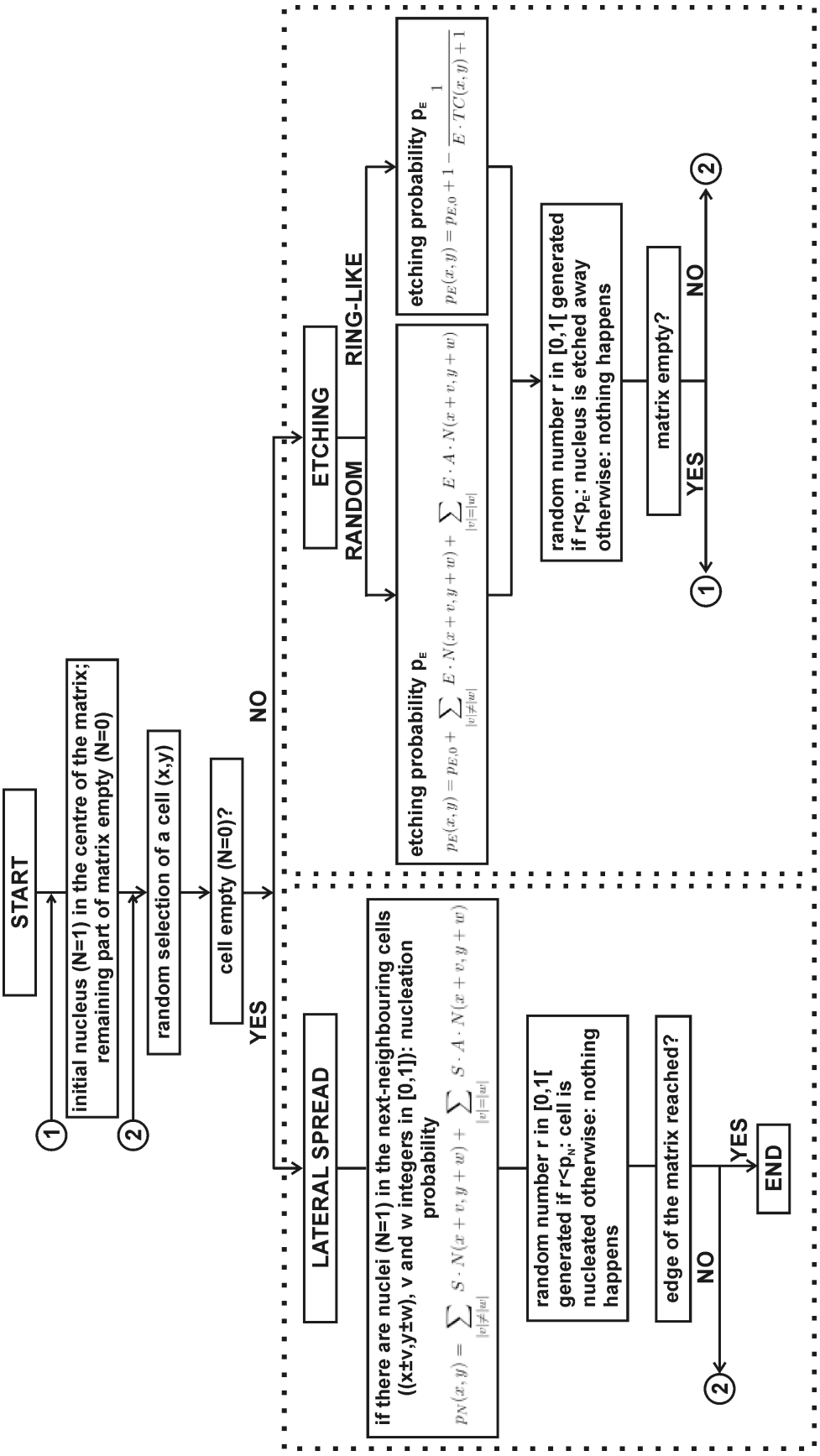

Figure 5.51 – Flow chart of the Monte Carlo simulation program. A detailed description of the parameters is included in the text.

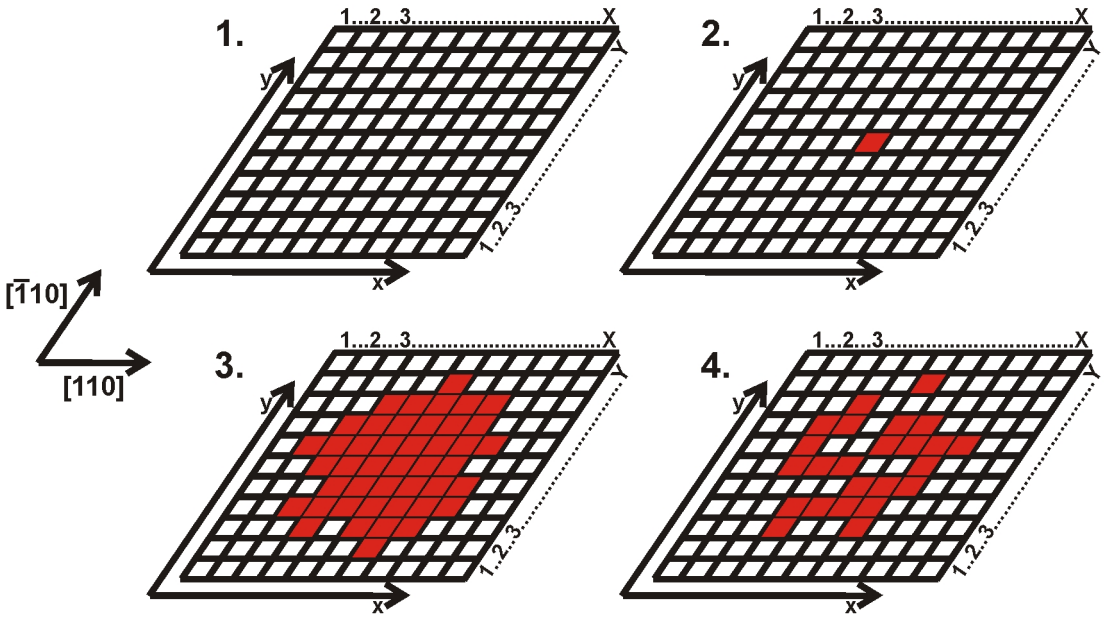

Figure 5.52 – Schematic drawing of the different stages involved in the MC simulations: 1) creation of the matrix; 2) setting of the first nucleus in the centre of the matrix; 3) lateral spread; 4) random etching.

8 next neighbouring cells is checked and p_E is calculated accordingly:

$$p_E(x,y) = p_{E,0} + \sum_{|v|\neq|w|} E \cdot N(x+v, y+w) + \sum_{|v|=|w|} E \cdot A \cdot N(x+v, y+w) \qquad (5.7)$$

where E is an externally set parameter (the *etching strength*) and $p_{E,0}$ is a constant etching probability which can be taken into account. A is the anisotropy parameter defined in the former section. The terms in equation 5.7 have analogous meaning as the ones in equation 5.6. According to this definition of p_E, etching is more probable in an area where the density of nuclei is smaller. The physical idea behind this assumption is that completely isolated nuclei can be more easily attacked and etched. This assumption is justified by the experimental observation of epitaxial grains mostly developing in aggregates rather than isolated. An increase in E implies an increase in the etching probability. As in the case of nucleation, the upper limit to the values of E and A are set so that, in case there are no nuclei in the next-neighbouring cells, the highest value for p_E equals 1.

Analogously to the case of nucleation, after the calculation of p_E, a pseudo-random number $r \in [0,1[$ is generated. If $r \leq p_E$, etching takes place. A new loop can then start, and another cell is selected. Under strong etching conditions (high values of E) it may happen that all the nuclei are etched away. In this case, the program sets again a nucleus in the centre of the matrix (the "parent" nucleus) and the simulation continues.

History-dependent etching

As an alternative to the random etching, an etching mechanism able to reproduce the *rings* and *corrals* was modelled. A higher erosion efficiency in the centre of a nucleated area could explain the observed structures. A mechanism able to reproduce such an effect could depend on the number of times a nucleus in the examined cell has been etched off and afterwards formed again. A physical reason for such a process could be a deterioration of the underlying iridium substrate due to the multiple etching events and to a consequent

decrease in crystalline quality, therefore stability, of the diamond nuclei formed on top of it with increasing number of etching events. A change in the nature of the Ir substrate during BEN could indeed explain the 5 nm deep craters observed in a former study after annealing at 1100°C of a sample showing domains [Gsell(05)]. Any major change due to nucleation in the underlying Ir was instead ruled out in a recent study by AFM analyses of a back-etched BEN layer [Schreck(09)-1]. As the rings have only been observed in very few samples, one can assume that such a deterioration due to multiple etching events may be effective only under particular conditions.

If the history-dependent etching mechanism is predominant, in case the cell contains a nucleus ($N(x,y) = 1$), the etching probability p_E is calculated according to this formula:

$$p_E(x,y) = p_{E,0} + 1 - \frac{1}{E \cdot TC(x,y) + 1} \tag{5.8}$$

where E is the *etching strength* and the constant etching probability $p_{E,0}$ has the same value as chosen for the random etching case, for consistency reasons. *TC(x,y)* is the number of times renucleation has taken place in the selected cell, which coincides with the number of etching events in the same cell plus one. For cells where the number of renucleations is zero (TC=0), $p_E = p_{E,0}$, *i.e.* the etching probability has a fixed value. Instead, for cells where renucleation has occured a large number of times ($TC \rightarrow \infty$), the negative term in equation 5.8 approaches zero and p_E reaches its maximum value. In pratice, for reasonably chosen values of *TC(x,y)*, which are related to the total number of cycles, E can be selected so that the maximum value of p_E is 1.

In analogy to the formerly described processes, the etching event is taking place if a new pseudorandom number $r \in [0,1[$ is lower than p_E.

5.4.3 Results of the Monte Carlo simulations

The program was run choosing different values for the parameters S, A and E and selecting the kind of active etching process (random or history-dependent). Simulations were firstly performed assuming isotropic spread with a constant etching probability of 10% (A=1.0, E=0.0, $p_{E,0}$=0.1) and assuming different values for S up to the maximum (S=1/8). The same value of $p_{E,0}$ was assumed in all the following simulations, since it gives a reasonable agreement with the observed patterns. The results show for all the selected values of S a roughly isotropic final pattern (in Figure 5.53(a) for S=1/8) , similar to the "circular" domains in Figure 5.49(a).

Secondly, anisotropy was included ($A \neq 1$) (Figures 5.53(b-d)). Up to the highest assumed value for the ratio A/S (S=1.25·10^{-5}, A=10^4) no substantial difference in the final pattern from the isotropic case (A=1) was observed. With the highest A/S ratio (Figures 5.53(d)), an artefact is however evident, consisting in an outer area where nuclei are only arranged along diagonal directions, due to a relatively low contribution of the the non-diagonal neighbours to the nucleation probability (equation 5.6). This result is however not realistic and it was indeed never experimentally observed in SEM.

An anisotropic pattern can be obtained only if second next neighbours are considered, which means that the sums in equation 5.6 extend over 24 terms instead of 8. In this case, both assuming anisotropy ($A \neq 1$) or isotropy (A=1), roughly rectangular patterns with edges aligned along <110> directions are obtained (Figures 5.54(a-b)). However, a higher effect of the second order neighbours than the first order ones is unrealistic, therefore being unlikely the reason of the formation of anisotropic domains. The inability of the model to reproduce the anisotropic pattern in Figure 5.49(b) could be explained by attributing the observed anisotropy to features of the underlying Ir substrates rather than to the lateral spread mechanism itself. In many cases terraces with the edges aligned along <110> directions were

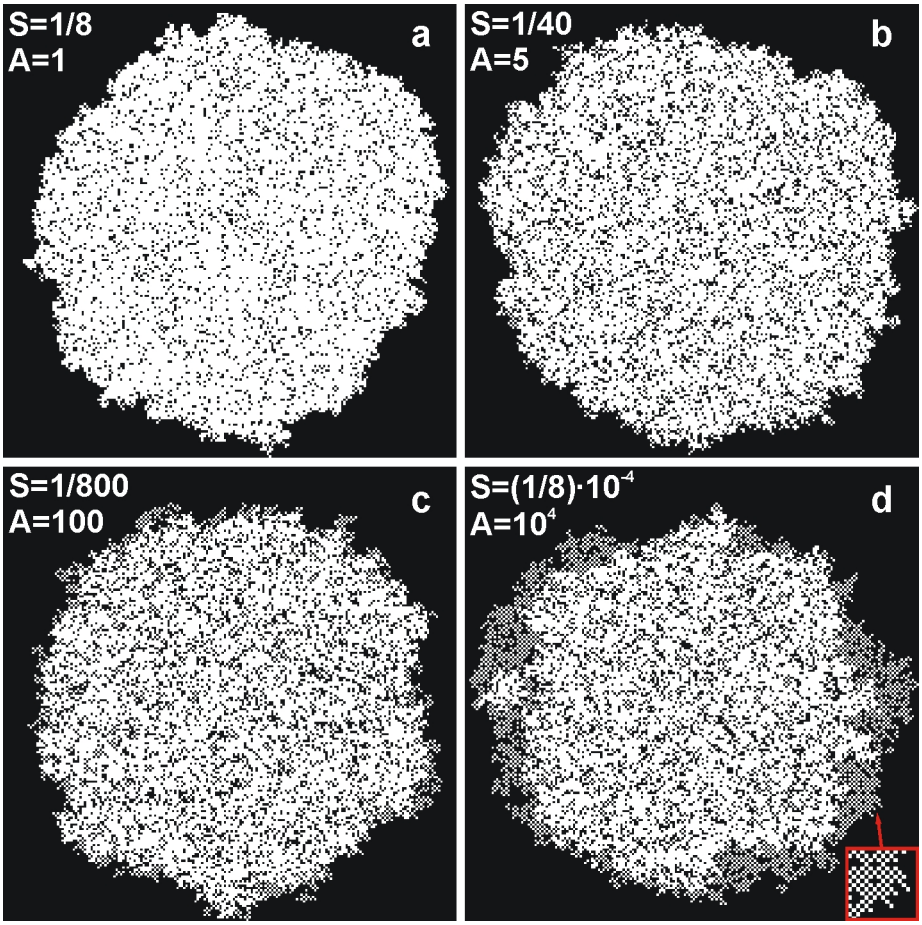

Figure 5.53 – Final patterns obtained via MC simulations for different values (shown in each pattern) of the parameters S and A with a fixed etching probability $p_{E,0}$=0.1 and E=0 (see equations 5.6 and 5.7). In (d) wide peripheral lighter areas are regions where the secondary nuclei are spreading exclusively along the diagonal directions (see inset at bottom right), due to the high value of the anisotropy parameter A.

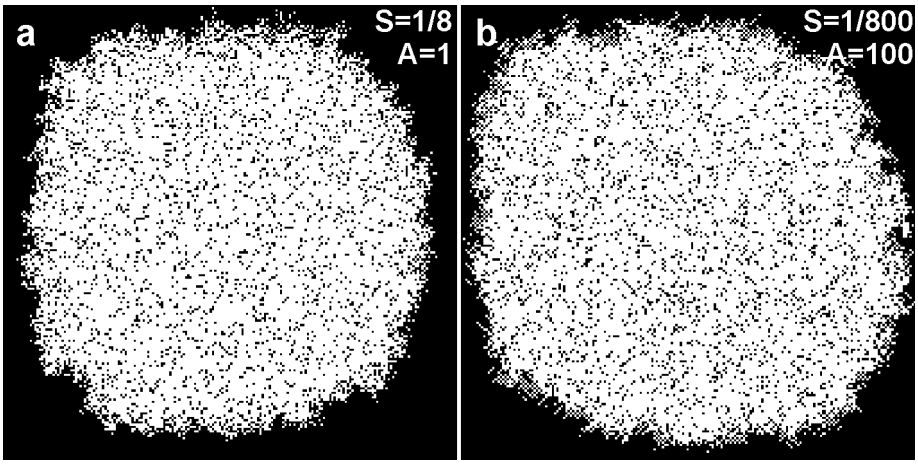

Figure 5.54 – Final patterns obtained via MC simulations considering the influence of both first and second next next neighbours. For these patterns a fixed etching probability is considered (E=0, $p_{E,0}$=0.1) and the values of S and A are indicated in each figure.

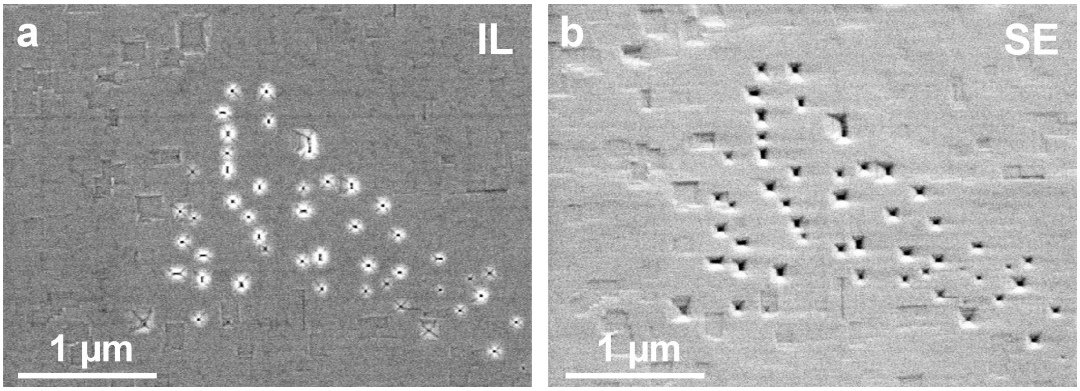

Figure 5.55 – *IL* and corresponding *SE*-SEM images acquired from a sample after BEN on Ir(001), showing pitches and terraces on the Ir substrate. The edges of the image are aligned along <110> directions.

indeed observed on Ir layers both prior to and after the BEN treatment (see Figure 5.55). An adaptation of the nucleation areas to the underlying Ir terrace structures could therefore explain the formation of anisotropic patterns. However, this interpretation of the results stands against previously reported studies, showing that the development of domains is not influenced by the topography of the substrate [Schreck(03)].

In all the following simulations, only the eight first order neighbours are considered, since the assumption of interactions between few nanometres-sized nuclei over distances longer than ≈20 nm does not seem to be realistic. This can be also deduced from the FE calculations presented in the former section, where no eleastic-strain-driven interactions were deduced at distances larger than few nm. At the same time, considering 24 next neighbours does not allow to reproduce the most common circular domains even if assuming isotropy (A=1). Since in the case of 8 next neighbours no anisotropic domains are obtained even with $A\neq1$, the remaining calculation were performed assuming an isotropic mechanism (A=1).

In the following simulations, stronger etching was introduced ($E\neq0$). First of all, random etching was assumed. By increasing the value of E, obvious differences were observed among the final nucleation patterns (see Figure 5.56). Assuming the highest possible value for the etching strength (at values higher than E=0.054, etching was too strong and all the nuclei were etched away), a pattern which covers about 1/4 of the surface of the largest circular pattern is obtained, showing large eroded areas (Figure 5.56(d)), resembling the features in

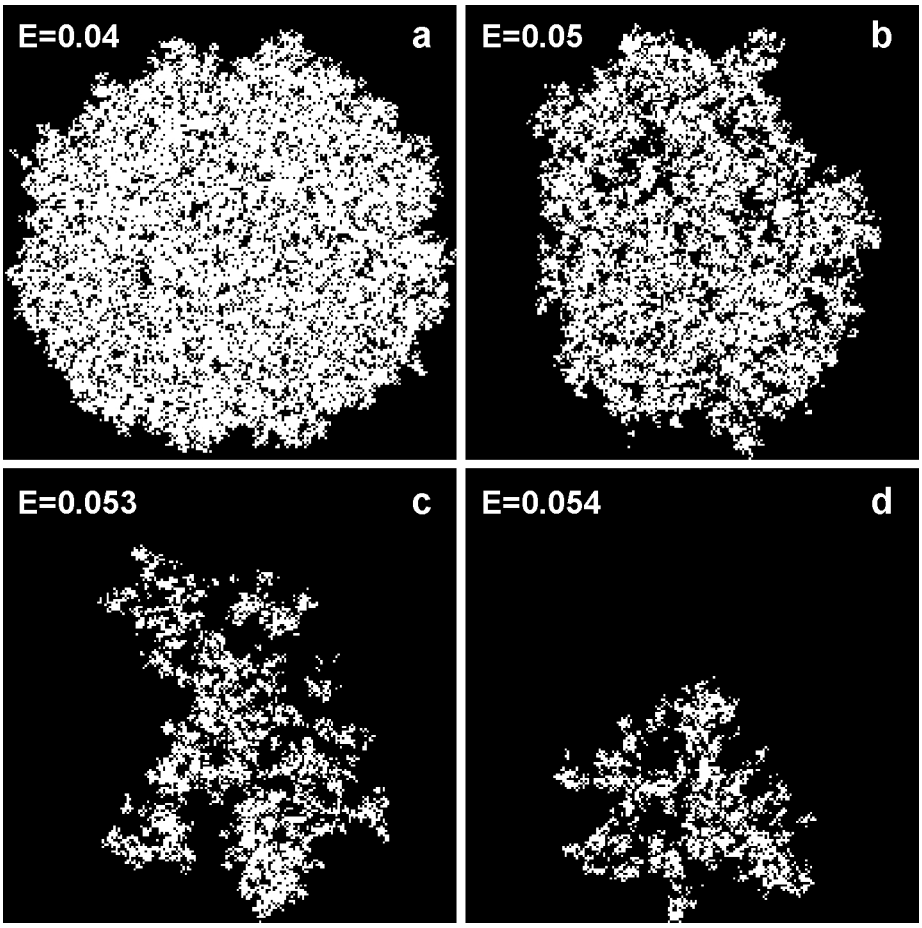

Figure 5.56 – Final patterns obtained via MC simulations in case of random etching. The simulation parameters are S=1/8, A=1 and variable E, indicated in the figure.

Figure 5.49(c).

The final set of simulations was performed assuming an etching probability that depends on the previous history of nucleation/etching at each position in the array. Also in this case an increase in the value of E results in a decrease of the nucleated area, which in this case means an increase in the radius of the inner area without nuclei (see Figure 5.57). Since the highest value of TC is about 20 and the highest assumed value for E is 0.06, the maximum value of p_E, assuming a constant etching probability $p_{E,0}$ of 10%, is 0.65 (equation 5.8).

5.4.4 Discussion

In the present section the structure and the results of a Monte Carlo simulation program have been described. A simple process involving lateral spread via secondary nucleation and etching of existing nuclei has been implemented, able to generate two-dimensional patterns with different shapes, analogous to the domains formed by BEN of diamond on Ir. A variation in few adjustable parameters, determining the relative strength of lateral spread and etching, allowed to reproduce the different patterns observed experimentally. Two different kinds of etching processes were assumed to be able to generate the fuzzy and the annular nucleation structures resulting from some of the BEN treatments. All the experimentally observed patterns were successfully reproduced, apart from the anisotropic domains in Figure 5.49(b), which might instead be explained by anisotropic topographic features of the underlying Ir substrate.

Mostly kinetic MC (KMC) methods have been used to implement simple models for

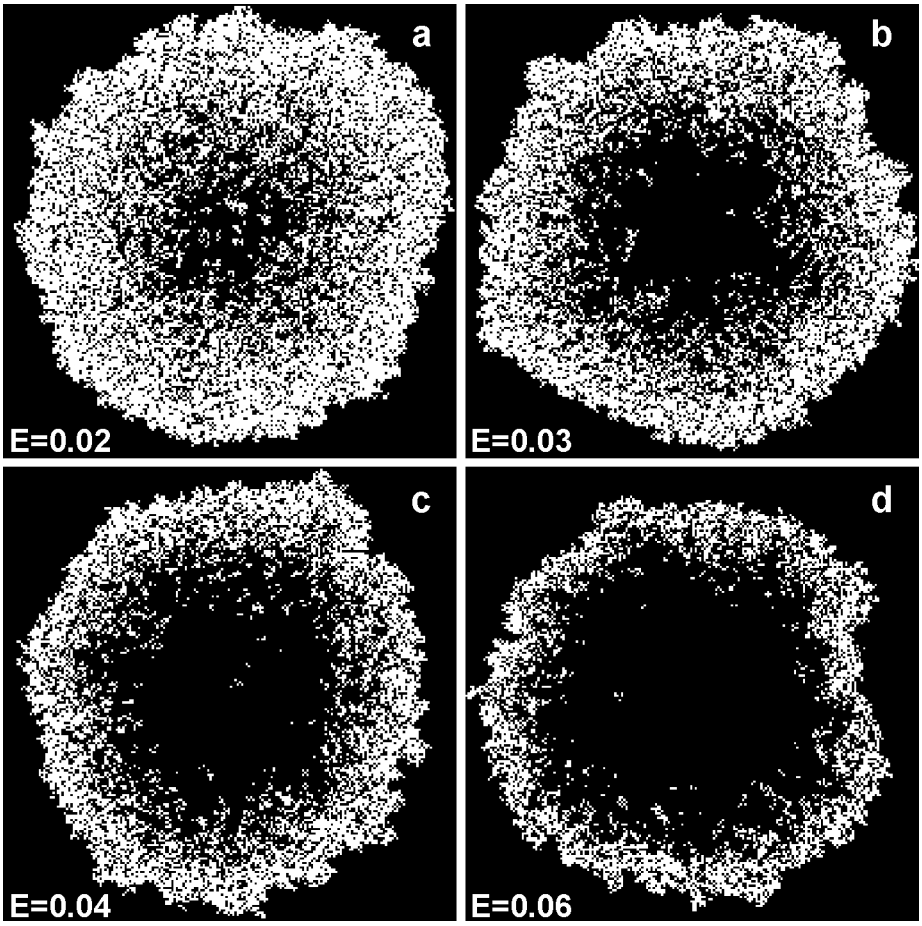

Figure 5.57 – Final patterns obtained via MC simulations in case of etching probability changing with previous etching/renucleation history of each cell. The simulation parameters are S=1/8, A=1 and variable E, shown in each pattern.

two-dimensional pattern formation, *e.g.* to predict island morphology during submonolayer epitaxy [Zhong(01)] or to explain the shape of self-organized metal patterns produced by ion beam etching [Stepanova(05)]. The models proposed in these cases are based on rate equations determining various equilibrium conditions. Different final patterns are obtained based on the values of fundamental physical parameters like diffusion coefficients, which depend on temperature, time constants and activation energies for the different postulated processes. In particular, Zhong et al. [Zhong(01)] propose a model explaining the formation of compact or fractal islands depending on the ratio between diffusion rates of the adatoms along the island edges and the corner-crossing rate. No etching process is taken into account to explain the fuzzy islands. Etching is instead considered relevant in the formation of patterns of pre-deposited metal films on Si substrates during ion-sputtering [Stepanova(05)]. The authors explain the formation of the observed networks based on the equilibrium between etching and coarsening via Ostwald ripening. In this case the equilibrium between the two mechanisms depends on the initial film roughness.

In the present system, the formation of the different types of domains is affected by the local conditions, like precursor density in the plasma, surface temperature, hence surface diffusion, electric field, which controls the energy of the incoming ions. All these parameters are hard to monitor locally. The proposed MC model does not intend to give a precise description, based on physical parameters and exact process rates, of the real system. The implemented model has the simple aim of mimicking the formation of the experimentally observed patterns by the combination of the two basic processes taking place during BEN, *i.e.* secondary nucleation and etching. The results of the simulations demonstrate that a change in the relative strength of the two mechanisms, driven by the change of the relative values of the corresponding parameters, leads to the formation of compact or randomly eroded patterns. A mechanism similar to the etching modelled by Stepanova et al. [Stepanova(05)] must be active in the domain case. A different etching process, dependent on the history of nucleation/etching events at a specific location, is capable to explain the annular patterns, observed less frequently than the former two. This mechanism is based on a damage of the substrate due to multiple nucleation and etching events, which has howeever not been observed in recent AFM analyses [Schreck(09)-1]. Nevertheless, it is possible that in particular conditions this deterioration is prominent.

5.5 Summary and comprehensive model of BEN of diamond on Ir

In the present chapter experimental and simulation works have been presented that were focussed on the understanding of the mechanisms taking place during the BEN treatment on iridium buffer layers. The various analyses and the results of the present chapter are briefly summarised here.

In Section 5.1.1 HRTEM analyses of the layer created by a successful MWPCVD BEN process on Ir/YSZ/Si(001) yield substantially identical results to those obtained on Ir/$SrTiO_3$(001) in previous studies, also identical to the results on the film formed in DC processes on Ir/YSZ/Si(001): the observed material is TEM-amorphous, with a thickness between 1 and 2 nm. This layer shows the same characteristics in HRTEM as the one formed during an unsuccessful BEN process. No diamond pattern is observed in RHEED after successful BEN on Ir/YSZ/Si(001) and on Ir/$SrTiO_3$(001), while XPD shows a clear four-fold pattern for the C 1s signal for both substrate systems. The quantification of the maximum anisotropy in the C 1s signal suggests the existence of a damaged epitaxial diamond matrix around the diamond nuclei, which yields the essential contribution to the XPD signal. Extremely short (5-120 s) growth experiments after BEN on Ir/YSZ/Si(001), show that after only 5 seconds

growth a weak signal of highly oriented diamond appears in RHEED and crystalline diamond structures are found in the early grains in HRTEM. After 10 seconds the TEM-amorphous carbon layer observed after BEN entirely disappears, leaving facetted grains that grow in all three directions with increasing deposition time. Moreover, the analyses of the BEN layer on a sample showing successful nucleation on Ir/YSZ/Si(111) by HRTEM, RHEED and XPD (Section 5.1.2) yield identical results, in terms of presence of the domains, structure and thickness of the BEN layer, to the ones obtained on Ir/YSZ/Si(001) and Ir/$SrTiO_3$(001).

The following Section 5.2 shows how ion-implantation-induced damage into thick heteroepitaxial diamond films can create conditions in which the RHEED coherence is lost, corresponding to an almost completely disappearing single crystal diamond pattern in the C 1s signal in XPD (maximum anisotropy ≈1%). This is substantially different from the results of successful BEN processes, as in that case still a clear XPD pattern is visible (maximum anisotropy ≈19%). This might be due to the different defect structure created by the two types of experiments, probably strongly influenced by the respective process temperatures. The estimation of the preservation of the nuclei for epitaxial diamond growth obtained by XPD analyses on ion-damaged films are in perfect agreement with post-ion-damage growth experiments, finally suggesting the latter ones as the most sensitive probe of the critical damage level for the complete loss of epitaxial orientation due to ion bombardment of diamond layers.

Finite element simulations (Section 5.3) indicate that misfit-strain-driven interactions between diamond islands/nuclei via the Ir layer during the BEN process on Ir(001) could explain a kind of repulsive interaction of neighbouring nuclei. However, the continuum approximation and the assumption of absence of partial relaxation of the stress make these results reliable only qualitatively. In addition to this, a simple process including lateral spread and appropriate etching mechanisms is shown to be able to explain the different shapes of the domains observed after BEN, as verified by Monte Carlo simulations (Section 5.4).

All the summarised results are useful to compose a comprehensive picture of the mechanisms taking place during the BEN treatment on Ir buffer layers, both with (001) and (111) orientations, which can be schematically described in three steps. This is schematised in Figure 5.58.

First of all, the bombardment of the Ir substrate with hydrocarbon ions leads to the formation of an amorphous hydrogenated carbon layer, with a thickness in the range of 1-2 nm (see Figure 5.58(a)). The thickness of this layer is also basically independent of the duration of the BEN process, which suggests that the BEN process is a combination of etching and deposition, in a dynamic equilibrium with each other. The invariable thickness of the layer depends on the particularly harsh conditions, in which thicker structures are not stable. Moreover, this layer has identical thickness to the one verified in the XPS and HRTEM analyses of a sample showing no domains after BEN (Figure 5.7 and [Gsell(08)]). Former X-ray absorption measurements showed that a high fraction of this precursor matrix is sp^2-bonded.

As described in a former work [Lifshitz(02)], under the continuous ion bombardment instabilities inside the sp^2 carbon precursor phase may induce the formation of nanometer-sized sp^3 clusters. Some of these clusters may form tiny crystalline diamond grains, which are stabilised by hydrogen termination of the external bonds (Figure 5.58(b)). The observed epitaxial orientation of such grains -after short deposition steps- suggests that the formation of such tiny diamond nuclei takes place directly at the interface with the Ir substrate. This is the real nucleation event, taking place in the central area of the domain that forms subsequently.

The bombardment of the surface via hydrocarbon ions and some diffusion processes make each tiny nucleus extend laterally, according to the classical nucleation theory, with the only difference that the nucleus does not grow perpendicular to the surface due to the harsh bombardment conditions (Figure 5.58(c)). The following development stages may be governed

by misfit strain-driven interactions, in case of at least partial pseudomorphic growth, as described by FE simulations. At some point the misfit strain makes the resulting pseudomorphic layer so unstable that its splitting into individual grains is energetically favoured over the prolongation of its lateral expansion (Figure 5.58(d) and Figure 5.48(a-b)). At a following stage the continuous ion bombardment leads to a preferential etching of the grains in the contact regions between neighbouring grains and deposition at their opposite sides, as this further reduces the misfit strain (Figure 5.58(e) and Figure 5.48(c-d)). This results in the formation of an array of grains at an equilibrium distance one from the other, surrounded by a damaged diamond phase generated by the destruction of pre-existing diamond grains. This process may extend to the first 5 seconds after switching off the bias voltage, as the presence of residues of amorphous carbon and extended diamond films in HRTEM studies seem to indicate. In some processes or just at some locations on a sample etching strongly competes with lateral growth so that the most frequent circular domains are replaced by fuzzy domains, or by annular domains. In the latter ones the multiple etching events induce such a high damage in the substrate in areas where the grains formed at the early stages of lateral growth that no diamond grains can be re-formed.

After 5 seconds deposition following the termination of the BEN process, crystalline grains appear and the amorphous phase has nearly completely vanished. Five seconds later (10 seconds total deposition time) both the hydrogenated amorphous layer and the defective diamond matrix are etched off, leaving only the epitaxial diamond grains grow not only laterally, but also perpendicular to the surface (Figure 5.58(f)).

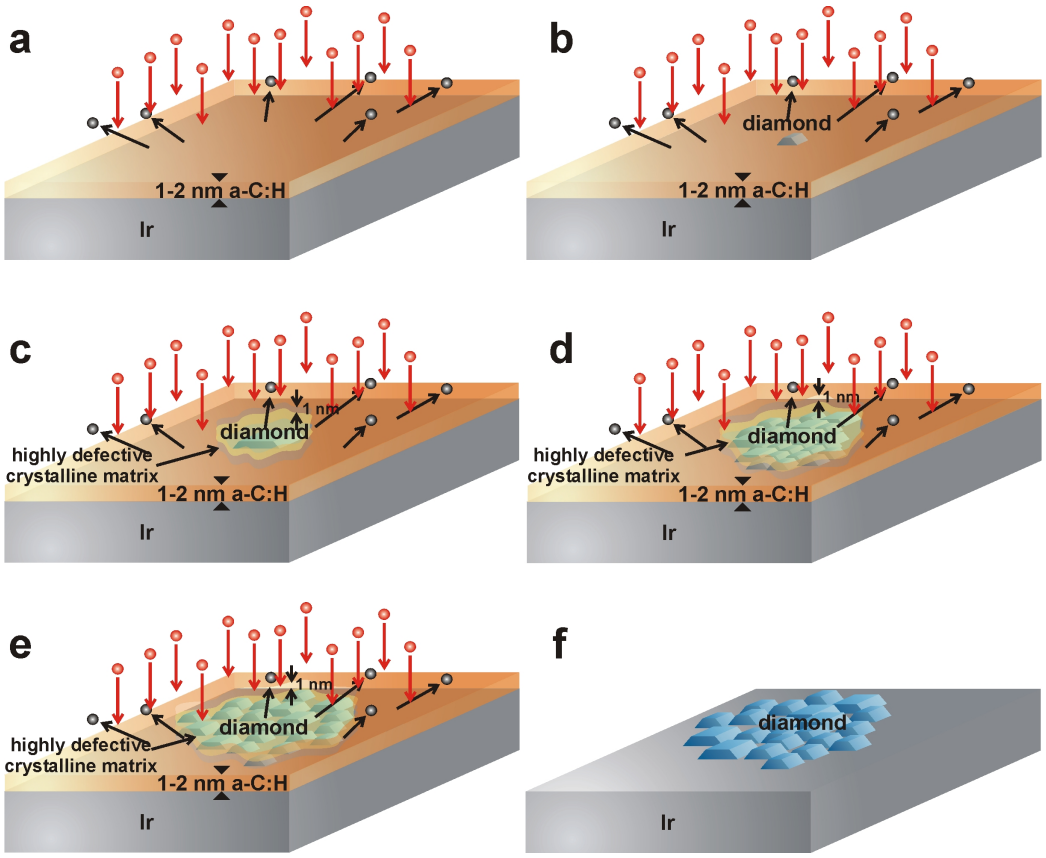

Figure 5.58 – Schematic drawing of the different stages of BEN and growth of diamond on Ir buffer layers, according to the described model: (a) formation of a 1-2 nm thick hydrogenated amorphous carbon precursor matrix; (b) formation of a nanometer-sized epitaxial diamond cluster at the interface with the Ir substrate; (c) lateral growth of the initial nucleus and formation of an extended pseudomorphic diamond film; (d) splitting of the continuous layer into individual grains; (e) formation of an array of isolated diamond grains surrounded by a damaged epitaxial diamond matrix; (f) three-dimensional growth of the structures formed during BEN after switching to deposition conditions.

Summary and conclusions

The present thesis is devoted to the study of the Ir/YSZ/Si epitaxial multilayer as a substrate for the nucleation and growth of diamond films. This system is one of the most promising in view of the technological application of diamond in fields in which large area and high structural quality are required. For this reason, a thorough characterisation and a full control over the quality of the various components are needed to optimize the overall structure. The thesis is composed of two main parts, the first one being related to the structure of epitaxial YSZ buffer layers on Si substrates and the second one to the mechanisms of nucleation of diamond on the chosen multilayer system.

In the first part of this work, the microstructure of epitaxial YSZ films with different crystal phases deposited on Si substrates has been analysed. Diffraction contrast TEM, and in particular two-beam bright field imaging, is able to emphasise the strain contrast due to structural defects such as dislocations and, therefore, to indirectly image them. The application of this imaging mode in cross-section TEM allowed to demonstrate the decrease of the threading dislocation density in the films of cubic YSZ with increasing thickness. An analogous effect was observed after high temperature annealing treatments. In addition to this qualitative result, a quantitative estimation of the dislocation density could be deduced by direct visualisation, in good agreement with former XRD studies performed on the same systems. On one hand, these results confirm former TEM studies on the evolution of dislocations in complex oxide systems upon high temperature treatments, indicating a promising pathway to improve the structural quality of this type of films. On the other hand, the complementarity of TEM and XRD in the analysis of these effects and their equivalence in terms of quantitative analyses, even if with rather different volume averaging characteristics, are clearly demonstrated here.

Due to the less symmetric crystal structure, epitaxial films of tetragonal YSZ on Si substrates contain different texture components, characterised by the longer axis (the *c*-axis) of the structure lying parallel or perpendicular to the substrate surface. The combination of TEM imaging and electron diffraction analyses allowed here to identify the different variants as specific features in the films. The evolution of the multi-component structure of the films with increasing thickness and/or with high temperature treatments was monitored. In contrast to previous literature reports, a higher volume fraction of the material exhibits the *c*-axis oriented perpendicular to the substrate surface after deposition. With high temperature annealing treatments, a distribution closer to the statistical one, but still with the *c*-oriented component dominating over the remaining two, was observed. Moreover, in sharp contrast to former reports, no twinning relationship among the various texture components was found for these films. This means that for all orientational variants the three axes of the tetragonal cells are parallel to the base vectors of the Si substrate. This behaviour in particular makes these films more suitable for the deposition of additional epitaxial layers.

In the second part of this work experimental and simulation studies have been carried out in order to derive a comprehensive picture of the mechanisms of BEN of diamond on Ir buffer layers. This process is fundamentally different from the analogous process on the more common Si and 3C-SiC substrates. In view of the exceptional epitaxial orientation obtained since the early stages of diamond growth, the mechanisms taking place during BEN on Ir need

to be thoroughly clarified. For the first time, BEN has been performed in this work on the Ir/YSZ/Si system that is, as already mentioned, the most interesting from the technological application point of view. On both (001)- and (111)-oriented Ir surfaces, substantial analogies have been observed as for epitaxial Ir films on other substrate systems ($Ir/SrTiO_3$, Ir/Al_2O_3, Ir/MgO): the product of BEN is an extremely thin (1-2 nm thick) carbonaceous film in which diamond features are extremely tricky to detect. The nuclei for the diamond epitaxial growth are created within localised areas, the domains, and they are too small and defective to generate coherent signals in HRTEM and RHEED. XPD instead can identify a successful BEN treatment, being able to detect a clear pattern ascribable to diamond for the C 1s signal in case the epitaxial nuclei are formed.

Extremely short growth steps after BEN were applied in this work with the aim of identifying the earliest appearance of diamond features in HRTEM and RHEED. Both techniques, indeed, start to detect crystalline diamond features after only 5 s growth following the interruption of the BEN treatment. In particular, this stage is very interesting as a transition step between BEN and growth: a mixture of individual diamond grains, extended epitaxial diamond layers and residues of the TEM-amorphous film created during BEN are found. In contrast, after 5 s further growth (10 s total growth time) only individual grains (8 nm wide) are found on top of the Ir substrate. The following evolution of crystalline diamond features, with increasing growth time (from 5 s to 2 min), allows to extrapolate the distribution of diamond nuclei corresponding to the termination of the BEN treatment (0 s growth): these should be 1.6 nm thick grains about 20 nm apart. Moreover, the lateral size extrapolated for the diamond grains at the end of the BEN process would be few nm. In addition to this, the quantitative analysis of the XPD C 1s patterns would suggest the presence of 9 nm wide diamond grains at the end of the BEN treatment. However, structurally perfect diamond grains with these dimensions would be clearly visible both in HRTEM images and in RHEED patterns. These results suggest that XPD patterns are not only generated by structurally perfect single crystalline grains (acting as nuclei for the following epitaxial growth). A substantial contribution may come from a diamond matrix characterised by a highly defective nature, which is not visible by HRTEM and RHEED and which is etched off to a large extent during the first seconds of the deposition process.

Attempts were made to generate artificially the damaged diamond phase produced by the BEN procedure on the Ir surface by implantation of a bulk diamond layer with high energy C^+ ions. At certain damage conditions, the RHEED pattern of diamond was lost, and a feeble XPD pattern was still observed for the C 1s signal. This result is qualitatively similar to the one obtained after a successful BEN treatment. However, the weakness of the XPD pattern indicates a higher disorder in the ion-implanted films than in the product of successful BEN processes. This is also confirmed by post-implantation growth experiments on thin diamond films, demonstrating the loss of the majority of epitaxial grains corresponding to the same damage conditions. These results overall suggest that there are profound differences between the defective crystalline structures formed by the incident ions during BEN at high temperature and the statistically distributed defects generated in the keV carbon ion implantation process at room temperature.

One additional peculiar aspect of BEN on Ir surfaces is represented by the spatial arrangement of the early epitaxial diamond grains, hence of the former nuclei. These are found within the domains, μm-sized patterns which are often observed as isolated regions on the Ir substrates. At the domain edges, a sharply defined boundary between nucleated and empty regions is found. Such a spatial distribution of epitaxial features within size-limited regions is hard to explain by assuming simultaneous formation of epitaxial grains, *e.g.* by condensation following switching off the bias voltage, as it was proposed in literature. It can also be ruled out that the nuclei are generated in independent events.

According to our model a single, or few, real nucleation events take place inside each

domain. Under the harsh ion bombardment during BEN, growth prependicular to the surface is hindered. However, this restriction does not apply to lateral growth. Thus, the latter is the basic mechanism giving rise to the unique pattern formation observed exclusively for diamond nucleation on Ir.

Only in one sample extended crystalline diamond regions have been found after 5 s growth. In all other samples, especially after longer growth steps, the diamond islands were observed isolated, at a typical distance of about 20 nm. As a consequence, lateral growth has to be combined with mechanisms that cause splitting into individual islands and the ordering of the islands. This ordering can be attributed to repulsive interactions between neighbouring grains via strain in the substrate, the strength of which was estimated here by finite element simulations. The outcome of the simulations qualitatively indicates that a film split into individual grains would be indeed characterised by a lower strain energy with respect to a 2D layer. This could explain the tendency of an initially extended pseudo-2D layer to split into smaller grains, under the ion-bombardment taking place during BEN. An even lower strain energy configuration is represented by grains that are few nanometers apart. These results would globally support the misfit-strain driven interaction among diamond islands on Ir as responsible of the observed arrays of early grains within the domains.

In addition to this, BEN experiments on Ir show a variety of shapes for the domains, ranging from circular to straight-edge ones, to fuzzy and annular shapes. These different morphologies are obtained under 'macroscopically' identical conditions, suggesting the fundamental influence of locally variable conditions. A simple generic Monte Carlo model assuming only two basic competing processes, *i.e.* the lateral spread of existing diamond nuclei and their back-etching, has been shown here to reproduce the observed variety. The simulations have shown that the competition between these two counteracting processes can nicely reproduce the patterns that have been observed experimentally. Further work will be done in order to describe the underlying processes on an atomistic level.

The peculiarities of BEN of diamond on Ir, *i.e.* the tiny amount of generated materal, the exceptional degree of epitaxial alignment since the very beginning of the growth process, the regular arrangement of nuclei and their localisation within well-defined areas, suggest that diamond nucleation on Ir will remain a scientifically challenging topic in the future. In spite of an extensive search for alternative materials that could also act as template for the heteroepitaxial deposition of diamond, Ir is indeed still the only single crystalline material that combines excellent epitaxial alignment with the potential for upscaling to wafer size dimensions. The resulting high technological potential should therefore guarantee that the interest in the described layer structure will rather increase than decrease in the near future.

Appendix A: Elastic strain tensor and elasticity coefficients

In case of linear elastic behaviour, the stress tensor $\underline{\sigma}$ is related to the elastic strain tensor $\underline{\epsilon}$ via the following relationship:

$$\underline{\sigma} = \underline{\underline{C}} \cdot \underline{\epsilon} \tag{5.9}$$

For cubic crystal systems, the elasticity tensor $\underline{\underline{C}}$ has only three independent components, due to the symmetry of the lattice. Therefore the equation 5.9 can be re-written as:

$$\begin{pmatrix} \sigma_{11} \\ \sigma_{22} \\ \sigma_{33} \\ \sigma_{23} \\ \sigma_{13} \\ \sigma_{12} \end{pmatrix} = \begin{pmatrix} c_{11} & c_{12} & c_{12} & 0 & 0 & 0 \\ c_{12} & c_{11} & c_{12} & 0 & 0 & 0 \\ c_{12} & c_{12} & c_{11} & 0 & 0 & 0 \\ 0 & 0 & 0 & c_{44} & 0 & 0 \\ 0 & 0 & 0 & 0 & c_{44} & 0 \\ 0 & 0 & 0 & 0 & 0 & c_{44} \end{pmatrix} \cdot \begin{pmatrix} \epsilon_{11} \\ \epsilon_{22} \\ \epsilon_{33} \\ 2\epsilon_{23} \\ 2\epsilon_{13} \\ 2\epsilon_{12} \end{pmatrix}$$

The values for the coefficients c_{ii} in the case of the materials of interest are reported below:

Table 5.4 – Elements of the elasticity tensor $\underline{\underline{C}}$ for YSZ, iridium and diamond.

	c_{11} (GPa)	c_{12} (GPa)	c_{44} (GPa)
YSZ, cubic [Landolt(79)]	449	55	65
Iridium [Brandes(92)]	580	242	256
Diamond [vonKänel(97)]	1076	125	577

Appendix B: Thermal expansion coefficients

Table 5.5 – Parameters giving the temperature dependence of thermal expansion coefficients for silicon, cubic YSZ, iridium and diamond.

	c_0 (K^{-1})	c_1 (K^{-2})	c_2 (K^{-3})
Silicon [Touloukian(77)]	$1.887 \cdot 10^{-6}$	$3.868 \cdot 10^{-9}$	$-1.36 \cdot 10^{-12}$
YSZ, cubic [Fork(90)]	$11.4 \cdot 10^{-6}$		
Iridium [Touloukian(77)]	$3.776 \cdot 10^{-6}$	$8.847 \cdot 10^{-9}$	$-4.230 \cdot 10^{-12}$
Diamond [Touloukian(77)]	$-5.911 \cdot 10^{-7}$	$6.640 \cdot 10^{-9}$	$-1.663 \cdot 10^{-12}$

Appendix C: Tetragonal YSZ films on Si(001): lattice parameters

Table 5.6 – List of tetragonal YSZ films analysed by TEM in Section 4.2.1, with indication of the film thickness and the values of the lattice parameters a and c extracted from SAED patterns, compared to the ones obtained by XRD ϑ-2ϑ– scans (ref. [Gsell(07)-2]). All these samples were deposited by PLD using a tetragonal YSZ target (5.1 mol.% $YO_{1.5}$) on Si(001) substrates as described in Section 3.1. Some of the samples (ann.) were annealed in air for 16 h at 1200℃ after deposition. XRD data are not available (NA) for the sample YSZ062, while for the as-grown films the SAED pattern showed only one lattice parameter (a), due to the preferential c-orientation of the material in the film. The individual values of a and c determined by SAED are reliable, with an error <1%, only for sample YSZ15, for which the SAED pattern included Si-related spots. For the remaining samples an internal calibration is not possible, therefore they are possibly affected by systematic error, due to *e.g.* electron energy drift. However, the c/a ratio, not affected by calibration errors, indicates the lack of appreciable strain effects in the films.

	Thickness (nm)	**a** (Å)		**c** (Å)		**c/a**	
		XRD	TEM	XRD	TEM	XRD	TEM
YSZ15	30-40	5.111	5.11	5.163	–	1.010	–
YSZ15 ann.	30-40	5.087	4.95	5.157	5.02	1.014	1.014
YSZ229	100	5.15	4.97	5.171	–	1.004	–
YSZ229 ann.	100	5.101	4.96	5.175	5.04	1.015	1.016
YSZ229 ann. + 50 nm	150	5.099	4.95	5.173	5.01	1.015	1.012
YSZ062	150	NA	–	NA	–	–	–
YSZ062	240	NA	–	NA	–	–	–
YSZ062 ann.	250	NA	5.18	NA	5.26	–	1.015

Appendix D: BEN parameters used for analysed samples

Table 5.7 – List of essential parameters used for BEN processes corresponding to images reported in Chapter 5. All the processes were carried out with 30 mbar pressure in the chamber, 1100 W microwave power and 200 sccm total flow.

Name	**Figures**	**Time** (min)	**Pyrometer temperature** (°C)	CH_4/H_2 (%)	U_{bias} (V)
RBDIA005	5.2,5.55	45	790	10	300
RBDIA015	5.3(a),5.4,5.9	45	840	10	265
	5.3(b)	15	760	1	–
RBDIA019	5.49(b)	40	775	7	255
RBDIA020	5.49(a)	45	785	7	275
RBDIA021	5.5	45	790	10	265
RBDIA054	5.10(e)	60	755	10	275
		2	700	10	0
RBDIA074	5.10(d)	50	755	10	290
		1	700	10	0
RBDIA083	5.10(c)	40	730	10	285
		0.33	700	10	0
RBDIA095	5.18	40	730	10	260
		0.08	–	10	0
RBDIA096	5.10(a),5.16	40	750	10	260
		0.08	–	10	0
RBDIA099	5.15	45	750	10	260
		0.08	–	10	0
RBDIA104	5.49(d)	45	730	7	250
RBDIA129	5.10(b)	30	750	10	270
		0.17	–	10	0
RBDIA141	5.24,5.25,5.26	35	775	10	285
RBDIA157	5.23	35	730	10	270
		1	700	10	0
FH0032	5.6 [Schreck(06)]	45	725	6	265
SGDIA177	5.7 [Gsell(08)]	45	800	7	280
SGDIA007 3 3	5.8[Gsell(07)-1]	60	800	7	265 (DC plasma)
SGDIA180	5.49(c)	60	800	7	265

Bibliography

[Abaqus] http://www.simulia.com

[Abbaschian(05)] R. Abbaschian, H. Zhu, C. Clarke, *High pressurehigh temperature growth of diamond crystals using split sphere apparatus*, Diamond Relat. Mater. 14, 1916 (2005)

[Adamas] http://www.adamas.by/about-us.php

[Advanced Diamond Technologies] http://www.thindiamond.com/

[AOTC] http://aotc.com/real/growing-diamonds

[Aoyama(07)] T. Aoyama, N. Amano, T. Goto, T. Abukawa, S. Kono, Y. Ando, A. Sawabe, *Characterization of planar-diode bias-treatment in DC-plasma hetero-epitaxial diamond growth on Ir(001)*, Diamond Relat. Mater. 16, 594 (2007)

[Bachmann(91)] P. K. Bachmann, D. Leers, H. Lydtin, *Towards a general concept of diamond chemical vapour deposition*, Diamond Relat. Mater. 1, 1 (1991)

[Baither(97)] D. Baither, B. Baufeld, U. Messerschmidt, *Ferroelasticity of $t^{'}$-Zirconia: I, High Voltage Electron Micoscopy Studies of the Microstructure in Polydomain Tetragonal Zirconia*, J. Am. Ceram. Soc. 80, 1691 (1997)

[Bardal(94)] A. Bardal, Th. Matthée, J. Wecker, K. Samwer, *Initial stages of epitaxial growth of Y-stabilized ZrO_2thin films on a-SiO_x/Si(001) substrates*, J. Appl. Phys. 75, 2902 (1994)

[Barnes(93)] P. N. Barnes, R. L. C. Wu, *Nucleation enhancement of diamond with amorphous films*, Appl. Phys. Lett. 62, 37 (1993)

[Bauer(02)] Th. Bauer, M. Schreck, F. Hörmann, A. Bergmaier, G. Dollinger, B. Stritzker, *Analysis of the total carbon deposition during the bias enhanced nucleation of diamond on $Ir/SrTiO_3$ (001) using ^{13}C-methane*, Diamond Relat. Mater. 11, 493 (2002)

[Bechstedt(03)] F. Bechstedt, *Principles of Surface Physics*, Springer-Verlag Berlin Heidelberg (2003)

[Bednarski(03)] C. Bednarski, Z. Dai, A.-P. Li, B. Golding, *Studies of heteroepitaxial growth of diamond*, Diamond Relat. Mater. 12, 241 (2003)

[Bernhard(06)] P. Bernhard, C. Ziethen, G. Schoenhense, M. Schreck, T. Bauer, S. Gsell, B. Stritzker, *Structural Properties of the Diamond Nucleation Layer on Iridium Analyzed by Laterally Resolved X-Ray Absorption Spectroscopy*, Jpn. J. Appl. Phys. 45, L984 (2006)

[Binnig(86)] G. Binnig, C. F. Quate, Ch. Gerber, *Atomic force microscopy*, Phys. Rev. Lett. 56, 930 (1986)

[Bonaccorso(10)] F. Bonaccorso, Z. Sun, T. Hasan, A. C. Ferrari, *Graphene photonics and optoelectronics*, Nat. Photonics 4, 611 (2010)

[Brandes(92)] E. A. Brandes, G. B. Brook, *Smithells Metals Reference Book*, Seventh Edition, Butterworth-Heinemann Ltd (1992)

[Braun(99)] W. Braun, *Applied RHEED: reflection high-energy electron diffraction during crystal growth*, Springer-Verlag Berlin Heidelberg (1999)

[Bundy(89)] F. P. Bundy, *Pressure-temperature phase diagram of elemental carbon*, Physica A 156, 169 (1989)

[Casiraghi(07)] C. Casiraghi, J. Robertson, A. C. Ferrari, *Diamond-like carbon for data and beer storage*, Materials Today 10, 44 (2007)

[Crystallume] http://www.crystallume.com/

[Christiansen(95)] S. Christiansen, M. Albrecht, H. P. Strunk, P. O. Hansson, E. Bauser, *Reduced effective misfit in laterally limited structures such as epitaxial islands*, Appl. Phys. Lett. 66, 574 (1995)

[Christiansen(99)] S. H. Christiansen, M. Albrecht, H. P. Strunk, C. T. Foxon, D. Korakakis, I. Grzegory, S. Porowski, *Relaxation Processes of AlGaN/GaN Heterostructures Grown onto Single Crystal GaN(0001) Substrates*, phys. stat. sol. (a) 176, 285 (1999)

[Dai(03)] Z. Dai, C. Bednarski-Meinke, R. Loloee, B. Golding, *Epitaxial (100) iridium on A-plane sapphire: A system for wafer-scale diamond heteroepitaxy*, Appl. Phys. Lett. 82, 3847 (2003)

[Desjonquères(93)] M.-C. Desjonquères, D. Spanjaard, *Concepts in Surface Physics*, Springer-Verlag Berlin Heidelberg (1993)

[Dhatt(12)] G. Dhatt, G. Touzot, E. Lefrancois, *Finite Element Method*, ISTE (London) and Wiley-VCH (Hoboken) (2012)

[Dischler(98)] B. Dischler, C. Wild (Eds.), *Low-Pressure Synthetic Diamond. Manifacturing and Applications*, Springer-Verlag Berlin Heidelberg (1998)

[Ditabis] http://www.ditabis.de/index.html

[Eason(06)] R. Eason, *Pulsed Laser Deposition of Thin Films*, Wiley (2006)

[Element Six] http://www.e6.com

[Erni10] R. Erni, M. D. Rossell, P. N. H. Nakashima, *Optimization of exit-plane waves restored from HRTEM through-focal series*, Ultramicroscopy 110, 151 (2010)

[Field(79)] J. E. Field, *The properties of diamond*, Academic Press, London (1979)

[Fischer(06)] M. Fischer, *Wachstum epitaktischer Oxid- und Metallschichten auf Si*, Diploma Thesis (2006)

[Fischer(08)] M. Fischer, R. Brescia, S. Gsell, M. Schreck, T. Brugger, T. Greber, J. Osterwalder, B. Stritzker, *Growth of twin-free heteroepitaxial diamond on Ir/YSZ/Si(111)*, J. Appl. Phys. 104, 123531 (2008)

[Fork(90)] D.Fork, D.Fenner, G.Conneil, J.Phillips, T.Geballe, *Epitaxial yttria-stabilized zirconia on hydrogen-terminated Si by pulsed laser deposition*, Appl. Phys. Lett. 57, 11 (1990)

[Fujisaki(03)] T. Fujisaki, M. Tachiki, N. Taniyama, M. Kudo, H. Kawarada, *Initial growth of heteroepitaxial diamond on Ir(001)/MgO(001) substrates using antenna-edge-type microwave plasma assisted chemical vapor deposition*, Diamond Relat. Mater. 12, 246 (2003)

[Fultz(01)] B. Fultz, J. M. Howe, *Transmission Electron Microscopy and Diffractometry of Materials*, Springer-Verlag Berlin Heidelberg (2001)

[Geim(07)] A. K. Geim, K. S. Novoselov, *The rise of graphene*, Nat. Mater. 6, 183 (2007)

[Gerber(95)] J. Gerber, S. Sattel, K. Jung, H. Ehrhardt, J. Robertson, *Experimental characterisation of bias-enhanced nucleation of diamond on Si*, Diam. Relat. Mater. 4, 559 (1995)

[Goldfuß(05)] J. Goldfuß, *Herstellung und Modifizierung heteroepitaktischer Oxidschichten auf Si*, PhD Thesis (2005)

[Golding(04)] B. Golding, C. Bednarski-Meinke, Z. Dai, *Diamond heteroepitaxy: pattern formation and mechanisms*, Diamond Relat. Mater. 13, 545 (2004)

[Grobert(07)] N. Grobert, *Carbon nanotubes - becoming clean*, Materials Today 10, 28 (2007)

[Gsell(04)] S. Gsell, T. Bauer, J. Goldfuß, M. Schreck, B. Stritzker, *A route to diamond wafers by epitaxial deposition on silicon via iridium/yttria-stabilized zirconia buffer layers*, Appl. Phys. Lett. 84, 4541 (2004)

[Gsell(05)] S. Gsell, M. Schreck, T. Bauer, H. Karl, G. Thorwarth, A. Bergmaier, G. Dollinger, B. Stritzker, *The nucleation centers formed during bias-enhanced nucleation of diamond on iridium: structure and stability*, Diamond Relat. Mater. 14, 328 (2005)

[Gsell(06)] S. Gsell, M. Fischer, Th. Bauer, M. Schreck, B. Stritzker, *Yttria-stabilized zirconia films of different composition as buffer layers for the deposition of epitaxial diamond/Ir layers on Si(001)*, Diamond Relat. Mater. 15, 479 (2006)

[Gsell(07)-1] S. Gsell, M. Schreck, G. Benstetter, E. Lodermeier, B. Stritzker, *Combined AFM-SEM study of the diamond nucleation layer on Ir(001)*, Diamond Relat. Mater. 16, 665 (2007)

[Gsell(07)-2] S. Gsell, *Wachstum von großflächigen einkristallinen Diamantschichten mittels Heteroepitaxie auf Silizium: Entwicklung von Pufferschichtsystemen und Untersuchung der Nukleationsmechanismen*, PhD Thesis (2007)

[Gsell(08)] S. Gsell, S. Berner, T. Brugger, M. Schreck, R. Brescia, M. Fischer, T. Greber, J. Osterwalder, B. Stritzker, *Comparative electron diffraction study of the diamond nucleation layer on Ir(001)*, Diamond Relat. Mater. 17, 1029 (2008)

[Hassel(24)] O. Hassel, H. Mark, *Über die Kristallstruktur des Graphits*, Z. Phys. 25, 317 (1924)

[Hawkes(09)] P. W. Hawkes, *Aberration crrection past and present*, Phil. Trans. R. Soc. A367, 3637 (2009)

[Helming(95)] K. Helming, S. Geier, M. Schreck, R. Hessmer, B. Stritzker, B. Rauschenbach, *Texture analysis of chemical vapor deposited diamond films on silicon by the component method*, J. Appl. Phys. 77, 4765 (1995)

[Heuer(88)] A. H. Heuer, R. Chaim, V. Lanteri, *Review: Phase Transformations and Microstrctural Characterization of Alloys in the System Y_2O_3-ZrO_2*, Adv. Ceram. 24, 3 (1988)

[Hojo(11)] H. Hojo, E. Tochigi, T. Mizoguchi, H. Ohta, N. Shibata, B. Feng, Y. Ikuhara, *Atomic structure and strain field of threading dislocations in CeO2 thin films on yttria-stabilized ZrO2*, Appl. Phys. Lett. 98, 153104 (2011)

[Hörmann(01)] F. Hörmann, M. Schreck, B. Stritzker, *First stages of diamond nucleation on iridium buffer layers*, Diamond Relat. Mater. 10, 1617 (2001)

[Hüfner(96)] S. Hüfner, *Photoelectron Spectroscopy*, 2nd Edition, Springer-Verlag, Berlin (1996)

[Igarashi(06)] M. Igarashi, Y. Sato, N. Shibata, T. Yamamoto, Y. Ikuhara, *HRTEM study of [001] low-angle tilt grain boundaries in fiber-textured $BaTiO_3$ thin films*, J. Mater. Sci. 41, 5146 (2006)

[Isberg(02)] J. Isberg, J. Hammersberg, E. Johansson, T. Wikström, D. J. Twitchen, A. J. Whitehead, S. E. Coe, G. A. Scarsbrook, *High carrier mobility in single-crystal plasma-deposited diamond*, Science 297, 1670 (2002)

[Jiang(94)] X. Jiang, K. Schiffmann, C.-P. Klages, *Nucleation and initial growth phase of diamond thin films on (100) silicon*, Phys. Rev. B 50, 8402 (1994)

[Jiang(00)] X. Jiang, M. Fryda, C. L. Jia, *High quality heteroepitaxial diamond films on silicon: recent progresses*, Diamond Relat. Mater. 9, 1640 (2000)

[Johnson(97)] H. T. Johnson, L. B. Freund, *Mechanics of coherent and dislocated island morphologies in strained epitaxial material systems*, J. Appl. Phys. 81, 6081 (1997)

[vonKänel(95)] H. von Känel, N. Onda, L. Miglio, *Heteroepitaxy*, from *Science and Technology of Thin Films*, F.C. Matacotta, G. Ottaviani (Eds.), World Scientific, Singapore (1995)

[vonKänel(97)] Y. von Kaenel, J. Stiegler, J. Michler, E. Blank, *Stress distribution in heteroepitaxial chemical vapor deposited diamond films*, J. Appl. Phys. 81, 1726 (1997)

[Katai(00)] Sz. Kátai, A. Kováts, I. Maros, P. Deák, *Ion energy distributions and their evolution during bias-enhanced nucleation of chemical vapor deposition of diamond*, Diamond Relat. Mater. 9, 317 (2000)

[Kawarada(97)] H. Kawarada, C. Wild, N. Herres, R. Locher, P. Koidl, H. Nagasawa, *Heteroepitaxial growth of highly oriented diamond on cubic silicon carbide*, J. Appl. Phys. 81, 3490 (1997)

[Kisi(98)] E. H. Kisi, C. J. Howard, *Crystal Structures and Zirconia Phases and their Inter-Relation*, Zirconia Engineering Ceramics, Key Engineering Materials, Vol. 153-154, 1 (1998)

[Kittel(05)] C. Kittel, *Introduction to Solid State Physics - Eighth Edition*, John Wiley and Sons (2005)

[Koizumi(90)] S. Koizumi, T. Murakami, T. Inuzuka, K. Suzuki, *Epitaxial growth of diamond thin films on cubic boron nitride {111} surfaces by dc plasma chemical vapor deposition*, Appl. Phys. Lett. 57, 563 (1990)

[Koizumi(97)] S. Koizumi, M. Kamo, Y. Sato, H. Ozaki, T. Inuzuka, *Growth and characterization of phosphorous doped {111} homoepitaxial diamond thin films*, Appl. Phys. Lett. 71, 1065 (1997)

[Komet-Rhobest] http://www.kometgroup.com/plus-navigation/plus/komet-rhobest.html

[Kono(04)] S. Kono, T. Takano, T. Goto, Y. Ikejima, M. Shiraishi, T. Abukawa, T. Yamada, A. Sawabe, *Effect of bias treatment in the CVD diamond growth on Ir(001)*, Diamopnd Relat. Mater. 13, 2081 (2004)

[Kono(05)] S. Kono, M. Shiraishi, N. I. Plusnin, T. Goto, Y. Ikejima, T. Abukawa, M. Shimomura, Z. Dai, C. Bednarski-Meinke, B. Golding, *X-Ray Photoelectron Diffraction Study of the Initial Stages of CVD Diamond Heteroepitaxy on Ir(001)/$SrTiO_3$*, New Diamond and Frontier Carbon Technology 15, 363 (2005)

[Küttel(94)] O. M. Küttel, R. G. Agostino, R. Fasel, J. Osterwalder, L. Schlapbach, *X-ray photoelectron and Auger electron diffraction study of diamond and graphite surfaces*, Surf. Science 312, 131 (1994)

[Landolt(79)] *Landolt-Börnstein*, New Series III/11, Springer Verlag, Berlin (1979)

[Landolt(92)] *Landolt-Börnstein*, New Series III/29a, Springer Verlag, Berlin (1992)

[Lei(01)] C. H. Lei, G. Van Tendeloo, M. Siegert, J. Schubert, Ch. Buchal, *Structural investigation of the epitaxial yittria-stabilized zirconia films deposited on (001) silicon by laser ablation*, Journal of Crystal Growth 222, 558 (2001)

[Li(89)] Q. Li, O. Meyer, X. X. Xi, J. Geerk, G. Linker, *Growth of YBaCuO thin films on random and (100) aligned ZrO_2 substrates*, Appl. Phys. Lett. 55, 1792 (1989)

[Li(02)] J. Li, K. J. Van Vliet, T. Zhu, S. Yip, S. Suresh, *Atomistic mechanisms governing elastic limit and incipient plasticity in crystals*, Nature 418, 307 (2002)

[Lifshitz(02)] Y. Lifshitz, T. Köhler, T. Frauenheim, I. Guzmann, A. Hoffmann, R. Zhang, X. Zhou, S. Lee, *The Mechanism of Diamond Nucleation from Energetic Species*, Science 297, 1531 (2002)

[Liu(05)] B. Liu, H. Jiang, Y. Huang, S. Qu, M. F. Yu, K. C. Hwang, *Atomic-scale finite element method in multiscale computation with applications to carbon nanotubes*, Phys. Rev. B 72, 035435 (2005)

[Lu(07)] L. Lu, B. Shen, F. J. Xu, J. Xu, B. Gao, Z. J. Yang, G. Y. Zhang, X. P. Zhang, J. Xu, D. P. Yu, *Morphology of threading dislocations in high-resistivity GaN films observed by transmission electron microscopy*, J. Appl. Phys. 102, 033510 (2007)

[Metropolis(49)] N. Metropolis, S. Ulam, *The Monte Carlo Method*, J. Am. Stat. Ass. 44, 335 (1949)

[Michler(99)] J. Michler, M. Mermoux, Y. von Kaenel, A. Haouni, G. Lucazeau, E. Blank, *Residual stress in diamond films: origins and modelling*, Thin Solid Films 357, 189 (1999)

[Miskys(03)] C. R. Miskys, J. A. Garrido, C. E. Nebel, M. Hermann, O. Ambacher, M. Eickhoff, M. Stutzmann, *AlN/diamond heterojunction diodes*, Appl. Phys. Lett. 82, 290 (2003)

[Mo(09)] Y. Mo, K. T. Turner, I. Szlufarska, *Friction laws at the nanoscale*, Nature 457, 1116 (2009)

[Morales(09)] F. M. Morales, R. García, S. I. Molina, A. Aouni, P. A. Postigo, C. G. Fonstad, *Microstructural improvements of InP on GaAs (001) grown by molecular beam epitaxy by in situ hydrogenation and postgrowth annealing*, Appl. Phys. Lett. 94, 041919 (2009)

[NBS(53)] Natl. Bur. Stand. (U.S.), Circ. 539 II, 5 (1953)

[Nebel(03)] C. E. Nebel, J. Ristein, *Thin-film diamond*, Elsevier, Amsterdam (2003)

[New Age Diamonds] http://www.newagediamonds.com/

[Nix(89)] W. D. Nix, *Mechanical properties of thin films*, Metall. Trans. A 20, 2217 (1989)

[Novoselov(05)] K. S. Novoselov, A. K. Geim, S. V. Morozov, D. Jiang, M. I. Katsnelson, I. V. Grigorieva, S. V. Dubonos, A. A. Firsov, *Two-dimensional gas of massless Dirac fermions in graphene*, Nature 438, 197 (2005)

[Ohtsuka(96)] K. Ohtsuka, K. Suzuki, A. Sawabe, T. Inuzuka, *Epitaxial Growth of Diamond on Iridium*, Jpn. J. Appl. Phys. 35, L1072 (1996)

[Park(88)] S. K. Park, K. W. Miller, *Random Number Generators: Good Ones Are Hard To Find*, Communications of the ACM 31, 1192 (1988)

[Prawer(95)] S. Prawer, R. Kalish, *Ion-beam-induced transformation of diamond*, Phys. Rev. B 51, 15711 (1995)

[Prelas(98)] M. A. Prelas, G. Popovici, L. K. Bigelow, *Handbook of industrial diamonds and diamond films*, M. Dekker, New York (1998)

[Prins(92)] J. F. Prins, *Ion-implanted structures and doped layers in diamond*, Mater. Sci. Rep. 7, 275 (1992)

[Prins(03)] J. F. Prins, *Ion implantation of diamond for electronic applications*, Semicond. Sci. Technol. 18, S27 (2003)

[Reimer(85)] L. Reimer, *Scanning electron microscopy*, Springer-Verlag Berlin Heidelberg (1985)

[Robertson(02)] J. Robertson, *Diamond-like amorphous carbon*, Materials Science and Engineering R 37, 129 (2002)

[Saito(98)] T. Saito, S. Tsuruga, N. Ohya, K. Kusakabe, S. Morooka, H. Maeda, A. Sawabe, K. Suzuki, *Epitaxial nucleation of diamond on an iridium substrate by bias treatment, for microwave plasma-assisted chemical vapor deposition*, Diamond Relat. Mater. 7, 13811384 (1998)

[Samoto(08)] A. Samoto, S. Ito, A. Hotta, T. Hasebe, Y. Ando, A. Sawabe, T. Suzuki, *Investigation of heterostructure between diamond and iridium on sapphire*, Diamond Relat. Mater. 17, 1039 (2008)

[Sawabe(00)] A. Sawabe, H. Fukuda, T. Suzuki, Y. Ikuhara, T. Suzuki, *Interface between CVD diamond and iridium films*, Surf. Science 467, L845L849 (2000)

[Schaller(95)] E. Schaller, O. M. Küttel, P. Aebi, L. Schlapbach, *X-ray photoelectron diffraction of (100)-oriented chemical vapor deposited diamond films on silicon (100)*, Appl. Phys. Lett. 67, 1533 (1995)

[Schoenlein(80)] L. H. Schoenlein, L. W. Hobbs, A. H. Heuer, *Precipitation and ordering in calcia- and yttria-stabilized zirconia*, J. Appl. Cryst. 13, 375-379 (1980)

[Schreck(95)] M. Schreck, T. Baur, B. Stritzker, *Optical characterization of the cathode plasma sheath during the biasing step for diamond nucleation on silicon*, Diamond Relat. Mater. 4, 553-558 (1995)

[Schreck(97)] M. Schreck, K.-H. Thürer, R. Klarmann, B. Stritzker, *Influence of the nucleation process on the azimuthal misorientation of heteroepitaxial diamond films on Si(001)*, J. Appl. Phys., 81, 30963102 (1997)

[Schreck(99)] M. Schreck, H. Roll, B. Stritzker, *Diamond/Ir/$SrTiO_3$: A material combination for improved heteroepitaxial diamond films*, Appl. Phys. Lett. 74, 650 (1999)

[Schreck(00)] M. Schreck, H. Roll, J. Michler, E. Blank, B. Stritzker, *Stress distribution in thin heteroepitaxial diamond films on Ir/$SrTiO_3$ studied by x-ray diffraction, Raman spectroscopy, and finite element simulations*, J. Appl. Phys. 88, 2456 (2000)

[Schreck(01)-1] M. Schreck, F. Hörmann, H. Roll, T. Bauer, B. Stritzker, *Heteroepitaxial diamond films on silicon substrates and on iridium layers: Analogies and differences in nucleation and growth*, New Diam. Front. Carbon Technol. 11, 189205 (2001)

[Schreck(01)-2] M. Schreck, F. Hörmann, H. Roll, J. K. N. Lindner, B. Stritzker, *Diamond nucleation on iridium buffer layers and subsequent textured growth: A route for the realization of single-crystal diamond films*, Appl. Phys. Lett. 78, 192 (2001)

[Schreck(02)] M. Schreck, A. Schury, F. Hörmann, H. Roll, B. Stritzker, *Mosaicity reduction during growth of heteroepitaxial diamond films on iridium buffer layers: Experimental results and numerical simulations*, J. Appl. Phys. 91, 676 (2002)

[Schreck(03)] M. Schreck, Th. Bauer, S. Gsell, F. Hörmann, H. Bielefeldt, B. Stritzker, *Domain formation in diamond nucleation on iridium*, Diamond Relat. Mater. 12, 262 (2003)

[Schreck(06)] M. Schreck, F. Hörmann, S. Gsell, Th. Bauer, B. Stritzker, *Transmission electron microscopy study of the diamond nucleation layer on iridium*, Diamond Relat. Mater. 15, 460 (2006)

[Schreck(09)-1] M. Schreck, S. Gsell, R. Brescia, M. Fischer, P. Bernhard, P. Prunici, P. Hess, B. Stritzker, *Diamond nucleation on iridium: Local variations of structure and density within the BEN layer*, Diamond Relat. Mater. 18, 107 (2009)

[Schreck(09)-2] M. Schreck, *Heteroepitaxial Growth*, from *CVD Diamond for Electronic Devices and Sensors*, Ed. R. S. Sussmann Wiley, UK (2009)

[Scott(75)] H. G. Scott, *Phase relationships in the zirconia-yttria system*, Journal of Materials Science 10, 1527 (1975)

[SRIM] http://www.srim.org/

[Stepanova(05)] M. Stepanova, S. K. Dew, D. S. Karpuzov, *Self-organized metal networks at ion-etched Cu/Si and Ag/Si interfaces*, J. Appl. Phys. 97, 083536 (2005)

[Su(07)] D. Su, T. Yamada, V. O. Sherman, A. K. Tagantsev, P. Muralt, N. Setter, *Annealing effect on dislocations in $SrTiO_3/LaAlO_3$ heterostructures*, J. Appl. Phys. 101, 064102 (2007)

[Sumitomo] http://www.sumitomoelectricusa.com/

[Sun(04)] H. P. Sun, X. Q. Pan, J. H. Haeni, D. G. Schlom, *Structural evolution of dislocation half-loops in epitaxial $BaTiO_3$ thin films during high-temperature annealing*, Appl. Phys. Lett. 85, 1967 (2004)

[Tachibana(97)-2] T. Tachibana, Y. Yokota, K. Miyata, K. Kobashi, Y. Shintani, *Heteroepitaxial diamond growth process on platinum (111)*, Diamond Relat. Mater. 6, 266 (1997)

[Tachibana(97)] T. Tachibana, Y. Yokota, K. Kobashi, Y. Shintani, *X-ray diffraction pole figure measurements of diamond films grown on platinum (111)*, J. Appl. Phys. 82, 4327 (1997)

[Teufer(62)] G.Teufer, *The crystal structure of tetragonal ZrO_2*, Acta Crystallographica 15, 1187 (1962)

[Touloukian(77)] Y. S. Touloukian, R. K. Kirby, R. E. Taylor, T. Y. R. Lee, *Thermophysical Properties of Matter*, vol. 13, IFI/Plenum, New York (1977)

[Tsubota(00)] T. Tsubota, M. Ohta, K. Kusakabe, S. Morooka, M. Watanabe, H. Maeda, *Heteroepitaxial growth of diamond on an iridium (100) substrate using microwave plasma-assisted chemical vapor deposition*, Diamond Relat. Mater. 9, 1380 (2000)

[Ullmann(93)] J. Ullmann, A. Delan, G. Schmidt, *Ion etching behaviour and surface binding energies of hard diamond-like carbon and microwave chemical vapour deposition diamond films*, Diamond Relat. Mater. 2, 266 (1993)

[Vavilov(74)] V. S. Vavilov, V. V. Krasnopevtsev, Yu. V. Miljutin, A. E. Gorodetsky, A. P. Zakharov, *On structural transitions in ion-implanted diamond*, Radiation Effects 22, 141 (1974)

[Yan(04)] C. S. Yan, H. K. Mao, W. Li, J. Qian, Y. Zhao, R. J. Hemley, *Ultrahard diamond single crystals from chemical vapor deposition*, Phys. Stat. Solidi (a) 201, 25 (2004)

[Yang(95)] J. Yang, X. Su, Q. Chen, Z. Lin, *Si^+ implantation: A pretreatment method for diamond nucleation on a Si wafer*, Appl. Phys. Lett. 66, 3284 (1995)

[Yugo(91)] S. Yugo, T. Kanai, T. Kimura, T. Muto, *Generation of diamond nuclei by electric field in plasma chemical vapor deposition*, Appl. Phys. Lett. 58, 1036 (1991)

[Wang(11)] Y. Q. Wang, W. S. Liang, P. Kr. Petrov, N. McN. Alford, *Dissociation of misfit and threading dislocations in $Ba_{0.75}Sr_{0.25}TiO_3$ epitaxial film*, Mat. Character. 62, 294 (2011)

[Wild(94)] C. Wild, R. Kohl, N. Herres, W. Mller-Sebert, P. Koidl, *Oriented CVD diamond films: twin formation, structure and morphology*, Diamond Relat. Mater. 3, 373 (1994)

[Williams(09)] D. B. Williams, C. B. Carter, *Transmission electron microscopy, 2nd Ed.*, Springer Science+Business Media, New York (2009)

[Wort(08)] C. J. H. Wort, R. S. Balmer, *Diamond as an electronic material*, Mater. Today 11, 22 (2008)

[Wu(03)] Y. Wu, J. Qi, C. H. Lee, L. S. Hung, W. J. Zhang, I. Bello, Y. Lifshitz, S. T. Lee, *Diamond growth on $Ir/CaF_2/Si$ substrates*, Diamond Relat. Mater. 12, 1675 (2003)

[Zhang(94)] Y. Zhang, F. Zhang, G. Chen, *Surface energies and morphologies of chemical-vapor-deposited diamond films*, J. Appl. Phys. 76, 7805 (1994)

[Zhang(00)] W. J. Zhang, X. S. Sun, H. Y. Peng, N. Wang, C. S. Lee, I. Bello, S. T. Lee, *Diamond nucleation enhancement by direct low-energy ion-beam deposition*, Phys. Rev. B 61, 5579 (2000)

[Zhong(01)] J. Zhong, T. Zhang, Z. Zhang, M. G. Lagally, *Island-corner barrier effect in two-dimensional pattern formation at surfaces*, Phys. Rev. B 63, 113403 (2001)

[Ziegler(09)] J. F. Ziegler, J. P. Biersack, M. D. Ziegler, *The Stopping and Range of Ions in Matter*, Lulu Press Co., Morrisville (2009)

Acknowledgements

This work would not have been possible without the fundamental help of several people, among whom I would like to thank in particular:

- Prof. Dr. Bernd Stritzker, who allowed me to carry out my activity in the professional and stimulating, but at the same time friendly environment he built up in Lehrstuhl EPIV
- Dr. Matthias Schreck, an enthusiastic, rigorous and patient guide, always ready to thoroughly discuss and analyse any subject
- Prof. Dr. Ferdinand Haider for the readiness to co-supervise this work
- the Marie Curie Research and Training Network "Diamond Research on Interfaces for Versatile Electronics" (DRIVE) of the EU's Sixth Framework Programme for funding most of my project, and especially for giving me the opportunity to participate to international conferences and workshops as well as network meetings, which were fundamental to my formation and also pleasant due to the extremely friendly environment
- the STREP project NANOMESH of the EU's Sixth Framework Programme for funding part of my activity
- Dr. Stefan Gsell for his endless help and contagious passion in approaching the research work
- Prof. Dr. Jörg Lindner, Dr. Maik Häberlen and Dr. Javier García García, all of them having the patience to lead me into the "dark and green realm" of electron microscopy
- Dr. Frank Zirkelbach, who gave a fundamental contribution for the Monte Carlo simulations of 2D pattern formation under BEN (section 5.4), with his great computational experience, being not only a tireless teacher but also a true friend
- Dr. Thomas Brugger and Prof. Jürg Osterwalder (Physik-Institut, Universität Zürich) for the careful XPS and XPD analyses on the BEN and shortly grown samples
- Dr. Johann Michler and Dr. Kilian Wasmer from EMPA (Thun, Switzerland), who guided me in the use of the finite element simulation methods
- Sybille Heidemeyer, Birgit Knoblich and Wolfgang Reiber, who taught TEM preparation methods and assisted me in laboratory activities, but above all "adopted" me with their warmth, open-handedness and friendliness
- Conny Ludescher, the first one giving me a warm welcome to cold Bavaria, besides precious help to solve bureaucratic issues
- Dr. Martin Fischer, a precious co-worker, always ready to provide high quality single crystal diamond samples to be destroyed by TEM preparation or ion beam irradiation

- Wolfgang Brückner, for performing the ion implantation experiments (section 5.2) with great care
- Iulia Manolache, Dr. Andrea Falqui and Dr. Libero Manna (IIT, Genova, Italy), who always supported me at my new workplace
- Melanie, Silviu, Hadwig, Rosiana, Leonetta, Ilaria, Zoya, Michele, Tanguy, Fabio and Andrada, who accompanied me during my time in Augsburg and during the DRIVE RTN meetings and funny after-meeting trips
- last but not least, my family and my closest friends that have always been supporting me without hesitation at any moment: life would be dull and empty without this.